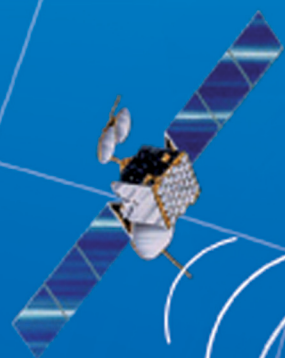




VTH INTERNATIONAL WORKSHOP ON ELECTROMAGNETIC WAVE SCATTERING



**AKDENIZ UNIVERSITY, DEPARTMENT OF ELECTRICAL
AND ELECTRONICS ENGINEERING
ANTALYA, TURKEY
OCTOBER 22-25, 2008**

SCIENTIFIC COMMITTEE MEMBERS:

CHAIRMAN:

Mithat IDEMEN (Yeditepe University), TURKEY

CO-CHAIRMAN:

Alinur BUYUKAKSOY (Gebze Institute of Technology), TURKEY

MEMBERS:

- Irsadi AKSUN (Koc University), TURKEY
- Ali ALKUMRU (Gebze Institute of Technology), TURKEY
- Jean-Michel BERNARD (CEA), FRANCE
- Tuncay BIRAND (Middle East Technical University), TURKEY
- Ovidio M. BUCCI (University of Naples), ITALY
- Dan CENSOR (Ben Gurion University of the Negev), ISRAEL
- Tuncay EGE (Gaziantep University), TURKEY
- Filiz GUNES (Yildiz Technical University), TURKEY
- Kerim GUNEY (Erciyes University), TURKEY
- Levent GUREL (Bilkent University), TURKEY
- Martti HALLIKAINEN (Helsinki University of Technology), FINLAND
- Masahiro HASHIMOTO (Osaka Electro-Communication University), JAPAN
- Altunkan HIZAL (Middle East Technical University), TURKEY
- Kazuya KOBAYASHI (Chuo University), JAPAN
- J. A. KONG (Massachusetts Institute of Technology), USA
- Mustafa KUZUOGLU (Middle East Technical University), TURKEY
- Michael LYALINOV (St. Petersburg University), RUSSIA
- Raj MITTRA (Pennsylvania State University), USA
- Frederic MOLINET (Societe MOTHESESIM), FRANCE
- Andrey OSIPOV (DLR), GERMANY
- Selcuk PAKER (Istanbul Technical University), TURKEY
- Prabhakar H. PATHAK (Ohio State University), USA
- Burak POLAT (Uludag University), TURKEY
- Alexei POPOV (IZMIRAN), RUSSIA
- Peter RUSSEY (Technical University of Munich), GERMANY
- Levent SEVGI (Dogus University), TURKEY
- Lotfollah SHAFI (University of Manitoba), CANADA
- Hiroshi SHIRAI (Chuo University), JAPAN
- Frank-Olme SPECK (Technical University of Lisbon), PORTUGAL
- Gokhan UZGOREN (Istanbul Kultur University), TURKEY
- Eldar VELIEV (Ukrainian National Academy of Sciences), UKRAINE
- Werner WIESBECK (University of Karlsruhe), GERMANY
- Erdem YAZGAN (Hacettepe University), TURKEY
- Nevzat YILDIRIM (Middle East Technical University), TURKEY
- Ning Yan ZHU (University of Stuttgart), GERMANY

ORGANIZING COMMITTEE MEMBERS:

GENERAL CHAIRMAN

Prof.Dr. A. Hamit SERBEST (Cukurova University), TURKEY

WORKSHOP CHAIRMAN

Prof.Dr. Ayhan ALTINTAS (Bilkent University), TURKEY

SECRETARY

Dr. Gokhan CINAR (Gebze Institute of Technology), TURKEY

Dr. Selcuk HELHEL (Akdeniz University), TURKEY

Dr. Ismail Hakki TAYYAR (Gebze Institute of Technology), TURKEY

AKDENIZ UNIVERSITY - LOCAL ORGANIZING COMMITTEE

Dr. Selcuk HELHEL (Akdeniz University), TURKEY

Dr. Sukru Ozen (Akdeniz University), TURKEY

Dr. Omer Colak (Akdeniz University), TURKEY

Dr.Huseyin Goksu (Akdeniz University), TURKEY

Dr.Ali Sukru Onural (Akdeniz University), TURKEY

Cumhur Basaran (Akdeniz University), TURKEY

I. Burcu Toprak (Akdeniz University), TURKEY

Dear Friends,
Dear Masters of the *Electromagnetism*,

Welcome to your own meeting in Antalya.

I thank you very much for accepting our invitation to attend this periodical *International Workshop on Electromagnetic Wave Scattering* and discuss the recent developments as well as your own achievements with your colleagues from all around the World.

We appreciate the Electromagnetic Theory because we know that it, together with the classical and quantum mechanics, is one of the basic three scientific pillars of the contemporary civilization. We are also fond of it because it constitutes a common intellectual world for all us. Its seemingly simple basic equations had unified, one hundred and thirty years ago, the three separate scientific continents of those days, namely: the electricity, the magnetism and the optics. Thus it had been an enthusiastic subject for all scientist including mathematicians, physicists and philosophers. It had also been an interesting and important example for the theory preceding experiments because it had claimed the existence of the electromagnetic waves which are, today, our common hobby. Today it still continues to open new areas for rather sophisticated technical applications such as satellite communications, medical tomography, non-destructive probing, radio-astronomy etc in addition to the classical wireless communication. We contemplate all these applications with deep admiration. So, we are indebted to all pioneers who have established and entrusted this monument to us. Among them I remember Coulomb, Ampère, Biot, Savart, Priestley, Ørsted, Faraday, Maxwell and so on. To this very short list I would like to add also Lorentz and Einstein who had believed and used this theory to re-establish the rational mechanics (i.e. the relativistic mechanics) and fundamental concepts such as the time, length, energy, mass (or momentum), etc.

I think in this *workshop*, during three days of intensive discussions, we will learn many new and interesting theoretical as well as engineering aspects of the *Electromagnetic Theory* .

With these sentiments I hope you friendly discussions and happy days in Antalya.

Prof. Dr. Mithat Idemen
Chairman
Scientific Committee of EWS'2008

Dear Colleagues,

On behalf of the Organization Committee, I am pleased to welcome you to the V. INTERNATIONAL WORKSHOP ON ELECTROMAGNETIC WAVE SCATTERING, organized by Akdeniz University and URSI Commission-B of National Committee of Turkey.

As known, EWS was initiated by a group of scientists from Turkey, Japan and Germany under the leadership of Professors Mithat İdemen and Masahiro Hashimoto and Dr. Ernst Luneburg. The previous workshops were organized in June 1991, September 1995, September 2000, October 2006, respectively. Regarding the interest which these meetings had created in the electromagnetics community, it is decided to be organized regularly every two years in Turkey.

Selected papers presented at the first workshop in 1991 are published in "Analytical and Numerical Methods in Electromagnetic Theory" by Science House Co., Tokyo, 1993. Addison Wesley Longman Ltd. printed selected papers from the second workshop in 1995 under the title "Direct and Inverse Electromagnetic Scattering," Pitman Research Notes in Mathematics Series-361, Great Britain, 1996. Finally in 2006, "Progress In Electromagnetics Research" (PIER) journal accepted to publish a Special Issue on EWS 2006. This Special Issue contains 20 papers, all of which are based on the papers presented at the EWS'2006. I am thankful to late Professor Jin Au Kong, Chief Editor of PIER for this kind consideration.

Concerning the organization of this workshop, I would like to thank to the Electronics Department of Akdeniz University and the members of the Local Organizing Committee. My special thanks and sincere gratitude goes to Assistant Professors Selçuk Helhel and Gökhan Çınar who spent almost all their time for the organization of the EWS'2008.

I would also like to thank Professor Ayhan Altıntaş from Bilkent University who is the Chairman of the Commission-B of National Committee of Turkey and also acted as the Workshop Chairman of EWS'2008.

Finally, I am sure that this conference will provide an international forum for reporting progress and recent advances in the modern development of Wave Scattering Theory. I also hope that the conference will be enjoyable for all participants.

Prof. Dr. A. Hamit Serbest

Chairman

Organizing Committee of EWS'2008

CONTENTS

SECTION 1

- 1.1. V. B. Yurchenko and E. V. Yurchenko, “*Enhanced Dual-Layer Grid Polarizers for THz Applications*” 1-1
- 1.2. K. Tap and P. H. Pathak, “*CSP beam concept, and of CSP expansion methods applied to reflector antennas, to CSP-MoM, and to Near Field-Far Field transformations*” 1-7
- 1.3. V. B. Yurchenko and L. V. Yurchenko, “*Self-Consistent Time-Domain Modeling of Short-Pulse Oscillations and Multiple Switching in a Dispersive Transmission-Line Network of Active Devices*” 1-9

SECTION 2

- 2.1. Frederic Molinet, “*Radiation of a dipole on a strongly elongated convex body*” 2-1
- 2.2. Alexei Popov, “*Parametric Theory of Parametric Resonance*” 2-9

SECTION 3

- 3.1. Dan Censor and Martin McCall, “*Ubteaching Special-Relativity: Kinematical Derivation of the Lorentz Transformation*” 3-1
- 3.2. M. V. Ivakhnychenko and E. I. Veliev, “*Scattering Properties of the Strip with Fractional Boundary Conditions*” 3-13
- 3.3. V. S. Serov, “*Some inverse scattering problems for nonlinear Schrodinger operator in 2D*” 3-19

SECTION 4

- 4.1. Mithat Idemen, Ali Alkumru, “*On the Definition and Computation of the Spreading Resistance by Tikhonov Regularization*” 4-1
- 4.2. Masahiro Hashimoto, “*Edge-Scattering from Polygonal Cylinders: Regularization of EM waves*” 4-9
- 4.3. Burak Polat, “*Field Relations on Sources Described by Zeroth and First Order Distributions in Arbitrary Motion*” 4-17

SECTION 5

- 5.1. Ozgur Ergul and Levent Gurel, “*Field-Based-Stabilized Combined Tangential Formulation for the Accurate Solution of Scattering Problems Involving Low-Contrast Dielectric Objects*” 5-1
- 5.2. Ozlem Ozgun, Raj Mittra and Mustafa Kuzuoglu, “*Characteristic Basis Finite Element Method (CBFEM-MPI) - A Parallel, Non-iterative Domain Decomposition Algorithm for the Solution of Large-scale Electromagnetic Scattering Problems*” 5-15
- 5.3. Elvin Yalçın, C. Girard, M. Cabellic, M.Héliier, G. Alquié, J.-L. Montmagnon, “*Modelling Interference Phenomena between Cosite Radiocommunication Equipments to Evaluate Systems Performance Degradation*” 5-25

SECTION 6

- 6.1. Ozgur Ergul and Levent Gurel, “*Contamination of the Accuracy of the Surface Integral Equations with the Discretization Error of the Identity Operator*” 6-1
- 6.2. Tahir Malas and Levent Gurel, “*Iterative Block Near-Field Preconditioners for Surface Integral-Equation Formulations of Dielectric Problems*” 6-13

SECTION 7

- 7.1. Jianping Zheng and Kazuya Kobayashi, “*Diffraction by a Semi-Infinite Parallel-Plate Waveguide with Sinusoidal Corrugation: Combined Wiener-Hopf and Perturbation Analysis*” 7-1
- 7.2. Feray Hacivelioglu, Alinur Büyükaksoy and Gökhan Uzgören, “*Radiation characteristics of a coaxial waveguide with opposing dielectric filled grooves*” 7-3
- 7.3. Burak Polat, “*Approximate Boundary Conditions on an Arbitrary Penetrable Sheet*” 7-5

SECTION 8

- 8.1. Ozlem Ozgun and Mustafa Kuzuoglu, “*Realization of Anisotropic Metamaterials via Coordinate Transformations*” 8-1
- 8.2. Yu. V. Shestopalov, Yu. G. Smirnov and V. V. Yakovlev, “*Development of Mathematical Methods for Reconstructing Complex Permittivity of a Scatterer in a Waveguide*” 8-11
- 8.3. Ali Eren Culhaoglu, Andrey Osipov and Peter Russer, “*Numerical analysis of focusing by a metamaterial lens*” 8-13

SECTION 9

- 9.1. Yusuf Z. Umul, “*Nonuniform currents of the physical theory of diffraction in terms of the modified theory of physical optics*” 9-1
- 9.2. Ugur Saynak, Alper Colak, Yasin Avcibasi, Deniz Bolukbas, I. Hakki Tayyar and Caner Ozdemir, “*2-D ISAR Imaging of Complex Objects Using Shooting-Bouncing Ray (SBR) and Physical Theory of Diffraction (PTD) Techniques*” 9-7
- 9.3. H. Avni Serim, H. Arda Ülkü, Soner Karaca, Hilmi Öztürk, and A. Arif Ergin, “*Geometric Evaluation of Physical Optics Integrals Using A Time-Domain Approach*” 9-15

SECTION 10

- 10.1. Beyza Ardic, Adnan Kaya, Ozlem Coskun and Ahmet Irkin, “*Slot-Loaded Microstrip Antenna Design of Broadband Transceiver for Wireless Data Communication in ISM Band*” 10-1
- 10.2. Ozgur Ergul and Levent Gurel, “*Hierarchical Parallelization of MLFMA for the Efficient Solution of Large-Scale Electromagnetics Problems*” 10-3

SECTION 11

- 11.1. M. B. Tabakcioglu and A. Kara, “*Discussions of Various UTD and PO Solutions for Multiple-Edge Diffractions in Urban Radio Propagation Modeling*” 11-1
- 11.2. V. B. Yurchenko and A. Altintas , “*Advanced Physical Optics Modeling of THz Dielectric Lenses*” 11-7
- 11.3. Mustafa Turkmen, Sabri Kaya, Celal Yildiz and Kerim Guney, “*Adaptive Neuro-Fuzzy Inference System for Calculating the Characteristic Impedances of Multilayer Homogeneous Coupling Structures*” 11-15
- 11.4. A. Kara, E. Uray Aydin, M.E. Ozbek, N. Cagiltay, R. Oktem, C.C. Aydin, E. Ozyurt, M. Atas and A.C. Yapici, “*Remote Experimentation in RF and Microwaves*” 11-21

SECTION 1

- 1.1. V. B. Yurchenko and E. V. Yurchenko, “*Enhanced Dual-Layer Grid Polarizers for THz Applications*” 1-1
- 1.2. K. Tap and P. H. Pathak, “*CSP beam concept, and of CSP expansion methods applied to reflector antennas, to CSP-MoM, and to Near Field-Far Field transformations*” 1-7
- 1.3. V. B. Yurchenko and L. V. Yurchenko, “*Self-Consistent Time-Domain Modeling of Short-Pulse Oscillations and Multiple Switching in a Dispersive Transmission-Line Network of Active Devices*” 1-9

Enhanced Dual-Layer Grid Polarizers for THz Applications

V. B. Yurchenko¹ and E. V. Yurchenko²

¹Institute of Radiophysics and Electronics, National Academy of Sciences of Ukraine
12 Proskura St., Kharkov, Ukraine

²“Precision Devices”, 12 Proskura St., Kharkov, Ukraine

Abstract – Dual-layer frequency-selective wire-grid polarizers are proposed for THz and sub-THz applications. Dual-layer grid polarizers possess enhanced (squared) polarizing efficiency at a sequence of discrete frequencies in reflection and within extended frequency bands in transmission as compared to conventional single grids.

1. INTRODUCTION

This work is concerned with development of enhanced dual-layer grid polarizers of record-breaking performance in THz and sub-THz bands as compared to conventional grids. Enhanced THz polarizers are needed in astrophysics (detection of cosmic microwave background polarization at the level of -80 dB), polarization interferometry (space-borne defense-related systems), polarimetric remote sensing and security checks (target detection and recognition), spectroscopy (atmospheric research, chemical and pharmaceutical industry) and other areas.

Despite the availability of advanced technologies, manufacturing high-quality THz band polarizers is a complicated problem [1]. Ideally, the finer grid, the better is the polarizer. In practice, finite conductivity of wires and irregularities of grids impose limitations, which become more restrictive for finer grids at the higher operation frequencies. Eventually, finite conductivity sets an absolute upper limit on the efficiency of THz polarizers when extremely thin wires are used in these devices.

A possible way of relaxing the limitations is the use of multi-layer grid structures (photonic devices) of subwavelength period of each grid, though of resonant inter-layer spacing. The latter should improve the polarizer performance and increase the efficiency in THz band when using relatively coarse grids of thick wires, which are less expensive and much easier to produce and operate.

Though multi-grid structures have been studied for many applications [2, 3], there is only one report published recently that suggests a possibility of multiplication of extinction ratio of two polarizers in tandem [4]. In that instance, however, the authors based their conclusions on Mueller matrices of abstract polarizers that do not account for the correct self-consistent solution of the electromagnetic problem and, as a result, missed a range of frequency-selective properties (the fact that the extinction ratio increases at certain frequencies while decreases at others, the dependence of the effect on transmission or reflection mode of operation, etc).

Computer simulations made recently for special dual-layer grids [5] predict a resonant growth of polarization extinction ratio (up to 80 dB instead of the initial 40 dB for some realistic design, in line with proposition [4]) which is expected in certain frequency bands or at particular frequencies, depending on the choice of either transmission or reflection mode of operation (a notion of strong frequency effects has been missed in [4]).

The aim of this work is to develop a practical design and undertake experimental manufacturing of a few sets of polarizer-analyzer pairs of dual-layer wire-grid polarizers with subsequent experimental testing of their polarizing efficiency. The sets would include both the fine-grid devices for high-frequency (sub-THz) electromagnetic performance and relatively coarse model structures for detailed measurements of their polarization characteristics at relatively low frequencies in the band of $f = 50 - 80$ GHz.

2. NUMERICAL SIMULATIONS

Developing THz and sub-THz polarizers is a challenging issue because of constrained manufacturing and operation requirements. Numerical simulations allow one to optimize the design of dual-layer grid structures with account of realistic parameters of devices and their operation conditions.

When simulating dual-layer grid polarizers, one can use an asymptotic model based on the effective boundary conditions for subwavelength grids obtained by L. A. Wainshtein. The conditions relate the averaged (smoothed) values of the electric and magnetic fields on the opposite sides of a subwavelength grid for both polarizations of the incident wave. By using the boundary conditions, one can evaluate, as a self-consistent electromagnetic solution, both the transmission and reflection coefficients of a composite structure made of a few layers of grids of any orientation and a few layers of any dielectric materials, for any polarization and inclination of incident electromagnetic wave [5].

The model developed in our simulations takes into account both the geometrical parameters of grids (the wire diameter w , the grid period p , the inter-layer spacing b) and the electrical conductivity σ of wires (the model assumes $b \sim \lambda \gg p$ where λ is the radiation wavelength). For the purpose of manufacturing and electromagnetic testing of polarizers in the frequency band of $f = 50 - 80$ GHz available in the experiment ($\lambda = 6.00 - 3.75$ mm), we simulated dual-layer grid structures characterized by the following set of parameters: $w = 0.08$ mm, $p = 0.32$ mm, $b = 1.3$ mm, and $\sigma = 10^7$ Sm/m (Figs. 1- 5).

Keeping in mind essential systematic effects common for experimental and real operation conditions (a limited beam width of radiation in connection with angular dependence of polarizer performance), both the uniform plane wave (curves “n_1” and “n_2”) and the actual Gaussian beam excitation typical for the experiment (curves “ns_1” and “ns_2”) have been considered and taken into account.

Computer simulations reveal the following properties of dual-layer grid polarizers:

(a) a significant (quadratic) growth of polarization ratio in reflected waves (the ratio $R_{RE} = E_R / H_R$ of reflected amplitudes for the incident E- (co-) and H- (cross-) polarized waves when either E or H field is parallel to grid wires) that happens at certain "spike" frequencies f_n (Fig. 1, a),

(b) a similar quadratic growth of polarization ratio in transmitted waves (the ratio $R_{TR} = H_T / E_T$ of transmitted amplitudes for the incident H- (cross-) and E- (co-) polarized waves) that occurs in extended frequency bands centered around the "spike" frequencies f_n (Fig. 1, b),

(c) a similar kind of effects for polarization ratios defined by relating reflected and transmitted waves of the same incident polarization, $R_H = H_T / H_R$ and $R_E = E_R / E_T$, respectively (Fig. 2, a and b),

(d) a precise 3dB splitting of the incident non-polarized beam into reflected and transmitted polarized waves that occurs at the "spike" frequencies f_n regardless of the parameters of separate grids (Fig. 3, a),

(e) a significant resonant absorption that occurs at the resonant frequencies f_n^{RES} (Fig. 3, b), that, however, is not critical, since the structure is not going to be used at the resonant frequencies.

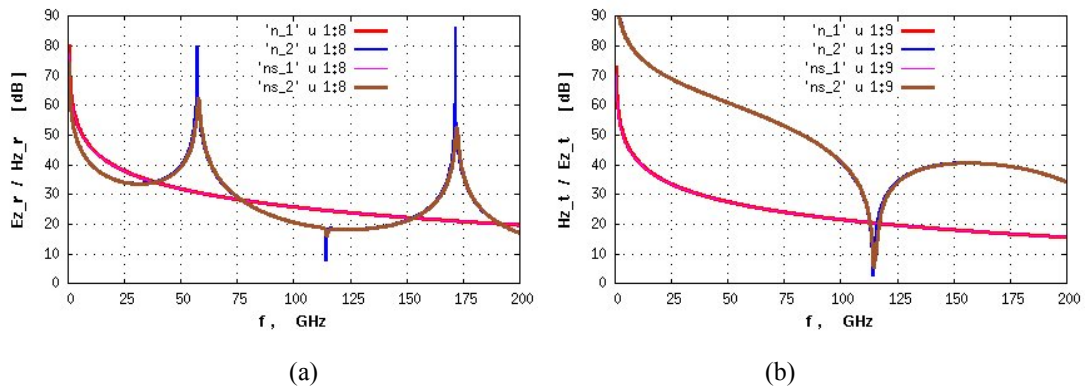


Figure 1. Polarization ratio (a) $R_{RE} = E_R / H_R$ and (b) $R_{TR} = H_T / E_T$ defined by considering reflected and transmitted waves at relevant polarizations of the incident field in the case of single-layer (n1, ns1) and dual-layer grids (n2, ns2) under the plane wave (n1, n2) and the Gaussian beam (ns1, ns2) excitation.

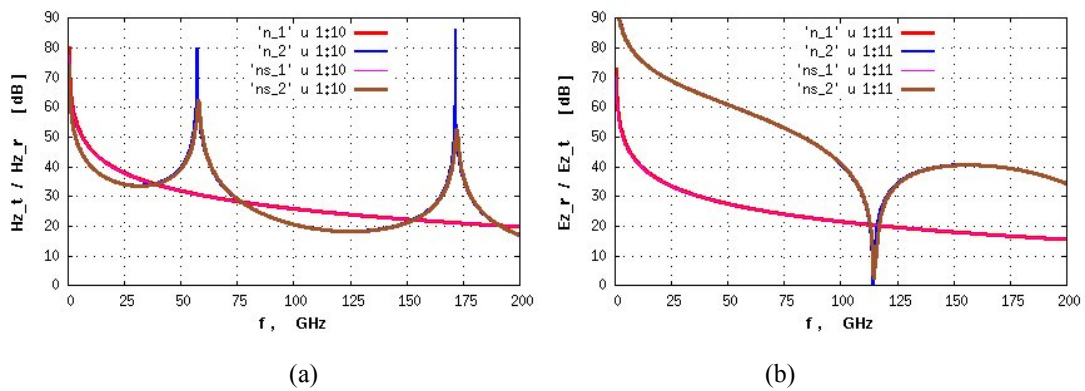


Figure 2. Polarization ratio (a) $R_H = H_T / H_R$ and (b) $R_E = E_R / E_T$ defined by relating reflected and transmitted waves of the same incident polarization.

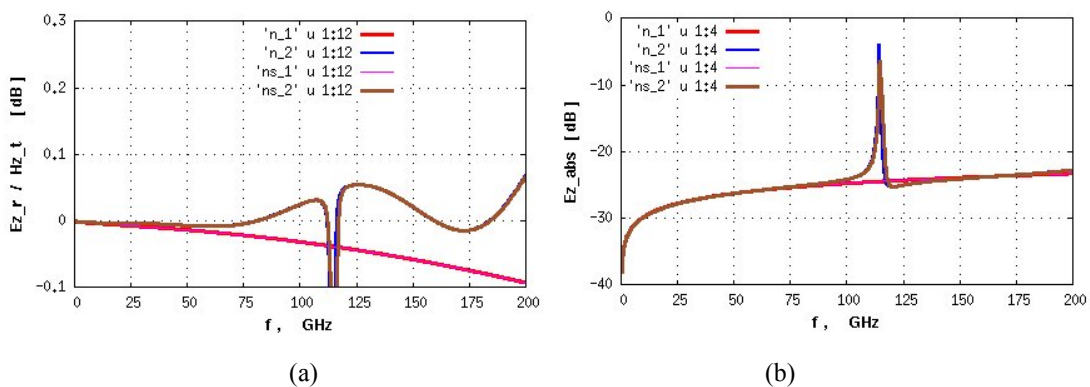


Figure 3. (a) Polarizing beam power splitting and (b) power absorption by a dual-layer (n2, ns2) and a single-layer (n1, ns1) grid structure.

Notice, the angular divergence of Gaussian beam (estimated to be in the range of 20 - 16 degrees in the frequency band of $f = 50 - 80$ GHz in this example) imposes a limit on polarization ratio at the “spike” frequencies in reflection as compared to the plane wave incidence, though no reduction of polarization is observed in transmission (other imperfections, e.g., non-uniform inter-layer spacing, produce similar effects). In this case, for the given dual-layer polarizer and beam parameters, we obtain the same polarization ratio at the “spike” frequency $f_i = 57.7$ GHz at the level of 60 dB in both reflection and transmission as compared to 30 dB for a similar grid of a single-layer device.

Figures 4 and 5 explain the enhancement of dual-layer grid polarizers by showing the frequency dependence of reflected and transmitted power of co- and cross-polarized waves. The reason for the enhancement is the suppression of (small) reflected cross-polarized component (H wave, with E field orthogonal to grid wires) and transmitted co-component (E wave, with E field parallel to grid wires) that occurs due to destructive interference of relevant waves. This happens at the “quarter-wave-plate” condition on the inter-grid spacing $d = (2n-1) \lambda/4$ where $n = 1, 2, 3, \dots$. This is precisely the condition of "spike" frequencies f_n . Meanwhile, conventional half-wavelength resonant frequencies ($d = n \lambda/2$) correspond to the dips of polarizing efficiency due to increased transparency of dual-layer grids for co-polarized waves at the resonant conditions.

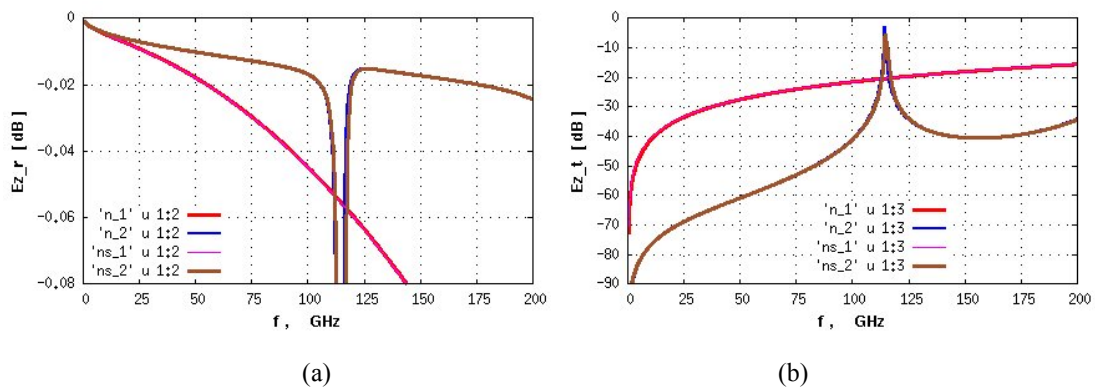


Figure 4. (a) Reflected and (b) transmitted waves of E polarization in the case of single-layer and dual-layer grids.

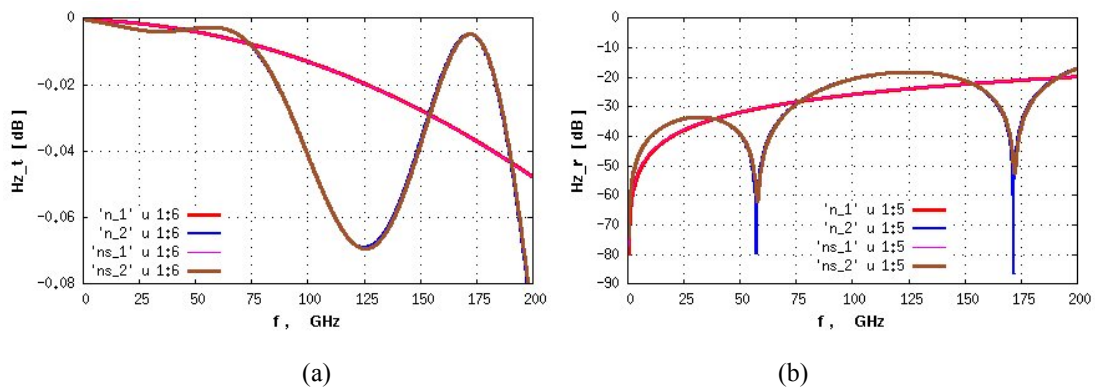


Figure 5. (a) Transmitted and (b) reflected waves of H polarization in the case of single-layer and dual-layer grids.

3. EXPERIMENTAL ISSUES

A few sets of dual-layer grid polarizers are going to be manufactured, with each polarizer being made as an assembly of two parallel wire grids stretched over the frame of appropriate aperture and thickness. The grids in each assembly should be sufficiently planar and parallel, with non-planarity and non-parallelism of grid planes less than plus-minus 0.02 mm over the aperture area in order to keep polarization ratio at the “spike” frequencies in reflection at the same level of 60 dB as discussed above. Similarly, misalignment of wires of two grids should be better than 3 arcminutes that corresponds to misfit of wires of different grids by about $w = 0.08$ mm (about one wire diameter) at one end of the grid pair as compared to the other end (assuming the grid aperture size $L_G = 90$ mm).

A pair of dual-layer polarizers that constitutes one polarizer-analyzer set is needed for polarization experiments. Dual-layer polarizers of one set made of the wire grids described above are going to be tested at relatively low frequencies of $f=50-80$ GHz. The other sets based on the finer grids will be used at the higher frequencies, e.g., in the frequency band of $f=110-150$ GHz and, eventually, at the frequencies up to $f=300$ GHz.

Requirements for high-frequency testing of enhanced polarizers are demanding. In addition to precise positioning of polarizers in cross-orientation with accuracy better than 3 arcminutes for maintaining spurious signals below -60dB (1 arcminute for -70dB), detection of signals of ultra-low level is needed. As a promising way of solving the problem, one may use a resonator technique being developed for electromagnetic testing of ultra-low-loss materials [6].

If using an open resonator designed for the frequency band of $f=50-80$ GHz, which is made of two concave mirrors of the diameter $D_M=100$ mm and the curvature radius $R_M=110$ mm placed at the distance $L_M=160$ mm one from another, one obtains a Gaussian beam of half-width $w_0=10-7.5$ mm at the beam waist and $w_M=20-15$ mm at the resonator mirrors. The beam of this kind is characterized by the angular divergence of 20-16 degrees mentioned above and maintains a spurious signal at the rim of the grid aperture of typical size $L_G = 90$ mm at the level below -60 dB while having the grid in the middle of the resonator tilted at 45 degrees with respect to the resonator axis (at the normal grid orientation, the grid aperture size has to be $L_G > 52$ mm at the beam waist and $L_G > 104$ mm at the resonator mirrors).

When expressing electromagnetic properties of a subwavelength grid in terms of homogenized parameters, one can compute the effective permittivity of grid in both co- and cross-polarized orientations (in co-polarization, the effective permittivity is negative and resembles the permittivity of plasma below the plasma frequency). Then, by measuring the effective permittivity of a dual-layer grid, one can verify the electromagnetic parameters of the entire structure against numerical simulations.

An alternative representation of the same data is the plot of complex scattering matrix coefficients S_{11} , S_{12} that shows specific features of resonant behavior of dual-layer grid polarizers, thus providing both the qualitative and quantitative characterization of these devices.

4. CONCLUSIONS

In conclusion, dual-layer grid polarizers are expected to have the following advantages as compared to conventional grids:

- (a) a significant increase of efficiency, even in the case of coarse grids of thick wires with account of possible grid irregularities and imperfections,

- (b) an increase of the absolute upper limit of efficiency achievable with fine grids,
- (c) frequency-selective performance in either broad (in transmission) or narrow (in reflection) frequency bands, and
- (d) a possibility of tuning the operation bands by varying the device inter-layer spacing or tilting the polarizer with respect to the incident wave.

Further development of dual-layer grid polarizers may require the fabrication of grids on thin-film low-loss dielectric substrates by using photolithographic methods for the better control of tolerances as necessary for pushing the operating frequencies higher into the THz band.

ACKNOWLEDGEMENT

Effort sponsored by the Air Force Office of Scientific Research, Air Force Material Command, USAF, under grant number FA8655-08-1-3049. The U.S. Government is authorized to reproduce and distribute reprints for Governmental purpose notwithstanding any copyright notation thereon.

REFERENCES

- [1] Wang, J. J. et al., "Innovative high-performance nanowire-grid polarizers and integrated isolators," *IEEE J. Select. Topics Quantum Electron.*, Vol. 11, No. 1, 241-253, 2005.
- [2] Deguzman, P. C. and G. P. Nordin, "Stacked subwavelength gratings as circular polarization filters," *Appl. Optics*, Vol. 40, No. 31, 5731-5737, 2001.
- [3] Arzhannikov, A. V. and S. A. Kuznetsov, "Multigrid interference structures with variable selective characteristics," in *Digest of the 2004 Joint 29th Int. Conf. on Infrared and Millimeter Waves and 12th Int. Conf. on Terahertz Electronics*, September - October 2004, 353-354.
- [4] Boer, J. H. W. G. den, G. M. W. Kroesen, W. de Zeeuw and F. J. de Hoog, "Improved polarizer in the infrared: Two wire-grid polarizers in tandem," *Opt. Lett.*, Vol. 20, No. 7, 800-802, 1995.
- [5] Yurchenko, V. B. and E. V. Yurchenko, "Dual-layer frequency-selective subwavelength-grid polarizers for THz applications," in *Proceedings of the 6th Intl. Kharkov Symposium on Physics and Engineering of Microwaves, Millimeter and Submillimeter Waves and Workshop on Terahertz Technologies (MSMW'07)*, Kharkov, Ukraine, June 2007, 222-224.
- [6] Krupnov, A. F., V. N. Markov, G. Y. Golubyatnikov, I. I. Leonov, Y. N. Konoplev and V. V. Parshin, "Ultra-low absorption measurement in dielectrics in millimeter- and submillimeter-wave range," *IEEE Trans. Microwave Theory Tech.*, Vol. 47, No. 3, 284-289, 1999.

CSP beam concept, and of CSP expansion methods applied to reflector antennas, to CSP-MoM, and to Near Field-Far Field transformations

K. Tap and P. H. Pathak

Not available at the time of publication

Self-Consistent Time-Domain Modeling of Short-Pulse Oscillations and Multiple Switching in a Dispersive Transmission-Line Network of Active Devices

V. B. Yurchenko and L. V. Yurchenko

Institute of Radiophysics and Electronics, National Academy of Sciences of Ukraine
12 Proskura St., Kharkov, Ukraine

Abstract – Time-domain simulations of active systems with Gunn diodes connected by sections of microstrip transmission lines (TL) are carried out. Self-generation of Gunn diodes mounted in various ways in the TL circuits has been investigated. Complex dynamics of electromagnetic field radiated into an open end of the TL are observed. Trains of high-frequency pulses are shown to emerge when active devices are separated from compact resonant circuits by extended sections of the TL providing a time-delayed feedback.

1. INTRODUCTION

We perform time-domain computer simulations of nonlinear self-oscillations in distributed microstrip transmission line systems with active devices specified by negative differential resistance (NDR) of current-voltage characteristics such as of Gunn diodes and similar structures. There are two main goals of this research which concern both the theoretical and practical aspects of the problem:

- 1) Developing mathematical models, numerical techniques and computer codes for the efficient self-consistent time-domain simulation of high-frequency excitation in distributed systems with a strong time-delayed coupling between active devices connected by sections of transmission lines;
- 2) Investigating available options of microstrip implementation of nonlinear power combining (superlinear in the number of devices) and non-conventional spectral effects (ultra-wideband chaotic oscillations etc) for possible practical applications in high-frequency electronic systems (ultra-short pulse generation, noise radars, etc).

Microwave power combining has been investigated for a long time. Initially, there were lumped circuits being considered. Later on, waveguide network [1, 2] and quasi-optical array systems [3, 4] have been proposed. Despite numerous achievements [4, 5], efficient power combining remains a challenging problem. There are important physical reasons for this, such as the distributed character of systems whose size is large compared to the wavelength (especially, when considering open radiating systems), broadband and multi-frequency dynamics of oscillations, etc.

Nowadays, the major goal is the power combining in the THz bands where the power output of individual devices is intrinsically limited by the physical processes involved (the main relaxation channels in both the devices and the environment occur precisely in this domain). In the meantime, conventional design and simulation techniques (e.g., the impedance analysis method) are insufficient for these systems [6, 7], being only valid in a small-signal approximation for narrow-band applications. On the other hand,

advanced numerical methods (e.g., [8]) require huge computational resources and become inefficient in many cases.

The active character of devices specified by instability and nonlinearity makes common simulation tools (e.g., Flomerics Micro-Strips etc) inadequate for the rigorous modeling of such systems. Other software, such as SPICE, cannot cope with distributed systems where the wave propagation between the devices is an essential part of the system operation. A promising approach is the hybrid numerical methods [9] that combine both the frequency-domain and the time-domain computations, though they also suffer from various limitations (narrow-band approximation etc).

For these reasons, the design of active structures is usually split in two separate stages dealing with either linear or nonlinear parts of the system. In this method, the attention is focused on passive components whose design is carried out in much detail. As a price for this simplification, some assumptions are supposed to be met such as the operation of the system in the narrow band or in a given set of a few narrow bands, etc.

In this work, we choose an alternative approach and focus our attention on the nonlinear part of the problem, while the linear part is chosen to be relatively simple. In this approach, the aim is the accurate self-consistent modeling of nonlinear effects through rigorous solutions of governing equations and, specifically, accurate time-domain simulations of nonlinear oscillations and non-conventional dynamics (chaos, pulses) emerging in various conditions [10-13]. As a practical issue, nonlinear power combining is investigated in a rigorous manner.

By reducing the linear part of the problem to the simplest form, we arrive at a set of discrete devices connected by sections of one-dimensional transmission lines, e.g., microstrips. Microstrips excited by solid-state devices are rather practical solutions for various applications. A study of one-dimensional models provides also a benchmark for testing various computational methods ranging from analytic approximations to advanced numerical tools.

In quasi-optical applications, parallel coupling of active devices in a single array is used for increasing the power output [4] (in microwaves, similar ideas were implemented in the waveguides [1]). A one-dimensional analogue of this system is the parallel connection of transmission line circuits, with microwave power being radiated into an open infinite section of the line (the latter models the radiation of the electromagnetic waves from the antennas into free space in three-dimensional open systems).

As an alternative system, a series connection of active devices in a long transmission line (a ladder-type oscillator) represents a simple model of an open active structure with distributed elements that could be used for the efficient spectrum modification of THz radiation. Recent simulations of a chain of Gunn diodes [10] revealed an interesting dynamics of the electromagnetic field in this system, though more detailed analysis of this structure is needed.

The interest in the systems of this kind is justified by their potential applications as the sources of chaotic signals for the emerging field of the noise radar technology [14]. This technology provides a number of benefits such as an ultra-wideband spectrum of radiation, simultaneous detection of the position and the velocity of the target, operation below the noise level of the environment, and other advantages. For these reasons, THz applications and, especially, MMIC implementations of these systems are of particular interest.

2. SIMULATION OF PARALLEL TIME-DELAY NETWORKS OF ACTIVE DEVICES

Simulation approach outlined above was applied earlier to a few kinds of time-delay circuits with active devices (Gunn diodes) of relatively simple configurations [10-13]. They were mostly series networks of a few devices with time-delay microstrip coupling or single-diode systems with time-delay feedback where complicated dynamics of high-frequency radiation field have been predicted [10-13].

Here we consider another system, which is a parallel time-delay network of active devices as shown in Fig. 1, a. All active blocks in this network ($n = 1, \dots, N$) are identical, being of the kind shown in Fig. 1, b. A common passive block ($n=0$) is of the kind shown in Fig. 1, c. The block operates as a remote resonator for the given set of active devices and, in the same time, as a resonant antenna that transmits electromagnetic radiation into an open (infinite) section of microstrip line as shown in Fig. 1, a. Microstrip lines of length d_n and d_{sn} provide time-delay coupling and feedback in this system. They are supposed to be sufficiently long as compared to characteristic wavelength of emerging radiation.

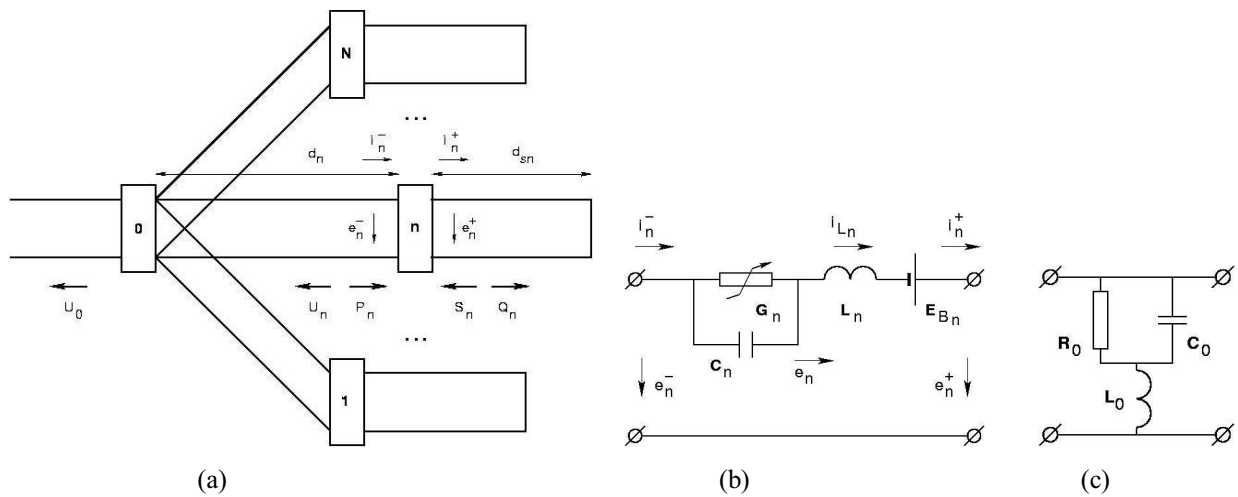


Figure 1. (a) A network of active circuits connected by sections of microstrip transmission lines and schematics of (b) active circuits used in the network and (c) a resonant circuit used as an antenna node $n=0$.

When considering a network with a single active circuit ($N=1$), we found a possibility for the system to generate a train of high-frequency pulses radiated into an open section of microstrip line (Fig. 2). The pulses are excited when the bias voltage E_{Bn} is increased above a threshold value (the system is turned on) and cease when E_{Bn} is reduced below the threshold.

A characteristic feature of the effect is that the pulse duration t_p equals to the time interval between the pulses Δt_p and each of them is close to the duration of the round trip of a signal from the active device ($n=1$) to the remote resonator ($n=0$) and back to the active device ($n=1$). Thus, the spatial length of each pulse in an infinite microstrip line $L_p = c t_p$ (c is the speed of wave in the line) is about twice the length of the microstrip section, $L_p = 2d_n$.

The carrier frequency of each pulse ω is determined by the intrinsic frequency of active circuits, and the optimal condition for the formation of a clear sequence of pulses is the coincidence of intrinsic frequencies of the remote resonator ($n=0$) and the active circuit ($n=1$), while the length of microstrip section d_n that provides a time-delay coupling is required to be large enough for the pulse duration t_p to be much greater than the oscillation period $\tau = 2\pi/\omega$.

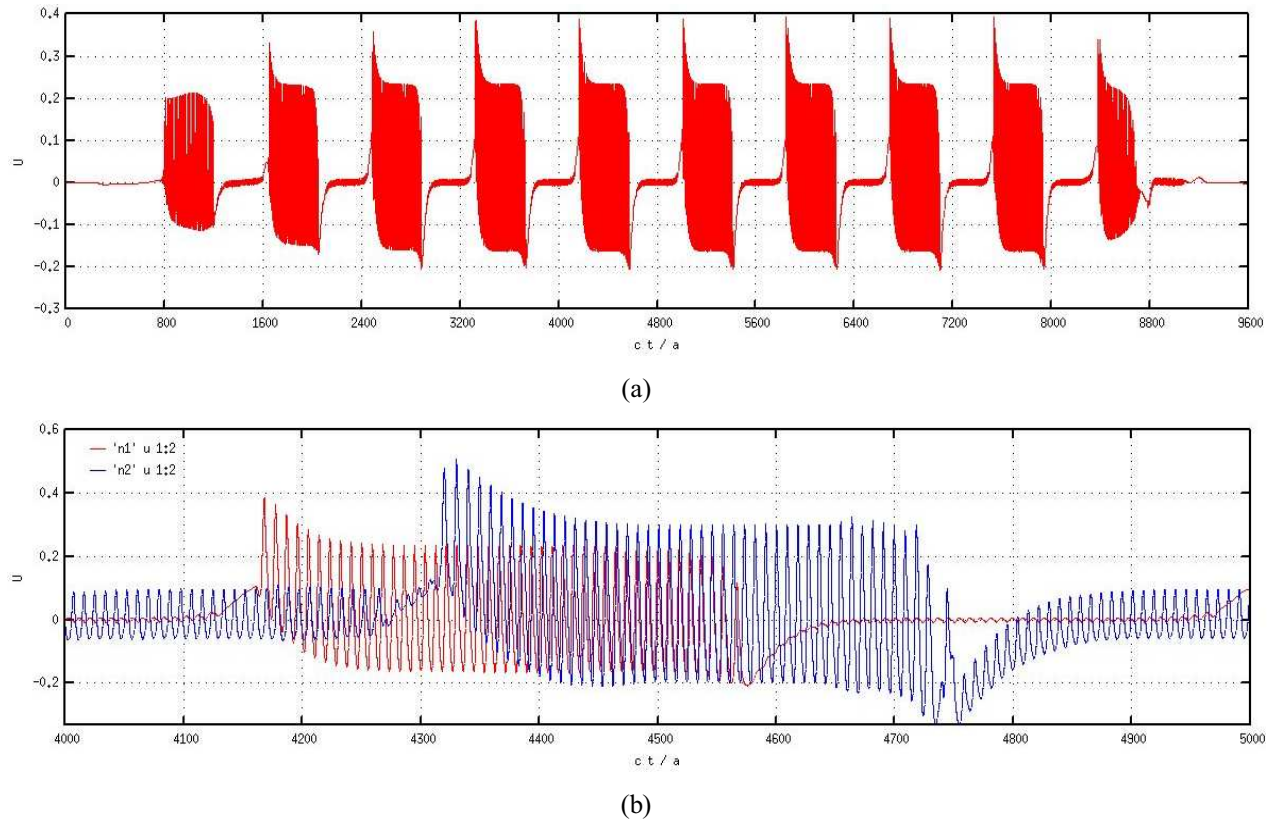


Figure 2. A train of high-frequency pulses radiated from the system of one Gunn-diode active circuit (red curves in a and b) and two identical active circuits (blue curve in b) when the circuits are connected to the antenna node $n=0$ by microstrip transmission lines of length $d_n = 200$ (in relative units where the pulse radiation wavelength is $\lambda=9.0$).

The formation of train of pulses and the main conditions for this could be explained as follows. If the active circuit is designed so that oscillations are excited when no resonator is present at the antenna node $n=0$, the oscillations arise and exist for the duration of time t_p until the feedback signal returns from the remote resonator ($n=0$) to the active node ($n=1$). Then, if the design of the entire system including both the active circuit and the remote resonator is of such a kind that oscillations cannot exist in the entire system, the oscillations cease for the period of time Δt_p when active circuit receives a feedback from the node $n=0$ and, in this way, “feels” the presence of remote resonator. After that time, the feedback disappears, the active circuit does not “feel” any remote resonator again, and a new pulse of oscillations arises.

When connecting two identical branches of active circuits in parallel to the antenna node, we obtain a similar train of pulses radiated from the system, though of slightly different parameters (Fig. 2, b). With increasing the number of branches, the oscillations may not cease completely between the pulses and the entire process becomes more complicated.

Keeping in mind the explanation of the effect given above, we may consider the networks of multiple time-delay branches of different length of microstrip sections. With account of different times of arriving time-delay feedbacks from different circuits and nonlinear mixing of oscillations in active devices, we can expect the development of complicated and, potentially, chaotic or quasi-chaotic oscillations that could be

of interest for certain applications [14].

Consider now the network of two branches of identical active circuits of the kind shown in Fig. 1, though of different and, preferably, non-commensurable length of time-delay microstrip sections d_n . In this case, despite the relative simplicity of active system, there will be a complicated mixing of time-delay feedbacks in different branches of active devices, thus, providing a complicated (virtually, quasi-chaotic in the lower frequency bands) nonlinear oscillations as shown, e.g., in Fig. 3 (a similar effect should also arise in the networks of dispersive transmission lines because of different propagation time of different frequency components).

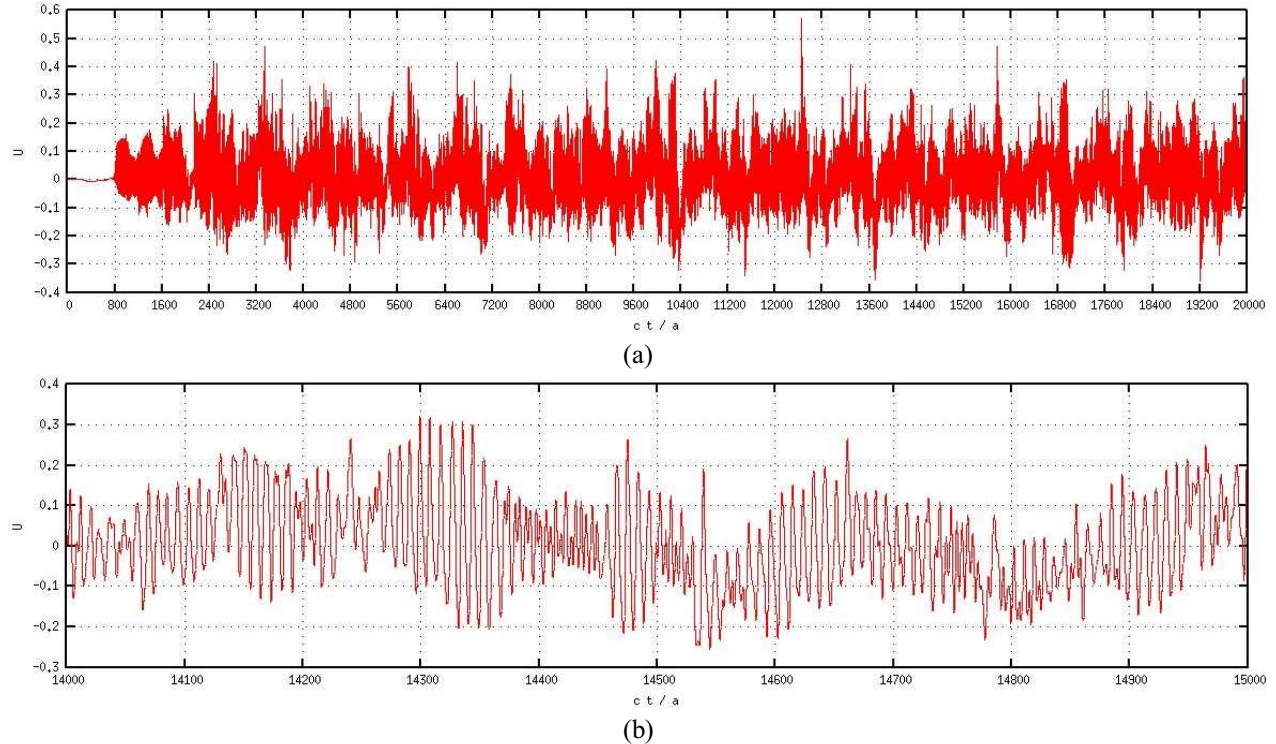


Figure 3. A quasi-chaotic signal radiated from a system of two active circuits connected to the antenna node by transmission lines of length $d_1 = 200$ and $d_2 = 266.67$, respectively, when the basic radiation wavelength at the emerging carrier frequency is $\lambda = 8.6$.

In this example, even though there is a certain carrier frequency due to intrinsic oscillations of active circuits, the entire waveform that corresponds to the lower frequency band as compared to the carrier frequency, is rather chaotic and remains so for a long period of time being simulated (here we choose the length parameters $d_1 = 200$ and $d_2 = 266.67$ in relative units, while the carrier oscillation period is $\tau = 8.6$).

Quasi-chaotic character of low-pass-band signal radiated from the system is well illustrated by the plots of auto-correlation function and Poincare section computed for the emerging oscillations (Figs. 4–5). When comparing auto-correlation functions (Fig. 4) of train of pulses and quasi-chaotic signal, one can see a reversal of correlation over the period of pulse repetition (at $\tau \sim 840$ in Fig. 4) and a significant loss of correlation in quasi-chaotic signal at all times exceeding the period of oscillations ($\tau = 8.6$).

In a similar way, Poincare sections (Fig. 5) clearly show the presence of periodicity in the train of pulses over a long period of time and the lack of long-term periodicity in quasi-chaotic signal of Fig. 3

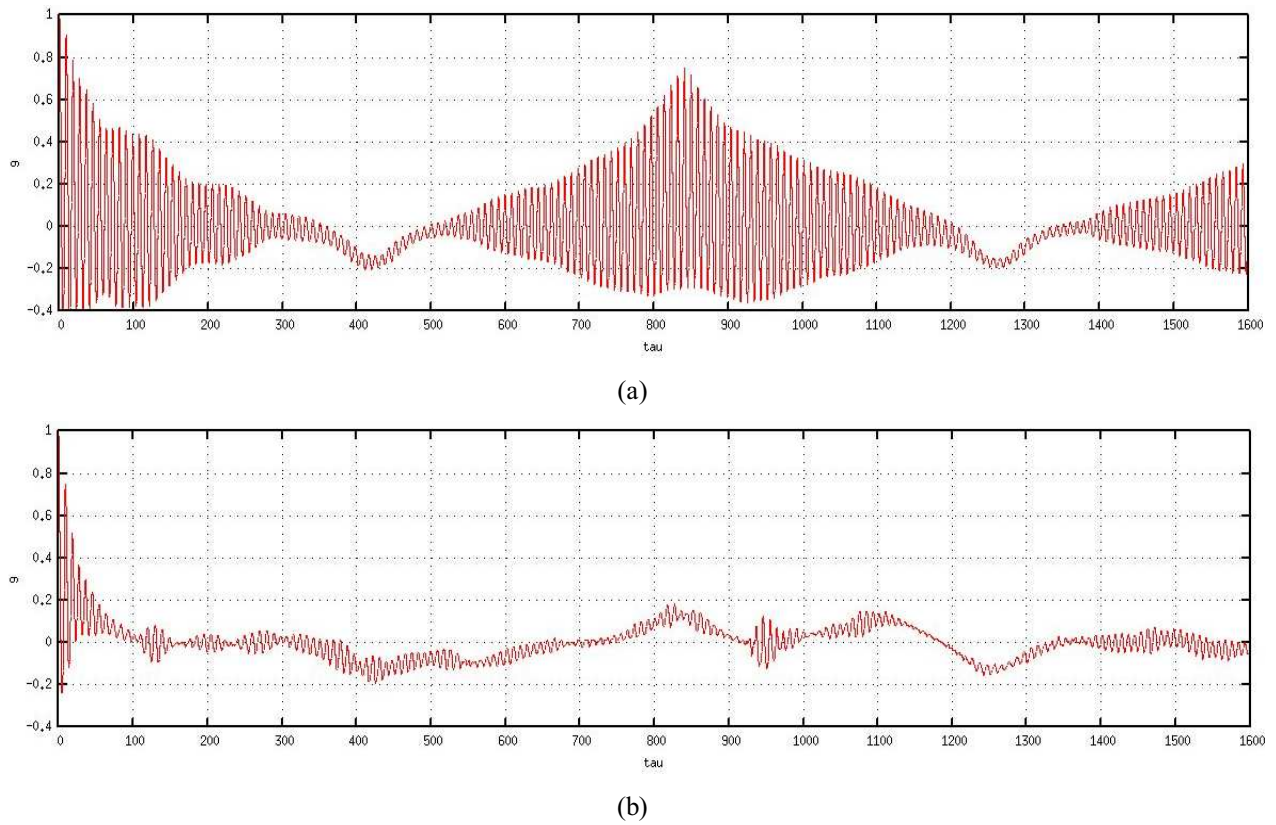


Figure 4. Auto-correlation function of (a) train of pulses of Fig. 2 and (b) quasi-chaotic signal of Fig. 3 computed over the time interval $t = 1000-9000$ and $t = 2000-20000$, respectively.

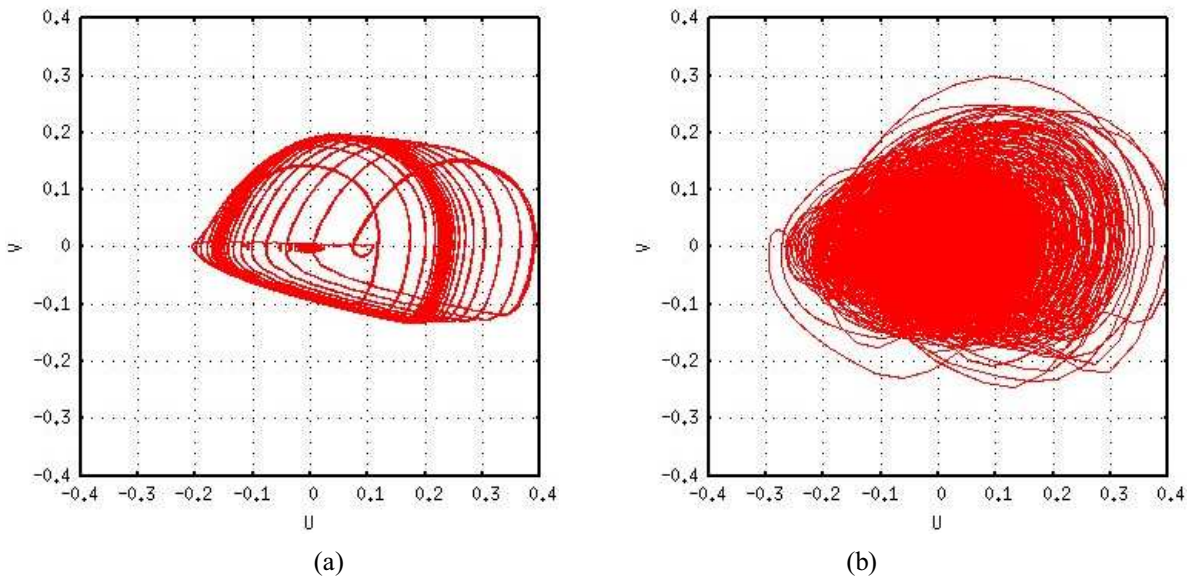


Figure 5. Poincare section U vs dU/dt of (a) train of pulses of Fig. 2 and (b) quasi-chaotic signal of Fig. 3 computed over the time interval $t = 4000-8000$.

4. CONCLUSIONS

Time-domain simulations of distributed networks of active circuits connected by sections of microstrip transmission lines have shown a possibility of generation of trains of high-frequency pulses radiated into an open section of transmission line. The trains of pulses can emerge when active devices are separated from compact resonant circuits by extended sections of transmission lines providing a time-delay feedback. When using a few branches of active circuits with different length of time-delay transmission lines, a complicated quasi-chaotic signal can be generated by the system that could be of interest for emerging applications.

REFERENCES

- [1] Kurokawa, K., "The Single-Cavity Multiple-Device Oscillator," *IEEE Trans. Microwave Theory Techn.*, Vol. MTT-19, 793–801, 1971.
- [2] Russell, K. J., "Microwave Power Combining Technique," *IEEE Trans. Microwave Theory Techn.*, Vol. MTT-27, 472–478, 1979.
- [3] Mink, J. W., "Quasi-Optical Power Combining of Solid-State Millimeter-Wave Sources," *IEEE Trans. Microwave Theory Techn.*, Vol. MTT-34, 273–279, 1986.
- [4] DeLisio, M. P. and R. A. York, "Quasi-Optical and Spatial Power Combining," *IEEE Trans. Microwave Theory Techn.*, Vol. MTT-50, 929–936, 2002.
- [5] Siegel, P. H., "Terahertz Technology," *IEEE Trans. Microwave Theory Techn.*, Vol. MTT-50, 910–928, 2002.
- [6] Liao, S. Y., *Microwave Circuit Analysis and Amplifier Design*, Prentice-Hall, New Jersey, 1987.
- [7] Lee, C. A. and G. C. Dalman, *Microwave Devices, Circuits and their Interaction*, John Willey and Sons, New York, 1994.
- [8] Taflove, A. and S. C. Hagness, *Computational Electrodynamics: the Finite-Difference Time-Domain Method*, Artech House, New York, 2000.
- [9] Erturk, V. B., R. G. Rojas and P. Roblin, "Hybrid Analysis/Design Method for Active Integrated Antennas," *IEE Proc. - Microw. Antennas Propag.*, Vol. 146, 131–137, 1999.
- [10] Yurchenko, V. and L. Yurchenko, "Time-Domain Simulation of Power Combining in a Chain of THz Gunn Diodes in a Transmission Line," *Int. J. Infrared and Millimeter Waves*, Vol. 25(1), 43–54, 2004.
- [11] Yurchenko, V. B. and L. V. Yurchenko, "Self-Excitation of a Chain of Gunn Diodes Connected by Transmission Lines," in *Proceedings of the URSI-Turkey'2004 Symposium*, Bilkent University, Ankara, Turkey, September 2004, 460–462.
- [12] Yurchenko, V. B. and L. V. Yurchenko, "Self-Generation of Ultra-Short Pulses in a Cavity with a Dielectric Mirror Excited by an Array of Active THz Devices," in *Proceedings of the 8th Int. Conf. on Terahertz Electronics*, Darmstadt, Germany, September 2000, 49–52.
- [13] Yurchenko, L. V. and V. B. Yurchenko, "Ultra-Short Pulses Generation in a Cavity with an Active Layer and a Dielectric Mirror," *Applied Radio Electronics*, No. 2, 2005.
- [14] Lukin, K. A., "Noise Radar Technology for Short Range Applications," in *Proceedings of the 5th Int. Conf. on Radar Systems*, Brest, France, May 1999.

SECTION 2

- 2.1. Frederic Molinet, “*Radiation of a dipole on a strongly elongated convex body*” 2-1
- 2.2. Alexei Popov, “*Parametric Theory of Parametric Resonance*” 2-9

Radiation of a dipole on a strongly elongated body

F. A. Molinet

MOTHESSIM, Centre de la Boursidière, RN 186, BP 182, 92357 Le Plessis-Robinson, France

Abstract – The boundary layer method extended by Andronov and Bouche [1] to strongly elongated objects is applied to the field radiated by a source located on a strongly elongated axisymmetric body. Both perfectly conducting and impedance boundary conditions are considered. The author develops explicit solutions for the asymptotic currents on the surface in the paraxial direction. By matching these solutions with the classical creeping wave solutions on a non elongated object valid outside the paraxial region, uniform solutions have also been derived. Some numerical results comparing the new creeping wave asymptotics with the classical one, on a prolate ellipsoid, are shown.

1. INTRODUCTION

In this article, the radiation problem of an infinitesimal tangential magnetic dipole or normal electric dipole excitation on a perfectly conducting strongly elongated body of revolution is considered and the magnetic field on the surface is analysed. Away from the caustic boundary layer of the source, the theory of creeping waves on strongly elongated bodies is applied. Close to the source the field on the surface has been approximated by the known solution of a dipole on an infinite PC plane. In the paraxial direction this solution has been matched with the creeping wave solution for a strongly elongated body. It is shown that the amplitude of the field in the paraxial direction is enhanced due to a weaker attenuation constant of the magnetic creeping wave. Away from the paraxial direction our solution blends respectively with the solution of Pathak and Wang [2] for a double curved PC surface and the solution of Munk [3] for an impedance surface.

The paper is organized as follows. In section 2 we recall the main steps of the boundary layer theory extended to strongly elongated bodies for PC and impedance boundary conditions and apply this theory to the specific problem of a dipole excitation. Explicit expressions are derived for the Green's functions along a geodesic without torsion in the penumbra zone. In section 3 we describe the technique used to match the solution in the penumbra region with the solution given by the tangent plane approximation in the vicinity of the source, for PC and impedance boundary conditions. Numerical results will be shown in section 4 and some concluding remarks are given in section 5.

2. CREEPING WAVES ON A STRONGLY ELONGATED BODY EXCITED BY A DIPOLE

The behavior of acoustic or electromagnetic creeping waves propagating on the surface of a strongly elongated convex body has been first studied by Andronov and Bouche [1] using the boundary layer method. The main steps of their approach, applied to electromagnetic creeping waves are also presented in [4] and a short description of the method is given in [5]. The Maxwell equations are written in the semi-geodesic curvilinear co-ordinate system (s, a, n) where s denotes the curvilinear abscissa along a geodesic, a denotes the curvilinear abscissa along a reference curve orthogonal to the geodesics and n denotes the distance of the observation point to the surface. The curves orthogonal to the geodesics are also the wave fronts of the creeping waves on the surface. Let \vec{e}, \vec{h} denote the e.m. field. With the notations :

$$\sqrt{\epsilon} \vec{e} = \vec{E} \quad , \quad \sqrt{\mu} \vec{h} = \vec{H} \quad (1)$$

Maxwell's equations in vacuum, with the $e^{-i\omega t}$ time convention, read

$$\text{rot } \vec{E} = ik \vec{H} \quad , \quad \text{rot } \vec{H} = -ik \vec{E} \quad (2)$$

In the co-ordinate system (s, a, n) the first equation (2) becomes :

$$\begin{aligned}
ikH^s &= \frac{1}{\sqrt{g}}(\partial_a E_n - \partial_n E_a) \\
ikH^a &= \frac{1}{\sqrt{g}}(\partial_n E_s - \partial_s E_n) \\
ikH^n &= \frac{1}{\sqrt{g}}(\partial_s E_a - \partial_a E_s)
\end{aligned} \tag{3}$$

where g is the determinant of the matrix tensor g_{ij} ($i, j = s, a, n$). The second equation (2) gives three other equations which may be deduced from (3) by the substitution $\vec{E} \rightarrow \vec{H}$, $\vec{H} \rightarrow -\vec{E}$. By using \therefore

$$V_i = g_{ij} V^j \tag{4}$$

Maxwell's equations may be expressed with only contravariant components. In order to solve these equations, the solution is stated in the form of an asymptotic expansion in powers of $k^{-1/3}$, the coefficients of which are determined recursively by substituting the stated form into the Maxwell equations and boundary conditions and equating terms of similar order in the large parameter k . In the boundary layer, n is small, of order $k^{-2/3}$. However since $\rho_t = 0(k^{-2/3})$ for a strongly elongated object, we must retain the terms $\frac{n^2}{\rho_t}$ and $\frac{n^2}{\rho_t^2}$ which are respectively of order $k^{-2/3}$ and 1. The details concerning the derivation of the expressions for the two principal order terms are given in [1] and [4].

By introducing the parameters $\kappa = \frac{k \rho_t}{m}$ and the reduced variables in the penumbra region :

$$\sigma = \frac{ms}{\rho} \quad , \quad \nu = \frac{kn}{m} \quad , \quad m = \left(\frac{k\rho}{2} \right)^{1/3} \tag{5}$$

and Fourier transforming with respect to σ the system of differential equations verified by E^a and H^a in the boundary layer along a geodesic without torsion, we obtain instead of the usual Airy equation, the following Heun equation :

$$\frac{\partial^2 U_o}{\partial \nu^2} + \frac{3}{\nu + \kappa} U_o + (\nu - \xi) U_o = 0 \tag{6}$$

where U_o is the Fourier transform of either E_o^a or H_o^a . and ξ the spectral variable. Similarly, by writing the boundary conditions in the co-ordinate system (s, a, n) and using the same « Ansatz » for \vec{E} and \vec{H} , the following conditions are obtained on the surface ($\nu = 0$) :

$$\left. \begin{aligned}
\frac{\partial \tilde{H}_o^a}{\partial \nu} + \left(imZ + \frac{2}{\kappa} \right) \tilde{H}_o^a &= 0 \\
\frac{\partial \tilde{E}_o^a}{\partial \nu} + \left(\frac{im}{Z} + \frac{2}{\kappa} \right) \tilde{E}_o^a &= 0
\end{aligned} \right\} \nu = 0 \tag{7}$$

where \tilde{E}_o^a and \tilde{H}_o^a are the Fourier transform of E_o^a and H_o^a respectively and where Z is the surface impedance. For a P.C. surface these conditions reduce to :

$$\frac{\partial \tilde{H}_o^a}{\partial \nu} + \frac{2}{\kappa} \tilde{H}_o^a = 0 \quad , \quad \frac{\partial \tilde{E}_o^a}{\partial \nu} = 0 \tag{8}$$

Until now, we have not specified the source which can be at finite or infinite distance from the object. If the incident field is a plane wave or a local plane wave the creeping wave starts at the shadow boundary and equations (6) to (8) are valid in the penumbra region. In the case of a point source located close to the surface in the boundary layer or on the surface, the creeping wave starts away from the point caustic region surrounding the source, in the penumbra region where the shadow boundary of the rays emanating from the source and the boundary layer of the creeping rays coalesce. In this region, the validity of equations (6) to (8) is submitted to the condition that ρ and ρ_t vary slowly with s . This condition is generally satisfied in the paraxial region of a strongly elongated object.

Equation (6) is verified in vacuum by any solution of Maxwell's equations expressed in the coordinates (s, a, n) satisfying the special conditions verified on a strongly elongated object. It is therefore verified by the incident field, the total field and the diffracted field. Consider now Heun's differential equation :

$$\frac{d^2V}{dv^2} + \frac{3}{v+\kappa} \frac{dV}{dv} + (v-\xi)V = 0. \quad (9)$$

By applying the transformation :

$$Y = (v+\kappa)^{3/2} V \quad (10)$$

equation (9) reduces to :

$$\frac{d^2Y}{dv^2} + \left(v-\xi - \frac{3}{4(v+\kappa)^2} \right) Y = 0 \quad (11)$$

We see that when $v \rightarrow \infty$ or $\kappa \rightarrow \infty$, Y verifies the Airy equation :

$$\frac{d^2Y}{dv^2} + (v-\xi)Y = 0 \quad (12)$$

We denote by $W_1(\xi-v)$ and $W_2(\xi-v)$ the two independent solutions of (12) known as the Miller type Airy functions.

Let $Y_\xi^{(1)}(v, \kappa)$ and $Y_\xi^{(2)}(v, \kappa)$ be the two independent solutions of (11) which behave respectively like $W_1(\xi-v)$ and $W_2(\xi-v)$ when v tends to infinity and let :

$$V_\xi(v, \kappa) = Y_\xi^{(1)}(v, \kappa) + Y_\xi^{(2)}(v, \kappa) \quad (13)$$

Then it follows from (11) that when $\kappa \rightarrow \infty$ $Y_\xi^{(1)}(v, \kappa)$ tends to $W_1(v-\xi)$ and $V_\xi(v, \kappa)$ tends to

$$V(v-\kappa) = W_1(v-\xi) + W_2(v-\xi).$$

Another consequence of (11) is $\frac{dW}{dv} = 0$ where W is the Wronskian of two independent solutions of

(11). Hence $W(Y_\xi^{(1)}, V_\xi)$ and $W(Y_\xi^{(1)}, Y_\xi^{(2)})$ are independent of v and are respectively equal to $W(W_1, V)$ and $W(W_1, W_2)$ which are known and given by 1 and $-2i$ respectively. These properties together with the radiation condition, the boundary conditions and the reciprocity condition allow us to construct the Green functions $G_E(\sigma, v, v', \kappa)$ and $G_H(\sigma, v, v', \kappa)$ of an electric and a magnetic dipole respectively, located in the boundary layer and parallel to the binormal of a torsionless geodesic.

Let $\tilde{G}_E(\sigma, v, v', \kappa)$ and $\tilde{G}_H(\sigma, v, v', \kappa)$ be the Fourier transforms of G_E and G_H respectively. These Green's functions verify the Heun equation (9) and the boundary conditions (7) and (8). If we denote by G^i the Green's function of the source in free space, the Green's function G^d of the diffracted field is defined by $G = G^i + G^d$. Since \tilde{G}^i is a solution of (9), \tilde{G}^d is also a solution of

(9). Hence, by applying the transformation (10) and the radiation condition we see that \tilde{G}^d must be proportional to $(\nu + \kappa)^{-3/2} Y_\xi^{(1)}(\nu, \kappa)$. Taking into account the reciprocity theorem, we can write :

$$\tilde{G}^d(\xi, \nu, \nu', \kappa) = A(\xi, \kappa) \left(\frac{\kappa}{\nu' + \kappa} \right)^{-3/2} Y_\xi^{(1)}(\nu', \kappa) \left(\frac{\kappa}{\nu + \kappa} \right)^{-3/2} Y_\xi^{(1)}(\nu, \kappa) \quad (14)$$

Similarly, since for $\kappa \rightarrow \infty$, \tilde{G}^i must tend to the expression obtained for a non elongated object given in [6], we have :

$$\tilde{G}^i(\xi, \nu, \nu', \kappa) = \left(\frac{\kappa}{\nu_{>} + \kappa} \right)^{-3/2} Y_\xi^{(1)}(\nu_{>}, \kappa) \left(\frac{\kappa}{\nu_{<} + \kappa} \right)^{-3/2} Y_\xi^{(1)}(\nu_{<}, \kappa) \quad (15)$$

where $\nu_{>} = \max(\nu, \nu')$, $\nu_{<} = \min(\nu, \nu')$.

The unknown function $A(\xi, \kappa)$ is determined by applying the boundary conditions on the surface. Different expressions are obtained for an electric and a magnetic dipole and for a PC or an impedance surface. The case when both the source and the observation point are on the surface is encountered in the antenna coupling problem. For a magnetic dipole, by taking the inverse Fourier transform of $\tilde{G}_H^i + \tilde{G}_H^d$, we obtain :

$$G_H(\sigma, \nu = 0, \nu' = 0, \kappa) = -\frac{1}{2\pi} \int_{-\infty}^{+\infty} e^{i\sigma\xi} \frac{Y_\xi^{(1)}(o, \kappa) d\xi}{Y_\xi^{(1)'}(o, \kappa) + \left(imZ + \frac{1}{2\kappa} \right) Y_\xi^{(1)}(o, \kappa)} \quad (16)$$

By normalizing G_H for $\kappa \rightarrow \infty$ (See Logan [6]) we obtain the corresponding Nicholson's function :

$$: N_H(\sigma, \kappa, z) = \frac{e^{-i\frac{\pi}{4}}}{2\sqrt{\pi}} \sqrt{\sigma} \int_{-\infty}^{+\infty} e^{i\sigma\xi} \frac{Y_\xi^{(1)}(o, \kappa) d\xi}{Y_\xi^{(1)'}(o, \kappa) + \left(imZ + \frac{1}{2\kappa} \right) Y_\xi^{(1)}(o, \kappa)} \quad (17)$$

For an electric dipole parallel to the binormal of the geodesic, we obtain another Nicholson's function, the normalized form of which is obtained by replacing Z in (17) by Z^{-1} . For a PC surface, $G_E = 0$ but its mixed derivative with respect to ν and ν' is different from zero and defines another Nicholson's function, the normalized form of which is given by :

$$\bar{N}_E(\sigma, \kappa, z) = \frac{e^{-\frac{3i\pi}{4}}}{\sqrt{\pi}} \sigma^{3/2} \int_{-\infty}^{+\infty} e^{i\sigma\xi} \frac{Y_\xi^{(1)'}(o, \kappa)}{Y_\xi^{(1)'}(o, \kappa) + \frac{1}{2\kappa} Y_\xi^{(1)}(o, \kappa)} d\xi \quad (18)$$

3. MATCHING WITH THE SOLUTION IN THE SOURCE REGION

In the source region, the asymptotic solution is matched with the tangent plane approximation. For a magnetic dipole of intensity $d\vec{p}_m$ tangent to a PC surface, the magnetic field on the plane tangent to the surface is given by :

$$: \vec{H}(M) = 2\vec{H}^i(M) = \frac{2i}{\omega\mu_o} \text{rot rot}(d\vec{p}_m G), \quad G = \frac{e^{ik|\vec{r}-\vec{r}'|}}{4\pi|\vec{r}-\vec{r}'|}$$

In the co-ordinate system (s, a) on the surface, we get :

$$\vec{H}(M) = \frac{ik}{4\pi} 2Y_o d\vec{p}_m \cdot \left\{ \hat{a}' \hat{a} \left(1 + \frac{i}{kr} - \frac{1}{(kr)^2} \right) - \hat{s}' \hat{s} \left(2 \left(\frac{i}{kr} - \frac{1}{(kr)^2} \right) \right) \right\} \frac{e^{ikr}}{r} \quad (19)$$

where Y_o is the admittance of free space and $\hat{s}' = \hat{s}$, $\hat{a}' = \hat{a}$, $r = s$.

When the magnetic dipole is oriented in the direction of the binormal to the geodesic, the radiated magnetic field on the planar surface is given by :

$$\vec{H}(M) = \frac{ik}{4\pi} 2Y_o dp_m \hat{a} \left(1 + \frac{i}{kr} - \frac{1}{(kr)^2} \right) \frac{e^{ikr}}{r} \quad (20)$$

Since the dominant term of the creeping wave field along a strongly elongated PC body in the paraxial direction, is given by :

$$\vec{H}_o(M) = \frac{ik}{4\pi} 2Y_o dp_m \hat{a} N_h(\sigma, k) \frac{e^{iks}}{s} \quad (21)$$

We can match both solutions by writing :

$$\vec{H}(M) = \frac{ik}{4\pi} 2Y_o dp_m \hat{a} \left(1 + \frac{i}{ks} - \frac{1}{(ks)^2} \right) N_h(\sigma, k) \frac{e^{iks}}{s} \quad (22)$$

A similar procedure has been applied to an electric dipole normal to a PC surface.

If the magnetic dipole is tangent to a coated surface, the tangential component of the magnetic field is given by :

$$\vec{H}_t = -\frac{k}{4\pi} Y_o \left\{ d\vec{p}_m V_{oo} + \frac{1}{k^2} \nabla_t (d\vec{p}_m \cdot \nabla Q) \right\} \quad (23)$$

with :

$$Q = V_{oo} + \left(\frac{1}{\epsilon_r \mu_r} - 1 \right) W_{oo} \quad (24)$$

where V_{oo} and W_{oo} are the Sommerfeld integrals for a dipole above a dielectric layer of relative permittivity ϵ_r and permeability μ_r , backed by a perfect conductor [7].

In the co-ordinate system (s, a) , (23) takes a form similar to (19), given by :

$$\vec{H}_t = -\frac{k}{4\pi} Y_o d\vec{p}_m \cdot \left\{ \hat{a}' \hat{a} \left(V_{oo} + \frac{1}{k^2} \frac{1}{\rho} \frac{\partial Q}{\partial \rho} \right) - \hat{s}' \hat{s} \left[\frac{1}{k^2} \left(\frac{1}{\rho} \frac{\partial Q}{\partial \rho} + \frac{\partial^2 Q}{\partial z^2} \right) + \left(\frac{1}{\epsilon_r \mu_r} - 1 \right) W_{oo} \right] \right\} \quad (25)$$

For a magnetic dipole along the binormal to the geodesic, the dominant term is given by :

$$\vec{H}_t = -\frac{k}{4\pi} Y_o dp_m \hat{a} V_{oo} \quad (26)$$

Close to the source, we replace V_{oo} by its quasi-static approximation. The dominant term of the creeping wave field is given by :

$$\vec{H}_{ot} = \frac{ik}{4\pi} 2Y_o dp_m \hat{a} N_H(\sigma, k, \zeta_H) \frac{e^{iks}}{s} \quad (27)$$

By matching both solutions, we obtain :

$$\vec{H}_{ot} = \frac{ik}{4\pi} 2Y_o dp_m \hat{a} \left(1 + \frac{i}{ks} \right) N_H(\sigma, k, \zeta_H) \frac{e^{iks}}{s} \quad (28)$$

For an electric dipole normal to the surface, the tangential magnetic field on a coated planar surface is given by

$$\vec{H}_t = \frac{i}{4\pi} d\vec{p}_e \cdot \hat{n}' \hat{a} \frac{\partial V_{oo}}{\partial \rho} \quad (29)$$

and the matching procedure leads to :

$$\vec{H}_t = \frac{ik}{4\pi} d\vec{p}_e \cdot \hat{n}' \hat{a} \left(1 + \frac{i}{ks}\right) N_H(\sigma, k, \zeta_E) \frac{e^{iks}}{s} \quad (30)$$

The formulas resulting from the matching of the solution in the source region with the solution in the Fock region presented so far, are valid in the paraxial region of a strongly elongated object. It is possible to extend these solutions outside the paraxial region where the classical creeping wave formulation applies by replacing the Nicholson functions in the solutions established by Pathak and Wang [2] for a PC surface and by Munk [3] for a coated surface, by the new Nicholson's functions depending on κ . Outside the paraxial region, κ becomes large and the new Nicholson functions tend smoothly to the classical ones.

4. NUMERICAL RESULTS

The formulas established in this article have been applied to a magnetic dipole source located on the surface, in the middle of a prolate ellipsoid where the radius R of its cross-section is maximum. The dimensions of the ellipsoid are defined by its principal radii of curvature at the source: $R = 0.25 \text{ m}$, $\rho = 200 \text{ m}$ which gives a half-length of the ellipsoid approximately equal to 7 m . The curves on Fig. 1 give the variations with respect to the curvilinear abscissa s of the radius of curvature r_o of the geodesic in the plane of symmetry, the radius of curvature (r_{oT}) of the wave front along the geodesic (transverse radius of curvature), the parameter κ for $F = 1 \text{ GHz}$ and the torsion of the geodesic which for this particular geodesic is zero.

We see that r_{oT} remains less than 1 m and decreases very slowly for $s > 0.5 \text{ m}$. Likewise, the variation of the parameter κ is very slow and its values remain between 1 and 2 for $0.3 < s < 6.3$. Hence, in this domain of variation of s , the ellipsoid has the characteristics of a strongly elongated object at the frequency considered $F = 1 \text{ GHz}$.

The variation of the magnetic field on the surface radiated by a magnetic dipole oriented along the binormal to the geodesic following the generatrix, is given on Fig. 2 for a PC surface and compared to the curve with lower values obtained with the classical creeping wave formulation. These results show an enhancement of the field on a strongly elongated object.

If the same ellipsoid is coated with a dielectric material of 3 mm thickness with relative permittivity $\epsilon_r = 3.25$, ($\mu_r = 1$) giving $\zeta_H = -i0.0631$, the variation of the magnetic field radiated along the generatrix, by the same magnetic dipole, is shown on Fig. 3. The lower curve corresponds to the results obtained on a PC surface with the classical formulation. These results compared to the results of Fig. 2 show that the enhancement of the magnetic field due to the coating is further augmented on a strongly elongated object. Other results have been obtained showing that these phenomena are limited to the paraxial region. Outside that region the results tend smoothly to those obtained with the classical formulation.

5 CONCLUSION

Explicit formulas for the field radiated on the surface of a strongly elongated body by an electric or magnetic dipole respectively perpendicular or parallel to the surface have been derived for perfectly conducting and impedance boundary conditions (coated surface). Numerical results obtained on a strongly elongated prolate ellipsoid show that the binormal component of the magnetic field on the surface in the paraxial region, is enhanced compared to the results predicted by the classical creeping wave formulation. This analysis is of importance for the prediction of coupling between conformal antennas using UTD type ray solutions.

REFERENCES

- [1] Andronov, I., and Bouche D., " Asymptotics of creeping waves on a strongly prolate body ", *Annales des Télécommunications*, 49 (3-4), pp. 205-210, 1994.
- [2] Pathak, P.H., Wang, N., Burnside, W.D. and R.G. Kouyoumjian "A uniform GTD solution for the radiation from sources on a convex surface ", *IEEE Trans. on Antennas and Prop.*, Vol. AP 29, N° 4, July 1981.

- [3] Munk, P., " A Uniform Geometrical Theory of Diffraction for the radiation and mutual coupling associated with antennas on a material coated convex conducting surface ", *Ph. D. Dissertation*, The Ohio State University, Columbus, Ohio, 1996.
- [4] Molinet, F., Andronov, I., and Bouche, D., " Asymptotic and Hybrid Methods in Electromagnetics ", *IEE Electromagnetic Waves Series 51*, 2005.
- [5] Molinet, F., " Plane wave diffraction by a strongly elongated object illuminated in the paraxial direction ", *IVth International Workshop on Electromagnetic Wave Scattering*, Gebze, Turkey, 18 – 22 Sept. 2006.
- [6] Logan, N.A., " General Research in Diffraction Theory ", Vol. 1, *Technical Report LMSD-288087*, Lockheed Missiles and Space Division, Dec. 1959.
- [7] Chew. W.C., " Waves and Fields in Electromagnetic Media " *Van Nostrand Reinhold*, New York, 1990.

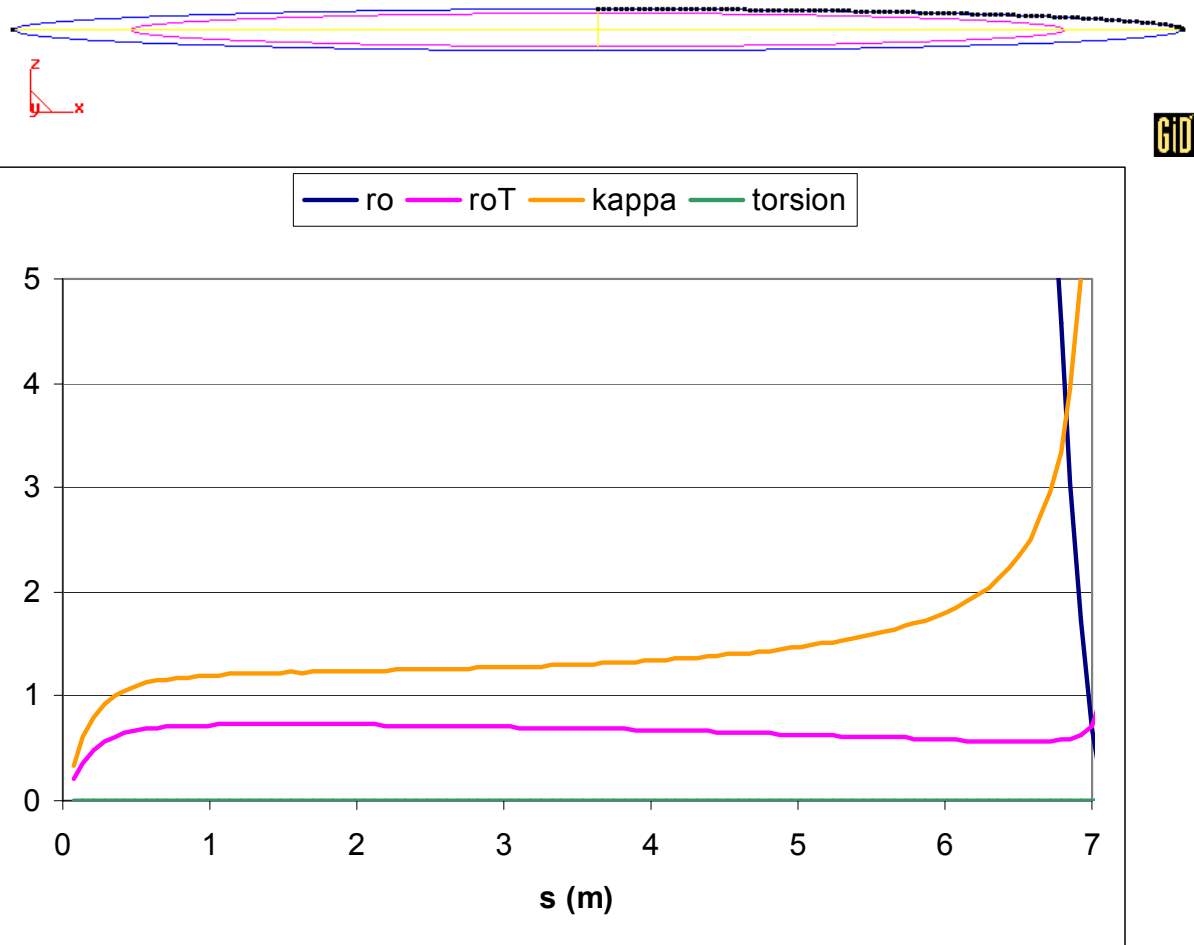


Fig. 1 : Shape of the ellipsoid and variation of the typical parameters along the geodesic

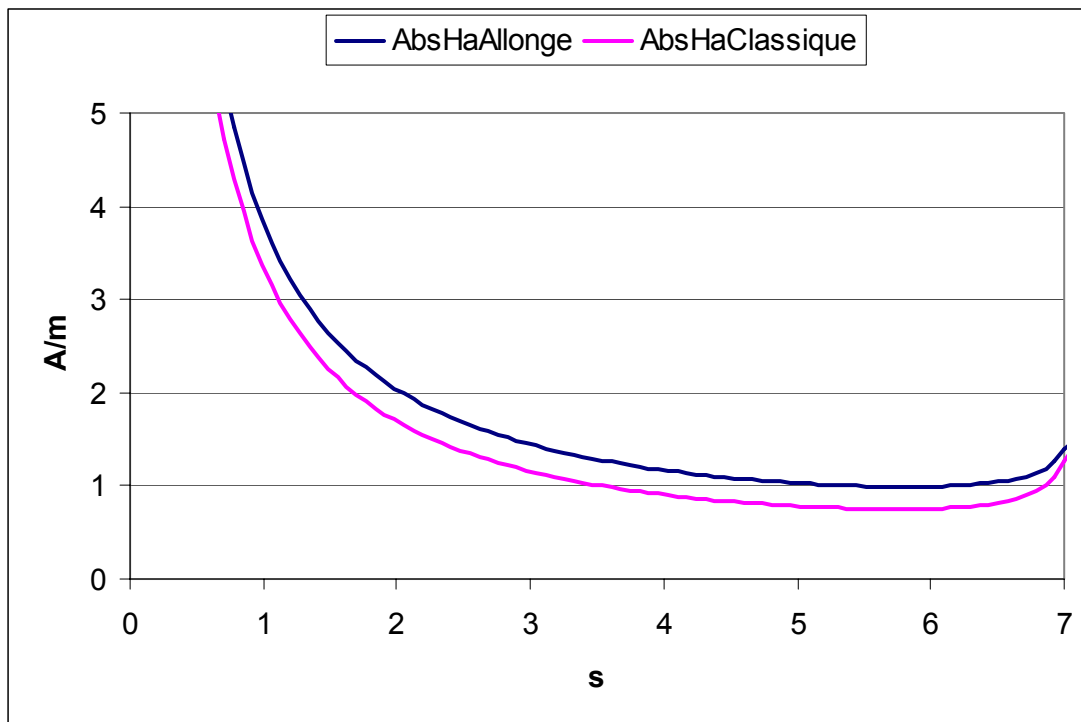


Fig. 2 : Results for the magnetic field on a P.C. ellipsoid

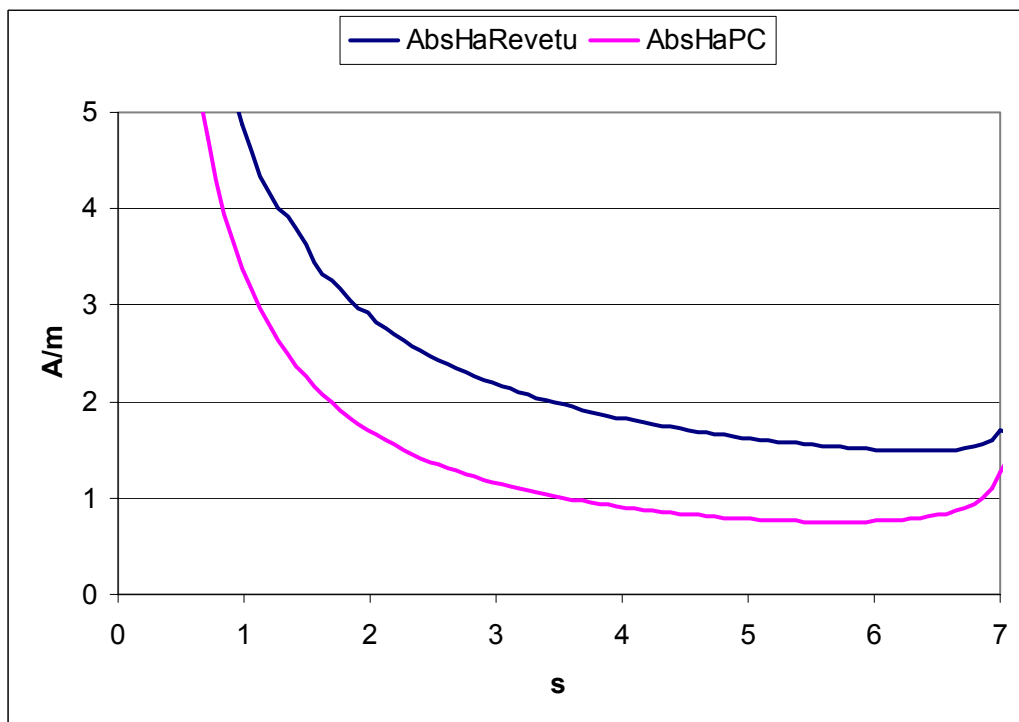


Fig. 3 : Results for the magnetic field on a coated ellipsoid

Parametric Theory of Parametric Resonance

Alexei Popov, *Member, IEEE*

Pushkov Institute of Terrestrial Magnetism, Ionosphere and Radio Wave Propagation
IZMIRAN, Troitsk, Moscow region, 142190 Russia, e-mail: popov@izmiran.ru

Abstract – The linear oscillator equation with varying angular frequency is solved analytically by taking the oscillation phase as a new independent variable. A closed-form Floquet solutions are constructed in the case of periodically modulated parameters. Explicit formulas for the increment of parametric oscillations are used in the inverse problem of optimal control. An analogy with Bloch waves in a periodically modulated medium allows one to use these results for the optimal design of multilayer mirrors and Bragg waveguides.

1. INTRODUCTION

Parametric resonance plays an important role in mechanics, electrical engineering and photonics. The simplest example from everyday life: a child rocking on a swing. Making it rock with increasing amplitude without mother's help, he or she solves a typical problem of optimal control. Mathematically, it is described by the oscillator equation with variable angular frequency. By choosing a proper periodical length variation the child easily realizes a Floquet solution with maximum possible amplitude increment. This easiness is in a drastic contrast with sophisticated mathematics involved in this inverse problem. In the absence of analytical solution one has to use approximations or numerical schemes to construct the solution of the direct problem for each set of parameters and to pick up the optimum solution by the trial-and-error method.

The secret of child's success is the use of a proper physical variable: the phase of the swing oscillations which the oscillator parameters must be synchronized with. In this work, we put this idea in a strict mathematical form: choosing oscillation phase as independent variable reduces the problem to a nonlinear equation set yielding an exact parametric solution for any law of the oscillator parameters variation. In this way we derive explicit formulas for the oscillation period and the Floquet increment allowing one to formulate and easily solve the optimization problem.

By analogy, we apply these results to wave propagation in periodic media, in particular, to the optimal design of multilayer mirrors and optical Bragg fibers providing maximum field confinement in the periodical dielectric cladding.

2. LINEAR OSCILLATOR. PARAMETRIC SOLUTION

Consider a linear oscillator equation with variable angular frequency $\omega(t)$:

$$u'' + \omega^2(t)u = 0 \quad (1)$$

For different $\omega(t)$ it may have oscillating solutions with arbitrarily varying period and amplitude – see Fig. 1(a). An important practical problem is optimal control of the oscillation parameters. One of the most interesting effects is parametric resonance caused by periodical variations of the angular frequency $\omega(t)$.

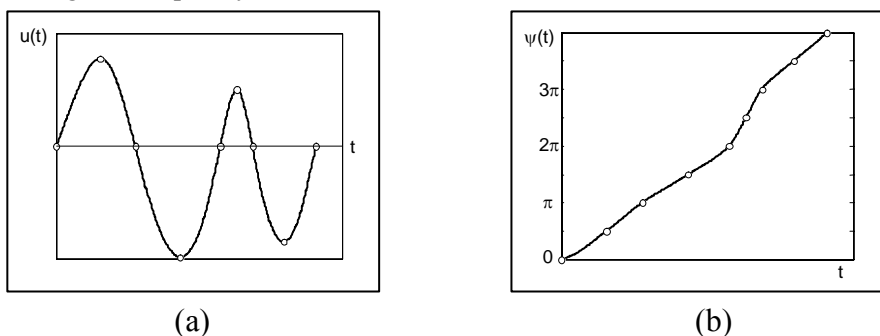


Fig.1. Oscillating solution $u(t)$ and its phase $\psi(t)$.

In the small perturbation case

$$\omega^2(t) = \omega_0^2(1 + h \cos \nu t), \quad h \ll 1 \quad (2)$$

it is well known [1] that for $\nu = 2\omega_0 + \delta\omega$, $-\frac{h\omega_0}{2} < \delta\omega < \frac{h\omega_0}{2}$ an exponentially growing solution arises:

$$u(t) \approx \cos \omega_0 t \cdot \exp(\mu t) \quad (3)$$

with the increment

$$\mu = \frac{1}{2} \sqrt{\left(\frac{h\omega_0}{2}\right)^2 - (\delta\omega)^2} \quad (4)$$

For stronger sinusoidal perturbations ($h \sim 1$) the result is given by the theory of Mathieu functions [2]. In a general case of periodic $\omega(t)$ calculation of the resonance bands and amplitude increments is a purely computational procedure providing numerical material scarcely helping to solve the inverse problem of optimal control.

We choose a direct analytical approach to the inverse problem. Let us introduce a new variable

$$\psi(t) = \cot^{-1} \left[\frac{u'(t)}{\omega(t)u(t)} \right] \quad (5)$$

being the phase of the oscillating solution $u(t)$. It is governed by the following nonlinear equation

$$\psi'(t) = \omega(t) + \frac{\omega'(t)}{2\omega(t)} \sin 2\psi \quad (6)$$

For $\omega(t) > 0$, $|\omega'(t)| < 2\omega^2(t)$ function $\psi(t)$ is monotonously growing – see Fig.1(b). Equation (6) still does not yield new analytical solutions. The situation changes if we consider $\omega(t)$ as a parametric function of the phase ψ :

$$\omega(t) = \Omega[\psi(t)] \quad (7)$$

It is easy to see that the functions $t = T(\psi)$ and $u(t) = U(\psi)$ satisfy the following set of nonlinear equations

$$\begin{aligned} \dot{T}(\psi) &= \frac{1}{\Omega(\psi)} - \frac{\dot{\Omega}(\psi)}{2\Omega^2(\psi)} \sin 2\psi \\ \frac{\dot{U}(\psi)}{U(\psi)} &= \cot \psi - \frac{\dot{\Omega}(\psi)}{\Omega(\psi)} \cos^2 \psi \end{aligned} \quad (8)$$

that can be solved in quadratures for any *a priori* chosen function $\Omega(\psi)$. From the first equation it follows

$$t \equiv T(\psi) = \int \left(\frac{1}{\Omega} - \frac{\dot{\Omega}}{2\Omega^2} \sin 2\psi \right) d\psi = t_0 + \frac{1}{\bar{\omega}} \int e^{g(\psi)} \left[1 + \frac{1}{2} \dot{g}(\psi) \sin 2\psi \right] d\psi \quad (9)$$

where the substitution $\Omega(\psi) = \bar{\omega} \exp[-g(\psi)]$ has been made for convenience. And the latter one integrates to yield an explicit analytical solution of Eq.(1)

$$u(t) \equiv U(\psi) = \frac{1}{\bar{\omega}} \sin \psi \exp \left[g(\psi) \cos^2 \psi + \int_0^\psi g(\varphi) \sin 2\varphi d\varphi \right] \quad (10)$$

satisfying the initial condition $u(t_0) = 0$, $u'(t_0) = 1$.

The second independent solution $v(t) \equiv V(\psi)$ satisfying $v(t_0) = 1$, $v'(t_0) = 0$ is derived from the Wronskian $u'v - uv' = 1$:

$$\begin{aligned}
v(t) \equiv V(\psi) &= \cos \psi \cdot e^{\int_0^\psi g(\varphi) \sin 2\varphi d\varphi} \\
&- \sin \psi e^{\int_0^\psi g(\varphi) \cos 2\varphi d\varphi} \int_0^\psi \dot{g}(\varphi) \sin 2\varphi e^{-\int_0^\varphi g(\chi) \cos 2\chi d\chi} d\varphi,
\end{aligned} \tag{11}$$

Formulas (10)-(11) describe exact solutions to the equation (1) for a very wide class of functions $\Omega(t)$. The only requirement is one-to-one correspondence between t and ψ . In particular, it is easy to construct a parametric solution for a periodic function $\Omega(t)$.

3. PERIODIC MODULATION. PARAMETRIC RESONANCE

Parametric resonance corresponds to an exponentially growing solution $u(t) = y(t) \exp(\mu t)$ of Eq.(1) which may exist for periodically varying oscillator parameters in virtue of the Floquet theorem. The above approach allows us to construct a continual set of Floquet solutions and reveals a very simple relation between the increment μ and the perturbation form $\omega(t)$. Let us define $g(\psi) = -\log[\Omega(\psi)/\bar{\omega}]$ as a periodic function of period π : $g(\psi + \pi) = g(\psi)$. Then

$$T(\psi + \pi) - T(\psi) = \frac{2}{\bar{\omega}} \int_\psi^{\psi+\pi} e^{g(\varphi)} \sin^2 \varphi d\varphi = \frac{2}{\bar{\omega}} \int_0^\pi e^{g(\varphi)} \sin^2 \varphi d\varphi \equiv \tau \tag{12}$$

Therefore, $T(\psi)$ is a sum of linear function $\tau\psi/\pi$ and some periodic function $\tilde{T}(\psi)$:

$$T(\psi) = \tau \frac{\psi}{\pi} + \tilde{T}(\psi), \quad \tilde{T}(\psi + \pi) = \tilde{T}(\psi) \tag{13}$$

and $\omega(t)$ is a τ -periodic function of t variable:

$$\omega(t + \tau) = \bar{\omega} e^{-g(\psi+\pi)} = \bar{\omega} e^{-g(\psi)} = \omega(x) \tag{14}$$

Furthermore, it follows from (10)

$$u(t) \equiv U(\psi) = \tilde{U}(\psi) e^{S(\psi)}, \quad S(\psi) = \int_0^\psi g(\varphi) \sin 2\varphi d\varphi \tag{15}$$

where $\tilde{U}(\psi)$ is a 2π -periodic function (anti-periodic on π interval) while the integral $S(\psi)$ contains a linear term:

$$S(\psi) = \tilde{S}(\psi) + \nu \frac{\psi}{\pi}, \quad \tilde{S}(\psi + \pi) = \tilde{S}(\psi), \quad \nu = \int_0^\pi g(\varphi) \sin 2\varphi d\varphi \tag{16}$$

Note an elementary integral representation of the coefficient ν , in contrast with standard approaches [3]. Inversion $T(\psi) \Rightarrow \psi(x)$ yields a Floquet solution with increment ν/τ and period 2τ :

$$u(x) = \tilde{u}(t) e^{\frac{\nu}{\tau} t}, \quad \tilde{u}(t + 2\tau) = \tilde{u}(t) \tag{17}$$

If the integral (16) is positive, the amplitude of oscillations $u(t)$ is exponentially increasing, the increment μ being proportional to the second odd harmonic of the modulation function $g(\psi)$

$$g(\psi) = a_0 + \sum_{m=1}^{\infty} (a_{2m} \cos 2m\psi + b_{2m} \sin 2m\psi) \tag{18}$$

Namely:

$$\mu \equiv \frac{\nu}{\tau} = \frac{\pi}{2\tau} b_2 \tag{19}$$

Equations (16-19) give an exact mathematical description of parametric resonance when the modulation period coincides with the half-period of the oscillations. In accordance with general theory [1], in $N\pi$ -periodic case: $g(\psi + N\pi) = g(\psi)$, higher-order resonances arise. Even values of N correspond to τ -periodic, and odd N numbers - to 2τ -periodic Floquet solution.

4. APPLICATION TO OPTIMAL DESIGN OF BRAGG WAVEGUIDES

There is a close analogy between parametric oscillations and wave propagation in a periodically modulated medium. In the simplest case monochromatic wave propagation is described by the 1D Helmholtz equation

$$u'' + q^2(x)u = 0, \quad q(x) = kn(x), \quad k = \omega/c \quad (20)$$

Reducing to Eq.(1) by substitution $t \rightarrow x$, $\omega(t) \rightarrow q(x)$. For a periodically modulated refraction index $n(x)$, Bloch waves arise whose dispersive properties are quite different from the case of uniform medium $n = Const$. In photonics, of great importance are evanescent Bloch waves in "forbidden" frequency bands [4,5] - exponentially descending solutions $u(x) = y(x) \exp(-\mu x)$ with periodic pre-exponent $y(x) = y(x + \Lambda)$, existing by virtue of the Floquet theorem. Due to parametric resonance, periodic dielectric layers may provide good wave field confinement even with low optical contrast $\delta n \ll 1$ and small number of layers. Here, an important practical problem arises: to find an optimum refraction index profile $n(x)$ providing maximum field decay in the multilayer structure. The above analysis allows us to give a rigorous solution to this problem of optimal design.

By denoting $q(x) \equiv Q(\psi) = \bar{q} \exp[g(\psi)]$ with a reference constant \bar{q} and arbitrary π -periodic function $g(\psi)$ we derive from (9-10) a wide class of exponentially descending Floquet solutions to Eq.(20), with period

$$\Lambda = \frac{2}{\bar{q}} \int_0^{\pi} e^{-g(\varphi)} \sin^2 \varphi d\varphi \quad (21)$$

and attenuation per period

$$\nu \equiv \mu \Lambda = \int_0^{\pi} g(\varphi) \sin 2\varphi d\varphi \quad (22)$$

Let the technological constraints set the upper and lower bounds of the refraction index:

$n_2 < n(x) < n_1$. Setting $\bar{q} = k\bar{n}$, we see that $g(\psi) = \log \frac{n[X(\psi)]}{\bar{n}}$ lies between the limits

$g_{1,2} = \log \frac{n_{1,2}}{\bar{n}}$. Taking into account the sign change of $\sin 2\varphi$ at $\varphi = \pi/2$ we easily deduce that the

step function $g(\psi) = \left\{ g_1, \quad 0 < \psi < \pi/2; \quad g_2, \quad \pi/2 < \psi < \pi \right\}$ provides the absolute maximum of the decrement ν within given constraints:

$$\max \nu = 2(g_1 - g_2) \int_0^{\pi/2} \sin 2\varphi d\varphi = g_1 - g_2 = \log \frac{n_1}{n_2} \quad (23)$$

It corresponds to an idealized quarter-wavelength meander profile: $n_1 \ell_1 = n_2 \ell_2 = \lambda/4$, $\Lambda = \ell_1 + \ell_2$ [4-6] and provides the highest reflection coefficient among the multilayer mirrors with given number of layers. A more realistic smooth index profile results from retaining in the Fourier series (14) the only essential harmonic:

$$g(\psi) = \delta \cdot \sin 2\psi, \quad q(\psi) = k\bar{n} e^{\delta \sin 2\psi} \quad (24)$$

The model parameters are set by the bounds of the refraction index $\bar{n} = k\sqrt{n_1 n_2}$, $\delta = \frac{1}{2} \log \frac{n_1}{n_2}$. By

substituting (24) into Eqs. (9-10) we obtain x coordinate as a function of phase ψ

$$x = X(\psi) = \frac{1}{\bar{q}} \int_{\psi_0}^{\psi} e^{-\delta \sin 2\varphi} \left(1 - \frac{\delta}{2} \sin 4\varphi \right) d\varphi \quad (25)$$

and a parametric representation of the descending Floquet solution

$$u(x) \equiv U(\psi) = \frac{1}{\bar{q}} \sin \psi e^{-\frac{\delta}{2} \left(\psi + \sin 2\psi + \frac{1}{4} \sin 4\psi \right)} \quad (26)$$

The structure period and the Floquet exponent are

$$\Lambda = \frac{1}{\bar{q}} \int_0^\pi e^{-\delta \sin 2\varphi} d\varphi = \frac{\pi}{\bar{q}} I_0(\delta), \quad \nu = \frac{\pi}{2} \delta = \frac{\pi}{4} \log \frac{n_1}{n_2} \quad (27)$$

Formula (24) suggests an optimum smooth index profile providing fastest wave field attenuation in the periodic dielectric layered structure (Fig.2).

This analytical solution can be directly used for the optimization of a planar Bragg waveguide – just by replacing the coefficient in Eq.(16) with $q^2(x) = k^2 n^2(x) - \beta^2$ where β is the effective wave number of a propagating TE mode:

$E_y = u(x) \exp(i\beta z)$ - see [7]. The optimal smooth index profile and transversal field distribution of the fundamental waveguide mode are depicted in Fig. 3.

5. CONCLUSION

Choosing an adequately defined phase of the oscillations function as a new independent variable reduces the parametric oscillator equation to nonlinear equations explicitly integrable for arbitrary form of the parameter modulation. In such a way we obtain an explicit description of parametric oscillations and derive a closed-form expression for the parametric resonance increment facilitating the solution of the problem of optimal control. An analogy with wave propagation in periodically modulated media allows one to apply these results to the design of photonic band-gap structures. It allows one to explicitly write down the parameter to be optimized and make use of standard variation calculus for the search of an optimum solution. We illustrate the method with examples of optimal multilayer mirror and Bragg waveguide providing maximum field decay in the periodic cladding structure.

REFERENCES

- [1] L. Landau, E. Lifshits. Mechanics, Course of Theoretical Physics, v. 1. Pergamon Press, London, 1976.
- [2] M. Abramovitz, I.A. Stegun. Handbook of Mathematical Functions. Dover, N.Y., 1965.
- [3] E.T. Whittaker, G.N. Watson .A Course of Modern Analysis. Cambridge Univ. Press, 1963.
- [4] A.Yariv, P. Yeh. Optical Waves in Crystals. Wiley-Interscience, New York, 2002.
- [5] J.D. Joannopoulos, S.G. Johnson, J.N. Winn, R.D. Meade. Photonic Crystals. Princeton Univ. Press, 2008.
- [6] D.V. Prokopovich, A.V. Popov, A.V. Vinogradov. Quantum Electronics, v. 37, No 9, 873-880 (2007).
- [7] A. Popov, A. Vinogradov, D. Prokopovich. Model problem of Bragg fiber design, ICTON 2008, 10th Internat. Conf. on Transparent Optical Networks, v. 1, pp. 242-245. IEEE, Athens, 2008.

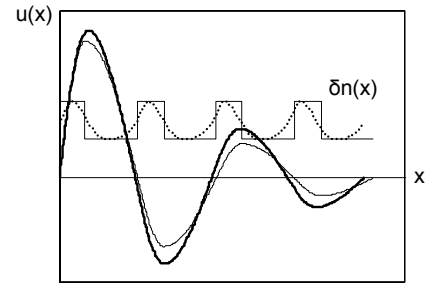


Fig. 2. Optimal index profiles $n(x)$ and corresponding wave functions: idealized quarter-wave stack (thin lines); realistic smooth profile (bold lines).

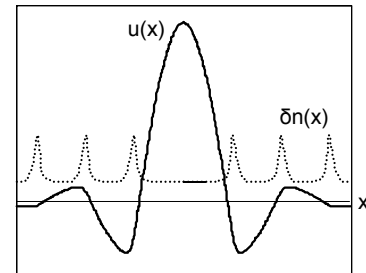


Fig. 3. Refraction index profile and fundamental mode of an optimal planar Bragg waveguide.

SECTION 3

- 3.1. Dan Censor and Martin McCall, "*Ubteaching Special-Relativity: Kinematical Derivation of the Lorentz Transformation*" 3-1
- 3.2. M. V. Ivakhnychenko and E. I. Veliev, "*Scattering Properties of the Strip with Fractional Boundary Conditions*" 3-13
- 3.3. V. S. Serov, "*Some inverse scattering problems for nonlinear Schrodinger operator in 2D*" 3-19

TEACHING SPECIAL-RELATIVITY: KINEMATICAL DERIVATION OF THE LORENTZ TRANSFORMATION

Dan Censor

*Department of Electrical and Computer Engineering,
Ben-Gurion University of the Negev, Beer-Sheva, Israel*

Martin McCall

Department of Physics, Imperial College London, United Kingdom SW7 2AZ

Abstract—Special Relativity is traditionally based on the two postulates introduced in Einstein’s 1905 paper. This often proves to be pedagogically problematic, especially in relation to the Lorentz Transformation of time. We derive here the low-velocity approximation of the Lorentz Transformation via simple kinematical ideas based on the propagation of tagged light pulses. This approach provides continuity with what students are familiar from elementary mechanics. The similarity and dissimilarity of the Lorentz and Galilean Transformations are discussed. Finally, the exact Lorentz Transformation and the prevalent axiomatic approach are discussed.

1. Introduction and Statement of the Problem

The prevalent textbook approach (e.g., see [1]) towards teaching the Lorentz Transformation (LT) of Einstein’s Special Relativity (SR) theory follows the methodology of his celebrated 1905 paper [2]. Einstein introduced SR *via* the two Postulates of Relativity stating that for all inertial observers: (i) the laws of physics (Einstein [2] specifically focused on Electromagnetism) take the same form; and (ii) the speed of light c is invariant. This axiomatic approach, sometimes with a few variations (see for example [3, 4]), is universally employed in teaching SR.

As well as its aesthetic appeal, the axiomatic approach has the advantage that it quickly confronts students with ideas such as time dilation and length contraction. However, to enable students to assimilate ideas incrementally, an alternative approach built around Newtonian kinematics may be beneficial.

Actually, Einstein’s postulates emerged only after his predecessors had grappled with relativistic ideas *via* kinematical arguments that nowadays seem to us as somewhat naïve [5]. Those arguments, notably Poincaré’s paper [6], were based on exchange of light signals. Arguments based on light propagation must a priori assume the kinematics of light propagation in free space (vacuum). Below we consider relatively moving observers, but assume the light waves to move in one frame (the S frame described below) only. Consequently Postulate (ii) does not feature at this stage.

Our goal is to explain in simple terms the elements involved in the LT without immediately invoking the invariance of the speed of light. Such a program can take various forms, e.g., see [7]. Like the forerunners of SR, we start with the low velocity approximation whereby the well-known relativistic factor $\gamma = (1 - v^2 / c^2)^{-1/2}$ is approximated by $\gamma = 1$. Crucially, we do not assume the Galilean approximation $t = t'$ but rather *derive* the correct low-velocity time transformation $t' = t - vx / c^2$.

Once students have assimilated the low-velocity transformations of space and time, these can be refined to their relativistically exact form by accounting for the symmetry of inertial systems and Postulate (ii) above. While the space transformation is straightforward, the time transformation is counter-intuitive and requires detailed expounding.

As with the early historical discussions [5], the arguments presented will be purely kinematical. But in contradistinction, our discussion is based on measurements of space and time made within a single inertial reference system S , referred to as the Lab System. We avoid velocity addition forms like $c \pm v$, obviously contradicting Postulate (ii), often appearing in early discussions [5].

The use of light signals facilitates the synchronization of clocks in arbitrary inertial systems. Accordingly, in each such system a latticework of rods is posited for establishing distances and locations. By emitting a pulse from a Master Clock (MC) placed, say, at the origin of the Lab system, all clocks in that system can be synchronized. This standard construction (e.g., see [1]) is discussed at the beginning of Einstein's paper [2]. The process of clock synchronization within a single inertial system is performed *without* the assumption that the speed of light c is the same for all inertial observers in relative motion, i.e., Postulate (ii) is not required at this stage.

Length separations and time durations measured in a system S' , moving with constant velocity relative to S will be deduced through their relationship to space-time coordinates in S .

2. Lorentz and Galilei Transformations

Consider frame S' moving with velocity v with respect to S along their co-aligned x -axes. When $v \ll c$, we assume $\gamma = (1 - v^2/c^2)^{-1/2} \approx 1$. In retrospect, already knowing Einstein's SR, we note that the LT takes the form (cf. [5])

$$x' = x - vt \tag{1}$$

$$t' = t - vx/c^2 \tag{2}$$

$$y' = y, z' = z \tag{3}$$

where c is the vacuum speed of light observed in S . Since we will obtain (1) and (2) without the second postulate we make no assumption about the speed of light in S' .

The Galilei transformation is obtained from (1)-(3) by taking in (2) the limiting case $c \rightarrow \infty$, leading to $t' = t$, i.e., becoming a statement that time is identical for all observers in relatively moving inertial systems. The Galilean approximation $t = t'$ is often ascribed to low velocities and/or small values of x . Mathematically this means that in (2) the condition $vx/c^2 \ll t$ must be satisfied, implying that at some arbitrary x the condition is satisfied only later than some time value t . For small time values $t \rightarrow 0$ the condition only holds near the origin $x \rightarrow 0$. Obviously this is too restrictive if we are seeking a description in which the spatial and temporal separation of events is arbitrarily. For such a description the limit $c \rightarrow \infty$ must be taken to arrive at $t = t'$. However, infinite light speed, with its attendant connotation of instantaneous communication (or instantaneous transmission of information, akin to action at a distance) is inconsistent with experiment and with theory in the context of Maxwell's equations. In other words, the Galilean Transformation $t = t'$ and Maxwell's

equations are incompatible in the sense that we cannot at the same time insist that $c \rightarrow \infty$ and discuss a theory that predicts light propagation at some finite speed^{*}.

3. The Spatial Transformation

A kinematical explanation of (1), dubbed as the spatial transformation, is straightforward. Written in the form

$$x = x' + vt \quad (4)$$

(1) describes the path of motion (aka equation of motion) along the x -axis of a point A whose initial position at time $t = 0$ is $x = x'$. See Fig. 1. In this sense the parameter x' in S is a constant. Differentiating (4) yields

$$dx' = 0 = dx - vdt \quad (5)$$

Therefore, by definition, v is the velocity of the point A when observed from S .

For a special choice $x' = 0$ (4) becomes

$$x = vt \quad (6)$$

the path for a point moving at velocity v , that at $t = 0$ coincided with the origin $x = 0$, depicted by the solid line in Fig. 1. Later on this point will be identified with the location of the Slave Clock (SC), introduced below.

So far (4) and (6) merely describe the paths of points moving according to generic (1). The key to defining another system of reference S' is the fact that the distance between arbitrary points moving at velocity v remains a constant. Thus if an observer is attached to one of these points, all the other points will appear at rest relative to his position.

Incorporating (3), the above arguments can be extended to three-dimensional space. Thus instead of the single path (1) one can assume the three-dimensional counterpart

$$\mathbf{r}' = \mathbf{r} - \mathbf{v}t \quad (7)$$

Designating some arbitrary point to be the origin, and considering \mathbf{r}' as an arbitrary location defines the frame of reference S' .

At this stage one cannot talk about (1) and (3), or (7), as a complete space-time transformation of coordinates, because we are not yet in possession of the associated temporal transformation (2). For that reason the question of simultaneity in its SR context is not yet applicable.

The analysis of the temporal transformation (2), is more complicated and needs a more detailed narrative.

4. The Temporal Transformation

^{*} Of course we cannot rule out the possibility of infinite speeds and "instantaneous action at a distance" in general.

To establish the temporal transformation (2), assume a master clock (MC) located at the origin $x = 0$, transmitting a discrete sequence of tagged electromagnetic pulses propagating at the velocity c in S . Thus each pulse actually consists of a spiked burst serving as marker and an associated signal occupying part of the dead time between pulses, coding the MC time at which the burst was emitted. Hence “the pulse emitted by the MC at $t = 0$ ” is understood to mean a pulse associated with the coding tag $t = 0$.

The main idea here is that the SC situated at $x' = 0$ is actuated by the tagged pulses received from the MC. The tag t' detected by the SC is then used to establish the ‘official’ time

$$t'' = t' |_{x'=0} \quad (8)$$

at the SC located at $x' = 0$. This information is then used to synchronize the time to arbitrary locations in S' , as explained below.

As depicted by the dashed lines in Fig. 1, The n -th pulse in the sequence is described by the world line

$$x = c(t - t'_n) \quad (9)$$

i.e., $t = t'_n$ at $x = 0$. In general we indicate the tag time as t' and (9) is rewritten as

$$x = c(t - t') \quad (10)$$

Solving (6) and (10), yields the intersection of the lines (Fig. 1) at

$$t' = t(1 - v/c) = t'' |_{x'=0} \quad (11)$$

where t' is the time tag detected by the SC and ascribed as the corresponding time t'' in S' for $x' = 0$ (later generalized for arbitrary x' as explained subsequently). For arbitrary points x' the intersection of the lines (1) and (10) yields

$$t' = t(1 - v/c) - x'/c \quad (12)$$

showing that for paths like (1), having at $t = 0$ an offset position $x = x'$, there is an additional delay of x'/c for the pulse tagged by t' , namely the time needed for the pulse to cover the extra distance x' . But instead of putting slave clocks in various locations x' , detecting different tags according to (12), only the SC at $x' = 0$ is considered for defining the time t'' at arbitrary locations x' . Such a statement begs the question: “how is this synchronization performed?”. Obviously we have to compensate for the extra time delay, i.e., knowing x' , and t' at arbitrary points according to (12), the time t'' is assigned throughout S' by computing

$$t'' = t' + x'/c \quad (13)$$

Note that the for the synchronization, only S data is exploited, hence questions of the velocity of propagation in S' , or Postulate (ii), are irrelevant.

Physically (11) is a manifestation of the Doppler Effect in its simplest form. It tells us that the motion of the SC relative to the pulses causes a delay in the reception time. At time t the SC already moved out a distance vt , therefore a pulse with an earlier tag emitted vt/c seconds earlier, is needed for the pulse to reach the SC at time t .

Pick a specific event occurring in S at space-time coordinates $\{x_e, t_e\}$ (for brevity the coordinates themselves are referred to as the 'event') such that

$$t_e = x_e / c \quad (14)$$

i.e., this event is chosen on the dashed line identified by the tag $t' = t'_0 = 0$ in Fig. 1, as given by (10) for $t' = 0$. Substituting (14) in (11) yields

$$t'_e = t_e - vx_e / c^2 = t''_e|_{x'=0} \quad (15)$$

Equation (15) relates the time t''_e at the location of the SC, which is also the time ascribed to all arbitrary points x' at rest with respect to $x' = 0$, i.e., all points defined as belonging to S' , to the space-time coordinates of the event $\{x_e, t_e\}$. Consequently (15) provides the temporal transformation (2) for the present specific case.

Arbitrary events $\{x, t\}$ are located on different dashed lines in Fig. 1, satisfying (10) instead of (14). For the same x_e we now have \bar{t}_e , shifted according to

$$\bar{t}_e = t_e + \bar{t}' \quad (16)$$

i.e., it is located on the world line of the pulse tagged by

$$x_e = c(\bar{t}_e - \bar{t}') \quad (17)$$

where (17) should be compared to (10) and (14). The later pulse, with its delayed tag \bar{t}' will also reach the SC at a later time, therefore in (15) the delay will be added to the two sides of the equation. Incorporating (16) we now have

$$t_e + \bar{t}' - vx_e / c^2 = \bar{t}_e - vx_e / c^2 = (t''_e + \bar{t}')|_{x'=0} \quad (18)$$

Defining

$$\bar{t}''_e = t''_e + \bar{t}' \quad (19)$$

We finally have

$$\bar{t}''_e|_{x'=0} = \bar{t}_e - vx_e / c^2 \quad (20)$$

once again recognized as (2), but now applying to arbitrary events $\{x, t\}$. The analog of (7) is the three-dimensional low velocity time transformation

$$t' = t - \mathbf{v} \cdot \mathbf{r} / c^2 \quad (21)$$

5. The Need for Symmetry and the Principle of Relativity

So far, our narrative has been based on the existence of a preferred Lab System S . This is *par excellence* a pre-relativistic notion. It served to establish (1)-(3) without Postulate (ii) and with a minimal appeal to Postulate (i), invoking the kinematics of light pulses. Once the non-Galilean time transformation (2) is established, introducing the rest of the SR fundamentals is straightforward. To order v/c inverting (1)-(3) yields

$$x = x' - v't' \quad (22)$$

$$t = t' - v'x' / c^2 \quad (23)$$

$$y = y', z = z' \quad (24)$$

showing that the privileged status of S used in the derivation of (1)-(3) was just temporary, since the transformation of spacetime coordinates from S' to S is the same as from S to S' with $v' = -v$ as required by the symmetry dictated by postulate (i).

The introduction of the γ -factor into the transformations now does require the second postulate and is easily assimilated by the discussion of light clocks in relative motions (see e.g. [1] p. 138). We then arrive at the usual Lorentz transformations

$$x' = \gamma(x - vt) \quad (25)$$

$$t' = \gamma(t - vx / c^2) \quad (26)$$

$$y' = y, z' = z \quad (27)$$

$$\gamma = (1 - v^2 / c^2)^{-1/2} \quad (28)$$

We can then, as above, appeal to the symmetry between S and S' to establish the inverse LT, involving $v' = -v$ and the same γ factor containing $v'^2 = v^2$. The three-dimensional analog of (25)-(28) is recast similarly to (7) and (21)

$$\mathbf{r}' = \tilde{\mathbf{U}} \cdot (\mathbf{r} - \mathbf{v}t), t' = \gamma(t - \mathbf{v} \cdot \mathbf{r} / c^2), \tilde{\mathbf{U}} = \tilde{\mathbf{I}} + (\gamma - 1)\hat{\mathbf{v}}\hat{\mathbf{v}} \quad (29)$$

where $\tilde{\mathbf{U}}$ is a dyadic (matrix) multiplying the coordinates perpendicular to \mathbf{v} by γ .

The complete LT leads to a discussion of concepts usually arising in this context, such as the light cone, sub-luminal and super-luminal velocities, length contraction and time dilation, which will not be revisited here.

In order to check consistency with Einstein's Postulate (ii), consider now the LT (25)-(27) in differential form

$$dx' = \gamma(dx - vdt) \quad (30)$$

$$dt' = \gamma(dt - vdx / c^2) \quad (31)$$

$$dy' = dy, dz' = dz \quad (32)$$

Define arbitrary sub-luminal speeds according to

$$u^2 = u_x^2 + u_y^2 + u_z^2 = (dx/dt)^2 + (dy/dt)^2 + (dz/dt)^2 \quad (33)$$

$$u'^2 = u_x'^2 + u_y'^2 + u_z'^2 = (dx'/dt')^2 + (dy'/dt')^2 + (dz'/dt')^2 \quad (34)$$

Substitution from (30)-(32) yields

$$u'^2 = [(u_x - v)^2 / (1 - vu_x / c^2)^2 + (u_y^2 + u_z^2) / \gamma^2] / (1 - vu_x / c^2)^2 \quad (35)$$

Upon assuming $u^2 = c^2$, i.e., that in S the speed of a point is c , or equivalently

$$u_y^2 + u_z^2 = c^2 - u_x^2 \quad (36)$$

we obtain from (34)

$$u'^2 = [(u_x - v)^2 + (c^2 - u_x^2) / \gamma^2] / (1 - vu_x / c^2)^2 = c^2 \quad (37)$$

So the complete LT (25)-(28) is compatible with Postulate (ii), namely if the speed is c in one inertial system, it is also c in another, showing that c is an invariant.

Einstein [2] started with Postulate (ii) and derived the LT, which is of course aesthetically more elegant, but sometimes more difficult for students to assimilate on their first encounter with SR.

Finally, it is noted that if both velocity components perpendicular to v vanish, i.e.

$$u_y = 0, u_z = 0 \quad (38)$$

then (28)-(30), for low velocities, leads to

$$\begin{aligned} u' &= dx' / dt' = (dx - vdt) / (dt - vdx / c^2) \\ &= (u - v) / (1 - vu / c^2) \end{aligned} \quad (39)$$

and for $u = c$ we obtain $u' = c$. Therefore caution must be exercised when dealing with such a specialized case.

6. Simultaneity And Moving Observers—An Example

According to the GT, time is identical in all reference systems: I am riding my horse and watching the time on the town's clock tower on the hill. Surely it is "logical" that the person sitting at the roadside will see the same time? We are, after all, watching the same clock. In hindsight, being already familiar with SR, we of course know the answer. *Watching the time* on the clock tower entails propagation of light waves, and unless we take into account the time retardation due to the finite speed of light propagation, we cannot be sure we are talking about the same time for all observers. The important distinction between the low velocity LT time transformation (2) and

the Galilean $t' = t$ can be appreciated by considering the following problem taken from [1]

Two individuals S' and S'' are walking towards each other along a road each at a speed of 3 ms^{-1} relative to the road. They cross at a site occupied by a stationary third observer, S . All agree to set their time origin at the crossover point, i.e. $t = t' = t'' = 0$. Near a star that lies on the line of the road, four light years away, a space ship at rest in the frame of S at location x , launches a missile at $t = 0$ destined to destroy the Earth some time in the future. Calculate the time when the missile launch occurs in the frames S' and S'' , stating carefully in each case whether it is earlier or later than in S . Ignore the effects of gravity and ignore the rotation of the Earth. Comment on which, if any, of the earthbound observers can actually discuss the Earth's fate when they meet.

Assume that S' (respectively S'') moves with velocity $v = +3\text{ ms}^{-1}$ ($v = -3\text{ ms}^{-1}$) relative to S . With $t = 0$, $x = 4 \times 365 \times 24 \times 60 \times 60 \times 3 \times 10^8 = 3.8 \times 10^{16}\text{ m}$ and $v = \pm 3\text{ ms}^{-1}$, we obtain From (2) $t' = -1.3\text{ s}$ and $t'' = +1.3\text{ s}$. Thus in S' (respectively S'') the missile is launched about one second before (after) S' (S'') meets S . The result illustrates the relativity of simultaneity occurring between frames moving at non-relativistic speeds. In the frame associated with S' , the missile is launched *before* the individual at the origin of S' meets his counterparts in S and S'' . However, since it would take at least four years for the information that the missile has been launched to reach S' , he cannot inform the other individuals about the fate of the earth when they meet.

7. Summary and Concluding Remarks

The teaching of special relativity poses special challenges. In many undergraduate physics courses, SR is taught very near the beginning (in one author's institution it is taught in the first semester). Whilst many students enjoy the provocative challenges that are immediately encountered with the traditional 'two postulates' approach (time dilation, length contraction, twins paradox etc.), others may benefit from a more seamless construction building on what they know from Newtonian mechanics. It is to these latter students that the approach developed in this paper is directed. A skeletal form of the First Postulate is used in assuming only that signals propagate according to simple kinematics, and that the time information carried by such signals can be freely exchanged between frames. The presentation is necessarily one-sided initially, giving the Master Clock in the Lab Frame preferred status. However, as we have shown, this asymmetry is easily removed once the transformations (1)-(3) have been obtained. The time transformation of (2) is the first departure from many student's intuition, and we have therefore presented an alternative narrative to arrive at this. Only once the low-velocity transformations are developed is the second postulate invoking the invariance of the speed of light introduced, and the full LT derived in the standard way. The symmetry between frames can then be used again to show that the full LTs are consistent with the first postulate.

8. References

1. M. W. McCall, *Classical Mechanics: A Modern Introduction* (John Wiley & Sons, Chichester, 2000).
2. A. Einstein, "Zur Elektrodynamik bewegter Körper," *Ann. Phys. (Lpz.)*, **17**, 891–921, (1905); English translation: "On the Electrodynamics of moving bodies," in "The Principle of Relativity," (Dover, 1952).
Available on the net, e.g., at
<http://www.ee.bgu.ac.il/~censor/relativity-directory/einstein.pdf>
3. D. Censor, "Electrodynamics, topsy-turvy special relativity, and generalized Minkowski constitutive relations for linear and nonlinear systems", *PIER-Progress In Electromagnetics Research*, vol. 18, pp. 261-284, Elsevier, 1998.
Available at <http://www.ee.bgu.ac.il/~censor/topsy-paper.pdf>.
4. D. Censor, "Relativistic electrodynamics: various postulate and ratiocination frameworks", *PIER—Progress In Electromagnetic Research*, Vol. 52, pp.301-320, 2005.
Available at <http://www.ee.bgu.ac.il/~censor/games-paper.pdf>
5. M.N. Macrossan, "A Note on Relativity before Einstein" *The British Journal for the Philosophy of Science*, Vol. 37, pp. 232-234, 1986.
Available at <http://eprint.uq.edu.au/archive/00002307/01/larmor.pdf>
6. H. Poincaré, 1900, "La theorie de Lorentz et la Principe de Reaction", *Archives Neerlandaises*, V, 253-78, 1900
7. H. A. Atwater, "Non Simultaneity in the Aberration of Starlight," *American Journal of Physics*, vol. 42, 1022–1024, 1974.

Figure Captions:

Figure 1: Spacetime diagram illustrating the motion of the SC (6) and the tagged light pulses.

Figure 2: Spacetime diagram illustrating the derivation of the time transformation.

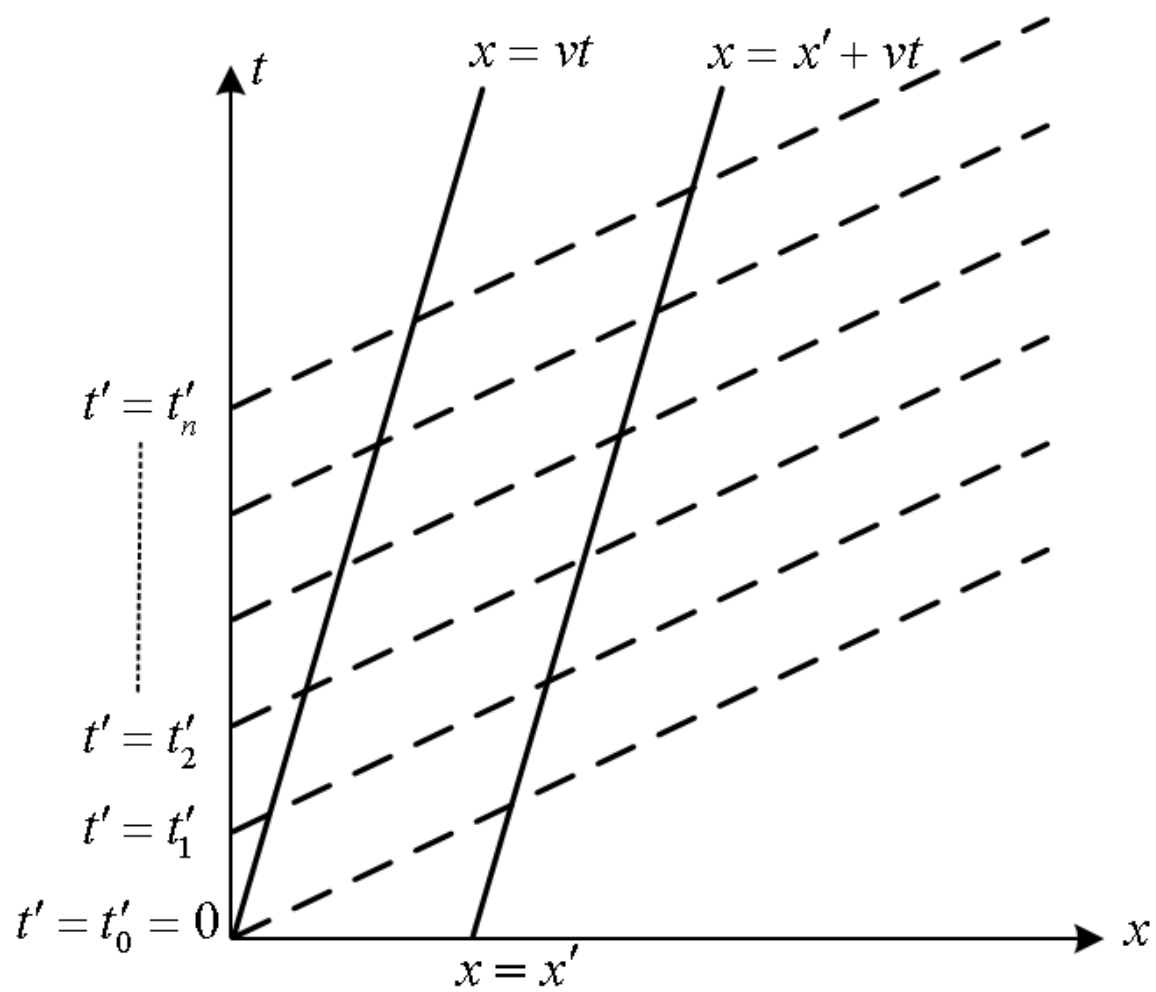


Figure 1

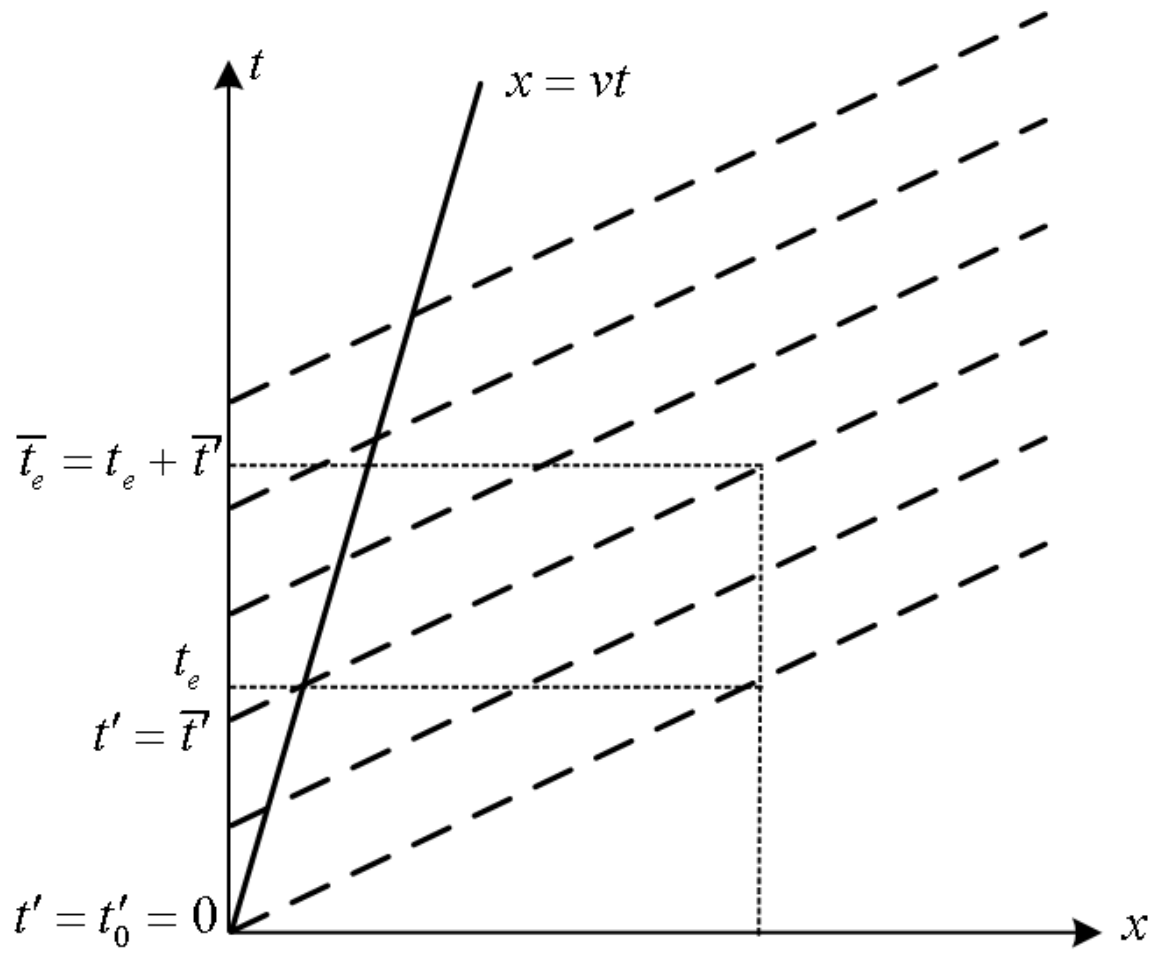


Figure 2

Scattering Properties of the Strip with Fractional Boundary Conditions

M. V. Ivakhnychenko and E. I. Veliev

Institute of Radiophysics and Electronics NASU, ul. Proskury 12, Kharkov 61085, Ukraine

Abstract - New fractional boundary conditions (FBC) on plane boundaries are introduced. FBC involve fractional derivatives of the tangential electric field components. FBC describe intermediate boundary between perfect electric conductor (PEC) and perfect magnetic conductor (PMC). FBC are studied by the example of problem of diffraction of E-polarized electromagnetic field by a strip. The method of solving this problem is presented. It is shown that “fractional strip” has scattering properties similar to the well-known impedance strip. The relation between the fractional order and the value of impedance is derived.

1. INTRODUCTION

In this paper we analyze application of fractional boundary conditions (FBC) to diffraction by strip. Following the ideas of fractional paradigm in electrodynamics proposed by N. Engheta [1] we introduce FBC as intermediate case between well-known perfect electric conductor (PEC) and perfect magnetic conductor (PMC):

$$D^n U(r) = 0, \quad r \rightarrow S \quad (1)$$

where the fractional order (FO) n is assumed to be between 0 and 1. D^n in (1) denotes the fractional derivative of Riemann-Liouville type [2] and is applied along direction normal to the surface S . In diffraction problems the function $U(r)$ denotes tangential component of electric or magnetic field. PEC and PMC boundaries are obtained from FBC (1) when FO n equal to 0 and 1, respectively.

Our interest is to study scattering properties of the two-dimensional strip with FBC on it. We refer a strip defined FBC as “fractional strip” in this paper. We will consider E-polarization case. The method of solving this problem will be presented later in this paper.

To understand properties of the boundaries described by FBC and relation to known boundaries we consider reflection problems first. It can be shown that infinite impedance boundary [3] with the value of impedance η can be simulated as boundary with FBC on it, i.e.

$${}_{-\infty} D_{ky}^n E_z = 0, \quad y \rightarrow +0 \quad (2)$$

FBC result in the reflection coefficient $R_v = -(-1)^v = -e^{i\pi v}$. Comparing the coefficients for impedance and fractional boundaries we get the equation which relate FO v and the impedance η :

$$v = \frac{1}{i\pi} \ln \frac{1 - \eta \sin \vartheta_0}{1 + \eta \sin \vartheta_0}, \quad \eta = -i \frac{1}{\sin \vartheta_0} \tan\left(\frac{\pi v}{2}\right) \quad (3)$$

Keeping in mind the relation (3) for infinite boundaries we can expect that “fractional strip” of finite width has scattering properties similar to an impedance strip if the FO v is related to impedance η as in (3). To compare “fractional” and impedance strips we independently solve both diffraction problems and compare physical characteristics such as cross sections and surface current densities.

2. PROBLEM FORMULATION

Consider a two-dimensional problem of electromagnetic wave diffraction by a strip of width $2a$ located at the plane $y=0$ and infinite along the axis z . An incident plane wave is described by the function $\bar{E}^i(x, y) = \bar{z}E^i(x, y) = \bar{z}e^{-ik_x x_0 + y\sqrt{1-a_0^2}}$, where $\mathbf{a}_0 = \cos \mathbf{q}_0$, \mathbf{q}_0 is the incidence angle.

Boundary conditions are FBC (1) with the surface $S = \{(x, y, z) : y = 0, -a < x < a\}$:

$${}_{-\infty}D_{ky}^n E_z(x, y)|_{y=0} = 0, \quad x \in (-a, a) \quad (4)$$

Here for convenience the fractional derivative is applied with respect to the non-dimensional variable ky .

The function $E_z(x, y)$ denotes the z -component of the total electric field $E_z(x, y) = E_z^i + E_z^s$ — a sum of the incident plane wave $E_z^i(x, y)$ and the scattered field $E_z^s(x, y)$.

The solution $E_z(x, y)$ should satisfy the following conditions:

- $E_z(x, y)$ satisfies the Helmholtz equation everywhere outside the strip: $(\frac{\partial^2}{\partial x^2} + \frac{\partial^2}{\partial y^2} + k^2)E_z(x, y) = 0$;
- $E_z^s(x, y)$ satisfies the radiation condition at infinity: $\lim_{r \rightarrow \infty} \sqrt{r} (\frac{\partial E_z^s}{\partial r} - iE_z^s) = 0$, $r = \sqrt{x^2 + y^2}$;
- the Meixner's condition on the edges of the strip;
- $E_z(x, y)$ satisfies FBC on the strip surface (4).

3. SOLUTION

Utilizing the fractional Green's theorem [4] we present the scattered field via the fractional Greens' function G^n [5, 6]

$$E_z^s(x, y) := \int_{-a}^a f^{1-n}(x') G^n(x-x', y) dx' \quad (5)$$

where $f^{1-n}(x)$ is an unknown function which we name “fractional potential density”. FGF G^n is

expressed in two-dimensional case as $G^n(x-x', y) = -i \frac{e^{\pm i p n / 2}}{4p} \int_{-\infty}^{\infty} e^{ik[(x-x')a + |y|\sqrt{1-a^2}]} (1-a^2)^{n-1/2} da$.

Following the method presented in [5] we use the Fourier transform $F^{1-n}(\mathbf{a}) = a \int_{-1}^1 f^{1-n}(ax) e^{-ieax} dx$ of the

fractional potential density $f^{1-n}(x)$:

$$E_z^s(x, y) = -i \frac{e^{\pm ipx/2}}{4p} \int_{-\infty}^{\infty} F^{1-n}(\mathbf{a}) e^{i[kxa + y\sqrt{1-a^2}]} (1-a^2)^{n-1/2} d\mathbf{a}, \quad \mathbf{e} = ka \quad (6)$$

Satisfying the function $E_z(x, y)$ FBC (4) we get integral equation (IE) [5]:

$$\frac{1}{e} \int_{-\infty}^{\infty} F^{1-n}(\mathbf{a}) \frac{\sin \mathbf{e}(\mathbf{a} - \mathbf{b})}{(\mathbf{a} - \mathbf{b})} (1-a^2)^{n-1/2} d\mathbf{a} = -4pe^{ip/2(1-n)} (1-a_0^2)^{n/2} \frac{\sin \mathbf{e}(\mathbf{b} + \mathbf{a}_0)}{\mathbf{e}(\mathbf{b} + \mathbf{a}_0)} \quad (7)$$

In order to solve the IE we represent the density function $f^{1-\nu}(x)$ by a uniformly convergent series [5]

and the Fourier transform $F^{1-n}(\mathbf{a})$ is expressed as

$$F^{1-n}(\mathbf{a}) = \frac{2p}{\Gamma(n+1)} \sum_{n=0}^{\infty} (-i)^n f_n^n \mathbf{b}_n^n \frac{J_{n+n}(\mathbf{e}\mathbf{a})}{(2\mathbf{e}\mathbf{a})^n} \quad (8)$$

where $J_{n+n}(\mathbf{e}\mathbf{a})$ denotes Bessel function.

As a result of this presentation the edge conditions are satisfied in form

$$f^{1-n}(x) = O((1-x^2)^{n-1/2}), \quad x \rightarrow \pm 1 \quad (9)$$

Substituting the series (8) into IE (7) we obtain a system of linear algebraic equations (SLAE) in respect to the coefficients f_n^ν . SLAE is solved with the method of reduction, after that the fractional density $f^{1-\nu}(x)$ is evaluated and other physical characteristics can be obtained as series in terms of the found coefficients f_n^ν .

Analyzing IE (7) for fractional strip it is seen that for the special case of $\nu = 0.5$ the kernel becomes simple and the IE can be solved analytically for any value of $\mathbf{e} = ka$:

$$F^{0.5}(\mathbf{a}) = -4i(1-a_0^2)^{1/4} e^{ip/4} \frac{\sin \mathbf{e}(\mathbf{a} + \mathbf{a}_0)}{\mathbf{a} + \mathbf{a}_0} \quad (10)$$

Another problem we consider in this paper is diffraction by impedance strip. Solution to this problem was given in [7]. In order to compare scattering properties of fractional and impedance strips we first consider surface currents existing in both cases. It can be shown that an E-polarized plane wave incident on a fractional strip excites two surface currents – electric and magnetic:

$$j_z^{(e)} = -2i \cos\left(\frac{p}{2}n\right) \frac{i}{4p} \int_{-\infty}^{+\infty} F^{1-n}(\mathbf{a}) e^{ikax} (1-a^2)^{\frac{n}{2}} d\mathbf{a}, \quad (11)$$

$$j_x^{(m)} = -2\sin\left(\frac{p}{2}n\right) \frac{i}{4p} \int_{-\infty}^{+\infty} F^{1-n}(\mathbf{a}) e^{ikax} (1-a^2)^{\frac{n}{2}-\frac{1}{2}} d\mathbf{a}$$

Similar current distributions are observed in the diffraction on an impedance strip: magnetic current is directed along the axis z and electric current is along the axis x .

We introduce the ratio $\zeta(x)$ for the fractional strip:

$$\zeta(x) := \frac{j_x^{(m)}(x)}{j_z^{(e)}(x)}, \quad x \in (-a, a) \quad (12)$$

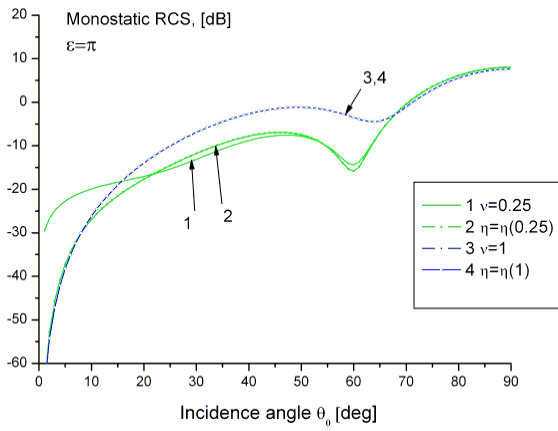


Figure 1. Monostatic RCS versus incidence angle for $\mathbf{e} = \mathbf{p}$. (1) fractional strip with $\mathbf{n} = 0.25$; (2) impedance strip with impedance \mathbf{h} corresponding to $\mathbf{n} = 0.25$; (3) fractional strip with $\mathbf{n} = 0.75$; (2) impedance strip with impedance \mathbf{h} corresponding to $\mathbf{n} = 0.75$.

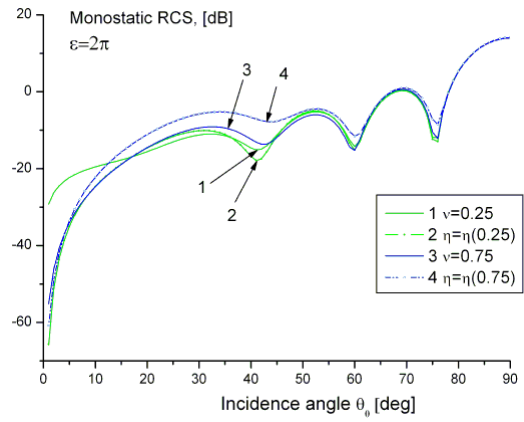


Figure 2. Monostatic RCS versus incidence angle for $\mathbf{e} = 2\mathbf{p}$. (1) fractional strip with $\mathbf{n} = 0.25$; (2) impedance strip with impedance \mathbf{h} corresponding to $\mathbf{n} = 0.25$; (3) fractional strip with $\mathbf{n} = 1$; (2) impedance strip with impedance \mathbf{h} corresponding to $\mathbf{n} = 1$.

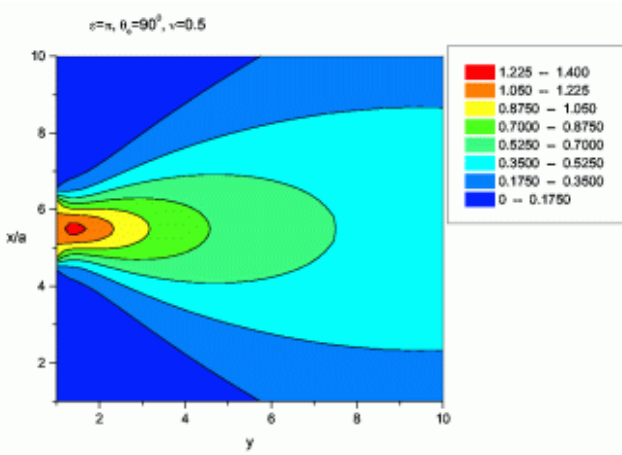


Figure 3. $|E_z|$ distribution for frequency parameter $\mathbf{e} = \mathbf{p}$, incident angle $\mathbf{q}_0 = 90^\circ$ and FO $\mathbf{n} = 0.5$.

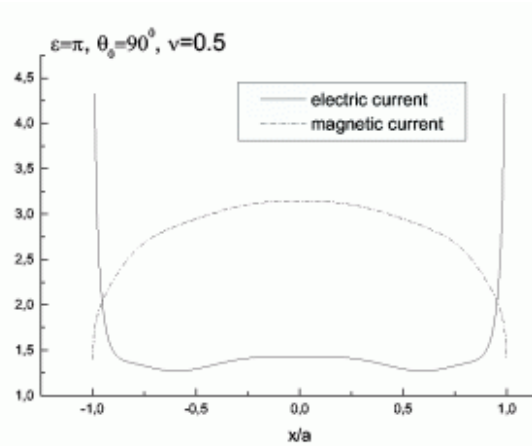


Figure 4. Magnetic and electric current densities for the same parameters as on Fig. 3.

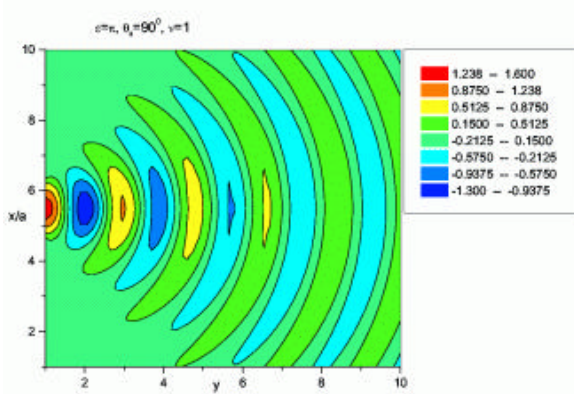


Figure 5. Distribution of real part of E_z for $\mathbf{e} = \mathbf{p}$, $\mathbf{q}_0 = 90^\circ$ and $\mathbf{n} = 1$.

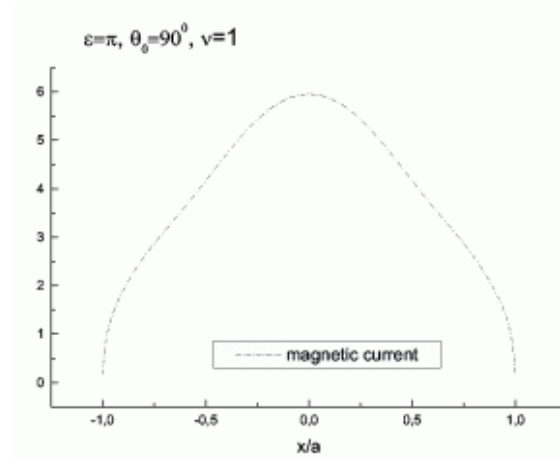


Figure 6. Magnetic current density for the same parameters as on Fig. 5. Electric current density equals to zero.

It should be noted that the ratio $\zeta(x)$ may depend on the coordinate x while the ratio $\eta = j_x^{v(m)}(x)/j_z^{v(e)}(x)$ for impedance strip is a constant η by the definition.

However, for one special value $\mathbf{n} = 0.5$ the IE can be solved analytically [5] and the function $\zeta(x)$ is a constant for any value of $\varepsilon = ka$: $\zeta(x)|_{\nu=0.5} = -i \sin^{-1} \theta_0$ [6]. For the physical optics (PO) approximation ($\varepsilon = ka \rightarrow \infty$) we can use asymptotic formulas for the integrals in equation (12) and the ratio $\zeta(x)$ is expressed analytically $\zeta(x) \sim -i \sin^{-1} \theta_0 \tan(\pi\nu/2) = \eta$. For finite boundaries in case of PO approximation we get exactly the same relation between the fractional order and the impedance (3). For arbitrary value of ε the ratio $\zeta(x)$ can be evaluated numerically. The relation for the currents proves the fact that the fractional boundary conditions are similar to the impedance boundary conditions. The closer $\zeta(x)$ to the constant for $-a < x < a$ the more the fractional boundary has properties of an impedance boundary.

4. NUMERICAL RESULTS

In the far-zone ($kr \rightarrow \infty$) the scattered field is expressed as $E_z^r(x, y) \approx A(kr) ?^n(\mathbf{j})$, where

$$A(kr) = \sqrt{\frac{2}{p}} ?^n r e^{ikr - i\frac{p}{4}}, \quad ?^n(\mathbf{j}) = -\frac{i}{4} (\pm i)^n F^{1-n}(\cos \mathbf{j}) \sin^n \mathbf{j} \quad (13)$$

The upper sign is chosen for the values $\mathbf{j} \in [0, \mathbf{p}]$, and the lower sign for $\mathbf{j} \in [\mathbf{p}, 2\mathbf{p}]$. The function $?^n(\mathbf{j})$ denotes the radiation pattern (RP) of the scattered field and can be expressed via the coefficients f_n^n found by solving SLAE.

Figures 1 and 2 show the comparison of the monostatic radar cross section (RCS) for different

values of the fractional order n and the frequency parameter $e = ka$. The results for $n = 0$ and $n = 1$ are in good agreement with the results obtained earlier [7]. All the curves for the monostatic RCS for all values of n have similar behavior and have the same value for the incident angle $q_0 = 90^\circ$. All the curves have minimums at the same values of q_0 . Figures 3 and 5 show field distribution for the fractional scattered field and corresponding densities of electric and magnetic currents are plotted on figures 4 and 6, respectively.

5. CONCLUSIONS

Scattering properties of the fractional strip defined by fractional boundary conditions has been analyzed. One important feature of the integral equations for the “fractional strip” is the fact that integral equation can be solved analytically for one special intermediate value of the FO equal to 0.5.

Detailed comparison analysis of the physical characteristics of the scattered fields for both fractional and impedance strips is presented. The fractional boundary supports both electric and magnetic currents. The analytical relation between the fractional order and the value of impedance is derived in cases of infinite boundaries and physical optics approximation. Similar to impedance boundary the ratio of surface current components is introduced for the strip with FBC. It is shown that in a wide range of input parameters the physical characteristics of the “fractional strip” are similar to the impedance strip.

REFERENCES

- [1] Engheta, N. “Fractional Paradigm in Electromagnetic Theory,” *a chapter in IEEE Press*, chapter 12, pp.523-553, 2000.
- [2] Samko, S.G., A.A. Kilbas and O.I. Marichev, *Fractional Integrals and Derivatives, Theory and Applications*, Gordon and Breach Science Publ., Langhorne, 1993.
- [3] Senior, T.B.A. and J.L. Volakis, *Approximate Boundary Conditions in Electromagnetics*, IEE Press, London, 1995.
- [4] Veliev, E.I. and N. Engheta, “Generalization of Green’s Theorem with Fractional Differintegration,” *2003 IEEE AP-S International Symposium & USNC/URSI National Radio Science Meeting*, 2003.
- [5] Veliev, E.I., M.V. Ivakhnychenko, and T.M. Ahmedov, “Fractional boundary conditions in plane waves diffraction on a strip,” *Progress In Electromagnetics Research, PIER* 79, 443–462, 2008.
- [6] Ivakhnychenko, M. V., E. I. Veliev and T. M. Ahmedov, “Scattering Properties of the Strip with Fractional Boundary Conditions and Comparison with the Impedance Strip,” *Progress In Electromagnetics Research C*, Vol. 2, pp. 189-205, 2008.
- [7] Ikiz, T., S. Koshikawa, K. Kobayashi, E. I. Veliev, and A. H. Serbest, “Solution of the plane wave diffraction problem by an impedance strip using a numerical-analytical method: *E*-polarized case,” *Journal of Electromagnetic Waves and Applications*, Vol. 15, No. 3, 315–340, 2001.

Some inverse scattering problems for nonlinear Schrödinger operator in 2D

Serov V.S.

Department of Mathematical Sciences, University of Oulu,
P.O. Box 3000, FIN-90014, Oulu, Finland, vserov@cc.oulu.fi

This work deals with the nonlinear Schrödinger equation in two dimensions

$$-\Delta u + \sum_{l=0}^m \alpha_l(x) |u|^l u = k^2 u, \quad k \in R. \quad (0.1)$$

Form (0.1) appears quite naturally in applications. It includes the linear case ($m = 0$) and the basic nonlinearities of cubic and cubic-quintic type. The latter two equations can be met, e.g., in optics. In addition to these cases, we allow here any finite combination of such powers of nonlinearity.

In direct scattering theory one considers the scattering solutions of (0.1), that is the solutions of the form

$$u(x, k, \theta) = u_0(x, k, \theta) + u_{sc}(x, k, \theta), \quad (0.2)$$

where $u_0(x, k, \theta) = e^{ik(x, \theta)}$ is the incident plane wave with direction $\theta \in S^1$ -unit sphere, and $u_{sc}(x, k, \theta)$ is the scattered wave. In inverse scattering problems we are asked to extract information about the coefficients of Eq.(0.1) from the knowledge of the scattered wave at large distances, i.e., from the so called scattering amplitude $A(k, \theta', \theta)$.

For the functions $\alpha_l(x)$ from $L^p_{loc}(R^2)$ with some special behaviour at the infinity we prove an analog of the well-known Saito's formula for this nonlinear Schrödinger operator

$$\lim_{k \rightarrow +\infty} k \int_{S^1 \times S^1} e^{-ik(\theta' - \theta, x)} A(k, \theta', \theta) d\theta d\theta' = 4\pi \int_{R^2} \frac{h(y)}{|x - y|} dy, \quad (0.3)$$

where $h(y) = \sum_{l=0}^m \alpha_l(y)$.

This formula allows us to prove the uniqueness theorem of the reconstruction of some special combinations of the unknown functions $\alpha_l(x)$.

The properties of the scattered wave and the definition of the scattering amplitude allow us to introduce the inverse Born approximation q_B as

$$q_B(x) := F^{-1}(A(k, \theta', \theta)). \quad (0.4)$$

Next we study the following problem: To estimate the smoothness of the terms from the Born approximation. And for the function h from $L^p_{loc}(R^2)$ the main result here is:

$$q_B(x) - h(x) \in H^t_{loc}(R^2). \quad (0.5)$$

SECTION 4

- 4.1. Mithat Idemen, Ali Alkumru, “*On the Definition and Computation of the Spreading Resistance by Tikhonov Regularization*” 4-1
- 4.2. Masahiro Hashimoto, “*Edge-Scattering from Polygonal Cylinders: Regularization of EM waves*” 4-9
- 4.3. Burak Polat, “*Field Relations on Sources Described by Zeroth and First Order Distributions in Arbitrary Motion*” 4-17

On the Definition and Computation of the Spreading Resistance Related to a Substrate Backed by a Metallic Plate

Mithat Idemen¹ and Ali Alkumru²

¹Yeditepe University, Faculty of Arts and Sciences, Department of Mathematics
Kayisdagi caddesi, 81120 Kayisdagi / Erenköy, Istanbul, Turkey

²Gebze Institute of Technology, Department of Electronics Engineering
41400, Kocaeli, Turkey

Abstract - The resistance associated with a nonparallel current flow in a substrate backed by a metallic plate is referred to as the spreading resistance of the substrate. The resistance in question, say R , can be defined either by the ratio W/I^2 or V/I , where W stands for the heat power dissipated inside the substrate, I is the total current entering into the substrate through the source plate while V denotes the potential difference between the source plate and back plate. The computation of R is first reduced into solution of dual integral equation of the first kind whose kernel is weakly singular and then solved numerically by a method which is based on the regularization in the sense of Tikhonov.

1. INTRODUCTION

The concept of spreading resistance has rather important issues in semiconductor technologies. For example, the heat flow between an active transistor (or integrated circuit) and an external heat sink makes the thermal spreading resistance to have important issues in the device carrier.

In spite of its importance, the works devoted to rigorous analysis of the spreading resistance are very few in the open literature because of the non-existence of the general theory to solve the mixed boundary-value problems related to this kind of a problem. To the best of our knowledge, the earlier work devoted to the rigorous analysis of the spreading resistance has been published by Kennedy [1] in 1960. In this study Kennedy had considered a finite cylindrical volume under the influence of a constant flux through a disc and defined the spreading resistance in terms of the maximum potential on the disc. Although the results of Kennedy are still used as reference in subsequent works, he had not formulated the problem rigorously as a mixed boundary-value problem. The first rigorous formulation of the problem as a mixed boundary-value problem was presented by Brooks and Mattes [2] in 1971. But, unfortunately, this work contains an obvious mathematical error which makes the results obtained there completely invalid. In a recently published interesting work [3] the problem is reduced to the same dual integral equations considered in [2] and solved by a method developed by Tranter [4], which aims to find the solution as an infinite series of the first kind Bessel functions of orders $(2n+1/2)$. But the determination of the coefficients of this series requires very hard computations.

The aim of the present work is to reconsider the same problem in a slightly different manner, and to reduce it first into an integral equation of the first kind and, then, by Tikhonov regularization method, into an equation of the second kind. An approximate solution to the latter, with high accuracy, can be obtained rather easily.

2. FORMULATION OF THE PROBLEM

A constant current I enters into a conducting slab of width d (substrate) through a metallic circular disc of radius a (see Fig.1.). The problem consists of finding the effect of the geometrical and physical parameters such as a , d , ϵ , μ and σ on the resistance R observed by the source. Here ϵ , μ and σ are assumed to be constant and signify the permittivity, permeability and conductivity of the substrate, respectively. The constitutive parameters of the half-space existing on the upper part of the substrate are, as usual, ϵ_0 , μ_0 and $\sigma = 0$. The bottom of the substrate is coated by a metallic plane. The current entering into the substrate spreads there to excite rotationally symmetric stationary electromagnetic fields which are by the following equations:

$$\text{curl}\mathbf{H} = \mathbf{J}, \quad \text{curl}\mathbf{E} = 0, \quad \text{div}\mathbf{D} = 0, \quad \text{div}\mathbf{B} = 0. \quad (1a,b,c,d)$$

Here \mathbf{E} , \mathbf{H} , \mathbf{D} and \mathbf{B} stand for the electric field, magnetic field, electric displacement and magnetic induction, respectively, while \mathbf{J} refers to the density of the current. Because of the rotational symmetry, all these quantities are functions of the polar coordinates r and z (independent of the angular coordinate ϕ).

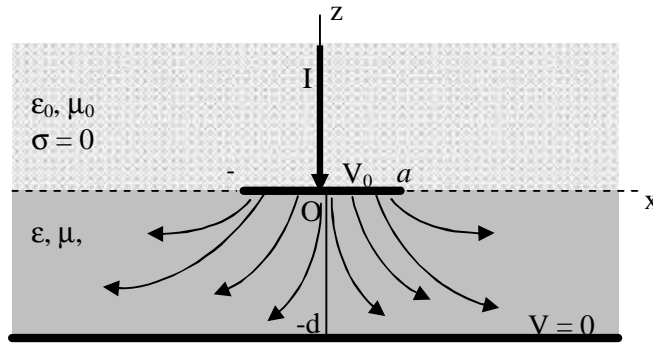


Fig.-1. Geometrical structure of the problem

The expressions of the current density \mathbf{J} is given by

$$\mathbf{J}(r,z) = \begin{cases} \mathbf{J}_n = -\frac{I}{2p} \frac{1}{r} \mathbf{d}(r) \mathbf{e}_z, & z > 0 \\ \mathbf{sE}, & z \in (-d,0). \end{cases} \quad (2)$$

In the region $z > 0$ for the ϕ -component of the magnetic field \mathbf{H} , say H_ϕ , from (1a) and (2) one gets

$$\frac{\partial}{\partial z} H_\phi = 0, \quad \frac{1}{r} \frac{\partial}{\partial r} (r H_r) = -\frac{I}{2p} \frac{1}{r} \mathbf{d}(r). \quad (3a,b)$$

By integrating (3b) on a disc with center at $(0,0,z)$ and radius r one gets

$$H_\phi(r) = -\frac{I}{2p} \frac{1}{r}. \quad (4)$$

It is significant to observe that in the region $z > 0$ H_ϕ is completely known beforehand and does not be affected by the substrate.

From (1b) and (1c) it is obvious that the electric field \mathbf{E} in this region is determined by the relation $\mathbf{E} = -\text{grad}V(r,z)$ where $V(r,z)$ is the scalar potential function which satisfies the well-known Laplace equation

$$\Delta V = \frac{1}{r} \frac{\partial}{\partial r} \left(r \frac{\partial}{\partial r} V \right) + \frac{\partial^2}{\partial z^2} V = 0. \quad (5)$$

Now consider the region $-d < z < 0$. The electric field \mathbf{E} in this region is obtained again by the relation $\mathbf{E} = -\text{grad}V(r,z)$ and here $V(r,z)$ satisfies also the same equation given in (5). (1a) and (2) show that H_ϕ depends on both r and z and satisfies

$$\frac{\partial}{\partial z} H_r = s \frac{\partial}{\partial r} V, \quad \frac{1}{r} \frac{\partial}{\partial r} (r H_r) = -s \frac{\partial}{\partial z} V. \quad (6a,b)$$

With the elimination of V between the equations in (6a,b) one obtains

$$\frac{\partial}{\partial r} \left[\frac{1}{r} \frac{\partial}{\partial r} (r H_r) \right] + \frac{\partial^2}{\partial z^2} H_r = 0 \quad . \quad (7)$$

The functions $V(r,z)$ and $H_\phi(r,z)$ are to be determined through (4), (5) and (7) by considering also the following boundary conditions:

$$V(r, -d) = 0, \quad r \in [0, \infty) \quad (8a)$$

$$V(r, -0) - V(r, +0) = 0, \quad r \in [0, \infty) \quad (8b)$$

$$V(r, 0) = V_0 = \text{constant (to be determined!)}, \quad r \in [0, a] \quad (8c)$$

$$H_\phi(r, -0) - H_\phi(r, +0) = 0, \quad r \in [a, \infty). \quad (8d)$$

$$|V(r,z)| < \infty \quad \text{as } z \rightarrow \infty \quad (8e)$$

It is worthwhile to remark that the boundary conditions given above are resulted from the perfect conductance of the metallic plates and the non-existence of the induced dipoles and surface currents on the interface $z = 0$. In connection with (8c) notice also that the potential function $V(r,0)$ is continuous for $r \in [0, \infty)$ because otherwise dipoles should exist on the cylinder $r = a$.

3. SOLUTION OF THE PROBLEM

Since the spectrum of the problem is continuous, in the regions $z > 0$ and $-d < z < 0$ the expressions of the solutions for the Laplace equation given by (5) can be obtained through the classical method of separation of variables and written as follows:

$$V(r,z) = \int_0^\infty A(\alpha) e^{-\alpha z} J_0(\alpha r) d\alpha, \quad z > 0 \quad (9)$$

and

$$V(r,z) = \int_0^\infty [B(\alpha) e^{\alpha z} + C(\alpha) e^{-\alpha z}] J_0(\alpha r) d\alpha, \quad z \in (-d, 0). \quad (10)$$

Here α stands for arbitrary separation parameter while $J_0(\alpha r)$ is the usual Bessel function. In (9-10) $A(\alpha)$, $B(\alpha)$ and $C(\alpha)$ denote the spectral coefficients to be determined through the boundary conditions (8a-d).

Similarly, the solution of the equation (7) which gives rise the ϕ -component of the magnetic field \mathbf{H} for $z \in (-d, 0)$ can be expressed as

$$H_\phi(r,z) = \sigma \int_0^\infty [-B(\alpha) e^{\alpha z} + C(\alpha) e^{-\alpha z}] J_1(\alpha r) d\alpha, \quad (11)$$

where (7a) being taken into account.

By considering the boundary conditions (8a,b) and the fact that that the Hankel transform

$$\hat{f}(\alpha) = \int_0^\infty f(r) r J_0(\alpha r) dr \quad (12a)$$

is invertible with its inverse [5]

$$f(r) = \int_0^\infty \hat{f}(\alpha) \alpha J_0(\alpha r) d\alpha, \quad (12b)$$

the potential function $V(r,z)$ and the magnetic field component $H_\phi(r,z)$ are written as follows:

$$V(r,z) = \begin{cases} \int_0^\infty A(a)e^{-az}J_0(ar)da, & z \geq 0 \\ \int_0^\infty A(a)\frac{\text{Sinh}[a(z+d)]}{\text{Sinh}(ad)}J_0(ar)da, & z \in [-d,0], \end{cases} \quad (13)$$

$$H_\phi(r,z) = \begin{cases} -\frac{I}{2\pi r}, & z > 0 \\ -s \int_0^\infty A(a)\frac{\text{Cosh}[a(z+d)]}{\text{Sinh}(ad)}J_1(ar)da, & z \in (-d,0). \end{cases} \quad (14)$$

These expressions show that the solution of the problem is reduced to the determination of the coefficient $A(\alpha)$. In order to determine this coefficient one inserts (13) and (14) into the remaining boundary conditions (8c,d) and gets

$$\int_0^\infty A(a)J_0(ar)da = V_0 = \text{constant}, \quad r \in [0, a] \quad (15a)$$

and

$$\int_0^\infty A(a)\text{Coth}(ad)J_1(ar)da = \frac{I}{2\pi s r}, \quad r \geq a. \quad (15b)$$

It is obvious that (15a,b) constitutes a pair of dual integral equations which will permit us to find an explicit expression of the unknown function $A(\alpha)$ whenever the right-hand sides are known. It is worthwhile to remark that in (15a) the constant V_0 is also an unknown which has to be determined.

For this purpose, by considering (14) and (15b) one writes

$$\int_0^\infty A(a)\text{Coth}(ad)J_1(ar)da = \begin{cases} \frac{I}{2\pi s r}, & r \geq a \\ -\frac{1}{s}H_f(r,-0), & r \in [0, a]. \end{cases} \quad (16)$$

Now let us multiply first (16) with r and then differentiate the obtained term with respect to r to get

$$\int_0^\infty aA(a)\text{Coth}(ad)J_0(ar)da = \begin{cases} 0, & r \geq a \\ f(r), & r \in [0, a]. \end{cases} \quad (17)$$

By considering (6b) or (13) it is obvious that $f(r) = \frac{\partial}{\partial z}V(r,-0) = -E_z(r,-0)$. From (17) one writes

$$A(\alpha) = \text{Tanh}(\alpha d) \int_0^a r f(r) J_0(ar) dr, \quad (18)$$

with (12a) and (12b) being taken into account. Finally, by inserting (18) into (15a) one obtains the integral equation

$$\int_0^a \mathbf{I} \mathbf{y}(\mathbf{I}) K(r, \mathbf{I}) d\mathbf{I} = 1 \quad , \quad r \leq a \quad (19a)$$

with

$$K(r, \lambda) = \int_0^\infty \text{Tanh}(a d) J_0(a r) J_0(a ?) da \quad (19b)$$

and

$$\psi(\lambda) = \phi(\lambda) / V_0 \quad , \quad r \in [0, a] . \quad (19c)$$

After having determined the expression of $\psi(\lambda)$ from (19a), it is an easy matter to compute the value of V_0 through (15b), (18) and (19c). Indeed, by inserting the expression of the coefficient $A(\alpha)$ given by (18) into (15b) and considering also (19c) one gets

$$V_0 = \left(\frac{I}{2\pi s} \right) \int_0^a \mathbf{I} \mathbf{y}(\mathbf{I}) d\mathbf{I} . \quad (20)$$

Here, it is worthwhile to notice that to obtain this value of V_0 the relation given by

$$\int_0^\infty J_0(a \mathbf{I}) J_1(ar) da = 1/r \quad , \quad \text{for } 0 < \lambda < r \quad (21)$$

has also been considered [6].

The power dissipated inside the substrate as heat energy is defined in [7] by

$$W = \sigma \iiint_{z < 0} \mathbf{E} \cdot \mathbf{E} dv . \quad (22a)$$

As explained in details in [8] this heat energy can also be expressed as

$$W = I V_0 \quad (22b)$$

If we define the spreading resistance R so that

$$W = R I^2 \quad (22c)$$

then from (22b) one gets

$$R = \frac{V_0}{I} \quad (23a)$$

by considering (20) the spreading resistance R given by (23a) can also be written as

$$R = \frac{1}{2\pi\sigma \int_0^a \lambda \psi(\lambda) d\lambda} . \quad (23b)$$

The expression given by (23a) shows that the resistance of the configuration modeled by Fig.-1, defined through the heat dissipation inside the substrate, can also be interpreted as to be the resistance

seen from the source (i.e. the ratio V_0/I) and, consequently, from (23b) it is obvious that the computation of this resistance requires the determination of $\psi(\lambda)$ from (19a).

In order to solve the integral equation (19a) let us rewrite first the kernel of this integral equation, which is given by (19b), as follows:

$$K(r,\lambda) = \int_0^\infty \{\text{Tanh}(\alpha d) - 1\} J_0(\alpha r) J_0(\alpha?) da + \int_0^\infty J_0(\alpha r) J_0(\alpha?) da . \quad (24)$$

It is obvious that the integrand of the first integral appearing in (24) decreases as $O\{\exp(-2\alpha d)/(\alpha d)\}$ as $\alpha \rightarrow \infty$. Therefore this integral can be computed numerically with very high accuracy by using standard methods. The second integral in (24) can be expressed as follows [6]:

$$\int_0^\infty J_0(\alpha r) J_0(\alpha?) da = \frac{1}{2} F\left(\frac{1}{2}, \frac{1}{2}, 1; \frac{r^2}{\lambda^2}\right), \quad r < \lambda, \quad (25)$$

where $F(a,b,c;z)$ stands for the usual hypergeometric function. Since the constant parameters of the hypergeometric function taking place in (25) satisfy the relation $a+b = c$, for $\lambda \rightarrow r$ it exhibits a logarithmic singularity [9]. Since $\{\log(\lambda - r)\} \in L[r - \epsilon, r + \epsilon]$ for all $\epsilon > 0$ this singularity will not cause any problem in computing the integral in (19a).

The analysis made above shows that the kernel $K(r,\lambda)$ of the integral equation (19a) is weakly singular and, hence, defines a compact operator [10]. Since the inverses of compact operators are never bounded [10], (19a) constitutes an ill-posed problem [10]. Therefore, to obtain an approximate expression of the solution, one has to use a regularization technique. Here the well-known Tikhonov regularization technique [10] which aims to reduce the solution for an equation of the form $\mathbf{A}u - f = 0$ to that of the following equation of the second kind:

$$\beta u + \mathbf{A}^* \mathbf{A} u = \mathbf{A}^* f \quad (26)$$

is preferred. In (26) \mathbf{A}^* denotes the conjugate operator to \mathbf{A} and $\beta > 0$ is referred to as the regularization parameter whose appropriate value is determined by inspection such that an acceptable relative error occurs.

In the case of (19a), one has

$$u \equiv u(\lambda) = \lambda \psi(\lambda) \quad , \quad f \equiv f(r) = 1 \quad (27a)$$

$$\mathbf{A}u = \int_0^a K(r, I) u(I) dI \quad , \quad \mathbf{A}^* j = \int_0^a K(r, I) j(r) dr \quad (27b)$$

with $K(r,\lambda)$ being given by (19b). Thus the regularized second kind integral equation which we have to solve numerically is as follows:

$$\beta u(I) + \int_0^a \int_0^a K(r, h) K(r, I) u(h) dh dr = \int_0^a K(r, I) dr . \quad (28)$$

Some values of R (normalized as $Ra\sigma$) computed by this method are presented in Table-1. The values of regularization parameter β were chosen to secure a relative error which is less than 0.015. In Table-1 one gives also the values of the same quantity computed by [3]. As it is seen obviously, the values obtained by two methods are very close to each other.

d/a	$Ra\sigma$ computed by (23b)	β	$Ra\sigma$ computed by [3]
10000	0.24943	0.00175	0.24999
1000	0.24902	0.00152	0.24989
400	0.24848	0.00125	0.24972
100	0.24794	0.00105	0.24889
10	0.24374	0.00100	0.23899
2	0.20111	0.00060	0.19747

Table-1. Computed values for the normalized spreading resistance ($Ra\sigma$)

4. CONCLUSIONS

From the analysis made above one concludes that the exact computation of the spreading resistance R which is defined inside a substrate by the ratio $R=V_0/I$ requires the solution of an integral equation of the first kind with a weakly singular kernel. Since this integral constitutes an ill-posed problem, the difficulties in finding numerical results can be avoided by using the well-known Tikhonov regularization technique. An illustrative application shows that the present method is applicable rather easily and quickly. A comparison of the results obtained by the method established here and that proposed in [3] shows that the accuracy of the new method is very good.

When the substrate is composed of two or more layers of different constitutive parameters as considered in [11], the kernel functions of the resulting set of dual integral equations become much more complicated, which makes the other methods very difficult and complex to apply. But the present method, which is based on regularization concept, seems to be still applicable by straightforward generalizations. A work in this direction is still running.

REFERENCES

- [1] Kennedy, D.P. "Spreading resistance in cylindrical semiconductor devices", *J.Appl.Phys.*, Vol.31, 1490-1497, 1960.
- [2] Brooks, R.D. and Mattes, H.G. "Spreading resistance between constant potential surfaces", *The Bell System Technical Journ.*, Vol.50, 775-784, 1971.
- [3] Denhoff, M.W. "An accurate calculation of spreading resistance", *J.Phys.D: Appl. Phys.*, Vol.39, 1761-1765, 2006.
- [4] Tranter, C.J., *Integral transforms in Mathematical Physics*, 2nd ed., Methuen (London), 1956.
- [5] Sneddon, I.A. *The use of integral transforms*, Mc Graw-Hill, N.Y., 1972.
- [6] Gradshteyn, I.S. and Ryzhik, I.M., *Table of integrals, series and products*, 5th, ed., Academic Press, N.Y., 1994.
- [7] Jones, D.S., *The theory of Electromagnetism*, Pergamon Press, 1964.
- [8] Idemen M. and Alkumru A. "A new method to compute the spreading resistance by Tikhonov regularization", *Int. J. Electron. Commun. (AEU)*, doi: 10.1016/j.aeue.2008.04.008, 2008.
- [9] Carrier, G.F., Krook, M. and Pearson, C.E., *Functions of a complex variable*, Mc Graw-Hill, N.Y., 1983.
- [10] Kress, R., *Linear Integral Equations*, Springer-Verlag, Berlin, 1989.
- [11] Yovanovich, M.M., Culham, J.R. and Teertstra, P. "Analytical modeling of spreading resistance in flux tubes, half spaces and compound disks", *IEEE Trans. Compon. Packag. Manuf. Technol. Part A*, Vol.21, 168-176, 1998.

Edge-Scattering from Polygonal Cylinders: Regularization of EM waves

Masahiro Hashimoto

Osaka Electro-Communication University, Neyagawa, Osaka 572-8530, Japan
Tel/Fax +81-72-820-4567, E-mail hashimot@isc.osakac.ac.jp

Abstract *The author showed in the report [1] that infinite sequences of zeros of the scattering pattern $\Pi(\theta)$ appear on the complex plane $z = \exp(i\theta)$ as a consequence of the wave scattering from polygonal cylinders, some of which correspond to the null points of $\Pi(\theta)$ measured in the far zone. The sequences start from the unit circle on the complex plane and finally terminate at the point of infinity. Knowing the exact distributions of these zeros leads to a complete description of scattering including geometrical scattering (GS) and edge-scattering (ES). The GS part will mainly be described by the zeros that distribute near the unit circle. The remaining zeros that also appear as infinite sequences can describe a static behavior of the field, which make the convergence of solutions very slow. The principal idea in this report is to constitute non singular solutions by removing from the scattering all zeros that distribute near the point of infinity. The truncated pattern can be represented in terms of two polynomials of degree n and these polynomials are exactly determined from the measured pattern $\Pi(\theta)$ in real space.*

1. Introduction

Mathematical expressions for waves in scattering problems, if rigorous, have analytic singularities at local points irrespective of their operating frequency. This situation arises from static nature of the fields involved in high-frequency ray fields, which makes edge scattering or edge diffraction extremely difficult to solve. The main reason is mathematical difficulty in solving the problem when we rely on the familiar mathematical tools such as special functions, complex analysis, Fourier integrals and so on. The circumstances are the same in the early report [1] in which the structure of the fields was discussed in terms of the locations of zeros of the spectrum amplitude (the radiation pattern) over the complex spectral plane. The present report describes an attempt to eliminate singularities from the distribution of zeros on the complex plane.

Let us start from the spectral theory of scattering and let us represent any kind of two-dimensional waves as a sum of plane waves propagating in the directions of complex angles. A complete expression for the scattering of EM waves has to invoke a complex integral of the plane wave spectrum over the complex plane.

$$u(z, \zeta) = i \int_{-i\infty - \pi/2 + \alpha_2}^{+i\infty + \pi/2 + \alpha_1} \Pi(\theta') e^{-ikr \cos(\theta - \theta')} d\theta' \quad (1)$$

where

$$z = x + iy \quad \zeta = x - iy \quad \text{and} \quad |\arg z - \alpha_1| < \pi/2 \quad |\arg \zeta + \alpha_2| < \pi/2 \quad (2)$$

The amplitude of plane wave spectrum appears explicitly in the far zone ($kr \gg 1$) far away from the source.

$$u(z, \zeta) \square \pi i \sqrt{\frac{2}{\pi kr}} e^{-ikr + i\frac{\pi}{4}} \Pi(\theta) \quad (3)$$

The spectrum amplitude $\Pi(\theta)$ in the real range of angles between 0 and 2π may therefore be called the radiation pattern. Analytic extension (analytic continuation in mathematical terminology) of the radiation pattern to the complex space provides us a full expression for the rigorous solution $u(z, \zeta)$. Singularities may in this case arise from the infinite zeros distributed near the point of infinity on the complex plane $z = \exp(i\theta)$. Fortunately, they are determined from the parameters of edge structure of the obstacle, which are exactly *known data* to be used. Subtraction of these known data from the spectrum amplitude is the *regularization of scattering* as referred in this report.

2. Factorization of the Spectrum Amplitude $\Pi(\theta)$

The general theory of two-dimensional scattering that was developed for N-polygonal cylinders [1][2] suggests that the spectrum amplitude $\Pi(\theta)$ has an infinite number of zeros that appear over the whole complex plane as shown in an example of Fig.1 and can thus be separated into the two groups, the group “+” of the zeros distributed outside the unit circle and the group “-” of those inside the unit circle. The spectrum amplitude can now be factorized into a product of the form

$$\Pi(\theta) = \psi^+(z) \psi^-(1/z) \quad \text{with } z = e^{i\theta} \quad (4)$$

where $\psi^+(z)$ and $\psi^-(z)$ are entire functions that are mathematically regular or analytic over the entire complex plane. All zeros for $\psi^+(z)$ and $\psi^-(z)$ are assumed to be located outside the unit circle [2]. These two analytic functions are closely related with each other when the value of z tends to infinity. Thus we are able to expect the locations of zeros of $\psi^+(z)$ from $\psi^-(z)$ in the neighborhood of the point of infinity [2]. By substituting Eq.(4) into Eq.(1), we have¹

$$u(z, \zeta) = \int_{-i\infty \exp(i\alpha_2)}^{+i0 \exp(i\alpha_1)} \psi^+(t) \psi^-\left(\frac{1}{t}\right) e^{-i\frac{k}{2}(\frac{z}{t} + \zeta t)} \frac{dt}{t} \quad (5)$$

The points of $t = 0$ and $t = \text{infinity}$ over the complex t -plane in Eq.(5) are singular points of $\psi^+(z)$ and $\psi^-(1/z)$ as well as those of the exponential function. The overall singularities may arise from the form of $z^\alpha e^{\beta z}$ where the algebraic growth at zero and infinity will be diminished by the rapidly decaying exponential factor. The integration of Eq.(5) can thus be carried out along the path. If $\psi^+(z)\psi^-(1/z)$ is

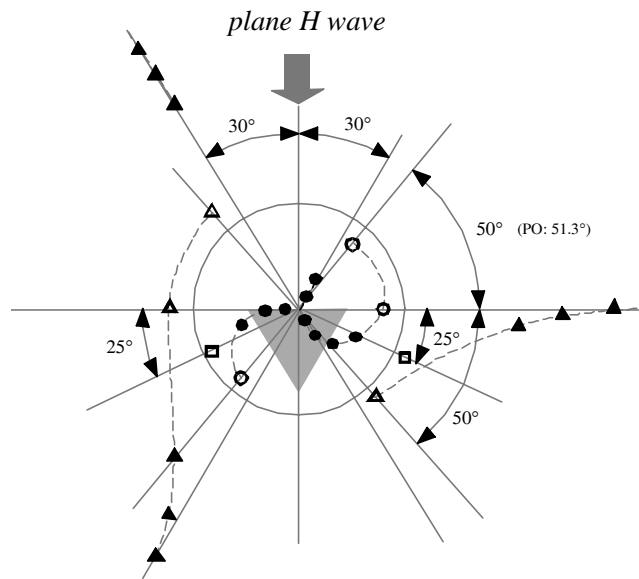


Fig.1 Zeros of the spectrum amplitude $\Pi(\theta)$ on the complex plane [1]

expanded into a Laurent series at $z = 0$ ($\dots a_{-2}z^{-2} + a_{-1}z^{-1} + a_0 + a_1z + a_2z^2 + \dots$), then the expression for u results in a series expansion in terms of outgoing cylindrical waves. The finite series obtained from the finite sum by means of truncation is an approximation to the exact solution if the remaining sum is negligible. However, in most cases, it is not so small even if the major terms are adequately summed up. This is because the remainder contains significant information on singular behaviors of waves at the edge points and thus it makes the convergence of the series rather weak. To cope with the difficulty, we need an idea something like the inversion technique given in the literature [6][7].

3. Regularization of the Scattering

We consider the form of

$$\psi^\pm(z) = \psi_n^\pm(z) \psi_{\varepsilon_n}^\pm(z) \tag{6}$$

where the subscripts n and ε_n denote *truncated* and *corrected*, respectively. The truncated series of the entire function, which is a polynomial of degree n , is represented by the finite product

Footnote 1: For a half-plane diffraction problem, the asymptotic theory is discussed to evaluate the edge-diffraction by means of the spectral integral given above [3]. The present theory may also be applicable to the diffraction problems where we must assume

$$\psi^\pm(z) \rightarrow \psi^\pm(\sqrt{z})/(z - z_{specular})$$

so as to produce the specular reflection in the illuminated region or the cancellation of the incident field in the shadow region whenever the integral path in Eq.(5) runs across the pole [4][5].

$$\begin{aligned}\psi_n^+(z) &= (1 - z/z_1^+)(1 - z/z_2^+) \cdots (1 - z/z_n^+) \\ \psi_n^-(z) &= (1 - z/z_1^-)(1 - z/z_2^-) \cdots (1 - z/z_n^-)\end{aligned}\quad (7)$$

Therefore

$$\Pi(\theta) = \Pi_n(\theta) \Pi_{\varepsilon_n}(\theta) \quad (8)$$

$$\Pi_n(\theta) = \psi_n^+(z) \psi_n^-(1/z), \quad \Pi_{\varepsilon_n}(\theta) = \psi_{\varepsilon_n}^+(z) \psi_{\varepsilon_n}^-(1/z) \quad (9)$$

From Eqs. (5) and (9), we have

$$u_{\varepsilon_n}(z, \zeta) = \int_{-i\infty \exp(i\alpha_2)}^{+i0 \exp(i\alpha_1)} \psi_{\varepsilon_n}^+(t) \psi_{\varepsilon_n}^-\left(\frac{1}{t}\right) e^{-i\frac{k}{2}(\frac{z}{t} + \zeta t)} \frac{dt}{t} \quad (10)$$

$$u(z, \zeta) = \psi_n^+\left(i\frac{2}{k} \frac{\partial}{\partial \zeta}\right) \psi_n^-\left(i\frac{2}{k} \frac{\partial}{\partial z}\right) u_{\varepsilon_n}(z, \zeta) \quad (11)$$

Equation (11) shows that the exact field u is symbolically derived from the corrected u_{ε_n} by a linear transformation (a differential operation). Physically speaking, u is expressed by expanding it into a multipole series in which u_{ε_n} acts as a leading term just like a monopole field in cylindrical harmonic series expansions. It may be remarkable that the field u is determined from u_{ε_n} and, for an adequately large n , u_{ε_n} is a known quantity [1][2].

The arguments stated above may be repeated again from another point of view. Introducing the Borel transform

$$f^\pm(z) = \frac{1}{2\pi i} \oint_{\gamma^\pm} F^\pm(t) e^{+i\frac{k}{2}zt} dt, \quad F^\pm(z) = i\frac{k}{2} \int_0^{-i\infty \exp(i\alpha)} f^\pm(t) e^{-i\frac{k}{2}t} dt \quad (12)$$

$$|\arg z + \alpha| < \frac{\pi}{2}$$

for

$$f^\pm(z) = \psi^\pm(z), \psi_{\varepsilon_n}^\pm(z), \quad F^\pm(z) = \Psi^\pm(z), \Psi_{\varepsilon_n}^\pm(z) \quad (13)$$

we have [1][2]

$$u(z, \zeta) = \frac{1}{(2\pi i)^2} \oint_{\gamma^-} dt \oint_{\gamma^+} d\tau K(z, \zeta; t, \tau) \Psi^-(t) \Psi^+(\tau) \quad (14)$$

$$K(z, \zeta; t, \tau) = \pi i H_0^{(2)}(k\sqrt{(z-t)(\zeta-\tau)}) \quad (15)$$

$$u_{\varepsilon_n}(z, \zeta) = \frac{1}{(2\pi i)^2} \oint_{\gamma^-} dt \oint_{\gamma^+} d\tau K(z, \zeta; t, \tau) \Psi_{\varepsilon_n}^-(t) \Psi_{\varepsilon_n}^+(\tau) \quad (16)$$

and obtain another version of Eq.(11):

$$\Psi^\pm(z) = \psi_n^\pm \left(i \frac{2}{k} \frac{\partial}{\partial z} \right) \Psi_{\varepsilon_n}^\pm(z) \quad (17)$$

This is an expression for multipole expansions of the field u written in the Borel domain. Geometrical optic nature of the field is described by the linear operator that generates multiple interference of waves.

4. Computational Algorithm to the Truncated Spectrum

As stated above, the truncated function for the spectrum amplitude is given by a polynomial

$$\begin{aligned} \psi_n(z) &= (1 - z/z_1)(1 - z/z_2) \cdots (1 - z/z_n) \\ &= 1 + c_1 z + c_2 z^2 + \dots + c_n z^n \end{aligned} \quad (18)$$

where the coefficients c_m s are written in terms of the zeros z_m s as follows:

$$\begin{aligned} c_1 &= -1/z_1 - 1/z_2 - \dots - 1/z_n \\ c_2 &= 1/z_1 z_2 + 1/z_1 z_3 + \dots + 1/z_{n-1} z_n \\ c_3 &= -1/z_1 z_2 z_3 - 1/z_1 z_2 z_4 - \dots - 1/z_{n-2} z_{n-1} z_n \\ &\quad \square \square \square \square \square \square \square \\ c_n &= (-1)^n 1/z_1 z_2 \cdots z_n \end{aligned} \quad (19)$$

If these zeros are not yet determined but, instead, the b_m s are already known in the form of

$$\begin{aligned} b_1 &= 1/z_1 + 1/z_2 + \dots + 1/z_n \\ b_2 &= 1/z_1^2 + 1/z_2^2 + \dots + 1/z_n^2 \\ b_3 &= 1/z_1^3 + 1/z_2^3 + \dots + 1/z_n^3 \\ &\quad \square \square \square \square \square \square \square \\ b_n &= 1/z_1^n + 1/z_2^n + \dots + 1/z_n^n \end{aligned} \quad (20)$$

then the c_m s can be computed by the Newton's algorithm [8]; *i.e.*,

$$\begin{aligned}
c_1 &= -b_1 \\
c_2 &= -\frac{1}{2}(b_2 - b_1^2) \\
c_3 &= -\frac{1}{3}(b_3 + c_1 b_2 + c_2 b_1) \\
&\square\square\square\square\square\square\square \\
c_m &= -\frac{1}{m}(b_m + c_1 b_{m-1} + c_2 b_{m-2} + \dots + c_{m-1} b_1) \\
&\square\square\square\square\square\square\square \\
c_n &= -\frac{1}{n}(b_n + c_1 b_{n-1} + c_2 b_{n-2} + \dots + c_{n-1} b_1)
\end{aligned} \tag{21}$$

and

$$c_{n+l} = 0 \quad l = 1, 2, 3, \dots \tag{22}$$

Equation (22) is readily derived from Eq. (21) and the associated Newton's formula

$$b_{n+l} = -c_1 b_{n+l-1} - c_2 b_{n+l-2} - \dots - c_n b_l \tag{23}$$

We go back to Eqs. (7) and apply Formulas (21) and (22) to calculate the coefficients of the polynomials that are under consideration. Namely,

$$\text{for } \psi_n^+(z), \quad b_m = -a_{-m} \quad (m = 1, 2, 3, \dots, n) \tag{24}$$

$$\text{and for } \psi_n^-(z), \quad b_m = a_m \quad (m = 1, 2, 3, \dots, n) \tag{25}$$

where

$$a_m = -m \frac{1}{2\pi} \int_0^{2\pi} e^{im\theta} \ln \Pi_n(\theta) d\theta \tag{26}$$

Although we have cited the final results from [8], the derivation of Eqs. (24) and (25) is not so difficult when substituting Eqs. (7) and (9) into Eq. (26) and carrying out the integration in the complex plane. If no errors are contained, we can determine the exact polynomials from Eq. (18). However, when n tends to infinity, Eq. (26) will converge slowly and, as a result, $\psi_n^+(z)$ and $\psi_n^-(z)$ will also converge very slowly. For a large number of n , the quantities described by the subscript ε_n may be small and are known data under static approximations. The truncated spectrum amplitude $\Pi_n(\theta)$ can be obtained by subtracting the known part from $\Pi(\theta)$.

5. Conclusions

Analytic singularities of the scattering from polygonal cylinders have been removed from the plane wave spectra. The regularized spectra have been described in terms of polynomials of finite degree, which are exactly determined by the Newton's algorithm. This is a sort of analytic continuation to the complex space from the numerical data on $\Pi(\theta)$. All zeros of $\Pi_n(\theta)$, although finite, are distributed over the complex z plane. Some are close to but outside the unit circle, and others may be apart from it. However, the major zeros never extend to infinity in the present regularization scheme.

References

- [1] M.Hashimoto, "Study of high-frequency scattered fields in connection with the location of their zeros on the spectral complex-plane," Proc. of IVth Int. workshop on Electromagnetic Wave Scattering (EWS2006), September 18-22, 2006, Gebze, Turkey, pp.4.9 – 4.14
- [2] M.Hashimoto:"Locations of zeros for electromagnetic fields scattered by polygonal objects," IEICE Trans. Electron., vol.E87-C, no.9, pp.1595 – 1606, September 2004.
- [3] D.Bouche, F.Molinet and R.Mitra, Asymptotic methods in electromagnetics, Chapt.4, Springer-Verlag, Berlin, 1997.
- [4] M.Hashimoto, "A note on bicomplex representation for electromagnetic fields in scattering and diffraction problems and its high-frequency and low-frequency approximations," IEICE Trans. Electron., vol.E80-C, no.11, pp.1448 –1456, November 1997.
- [5] M.Hashimoto, "Bicomplex waves in electromagnetic scattering and diffraction problems," IEICE Trans. Electron., vol.E83-C, no.2, pp.236 – 247, February 2000.
- [6] A.I.Nosich,," Method of analytical regularization based on the static part inversion in wave scattering by imperfect thin screens their zeros on the spectral complex-plane," Proc. of Int. workshop on Direct and Inverse Wave Scattering , Sept.25-29, 2000, Gebze, Turkey, pp.4.3 – 4.9.
- [7] Yu.A.Tuchkin, "Method of analytical regularization: State of art and new approaches," Proc. of IVth Int. workshop on Electromagnetic Wave Scattering (EWS2006), September 18 – 22, 2006, Gebze, Turkey, pp.2.43 – 2.48.
- [8] M.Hashimoto, "Some remarks on the extension of numerical data to the complex space for radiation patterns in electromagnetic scattering problems," IEICE Trans. Electron., submitted.

**Field Relations on Sources Described by Zeroth and First Order
Distributions in Arbitrary Motion**

Burak Polat

Not available at the time of publication

SECTION 5

- 5.1. Ozgur Ergul and Levent Gurel, “*Field-Based-Stabilized Combined Tangential Formulation for the Accurate Solution of Scattering Problems Involving Low-Contrast Dielectric Objects*” 5-1
- 5.2. Ozlem Ozgun, Raj Mittra and Mustafa Kuzuoglu, “*Characteristic Basis Finite Element Method (CBFEM-MPI) - A Parallel, Non-iterative Domain Decomposition Algorithm for the Solution of Large-scale Electromagnetic Scattering Problems*” 5-15
- 5.3. Elvin Yalçın, C. Girard, M. Cabellic, M.Héliier, G. Alquié, J.-L. Montmagnon, “*Modelling Interference Phenomena between Cosite Radiocommunication Equipments to Evaluate Systems Performance Degradation*” 5-25

Field-Based-Stabilized Combined Tangential Formulation for the Accurate Solution of Scattering Problems Involving Low-Contrast Dielectric Objects

Özgür Ergül^{1,2} and Levent Gürel^{1,2}

¹Department of Electrical and Electronics Engineering

²Computational Electromagnetics Research Center (BiLCEM)

Bilkent University, TR-06800, Bilkent, Ankara, Turkey

E-mail: ergul@ee.bilkent.edu.tr, lgurel@bilkent.edu.tr

Abstract — We present a robust stabilization technique, which enables the accurate solution of scattering problems involving dielectric objects with arbitrarily low contrasts via surface integral equations (SIEs). Conventional SIEs provide inaccurate results for the scattered fields when the contrast of an object is low, i.e., when the electromagnetic material parameters of the scatterer and the host medium are close to each other. The proposed technique is based on decomposing the equivalent currents into radiating and nonradiating parts, and extracting the dominant nonradiating currents. In addition, we rearrange the right-hand side of the equations by introducing fictitious incident fields to eliminate numerical problems for very low contrasts. The overall stabilization procedure is applied to a combined tangential formulation (CTF) with a negligible computational cost. We show that the resulting stable formulation, which is called the field-based stabilized CTF (FBS-CTF), provides accurate results even for extremely low-contrast objects, and its accuracy does not break down with finite-precision methods, such as the multilevel fast multipole algorithm.

1. INTRODUCTION

Surface integral equations (SIEs) are commonly used to formulate scattering problems involving three-dimensional dielectric objects with arbitrary shapes. Using equivalent electric and magnetic currents and applying the boundary conditions on the surface of the scatterer, a set of integral equations can be obtained. In the literature, various SIE formulations are derived by using diverse combinations of the boundary conditions, testing schemes, and scaling operations for the numerical solution of scattering problems [1]–[15]. Some of these formulations are stable and free of the internal-resonance problem, and they provide accurate results for dielectric objects with moderate dielectric parameters. Unfortunately, those formulations become inaccurate as the contrast of the object decreases, i.e., when the electromagnetic material properties of the object and the host medium become close to each other.

There are various applications that involve scattering from low-contrast objects, such as red blood cells in blood plasma [11],[16],[17], plastic mines buried in soil [18], polymeric materials [19], and dielectric photonic crystals [20]. When the contrast is low, however, traditional SIE formulations encounter stability problems, and the scattered fields cannot be calculated accurately with them. Those scattering problems can be solved accurately with volume integral equations (VIEs) [21], which are stable when the contrast is low. On the other hand, it is also desirable to extend the applicability of SIEs to low-contrast problems in order to use the advantages of the surface formulations, which are usually discretized with fewer unknowns compared to volume formulations.

This work was supported by the Scientific and Technical Research Council of Turkey (TUBITAK) under Research Grant 105E172, by the Turkish Academy of Sciences in the framework of the Young Scientist Award Program (LG/TUBA-GEBIP/2002-1-12), and by contracts from ASELSAN and SSM.

In this paper, we present a robust stabilization technique, which enables the accurate solution of low-contrast problems with SIEs. This technique is based on decomposing the equivalent currents into radiating and nonradiating parts [22],[23]. The nonradiating currents correspond to the tangential incident fields on the surface of the scatterer. When the contrast of the object is low, the nonradiating currents dominate the solution, and the radiating currents form very small portions of the total currents. Therefore, when the total currents are solved by employing the conventional surface formulations, it becomes difficult to perform the calculations accurately enough to capture the small radiating currents properly. By extracting the nonradiating currents, however, the radiating currents can be computed accurately even for low-contrast objects, i.e., when the radiating currents are numerically insignificant compared to the nonradiating currents.

Extraction of the nonradiating currents is necessary but not sufficient to solve problems with arbitrarily low contrasts. Numerical errors arising on the right-hand sides (RHSs) of integral equations become significant and deteriorate the accuracy of the results when the contrast decreases to very low values. As a remedy, we define fictitious incident fields and rearrange the RHSs of the equations. The overall stabilization procedure, which involves the extraction of the nonradiating currents and the rearrangement of the RHS, is applied to a combined tangential formulation (CTF). We show that the resulting stable formulation, which we call the field-based stabilized CTF (FBS-CTF), provides accurate results even for extremely low-contrast objects. FBS-CTF is easy to implement by modifying the existing codes for the conventional CTF, it has a negligible extra cost, and its accuracy does not break down with finite-precision methods, such as the fast multipole method [24] and the multilevel fast multipole algorithm (MLFMA) [25].

2. SURFACE INTEGRAL EQUATIONS

For homogenous dielectric objects, SIE formulations are constructed by combining tangential (T) and normal equations (N), namely, the tangential electric-field integral equation (T-EFIE), the normal electric-field integral equation (N-EFIE), the tangential magnetic-field integral equation (T-MFIE), and the normal magnetic-field integral equation (N-MFIE) [8]. In the T equations, boundary conditions are tested directly by sampling the tangential components of the electric and magnetic fields on the surface. In the N equations, however, electromagnetic fields are tested after they are projected onto the surface via a cross-product operation with the outward normal vector \hat{n} . These equations can be obtained for both the inner and outer regions, and they can be combined in diverse ways to derive various SIE formulations [1]–[15].

In general, SIE formulations can be categorized into three groups, i.e., tangential, normal, and mixed formulations, depending on the integral equations used to construct the formulation. The tangential formulations, such as the tangential Poggio-Miller-Chang-Harrington-Wu-Tsai (T-PMCHWT) formulation [2]–[4] and CTF [13], are obtained by using T-EFIE and T-MFIE. In both formulations, T-EFIE and T-MFIE are solved simultaneously, while the inner and outer equations are linearly combined to avoid internal resonances. Similar combinations of N-EFIE and N-MFIE lead to the normal formulations, such as the combined normal formulation (CNF) [13], the normal Müller formulation (NMF) [1], and the modified normal Müller formulation (MNMF) [14]. Finally, the mixed formulations, such as the electric and magnetic current combined-field integral equation (JMCFIE) [12],[26] and the combined PMCHWT Müller formulation (CPMF) [27], are obtained by combining the tangential and normal formulations appropriately. JMCFIE involves a combination of CTF and CNF, while CPMF is a similar combination of PMCHWT and MNMF. There are also other types of mixed formulations, which are generally called the combined-field integral equation (CFIE) formulations, where the T-EFIE, T-MFIE, N-EFIE, and N-MFIE are combined in various ways while the inner and outer problems are solved simultaneously [7]–[10].

Using a Galerkin scheme in the discretization of the surface formulations, i.e., using the same set of functions to expand the current densities (basis functions) and to test the boundary conditions (testing

functions), the normal and mixed formulations contain well-tested identity operators [13]. Therefore, these formulations usually produce well-conditioned matrix equations, which are easy to solve iteratively. However, the tangential formulations do not contain well-tested identity operators, and their discretizations may lead to ill-conditioned matrix equations. For the efficiency of the solutions, normal and mixed formulations are preferable, especially when problems involve large objects discretized with large numbers of unknowns [28],[29]. On the other hand, errors in the discretization of the well-tested identity operators may deteriorate the accuracy of the solutions obtained with the normal and mixed formulations [13]. The excessive error in those formulations compared to the tangential formulations can be significant [27],[28],[29], especially in conventional implementations employing the low-order Rao-Wilton-Glisson (RWG) functions [30]. In such cases, it is helpful to improve the discretizations either by employing higher-order basis functions [13],[31] or by reducing the size of the discretization elements, to obtain accurate results.

Conventional SIE formulations are stable and provide accurate solutions (with various levels of accuracy, depending on the existence of well-tested identity operators, types of the basis and testing functions, discretization method, geometry of the object, etc.), for problems involving objects with moderate contrasts. However, those formulations become inaccurate to calculate the scattered fields as the contrast of the object decreases, i.e., when the electromagnetic material properties of the object and the host medium become close to each other. This is one of the major drawbacks of the SIE formulations in comparison to VIE formulations, which do not break down for low contrasts. In this paper, we present a robust stabilization procedure to eliminate the low-contrast breakdown in surface formulations.

3. COMBINED TANGENTIAL FORMULATION

The stabilization procedure is applied to CTF (that is slightly different from the original CTF presented in [13]), although it can be generalized to other existing formulations in the literature. Consider scattering from a homogenous dielectric object with a three-dimensional arbitrary shape. We assume time-harmonic electromagnetic fields with $e^{-i\omega t}$ time dependence. Incident electromagnetic fields are created by some external sources located outside the object. To derive CTF, operators for the outside ($l = 0$) and inside ($l = 1$) the object are defined as

$$\mathcal{K}_l\{\mathbf{X}\}(\mathbf{r}) = \int_{PV,S} d\mathbf{r}' \mathbf{X}(\mathbf{r}') \times \nabla' g_l(\mathbf{r}, \mathbf{r}') \quad (1)$$

$$\mathcal{T}_l\{\mathbf{X}\}(\mathbf{r}) = ik_l \int_S d\mathbf{r}' \left[\mathbf{X}(\mathbf{r}') + \frac{1}{k_l^2} \nabla' \cdot \mathbf{X}(\mathbf{r}') \nabla \right] g_l(\mathbf{r}, \mathbf{r}'), \quad (2)$$

where $\mathbf{X}(\mathbf{r})$ is either the equivalent electric current $\mathbf{J}(\mathbf{r}) = \hat{\mathbf{n}} \times \mathbf{H}(\mathbf{r})$ or the equivalent magnetic current $\mathbf{M}(\mathbf{r}) = -\hat{\mathbf{n}} \times \mathbf{E}(\mathbf{r})$ on the surface of the object S , $k_l = \omega \sqrt{\mu_l \epsilon_l}$ is the wavenumber associated with medium l , and

$$g_l(\mathbf{r}, \mathbf{r}') = \frac{\exp(ik_l R)}{4\pi R} \quad \left(R = |\mathbf{r} - \mathbf{r}'| \right) \quad (3)$$

denotes the homogeneous-space Green's function.

CTF is obtained by combining the inner and outer tangential equations, i.e., T-EFIE₀ + T-EFIE₁ and T-MFIE₀ + T-MFIE₁, as

$$\hat{\mathbf{t}} \cdot \begin{bmatrix} \eta_0 \mathcal{T}_0 + \eta_1 \mathcal{T}_1 & -(\mathcal{K}_0 + \mathcal{K}_1) \\ \eta_0 \eta_1 (\mathcal{K}_0 + \mathcal{K}_1) & \eta_1 \mathcal{T}_0 + \eta_0 \mathcal{T}_1 \end{bmatrix} \cdot \begin{bmatrix} \mathbf{J} \\ \mathbf{M} \end{bmatrix}(\mathbf{r}) = -\hat{\mathbf{t}} \cdot \begin{bmatrix} \mathbf{E}^i(\mathbf{r}) \\ \eta_0 \eta_1 \mathbf{H}^i(\mathbf{r}) \end{bmatrix}, \quad (4)$$

where $\mathbf{E}^i(\mathbf{r})$ and $\mathbf{H}^i(\mathbf{r})$ are the incident electric and magnetic fields, $\eta_l = \sqrt{\mu_l / \epsilon_l}$ is the impedance of medium l , and $\hat{\mathbf{t}}$ is any tangential vector at the observation point \mathbf{r} on the surface. CTF in (4) does not contain any identity operator, and \mathcal{K} operators are not well-tested [13],[27]. On the other hand, \mathcal{T}

operators are well-tested and they are located in the diagonal blocks. For low contrasts, i.e., $\epsilon_1 \approx \epsilon_0$ and $\mu_1 \approx \mu_0$, the diagonal blocks in (4) are numerically well-balanced, which is a desirable property in terms of conditioning [13].

3.1. Discretization

For numerical solutions of CTF, surface currents are expanded in a series of RWG functions, i.e.,

$$\mathbf{J}(\mathbf{r}) = \sum_{n=1}^N x_n \mathbf{b}_n(\mathbf{r}) \quad (5)$$

$$\mathbf{M}(\mathbf{r}) = \sum_{n=1}^N y_n \mathbf{b}_n(\mathbf{r}), \quad (6)$$

where $\mathbf{b}_n(\mathbf{r})$ for $n = 1, 2, \dots, N$ represents the n th basis function with a spatial support of A_n , while x_n and y_n are unknown coefficients. Using a Galerkin scheme, we employ the same set of RWG functions to test the boundary conditions, i.e., $\mathbf{t}_m(\mathbf{r})$ for $m = 1, 2, \dots, N$. Discretization of CTF leads to $2N \times 2N$ dense matrix equations in the form of

$$\begin{bmatrix} \bar{\mathbf{Z}}_{11} & \bar{\mathbf{Z}}_{12} \\ \bar{\mathbf{Z}}_{21} & \bar{\mathbf{Z}}_{22} \end{bmatrix} \cdot \begin{bmatrix} \mathbf{x} \\ \mathbf{y} \end{bmatrix} = - \begin{bmatrix} \mathbf{v} \\ \eta_0 \eta_1 \mathbf{w} \end{bmatrix}, \quad (7)$$

where \mathbf{x} and \mathbf{y} are column vectors involving the unknown coefficients in (5) and (6), respectively. Matrix elements in (7) are derived as

$$\bar{\mathbf{Z}}_{11} = \eta_0 \bar{\mathbf{T}}_0 + \eta_1 \bar{\mathbf{T}}_1 \quad (8)$$

$$\bar{\mathbf{Z}}_{12} = -\bar{\mathbf{K}}_0 - \bar{\mathbf{K}}_1 \quad (9)$$

$$\bar{\mathbf{Z}}_{21} = \eta_0 \eta_1 \bar{\mathbf{K}}_0 + \eta_0 \eta_1 \bar{\mathbf{K}}_1 \quad (10)$$

$$\bar{\mathbf{Z}}_{22} = \eta_1 \bar{\mathbf{T}}_0 + \eta_0 \bar{\mathbf{T}}_1, \quad (11)$$

where

$$\bar{\mathbf{K}}_l[m, n] = \int_{A_m} d\mathbf{r} \mathbf{t}_m(\mathbf{r}) \cdot \int_{PV, A_n} d\mathbf{r}' \mathbf{b}_n(\mathbf{r}') \times \nabla' g_l(\mathbf{r}, \mathbf{r}') \quad (12)$$

$$\begin{aligned} \bar{\mathbf{T}}_l[m, n] &= ik_l \int_{A_m} d\mathbf{r} \mathbf{t}_m(\mathbf{r}) \cdot \int_{A_n} d\mathbf{r}' \mathbf{b}_n(\mathbf{r}') g_l(\mathbf{r}, \mathbf{r}') \\ &\quad - \frac{i}{k_l} \int_{A_m} d\mathbf{r} \mathbf{t}_m(\mathbf{r}) \cdot \int_{A_n} d\mathbf{r}' \nabla' \cdot \mathbf{b}_n(\mathbf{r}') \nabla' g_l(\mathbf{r}, \mathbf{r}') \end{aligned} \quad (13)$$

for $m, n = 1, 2, \dots, N$, and $l = 0, 1$. As it is commonly practiced in the T-EFIE formulations of perfectly-conducting objects [30], the hyper-singularity in (13) removed by placing the differential operator onto the divergence-conforming testing functions, i.e.,

$$\begin{aligned} \bar{\mathbf{T}}_l[m, n] &= ik_l \int_{A_m} d\mathbf{r} \mathbf{t}_m(\mathbf{r}) \cdot \int_{A_n} d\mathbf{r}' \mathbf{b}_n(\mathbf{r}') g_l(\mathbf{r}, \mathbf{r}') \\ &\quad + \frac{i}{k_l} \int_{A_m} d\mathbf{r} \nabla \cdot \mathbf{t}_m(\mathbf{r}) \int_{A_n} d\mathbf{r}' \nabla' \cdot \mathbf{b}_n(\mathbf{r}') g_l(\mathbf{r}, \mathbf{r}'). \end{aligned} \quad (14)$$

Integrals in (12) and (14) are evaluated accurately by employing Gaussian quadrature rules, adaptive integration methods, and singularity extraction techniques [32]–[37]. Finally, to calculate the elements of the RHS vector in (7), the integrals

$$\mathbf{v}[m] = \int_{A_m} d\mathbf{r} \mathbf{t}_m(\mathbf{r}) \cdot \mathbf{E}^i(\mathbf{r}) \quad (15)$$

$$\mathbf{w}[m] = \int_{A_m} d\mathbf{r} \mathbf{t}_m(\mathbf{r}) \cdot \mathbf{H}^i(\mathbf{r}) \quad (16)$$

are evaluated for $m = 1, 2, \dots, N$.

3.2. Solutions via MLFMA

Matrix equations obtained with CTF can be solved iteratively, where the required matrix-vector multiplications are performed efficiently by MLFMA in $\mathcal{O}(N \log N)$ time using $\mathcal{O}(N \log N)$ memory [25]. A tree structure of $\mathcal{O}(\log N)$ levels is constructed by placing the dielectric object in a cubic box and recursively dividing the computational domain into sub-boxes (clusters). Then, MLFMA calculates the distant interactions between the basis and testing functions in a group-by-group manner consisting of three stages called aggregation, translation, and disaggregation [38]. In each matrix-vector multiplication, these stages are performed on the tree structure in a multilevel scheme.

By factorizing the Green's function and performing a diagonalization [24], the matrix elements in (12) and (14) can be rewritten as

$$\bar{\mathbf{K}}_l[m, n] = \left(\frac{ik_l}{4\pi}\right)^2 \int d^2\hat{\mathbf{k}} \mathbf{F}_{mC}^{\mathcal{K}}(\mathbf{k}_l) \alpha_{L_l}(\mathbf{k}_l, \mathbf{R}_{CC'}) \cdot \mathbf{S}_{C'n}(\mathbf{k}_l) \quad (17)$$

$$\bar{\mathbf{T}}_l[m, n] = \left(\frac{ik_l}{4\pi}\right)^2 \int d^2\hat{\mathbf{k}} \mathbf{F}_{mC}^{\mathcal{T}}(\mathbf{k}_l) \alpha_{L_l}(\mathbf{k}_l, \mathbf{R}_{CC'}) \cdot \mathbf{S}_{C'n}(\mathbf{k}_l) \quad (18)$$

when the testing and basis functions are far from each other. In (17) and (18), $\hat{\mathbf{k}}$ is the angular direction, $\mathbf{k}_l = k_l \hat{\mathbf{k}}$, and

$$\alpha_{L_l}(\mathbf{k}_l, \mathbf{R}_{CC'}) = \sum_{t=0}^{L_l} i^t (2t+1) h_t^{(1)}(k_l R_{CC'}) P_t(\hat{\mathbf{R}}_{CC'} \cdot \hat{\mathbf{k}}) \quad (19)$$

is the translation operator expressed in terms of the spherical Hankel function of the first kind $h_t^{(1)}$ and the Legendre polynomial P_t . In (17) and (18), the radiation pattern of the n th basis function in cluster C' , i.e., $\mathbf{S}_{C'n}(\mathbf{k}_l)$, is translated into incoming fields for the testing functions in cluster C . The distance between the clusters is represented by the vector

$$\mathbf{R}_{CC'} = R_{CC'} \hat{\mathbf{R}}_{CC'} = \mathbf{r}_C - \mathbf{r}_{C'}, \quad (20)$$

where \mathbf{r}_C and $\mathbf{r}_{C'}$ are reference points of the clusters C and C' , respectively. Then, the incoming fields are received by using the receiving patterns of the m th testing function, i.e., $\mathbf{F}_{mC}^{\mathcal{K}}(\mathbf{k}_l)$ and $\mathbf{F}_{mC}^{\mathcal{T}}(\mathbf{k}_l)$. Using a Galerkin scheme, the radiation and receiving patterns are calculated as [8],[29]

$$\mathbf{S}_{C'n}(\mathbf{k}_l) = \int_{S_n} d\mathbf{r}' \exp[-i\mathbf{k}_l \cdot (\mathbf{r}' - \mathbf{r}_{C'})] (\bar{\mathbf{I}}_{3 \times 3} - \hat{\mathbf{k}}\hat{\mathbf{k}}) \cdot \mathbf{b}_n(\mathbf{r}') \quad (21)$$

$$\mathbf{F}_{mC}^{\mathcal{K}}(\mathbf{k}_l) = -\hat{\mathbf{k}} \times \{\mathbf{S}_{Cm}(\mathbf{k}_l)\}^* \quad (22)$$

$$\mathbf{F}_{mC}^{\mathcal{T}}(\mathbf{k}_l) = \{\mathbf{S}_{Cm}(\mathbf{k}_l)\}^*, \quad (23)$$

where $\bar{\mathbf{I}}_{3 \times 3}$ denotes the 3×3 unit dyad and “*” represents the complex-conjugate operation.

In MLFMA, the interactions in (17) and (18) are calculated in a multilevel scheme. During the aggregation stage, radiation patterns of the clusters are calculated from the bottom to the top of the tree structure. Then, translations are performed to obtain the incoming fields for all clusters. Finally, the disaggregation stage is performed from the top of the tree structure to the lowest level, where the incoming fields are received by the testing functions to complete the matrix-vector multiplications. For each cluster, radiation and receiving patterns are sampled at $(L_l + 1) \times (2L_l + 2)$ angular points, where L_l is the truncation number in (19) that is determined by the excess bandwidth formula [39]. Since L_l is proportional to the size of the clusters with respect to the wavelength, different tree structures are constructed for the inner and outer media.

3.3. Low-Contrast Breakdown

Scattered fields obtained by using conventional formulations, such as CTF, become inaccurate as the contrast of the object decreases, i.e., when the electromagnetic material properties of the object and the host medium become close to each other. To explain this breakdown, we note that any arbitrary solution can be decomposed as

$$\mathbf{J}(\mathbf{r}) = \mathcal{I}^{\times n}\{\mathbf{H}\}(\mathbf{r}) = \hat{\mathbf{n}} \times \mathbf{H}(\mathbf{r}) = \hat{\mathbf{n}} \times \mathbf{H}^i(\mathbf{r}) + \hat{\mathbf{n}} \times \mathbf{H}^r(\mathbf{r}) \quad (24)$$

$$\mathbf{M}(\mathbf{r}) = -\mathcal{I}^{\times n}\{\mathbf{E}\}(\mathbf{r}) = -\hat{\mathbf{n}} \times \mathbf{E}(\mathbf{r}) = -\hat{\mathbf{n}} \times \mathbf{E}^i(\mathbf{r}) - \hat{\mathbf{n}} \times \mathbf{E}^r(\mathbf{r}), \quad (25)$$

where $\{\mathbf{J}^i(\mathbf{r}), \mathbf{M}^i(\mathbf{r})\} = \{\hat{\mathbf{n}} \times \mathbf{H}^i(\mathbf{r}), -\hat{\mathbf{n}} \times \mathbf{E}^i(\mathbf{r})\}$ do not radiate, i.e.,

$$\begin{bmatrix} \eta_0 \mathcal{T}_0 & -\mathcal{K}_0 + 0.5\mathcal{I}^{\times n} \\ \mathcal{K}_0 - 0.5\mathcal{I}^{\times n} & \eta_0^{-1} \mathcal{T}_0 \end{bmatrix} \cdot \begin{bmatrix} \mathbf{J}^i \\ \mathbf{M}^i \end{bmatrix}(\mathbf{r}) = \begin{bmatrix} 0 \\ 0 \end{bmatrix}. \quad (26)$$

As the contrast goes to zero, the nonradiating currents dominate the total currents, while the radiating currents, i.e., $\{\mathbf{J}^r(\mathbf{r}), \mathbf{M}^r(\mathbf{r})\} = \{\hat{\mathbf{n}} \times \mathbf{H}^r(\mathbf{r}), -\hat{\mathbf{n}} \times \mathbf{E}^r(\mathbf{r})\}$, tend to vanish. Therefore, when the total currents are solved by employing the conventional surface formulations, it becomes difficult to perform the calculations accurately enough to capture the small radiating currents properly. The total currents $\mathbf{J}(\mathbf{r})$ and $\mathbf{M}(\mathbf{r})$ can be computed with relatively small error, but scattered fields may not be obtained accurately from them [22].

4. STABILIZATION OF CTF

For the accurate solution of scattering problems involving low-contrast objects, CTF is stabilized by extracting the nonradiating currents and solving only the radiating currents [23]. The resulting formulation, which we call stable CTF (S-CTF), can be written as

$$\begin{aligned} \hat{\mathbf{t}} \cdot \begin{bmatrix} \eta_0 \mathcal{T}_0 + \eta_1 \mathcal{T}_1 & -(\mathcal{K}_0 + \mathcal{K}_1) \\ \eta_0 \eta_1 (\mathcal{K}_0 + \mathcal{K}_1) & \eta_1 \mathcal{T}_0 + \eta_0 \mathcal{T}_1 \end{bmatrix} \cdot \begin{bmatrix} \mathbf{J}^r \\ \mathbf{M}^r \end{bmatrix}(\mathbf{r}) \\ = \hat{\mathbf{t}} \cdot \begin{bmatrix} \eta_0 \mathcal{T}_0 - \eta_1 \mathcal{T}_1 & -(\mathcal{K}_0 - \mathcal{K}_1) \\ \eta_0 \eta_1 (\mathcal{K}_0 - \mathcal{K}_1) & \eta_1 \mathcal{T}_0 - \eta_0 \mathcal{T}_1 \end{bmatrix} \cdot \begin{bmatrix} \mathbf{J}^i \\ \mathbf{M}^i \end{bmatrix}(\mathbf{r}). \end{aligned} \quad (27)$$

We note that the left-hand side (LHS) of S-CTF in (27) is the same as the LHS of CTF in (4), and the stabilization procedure alters only the RHS of the original formulation. Discretization of (27) leads to

$$\begin{bmatrix} \bar{\mathbf{Z}}_{11} & \bar{\mathbf{Z}}_{12} \\ \bar{\mathbf{Z}}_{21} & \bar{\mathbf{Z}}_{22} \end{bmatrix} \cdot \begin{bmatrix} \mathbf{x}^r \\ \mathbf{y}^r \end{bmatrix} = \begin{bmatrix} \bar{\mathbf{Y}}_{11} & \bar{\mathbf{Y}}_{12} \\ \bar{\mathbf{Y}}_{21} & \bar{\mathbf{Y}}_{22} \end{bmatrix} \cdot \begin{bmatrix} \mathbf{x}^i \\ \mathbf{y}^i \end{bmatrix}, \quad (28)$$

where

$$\bar{\mathbf{Y}}_{11} = \eta_0 \bar{\mathbf{T}}_0 - \eta_1 \bar{\mathbf{T}}_1 \quad (29)$$

$$\bar{\mathbf{Y}}_{12} = -\bar{\mathbf{K}}_0 + \bar{\mathbf{K}}_1 \quad (30)$$

$$\bar{\mathbf{Y}}_{21} = \eta_0 \eta_1 \bar{\mathbf{K}}_0 - \eta_0 \eta_1 \bar{\mathbf{K}}_1 \quad (31)$$

$$\bar{\mathbf{Y}}_{22} = \eta_1 \bar{\mathbf{T}}_0 - \eta_0 \bar{\mathbf{T}}_1. \quad (32)$$

In (28), $\{\mathbf{x}^r, \mathbf{y}^r\}$ and $\{\mathbf{x}^i, \mathbf{y}^i\}$ are two sets of column vectors involving the coefficients expanding the radiating and nonradiating currents, respectively, i.e.,

$$\{\hat{\mathbf{n}} \times \mathbf{H}^r(\mathbf{r}), -\hat{\mathbf{n}} \times \mathbf{E}^r(\mathbf{r})\} = \sum_{n=1}^N \{x_n^r, y_n^r\} \mathbf{b}_n(\mathbf{r}) \quad (33)$$

$$\{\hat{\mathbf{n}} \times \mathbf{H}^i(\mathbf{r}), -\hat{\mathbf{n}} \times \mathbf{E}^i(\mathbf{r})\} = \sum_{n=1}^N \{x_n^i, y_n^i\} \mathbf{b}_n(\mathbf{r}). \quad (34)$$

To obtain the coefficients expanding the known nonradiating currents, we solve the sparse matrix equation [23]

$$\begin{bmatrix} \bar{\mathbf{I}} & 0 \\ 0 & \bar{\mathbf{I}} \end{bmatrix} \cdot \begin{bmatrix} \mathbf{x}^i \\ \mathbf{y}^i \end{bmatrix} = \begin{bmatrix} \mathbf{w}^{\times n} \\ -\mathbf{v}^{\times n} \end{bmatrix}, \quad (35)$$

where

$$\bar{\mathbf{I}}[m, n] = \int_{A_m} d\mathbf{r} \mathbf{t}_m(\mathbf{r}) \cdot \mathbf{b}_n(\mathbf{r}) \quad (36)$$

$$\mathbf{w}^{\times n} = \int_{A_m} d\mathbf{r} \mathbf{t}_m(\mathbf{r}) \cdot \hat{\mathbf{n}} \times \mathbf{H}^i(\mathbf{r}) \quad (37)$$

$$\mathbf{v}^{\times n} = \int_{A_m} d\mathbf{r} \mathbf{t}_m(\mathbf{r}) \cdot \hat{\mathbf{n}} \times \mathbf{E}^i(\mathbf{r}). \quad (38)$$

Inserting (35) in (28), discretized S-CTF can be written as

$$\begin{bmatrix} \bar{\mathbf{Z}}_{11} & \bar{\mathbf{Z}}_{12} \\ \bar{\mathbf{Z}}_{21} & \bar{\mathbf{Z}}_{22} \end{bmatrix} \cdot \begin{bmatrix} \mathbf{x}^r \\ \mathbf{y}^r \end{bmatrix} = \begin{bmatrix} \bar{\mathbf{Y}}_{11} & \bar{\mathbf{Y}}_{12} \\ \bar{\mathbf{Y}}_{21} & \bar{\mathbf{Y}}_{22} \end{bmatrix} \cdot \begin{bmatrix} \bar{\mathbf{I}} & 0 \\ 0 & \bar{\mathbf{I}} \end{bmatrix}^{-1} \cdot \begin{bmatrix} \mathbf{w}^{\times n} \\ -\mathbf{v}^{\times n} \end{bmatrix}. \quad (39)$$

In S-CTF, the nonradiating currents are located on the RHS and only the radiating currents are solved for. This way, the radiating currents can be computed accurately for low-contrast objects, i.e., when the radiating currents are numerically insignificant compared to the nonradiating currents. Despite this corrective approach, even S-CTF breaks down and fails to provide accurate results for very low contrasts. The reason is the numerical errors arising during the computation of the RHS of S-CTF. On the RHS, \mathcal{K} and \mathcal{T} operators are applied on the nonradiating currents via matrix-vector multiplications, i.e.,

$$\begin{bmatrix} \bar{\mathbf{Y}}_{11} & \bar{\mathbf{Y}}_{12} \\ \bar{\mathbf{Y}}_{21} & \bar{\mathbf{Y}}_{22} \end{bmatrix} \cdot \begin{bmatrix} \mathbf{x}^i \\ \mathbf{y}^i \end{bmatrix} = \begin{bmatrix} \eta_0 \bar{\mathbf{T}}_0 & -\bar{\mathbf{K}}_0 \\ \eta_0 \eta_1 \bar{\mathbf{K}}_0 & \eta_1 \bar{\mathbf{T}}_0 \end{bmatrix} \cdot \begin{bmatrix} \mathbf{x}^i \\ \mathbf{y}^i \end{bmatrix} - \begin{bmatrix} \eta_1 \bar{\mathbf{T}}_1 & -\bar{\mathbf{K}}_1 \\ \eta_0 \eta_1 \bar{\mathbf{K}}_1 & \eta_0 \bar{\mathbf{T}}_1 \end{bmatrix} \cdot \begin{bmatrix} \mathbf{x}^i \\ \mathbf{y}^i \end{bmatrix}. \quad (40)$$

When the contrast decreases to very low values, the RHS of S-CTF is vanishingly small, but it is obtained by the subtraction of two terms that are relatively large. Then, depending on the accuracy of the matrix-vector multiplications in (40), the RHS of S-CTF may not be calculated accurately when the contrast is very low.

In order to obtain a stable formulation for arbitrarily low contrasts, we rearrange the RHS of S-CTF by introducing fictitious incident fields [40], i.e.,

$$\mathbf{E}_f^i(\mathbf{r}) = [\mathbf{E}^i(\mathbf{r})]_{\substack{\epsilon_0 \rightarrow \epsilon_1 \\ \mu_0 \rightarrow \mu_1}} \quad (41)$$

$$\mathbf{H}_f^i(\mathbf{r}) = [\mathbf{H}^i(\mathbf{r})]_{\substack{\epsilon_0 \rightarrow \epsilon_1 \\ \mu_0 \rightarrow \mu_1}}. \quad (42)$$

Similar to (26), the fictitious incident fields satisfy

$$\begin{bmatrix} \eta_1 \mathcal{T}_1 & -\mathcal{K}_1 + 0.5\mathcal{I}^{\times n} \\ \mathcal{K}_1 - 0.5\mathcal{I}^{\times n} & \eta_1^{-1} \mathcal{T}_1 \end{bmatrix} \cdot \begin{bmatrix} \hat{\mathbf{n}} \times \mathbf{H}_f^i \\ -\hat{\mathbf{n}} \times \mathbf{E}_f^i \end{bmatrix}(\mathbf{r}) = \begin{bmatrix} 0 \\ 0 \end{bmatrix}. \quad (43)$$

Using (43) in (27), we obtain

$$\begin{aligned} & \hat{\mathbf{t}} \cdot \begin{bmatrix} \eta_0 \mathcal{T}_0 + \eta_1 \mathcal{T}_1 & -(\mathcal{K}_0 + \mathcal{K}_1) \\ \eta_0 \eta_1 (\mathcal{K}_0 + \mathcal{K}_1) & \eta_1 \mathcal{T}_0 + \eta_0 \mathcal{T}_1 \end{bmatrix} \cdot \begin{bmatrix} \mathbf{J}^r \\ \mathbf{M}^r \end{bmatrix}(\mathbf{r}) \\ &= -0.5 \hat{\mathbf{t}} \cdot \begin{bmatrix} \mathbf{E}^i - \mathbf{E}_f^i \\ \eta_0 \eta_1 \mathbf{H}^i - \eta_0 \eta_1 \mathbf{H}_f^i \end{bmatrix}(\mathbf{r}) - \hat{\mathbf{t}} \cdot \begin{bmatrix} \eta_1 \mathcal{T}_1 & -\mathcal{K}_1 \\ \eta_0 \eta_1 \mathcal{K}_1 & \eta_0 \mathcal{T}_1 \end{bmatrix} \cdot \begin{bmatrix} \hat{\mathbf{n}} \times \mathbf{H}^i - \hat{\mathbf{n}} \times \mathbf{H}_f^i \\ -\hat{\mathbf{n}} \times \mathbf{E}^i + \hat{\mathbf{n}} \times \mathbf{E}_f^i \end{bmatrix}(\mathbf{r}). \end{aligned} \quad (44)$$

which we call FBS-CTF. Discretization of FBS-CTF leads to

$$\begin{bmatrix} \bar{\mathbf{Z}}_{11} & \bar{\mathbf{Z}}_{12} \\ \bar{\mathbf{Z}}_{21} & \bar{\mathbf{Z}}_{22} \end{bmatrix} \cdot \begin{bmatrix} \mathbf{x}^r \\ \mathbf{y}^r \end{bmatrix} = -0.5 \begin{bmatrix} \bar{\mathbf{I}} & 0 \\ 0 & \bar{\mathbf{I}} \end{bmatrix}^{-1} \cdot \begin{bmatrix} \mathbf{v}_f \\ \eta_0 \eta_1 \mathbf{w}_f \end{bmatrix} \\ - \begin{bmatrix} \eta_1 \bar{\mathbf{T}}_1 & -\bar{\mathbf{K}}_1 \\ \eta_0 \eta_1 \bar{\mathbf{K}}_1 & \eta_0 \bar{\mathbf{T}}_1 \end{bmatrix} \cdot \begin{bmatrix} \bar{\mathbf{I}} & 0 \\ 0 & \bar{\mathbf{I}} \end{bmatrix}^{-1} \cdot \begin{bmatrix} \mathbf{w}_f^{\times n} \\ -\mathbf{v}_f^{\times n} \end{bmatrix}, \quad (45)$$

where

$$\mathbf{v}_f[m] = \int_{A_m} d\mathbf{r} \mathbf{t}_m(\mathbf{r}) \cdot (\mathbf{E}^i(\mathbf{r}) - \mathbf{E}_f^i(\mathbf{r})) \quad (46)$$

$$\mathbf{w}_f[m] = \int_{A_m} d\mathbf{r} \mathbf{t}_m(\mathbf{r}) \cdot (\mathbf{H}^i(\mathbf{r}) - \mathbf{H}_f^i(\mathbf{r})) \quad (47)$$

$$\mathbf{v}_f^{\times n}[m] = \int_{A_m} d\mathbf{r} \mathbf{t}_m(\mathbf{r}) \cdot \hat{\mathbf{n}} \times (\mathbf{E}^i(\mathbf{r}) - \mathbf{E}_f^i(\mathbf{r})) \quad (48)$$

$$\mathbf{w}_f^{\times n}[m] = \int_{A_m} d\mathbf{r} \mathbf{t}_m(\mathbf{r}) \cdot \hat{\mathbf{n}} \times (\mathbf{H}^i(\mathbf{r}) - \mathbf{H}_f^i(\mathbf{r})). \quad (49)$$

In (46)–(49), real and fictitious incident fields are subtracted from each other analytically in the continuous space before the discretization. Then, the RHS of FBS-CTF in (45) is obtained as the sum of two terms, which are both small when the contrast is low, and it can be calculated accurately for arbitrarily low contrasts. FBS-CTF can easily be obtained from the conventional CTF implementation and its extra cost is negligible.

5. RESULTS

In order to demonstrate the accuracy of FBS-CTF compared to CTF and S-CTF for arbitrarily low contrasts, we consider the solution of scattering problems involving a sphere of radius $0.5\lambda_0$, where λ_0 is the wavelength outside the sphere. The sphere is located in free space and illuminated by a plane wave propagating in the z direction with the electric field polarized in the x direction. Discretization of the sphere with $\lambda_0/10$ mesh size leads to matrix equations with 1860 unknowns. Matrix elements are computed directly with 5×10^{-3} relative error. Fig. 1 depicts the bistatic radar cross section (RCS), when the relative permittivity of the sphere is 1.1, $1.0 + 10^{-3}$, $1.0 + 10^{-6}$, and $1.0 + 10^{-9}$. With these values, the contrast of the sphere, i.e., $(\epsilon_1 - \epsilon_0)/\epsilon_0$, changes from 0.1 to 10^{-9} . Normalized RCS (RCS/λ_1^2) is plotted in decibels (dB) as a function of the observation angle on the $\phi = 0^\circ$ plane, where 0° corresponds to the forward-scattering direction. RCS values are also computed analytically by a Mie-series solution. Fig. 1(a) shows that CTF, S-CTF, and FBS-CTF provide accurate results when the contrast is 0.1. As the contrast decreases to 10^{-3} and 10^{-6} , however, CTF breaks down and cannot provide accurate results. When the contrast is further reduced to 10^{-9} , S-CTF also fails to agree with the analytical solution. On the other hand, FBS-CTF provides accurate results for all contrast in Fig. 1.

Fig. 2 presents the RCS of the sphere with radius $0.5\lambda_0$, when the contrast is 10^{-6} and 10^{-9} . This time, the scattering problems are solved iteratively, where the far-field interactions are computed via FMM with two digits of accuracy. Fig. 2(a) shows that the FMM solution of S-CTF is significantly inaccurate when the contrast is 10^{-6} , as opposed to the MOM solution in Fig. 2(c). This is because the accuracy of S-CTF is sensitive to the accuracy of the matrix-vector multiplications when the contrast is very low. However, as demonstrated in Fig. 2, FBS-CTF is stable for arbitrarily low contrasts, even with finite-precision methods.

Fig. 3 presents the solution of large scattering problems, involving a sphere of radius $6\lambda_0$. The sphere is again located in free space and illuminated by a plane wave propagating in the z direction with the electric field polarized in the x direction. Discretization of the sphere with $\lambda_0/10$ mesh size leads to matrix equations with 264,006 unknowns. Scattering problems are solved iteratively via MLFMA with two digits of accuracy. Figs. 3(a) and 3(b) present the bistatic RCS values on the $\phi = 0^\circ$ plane

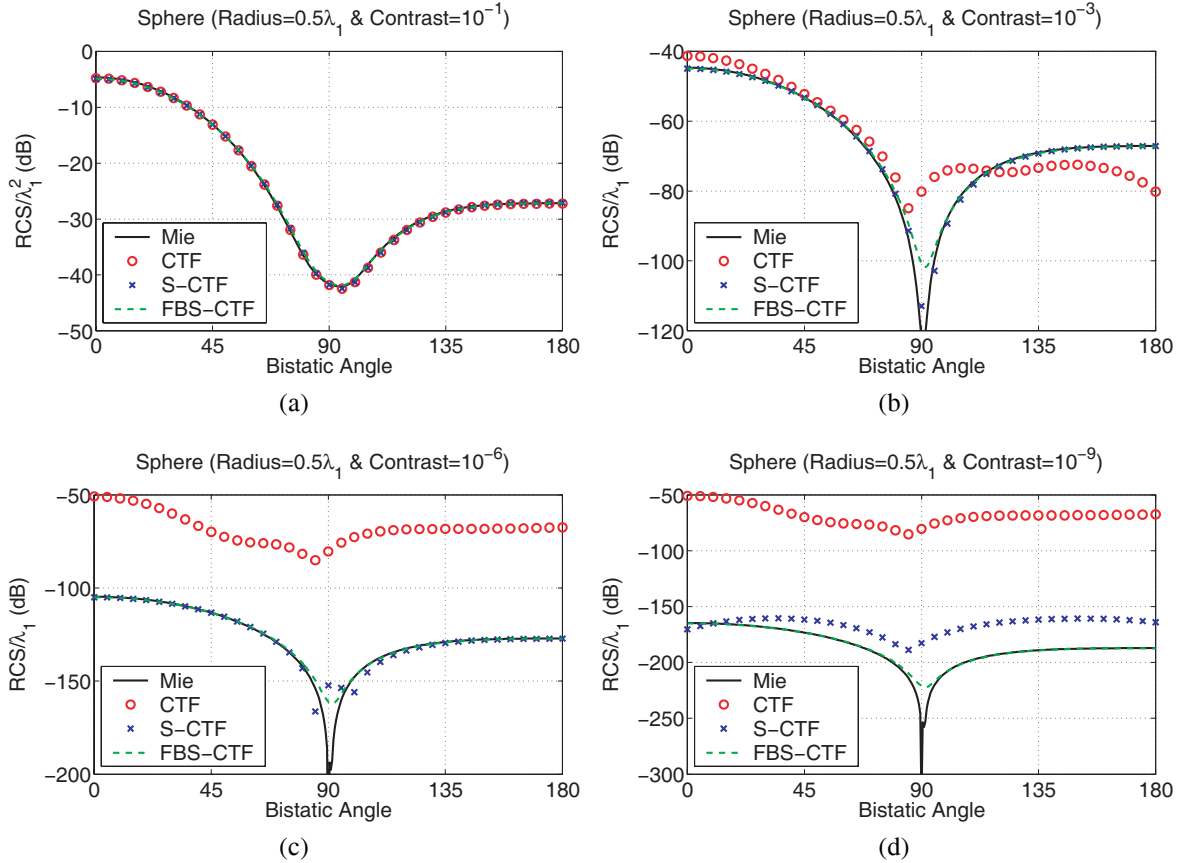


Fig. 1. Normalized bistatic RCS (RCS/λ_0^2 on the $\phi = 0^\circ$ plane) of a sphere of radius $0.5\lambda_0$, where λ_0 is the wavelength outside the sphere (free space), when the relative permittivity of the sphere is (a) $1 + 10^{-1}$, (b) $1 + 10^{-3}$, (c) $1 + 10^{-6}$, and (d) $1 + 10^{-9}$. The sphere is illuminated by a plane wave propagating in the z direction with the electric field polarized in the x direction.

when the contrast of the sphere is 10^{-3} and 10^{-6} , respectively. Similar to the previous examples, CTF is significantly inaccurate in both cases. When the contrast is 10^{-6} , RCS values obtained with S-CTF are also inaccurate and inconsistent with the analytical results, especially in the back-scattering direction. On the other hand, FBS-CTF provides accurate results for both 10^{-3} and 10^{-6} contrasts. RCS values provided by this formulation deviate from the analytical results only around 90° , where scattering is very low.

Finally, Fig. 4 presents the results of scattering problems involving a $\lambda_0 \times \lambda_0 \times \lambda_0/10$ dielectric slab, where $\lambda_0 = 1$ m is the wavelength outside the object (free space). The slab is located at the origin as depicted in the inset of Fig 4(a), and it is illuminated by a plane wave propagating in the z direction with the electric field polarized in the x direction. We consider four different relative permittivities for the slab, i.e., 2.0, 1.1, $1 + 10^{-3}$, and $1 + 10^{-6}$, corresponding to 1.0, 0.1, 10^{-3} , and 10^{-6} contrasts, respectively. The slab is discretized with $\lambda_0/20$ mesh size leading to matrix equations with 11,424 unknowns. Scattering problems are solved by using FMM, where the near-field interactions are calculated with 5×10^{-3} error and the far-field interactions are calculated with two digits of accuracy. We plot the bistatic RCS in dBms as a function of the observation angle on the $\phi = 0^\circ$ plane. RCS values obtained by using CTF and FBS-CTF are compared with those obtained by using the electric-field VIE [21], which is immune to low-contrast problems. As depicted in Fig. 4(a), CTF and FBS-CTF are consistent with VIE when the contrast of the slab is relatively large (1.0). As the contrast decreases to 0.1, 10^{-3} , 10^{-6} , however, RCS values obtained with CTF

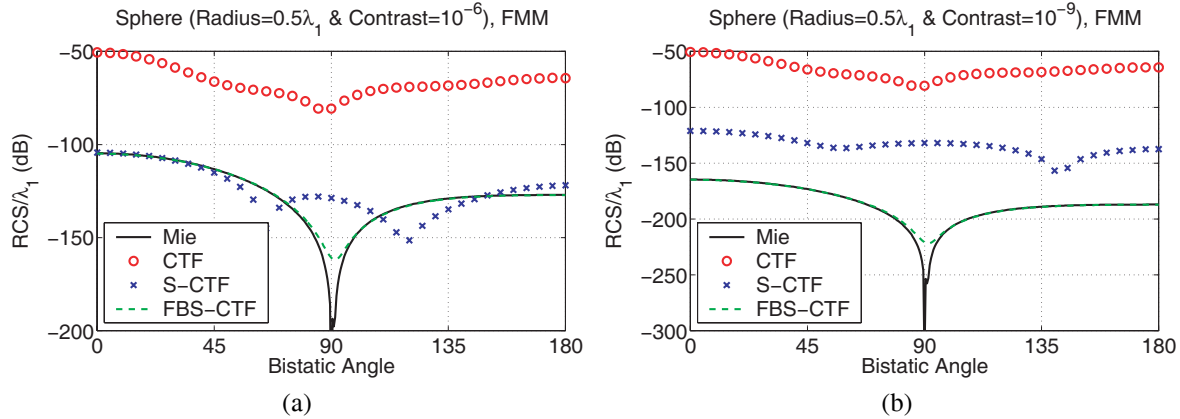


Fig. 2. Normalized bistatic RCS (RCS/λ_0^2 on the $\phi = 0^\circ$ plane) of a sphere of radius $0.5\lambda_0$, where λ_0 is the wavelength outside the sphere (free space), when the relative permittivity of the sphere is (a) $1 + 10^{-6}$ and (b) $1 + 10^{-9}$. Scattering problems are solved iteratively by using FMM.

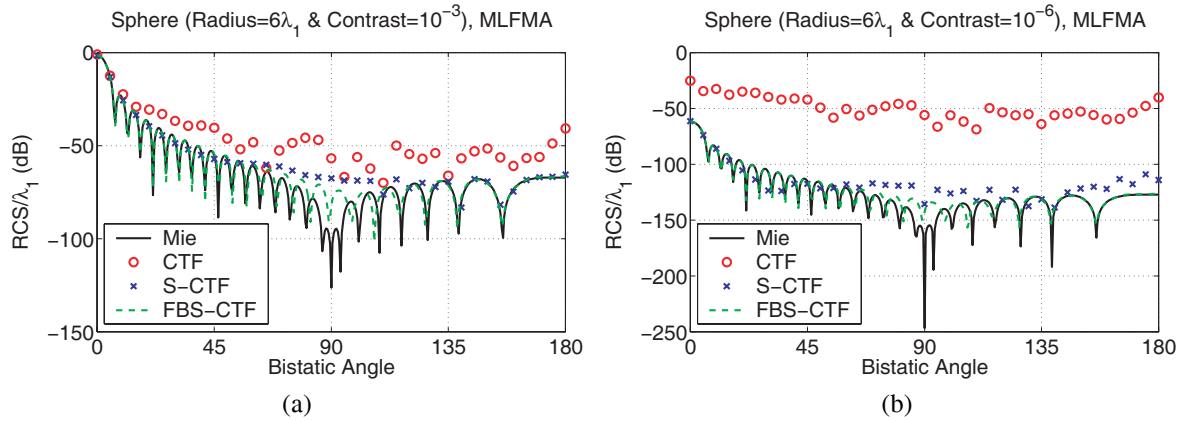


Fig. 3. Normalized bistatic RCS (RCS/λ_0^2 on the $\phi = 0^\circ$ plane) of a sphere of radius $6\lambda_0$, where λ_0 is the wavelength outside the sphere (free space), when the relative permittivity of the sphere is (a) $1 + 10^{-3}$ and (b) $1 + 10^{-6}$. Scattering problems are solved iteratively by using MLFMA.

become inconsistent with the values obtained with FBS-CTF and VIE. As in the previous examples, FBS-CTF is accurate and agrees well with the reference VIE for all contrasts.

6. CONCLUSION

We present a robust stabilization technique for the accurate surface formulations of dielectric bodies with arbitrarily low contrasts. The technique is based on extracting the nonradiating currents, using fictitious incident fields to rearrange the RHSs of the equations, and solving the modified equations to obtain the radiating currents very accurately. The stabilization is easy to implement by modifying the existing codes for the conventional formulations, and its computational cost is negligible. We apply the stabilization procedure to CTF, resulting in a stable formulation called FBS-CTF, which provides accurate results even for extremely low-contrast objects.

REFERENCES

- [1] C. Müller, *Foundations of the Mathematical Theory of Electromagnetic Waves*. New York: Springer, 1969.
- [2] A. J. Poggio and E. K. Miller, "Integral equation solutions of three-dimensional scattering problems," in *Computer Techniques for Electromagnetics*, R. Mittra, Ed. Oxford: Pergamon Press, 1973, Chap. 4.

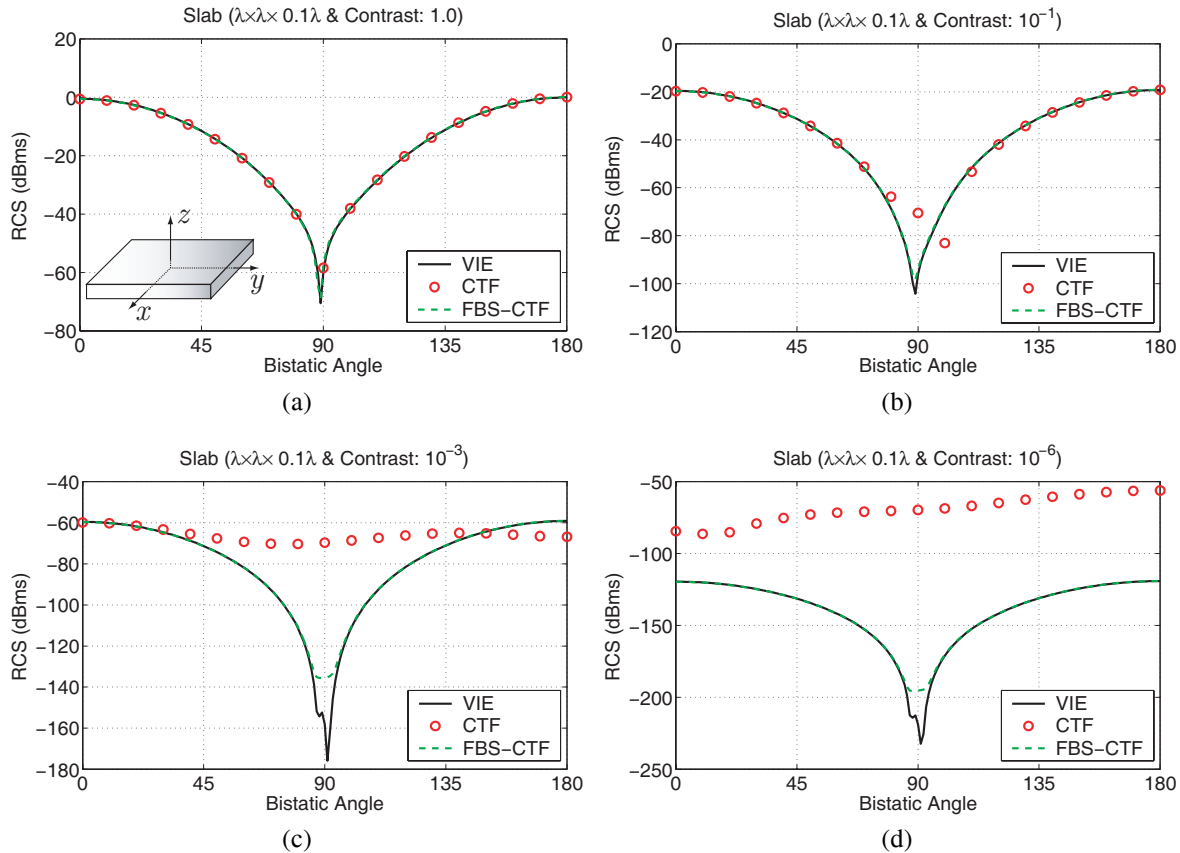


Fig. 4. Bistatic RCS (dBm²) of a $\lambda_0 \times \lambda_0 \times \lambda_0/10$ slab, where $\lambda_0 = 1$ m is the wavelength outside the slab (free space), when the relative permittivity of the sphere is (a) 2.0, (b) 1.1, (c) $1 + 10^{-3}$, and (d) $1 + 10^{-6}$. The slab is illuminated by a plane wave propagating in the z direction with the electric field polarized in the x direction, and the RCS values are plotted on the $\phi = 0^\circ$ plane.

- [3] T. K. Wu and L. L. Tsai, "Scattering from arbitrarily-shaped lossy dielectric bodies of revolution," *Radio Sci.*, vol. 12, pp. 709–718, Sep.-Oct. 1977.
- [4] Y. Chang and R. F. Harrington, "A surface formulation for characteristic modes of material bodies," *IEEE Trans. Antennas Propagat.*, vol. AP-25, pp. 789–795, Nov. 1977.
- [5] J. R. Mautz and R. F. Harrington, "Electromagnetic scattering from a homogeneous material body of revolution," *AEÜ*, vol. 33, pp. 71–80, Feb. 1979.
- [6] R. F. Harrington, "Boundary integral formulations for homogeneous material bodies," *J. Electromagn. Waves Applicat.*, vol. 3, no. 1, pp. 1–15, 1989.
- [7] S. M. Rao and D. R. Wilton, "E-field, H-field, and combined field solution for arbitrarily shaped three-dimensional dielectric bodies," *Electromagn.*, vol. 10, no. 4, pp. 407–421, Oct.-Dec. 1990.
- [8] X.-Q. Sheng, J.-M. Jin, J. Song, W. C. Chew, and C.-C. Lu, "Solution of combined-field integral equation using multilevel fast multipole algorithm for scattering by homogeneous bodies," *IEEE Trans. Antennas Propagat.*, vol. 46, no. 11, pp. 1718–1726, Nov. 1998.
- [9] P. Ylä-Oijala, "Application of a novel CFIE for electromagnetic scattering by dielectric objects," *Microwave and Opt. Technol.*, vol. 35, no. 10, pp. 3–5, Oct. 2002.
- [10] K. C. Donepudi, J.-M. Jin, and W. C. Chew, "A higher order multilevel fast multipole algorithm for scattering from mixed conducting/dielectric bodies," *IEEE Trans. Antennas Propag.*, vol. 51, no. 10, pp. 2814–2821, Oct. 2003.
- [11] T. W. Lloyd, J. M. Song, and M. Yang, "Numerical study of surface integral formulations for low-contrast objects," *IEEE Antennas Wireless Propagat. Lett.*, vol. 4, pp. 482–485, 2005.
- [12] P. Ylä-Oijala and M. Taskinen, "Application of combined field integral equation for electromagnetic

- scattering by dielectric and composite objects,” *IEEE Trans. Antennas Propagat.*, vol. 53, no. 3, pp. 1168–1173, Mar. 2005.
- [13] P. Ylä-Oijala, M. Taskinen, and S. Järvenpää, “Surface integral equation formulations for solving electromagnetic scattering problems with iterative methods,” *Radio Science*, vol. 40, RS6002, doi:10.1029/2004RS003169, Nov. 2005.
- [14] P. Ylä-Oijala and M. Taskinen, “Well-conditioned Müller formulation for electromagnetic scattering by dielectric objects,” *IEEE Trans. Antennas Propagat.*, vol. 53, no. 10, pp. 3316–3323, Oct. 2005.
- [15] P. Ylä-Oijala and M. Taskinen, “Improving conditioning of electromagnetic surface integral equations using normalized field quantities,” *IEEE Trans. Antennas Propagat.*, vol. 55, no. 1, pp. 178–185, Jan. 2007.
- [16] M. Hammer, D. Schweitzer, B. Michel, E. Thamm, and A. Kolb, “Single scattering by red blood cells,” *Appl. Optics*, vol. 37, no. 31, pp. 7410–7418, Nov. 1998.
- [17] J. Q. Lu, P. Yang, and X.-H. Hu, “Simulations of light scattering from a biconcave red blood cell using the finite-difference time-domain method,” *J. Biomed. Opt.*, vol. 10(2), no. 024022, March/Apr. 2005.
- [18] D. A. Hill, “Electromagnetic scattering by buried objects of low contrast,” *IEEE Trans. Geosci. Remote Sen.*, vol. 26, no. 2, pp. 195–203, Mar. 1988.
- [19] E. S. Thiele, “Scattering of electromagnetic radiation by complex microstructures in the resonant regime,” Ph.D. thesis, University of Pennsylvania, 1998.
- [20] P. Loschialpo, D. W. Forester, and J. Schelleng, “Anomalous transmission through near unit index contrast dielectric photonic crystals,” *J. Appl. Phys.*, vol. 86, no. 10, pp. 5342–5347, Nov. 1999.
- [21] D. H. Schaubert, D. R. Wilton, and A. W. Glisson, “A tetrahedral modeling method for electromagnetic scattering by arbitrarily shaped inhomogeneous dielectric bodies,” *IEEE Trans. Antennas Propagat.*, vol. AP-32, no. 1, pp. 77–85, Jan. 1984.
- [22] P. M. Goggans and A. Glisson, “A surface integral equation formulation for low contrast scatterers based on radiation currents,” *ACES Journal*, vol. 10, pp. 15–18, Mar. 1995.
- [23] Ö. Ergül and L. Gürel, “Stabilization of integral-equation formulations for the accurate solution of scattering problems involving low-contrast dielectric objects,” *IEEE Trans. Antennas Propagat.*, vol. 56, no. 3, pp. 799–805, Mar. 2008.
- [24] R. Coifman, V. Rokhlin, and S. Wandzura, “The fast multipole method for the wave equation: a pedestrian prescription,” *IEEE Ant. Propag. Mag.*, vol. 35, no. 3, pp. 7–12, Jun. 1993.
- [25] J. Song, C.-C. Lu, and W. C. Chew, “Multilevel fast multipole algorithm for electromagnetic scattering by large complex objects,” *IEEE Trans. Antennas Propagat.*, vol. 45, no. 10, pp. 1488–1493, Oct. 1997.
- [26] P. Ylä-Oijala, “Numerical analysis of combined field integral equation formulations for electromagnetic scattering by dielectric and composite objects,” *Progress in Electromagnetics Research C*, vol. 3, pp. 19–43, 2008.
- [27] P. Ylä-Oijala, M. Taskinen, and S. Järvenpää, “Analysis of surface integral equations in electromagnetic scattering and radiation problems,” *Engineering Analysis with Boundary Elements*, vol. 32, no. 3, pp. 196–209, Mar. 2008.
- [28] Ö. Ergül and L. Gürel, “Fast and accurate solutions of scattering problems involving dielectric objects with moderate and low contrasts,” in *Proc. 2007 Computational Electromagnetics Workshop*, 2007, pp. 59–64.
- [29] Ö. Ergül and L. Gürel, “Comparison of integral-equation formulations for the fast and accurate solution of scattering problems involving dielectric objects with the multilevel fast multipole algorithm,” *IEEE Trans. Antennas Propagat.*, submitted for publication.
- [30] S. M. Rao, D. R. Wilton, and A. W. Glisson, “Electromagnetic scattering by surfaces of arbitrary shape,” *IEEE Trans. Antennas Propagat.*, vol. AP-30, no. 3, pp. 409–418, May 1982.
- [31] Ö. Ergül and L. Gürel, “Linear-linear basis functions for MLFMA solutions of magnetic-field and combined-field integral equations,” *IEEE Trans. Antennas Propagat.*, vol. 55, no. 4, pp. 1103–1110, Apr. 2007.
- [32] D. A. Dunavant, “High degree efficient symmetrical Gaussian quadrature rules for the triangle,” *Int. J. Numer. Meth. Eng.*, vol. 21, pp. 1129–1148, 1985.
- [33] R. D. Graglia, “On the numerical integration of the linear shape functions times the 3-D Green’s function or its gradient on a plane triangle,” *IEEE Trans. Antennas Propagat.*, vol. 41, no. 10, pp. 1448–1455, Oct. 1993.

- [34] R. E. Hodges and Y. Rahmat-Samii, "The evaluation of MFIE integrals with the use of vector triangle basis functions," *Microwave Opt. Technol. Lett.*, vol. 14, no. 1, pp. 9–14, Jan. 1997.
- [35] Ö. Ergül, "Fast multipole method for the solution of electromagnetic scattering problems," M.S. thesis, Bilkent University, Ankara, Turkey, Jun. 2003.
- [36] P. Y.-Oijala and M. Taskinen, "Calculation of CFIE impedance matrix elements with RWG and $\hat{n} \times \text{RWG}$ functions," *IEEE Trans. Antennas Propagat.*, vol. 51, no. 8, pp. 1837–1846, Aug. 2003.
- [37] L. Gürel and Ö. Ergül, "Singularity of the magnetic-field integral equation and its extraction," *IEEE Antennas Wireless Propagat. Lett.*, vol. 4, pp. 229–232, 2005.
- [38] W. C. Chew, J.-M. Jin, E. Michielssen, and J. Song, *Fast and Efficient Algorithms in Computational Electromagnetics*. Boston, MA: Artech House, 2001.
- [39] S. Koc, J. M. Song, and W. C. Chew, "Error analysis for the numerical evaluation of the diagonal forms of the scalar spherical addition theorem," *SIAM J. Numer. Anal.*, vol. 36, no. 3, pp. 906–921, 1999.
- [40] Ö. Ergül and L. Gürel, "Novel electromagnetic surface integral equations for highly accurate computations of dielectric bodies with arbitrarily low contrasts," *Journal of Computational Physics*, doi:10.1016/j.jcp.2008.08.004, 2008.

Characteristic Basis Finite Element Method (CBFEM-MPI) — A Parallel, Non-iterative Domain Decomposition Algorithm for the Solution of Large-scale Electromagnetic Scattering Problems

Ozlem Ozgun^{1,2}, Raj Mittra² and Mustafa Kuzuoglu³

¹Dept. of Electrical Engineering, Middle East Technical University, Northern Cyprus Campus,
Guzelyurt, Mersin 10, TURKEY

²Electromagnetic Communication Laboratory, Pennsylvania State University,
University Park, PA 16802

³Dept. of Electrical Engineering, Middle East Technical University,
06531, Ankara, TURKEY

Abstract — We present a non-iterative and parallel finite element technique that is tailored for large-scale electromagnetic scattering problems. This approach, called the Characteristic Basis Finite Element Method (CBFEM-MPI), combines the domain decomposition technique with the use of *specially-defined* characteristic basis functions (CBFs). Two major advantages of this method are considerable reduction in the matrix size and convenient parallelization using MPI library, both of which make possible the direct solution of large-scale problems in an efficient manner. The accuracy of the proposed technique has been validated via a number of numerical simulations.

1. INTRODUCTION

The Finite Element Method (FEM) is a powerful technique for modeling and simulating real-world electromagnetic scattering problems, which involve electrically-large and geometrically-complex objects comprising of complex materials. However, the conventional FEM as well as other numerical methods yield ‘large’ matrices for such multi-scale problems whose solution may place a heavy burden, not only on the memory—even if a sparse storage scheme is used—but also the CPU time due to the slow and unstable nature of the convergence of iterative solvers, despite the use of preconditioners. Hence, alternative techniques, such as the domain decomposition (DD) methods, have been proposed during the last few years to break down a large-scale problem into a number of small and manageable subproblems.

In this study, we present the “Characteristic Basis Finite Element Method (CBFEM-MPI),” which is a novel domain decomposition finite element algorithm for the solution of electromagnetic scattering problems. This non-iterative technique has been parallelized by utilizing the Message Passing Interface (MPI) library. The characteristic basis functions (CBFs)—macro-domain basis functions that are constructed in each subdomain by considering the physics of the problem—have been originally proposed to solve time-harmonic electromagnetic problems in the context of the Method of Moments (MoM) that has employed *overlapping* subdomains [1]. However, the CBFEM-MPI is considerably different from all

previous approaches because of the details of its implementation, which partitions the original computational domain into a number of *non-overlapping* subdomains, and generates the CBFs by employing two novel procedures. Specifically, the CBFs are obtained *either* by calculating the fields radiated by a finite number of dipole-type sources [2], *or* by determining Physical Optics (PO) fields by illuminating the object at different incident angles, polarization and frequency [3]. The major advantages of this technique are twofold: (i) it leads to a substantially reduced-matrix, which can be easily handled by using direct solvers; and (ii) its parallelizable nature leads to a substantial decrease in the overall computation time through the use of multiple processors. We have validated the accuracy of the proposed technique via several 3D electromagnetic scattering problems, and presented a number of representative examples to illustrate the versatility of the method.

2. CBFEM-MPI FORMULATION

A general electromagnetic scattering problem is illustrated in Fig. 1(a). If the scatterer is perfectly conducting, we solve the boundary value problem governed by the vector wave equation for the scattered field as follows:

$$\nabla \times \nabla \times \vec{E}^s - k^2 \vec{E}^s = 0 \quad \text{in } \Omega_{\text{FS}} \quad (1.a)$$

$$\text{with BC: } \hat{n} \times \vec{E}^s = -\hat{n} \times \vec{E}^{\text{inc}} \quad \text{on } \partial\Omega_S \quad (1.b)$$

In a conventional FEM procedure, we arrive at a global matrix system $[A][x] = [b]$, where $[x]$ is the unknown scalar tangential fields along the edges of the FEM mesh; $[A]$ is the global matrix; and $[b]$ is the known RHS vector.

The CBFEM-MPI algorithm starts with partitioning the original problem into a number of non-overlapping subdomains. The main concern of the algorithm is to generate a set of CBFs that are *specially*-defined in each subdomain. The procedures for CBF generation are described in Sec. 2.1 and 2.2 in detail. In a broad outline of this technique, the unknown fields are expressed as a series of these CBFs that are weighted with unknown coefficients that are yet to be determined. Then, the matrix system in (1) is transformed into a “smaller” matrix—called the “reduced matrix”—using the Galerkin method, which employs the CBFs as both basis and testing functions. After solving the reduced matrix for the unknown coefficients, the fields inside the entire domain are obtained by substituting the coefficients into the series expressions. The most appealing feature of the proposed approach is that the reduced-matrix can still be solved by direct solvers (such as the LU factorization), even if the original problem size is very large. Therefore, in contrast to iterative solvers, multiple right hand side vectors (i.e., multiple illuminations in the scattering problem) can be handled efficiently with little additional computational burden.

2.1. CBF generation by employing dipoles

The CBFs can be generated by placing a finite number of *fictional dipoles* (or current elements in general) on the object’s boundary, as illustrated by the black arrows in Fig. 1(b), by assuming that the object is perfectly conducting. The fields that are radiated by these dipoles can be conveniently used as CBFs because they not only form the *natural* basis functions for the field distribution inside the entire computational domain,

but they also incorporate the physics of the problem. These dipoles can easily be chosen to lie along the edges of the usual finite element mesh pertaining to the boundary of the object (see Fig. 1(c)). If the object is dielectric, or conductor with full- or partial-dielectric coating, then we also place dipoles inside the dielectric regions, as demonstrated in Fig. 2. In this case, we may also employ both electric and magnetic dipoles, although the choice of electric dipoles alone is sufficient.

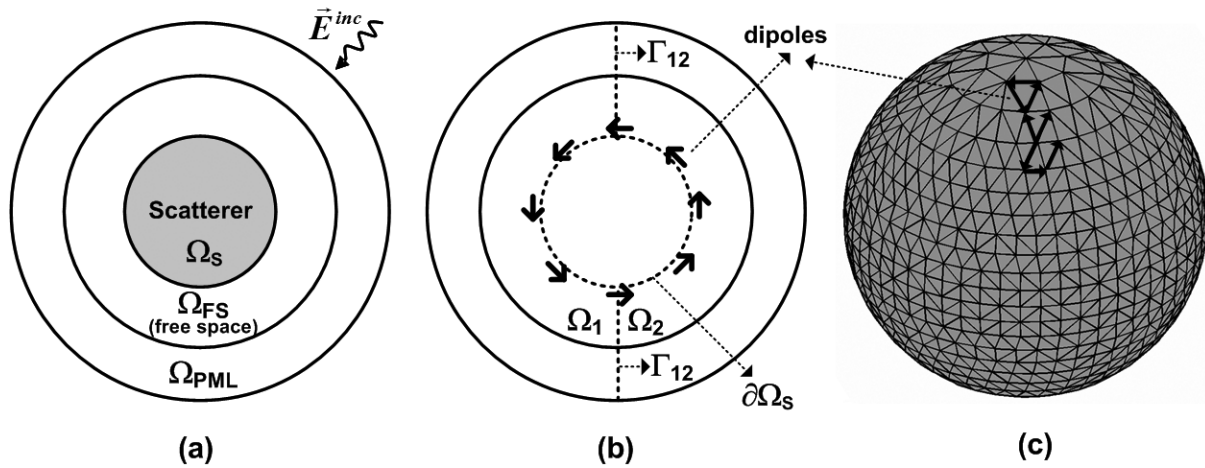


Figure 1. (a) Original scattering problem; (b) CBFEM approach for perfectly conducting object by employing dipoles; (c) Illustration of dipole positions on the boundary of object.

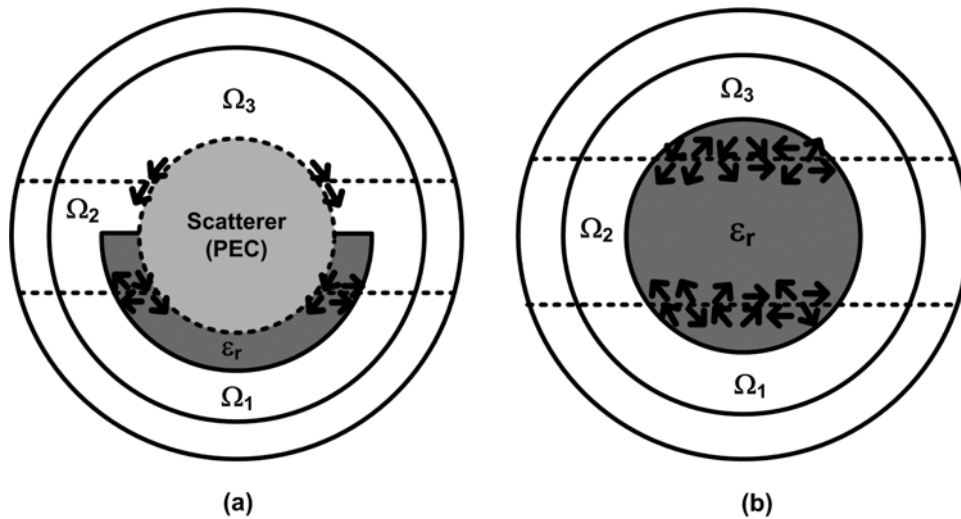


Figure 2. CBFEM approach for dielectrics by employing dipoles: (a) Partially-coated conducting object, (b) Pure-dielectric object.

2.2. CBF generation by employing PO fields

Alternatively, the CBFs can be determined by invoking the principles of Physical Optics (PO) in such a way that PO current sources, namely $\vec{J} = 2\hat{n} \times \vec{H}^{inc}$, are located on a portion of the scatterer boundary

(or on the entire boundary in some cases), assuming that the object is perfectly conducting and that the principle radii of curvature of the surface are large (see Fig. 3). The fields that are radiated by these sources, and integrated (or summed) over the corresponding boundary, for each incident angle, polarization and frequency, are used as “excitation sources” for the corresponding interfaces and subdomain. The CBFs are determined by illuminating the object with N_{PW} number of plane waves, which impinge upon at certain intervals of θ and ϕ angles, for the two orthogonal polarizations, and at a certain number of frequencies around the actual frequency of operation. The number N_{PW} is determined by the expression $N_{PW} = N_\theta \times N_\phi \times N_p \times N_k$, where N_θ is the number of θ angles in the interval $0 \leq \theta^{inc} \leq 180^\circ$, N_ϕ is the number of ϕ angles in the interval $0 \leq \phi^{inc} \leq 360^\circ$, $N_p = 2$ is the number of polarizations, and N_k is the number of frequencies (or wavenumbers). Since we have N_{PW} number of incident plane waves, we will eventually have N_{PW} number of CBFs for each interface.

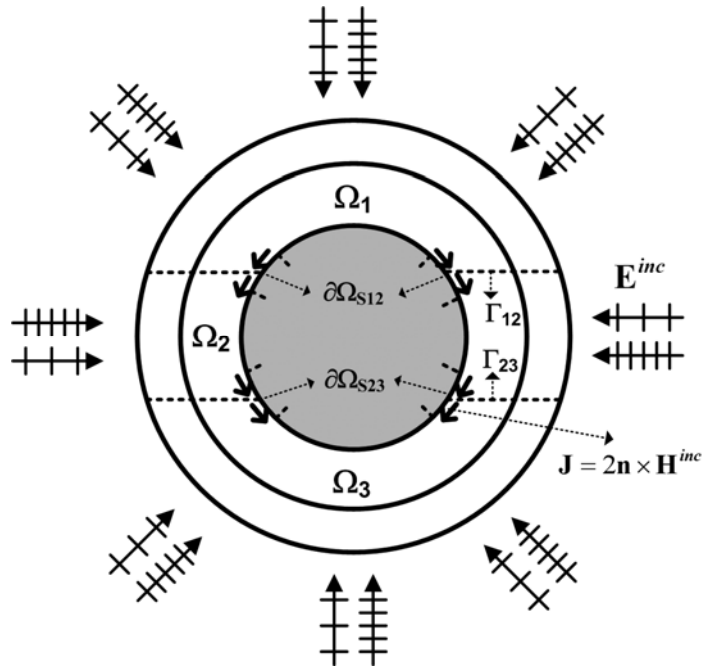


Figure 3. Generation of PO-based CBFs by using a plane wave spectrum using different incident angles, polarization, and frequency.

2.3. Main steps of the CBFEM-MPI algorithm

The basic steps in the implementation of the CBFEM-MPI algorithm are summarized below:

Step-1: We generate the CBFs by treating the subdomains and interfaces separately, by following the approaches in either Sec. 2.1 or 2.2. We first determine the CBFs along each individual interface (Γ_i), which has no common edges with other interfaces. The next step is to apply the singular value decomposition (SVD) procedure to reduce the redundancy in the CBFs by orthogonalizing them, and then setting a threshold on the singular values, which results in a reduction in the number of CBFs. Finally, on

each interface, we have M_i number of CBFs denoted as $\left(\left[u_{\Gamma_i}^{(1)} \right] \left| \left[u_{\Gamma_i}^{(2)} \right] \left| \dots \left| \left[u_{\Gamma_i}^{(M_i)} \right] \right)_{N_i \times M_i}$, where N_i is the number of interface points.

Step-2. In order to find the CBFs in each subdomain (Ω_j), we solve each sub-problem by assigning the post-SVD basis functions, derived in step-1, along the boundaries of the corresponding subdomain. Then, we apply the SVD operation once again, and determine M_j number of CBFs expressed as $\left(\left[u_j^{(1)} \right] \left| \left[u_j^{(2)} \right] \left| \dots \left| \left[u_j^{(M_j)} \right] \right)_{N_j \times M_j}$, where N_j is the number of points in the inner part of the j -th subdomain.

Step-3. We express the unknown fields for the j -th subdomain and for the i -th interface, respectively, as follows

$$\left[x_j \right]_{N_j \times 1} = \sum_{n=1}^{M_j} c_j^{(n)} \left[u_j^{(n)} \right]_{N_j \times 1} \quad \text{and} \quad \left[x_{\Gamma_i} \right]_{N_i \times 1} = \sum_{n=1}^{M_i} c_{\Gamma_i}^{(n)} \left[u_{\Gamma_i}^{(n)} \right]_{N_i \times 1} \quad (2)$$

We substitute these expressions into the global matrix system, and utilize the Galerkin approach to obtain the following reduced matrix system: $[S][c] = [e]$, where $[c]$ is the unknown coefficients, $[S]$ and $[e]$ are the reduced matrix and the new right-hand-side vector, respectively. The reduced matrix system can be solved for the weight coefficients either directly, or by using the Schur-complement approach, which decouples the unknowns on the interfaces, and thus, further reduces the size of the reduced-matrix (Here, the matrix size is equal to the total number of bases for interfaces). After solving the reduced matrix for unknown coefficients, the original unknowns (i.e., scattered fields) inside the entire domain are obtained by substituting the coefficients into the series expressions in (2).

3. NUMERICAL EXPERIMENTS

In this section, we report the results of numerical experiments to test the performance of the CBFEM–MPI technique. We assume that the wavelength λ is 1 m (i.e., the frequency is 300 MHz, and the wavenumber k is 6.2832).

The first example, which employs dipoles in CBF generation, is a benchmark scattering problem where a plane wave is incident to a sphere whose diameter is 6λ . The original domain is partitioned into 16 subdomains, as shown in the figure that is the inset of Fig. 4. For the original problem, the number of unknowns (edges or matrix size) is 313,958. Total number of dipoles chosen along the boundary of the sphere is 13,828. The CBFEM-MPI code yields a reduced-matrix whose size is 16,016, which is considerably less than the original matrix size. The bistatic RCS profile of the sphere is plotted in Fig. 4, which also compares it with both the conventional FEM and the Mie series results.

The second example considers a sphere whose diameter is 8λ , and employs the PO fields to generate CBFs. The original matrix size is 541,977, after a uniform $\lambda/10$ mesh discretization. The number of subdomains is 12, and the number of plane waves is 2,000, such that the θ and ϕ angle increments are 20° and 90° , respectively, and the wavenumbers are $\{1, \dots, 5, 6.2832, 7, \dots, 25\}$. The CBFEM-MPI algorithm yields a reduced matrix whose size is 14,498. The bistatic RCS profiles are plotted in Fig. 5.

The third example deals with a missile whose radome diameter is 2λ and length is 21λ , with an axial (nose-on) plane wave incidence. The number of unknowns in this problem is 563,147. The computational domain is decomposed into 25 subdomains. In this problem, we employ both dipoles and PO fields. In the dipole-case, number of dipoles is 39,582. The size of the reduced-matrix is obtained as 22,706. In the PO-case, the wavenumbers are $\{1, \dots, 5, 6.2832, 7, \dots, 15\}$. We choose the ϕ angle increment as 90° ; and the θ angle increment as 10° and 20° between 0° - 80° and 80° - 180° , respectively. The size of the reduced-matrix becomes 11,754. We plot the bistatic RCS profiles in Fig. 6.

In the last example, we consider multi-layered concentric dielectric spheres, as shown in Fig. 7, and employ dipoles in CBF generation. The original matrix size is 48,562, after a non-uniform mesh discretization (i.e., $\lambda/40$ in ϵ_{r1} , $\lambda/30$ in ϵ_{r2} , $\lambda/25$ in ϵ_{r3} & ϵ_{r4}). We partition the original problem into 3 subdomains, as shown in Fig. 7(b). The size of the reduced-matrix is obtained as 2,485. We plot the bistatic RCS profiles in Fig. 8.

4. CONCLUSIONS

We have introduced a domain decomposition finite element algorithm for efficient solution of large-scale electromagnetic problems, by using characteristic basis functions that are specially-tailored by employing dipole-type sources or PO fields. We have pointed out that the CBFEM algorithm is capable of reducing the matrix size, which allows us to make use of the direct rather than iterative solvers, and lends itself to convenient parallelization. We have observed that the PO approach is more efficient in terms of the size of the reduced matrix and the number of CBFs. However, the dipole approach is more general and can be applied to both conducting and dielectric structures. To illustrate the versatility of the proposed method, we have presented a number of representative examples. We have observed that the CBFEM-MPI results are close to the reference results, and this leads us to conclude that the accuracy of the algorithm is validated.

ACKNOWLEDGEMENT

This work was supported in part by a grant from The Scientific and Technological Research Council of Turkey (TUBITAK). While this research was conducted, the first author was with the Electromagnetic Communication Laboratory, Pennsylvania State University, University Park, PA 16802

REFERENCES

- [1] Prakash V.V.S., and Mittra R., "Characteristic basis function method: A new technique for efficient solution of method of moments matrix equations," *Microwave Opt. Technol. Lett.*, vol. 36, pp. 95-100, 2003.
- [2] Ozgun O., Mittra R., and Kuzuoglu M., "Parallelized Characteristic Basis Finite Element Method (CBFEM-MPI) — A Non-iterative Domain Decomposition Algorithm for Electromagnetic Scattering Problem," *J. of Computational Physics*, (to appear).
- [3] O. Ozgun, R. Mittra, and M. Kuzuoglu, "PO-based Characteristic Basis Finite Element Method (CBFEM-PO) — A Parallel, Iteration-free Domain Decomposition Algorithm using Perfectly Matched Layers for Large-scale Electromagnetic Scattering Problems," *Radio Science*, (to appear).

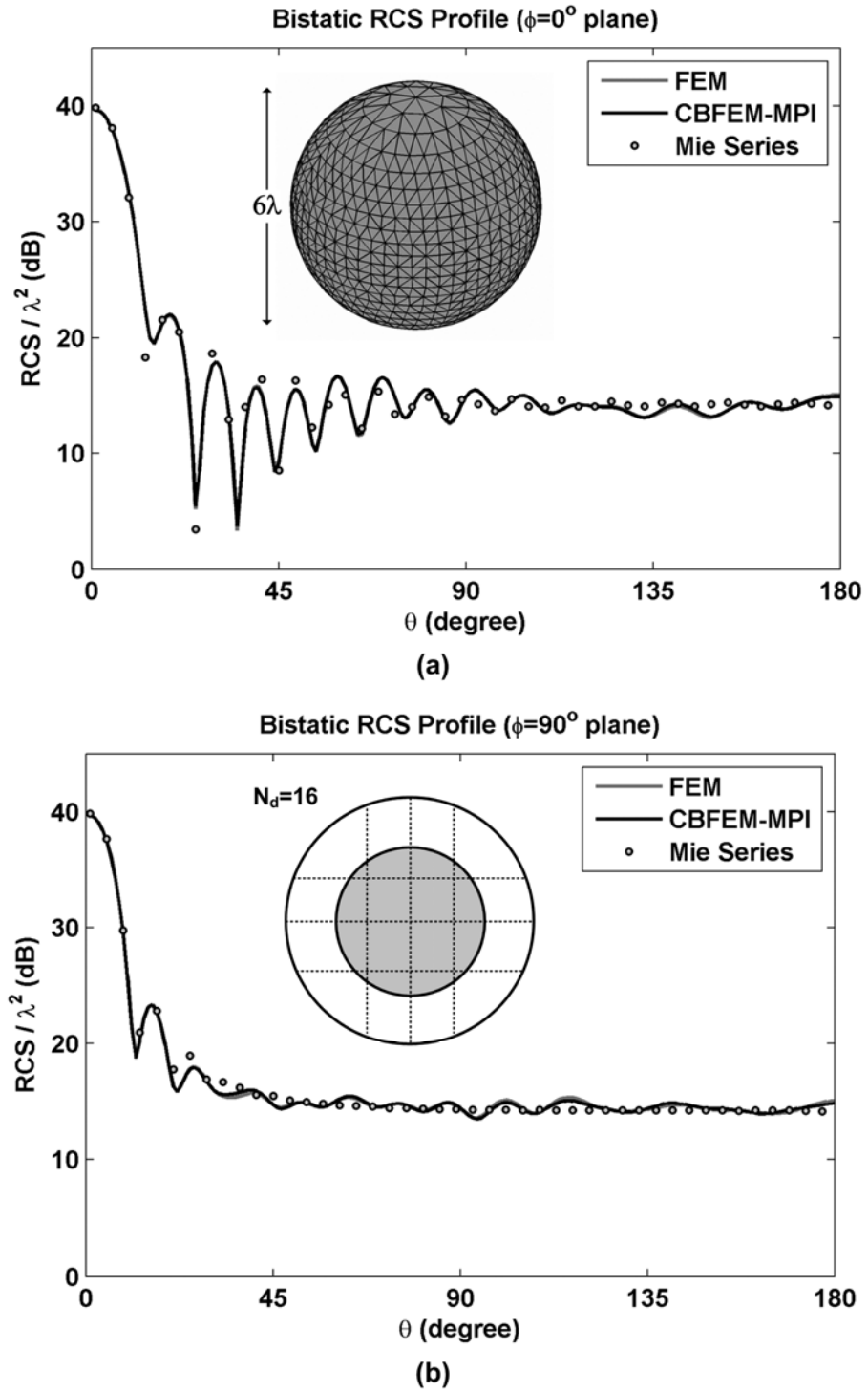


Figure 4. Bistatic RCS profile of 6λ -sphere (using dipoles): (a) $\phi=0^\circ$ plane, (b) $\phi=90^\circ$ plane.

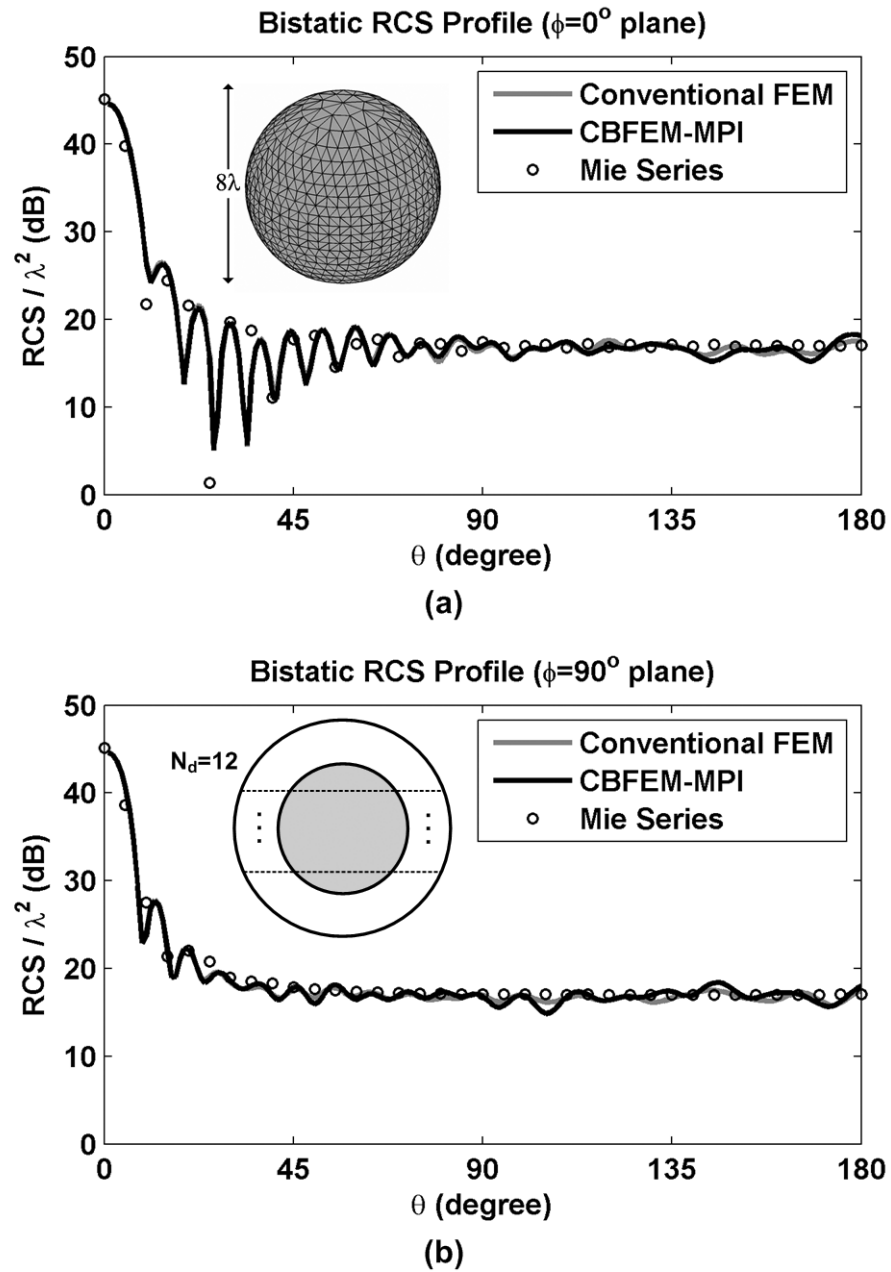


Figure 5. Bistatic RCS profile of 8λ -sphere (using PO fields): (a) $\phi=0^\circ$ plane, (b) $\phi=90^\circ$ plane.

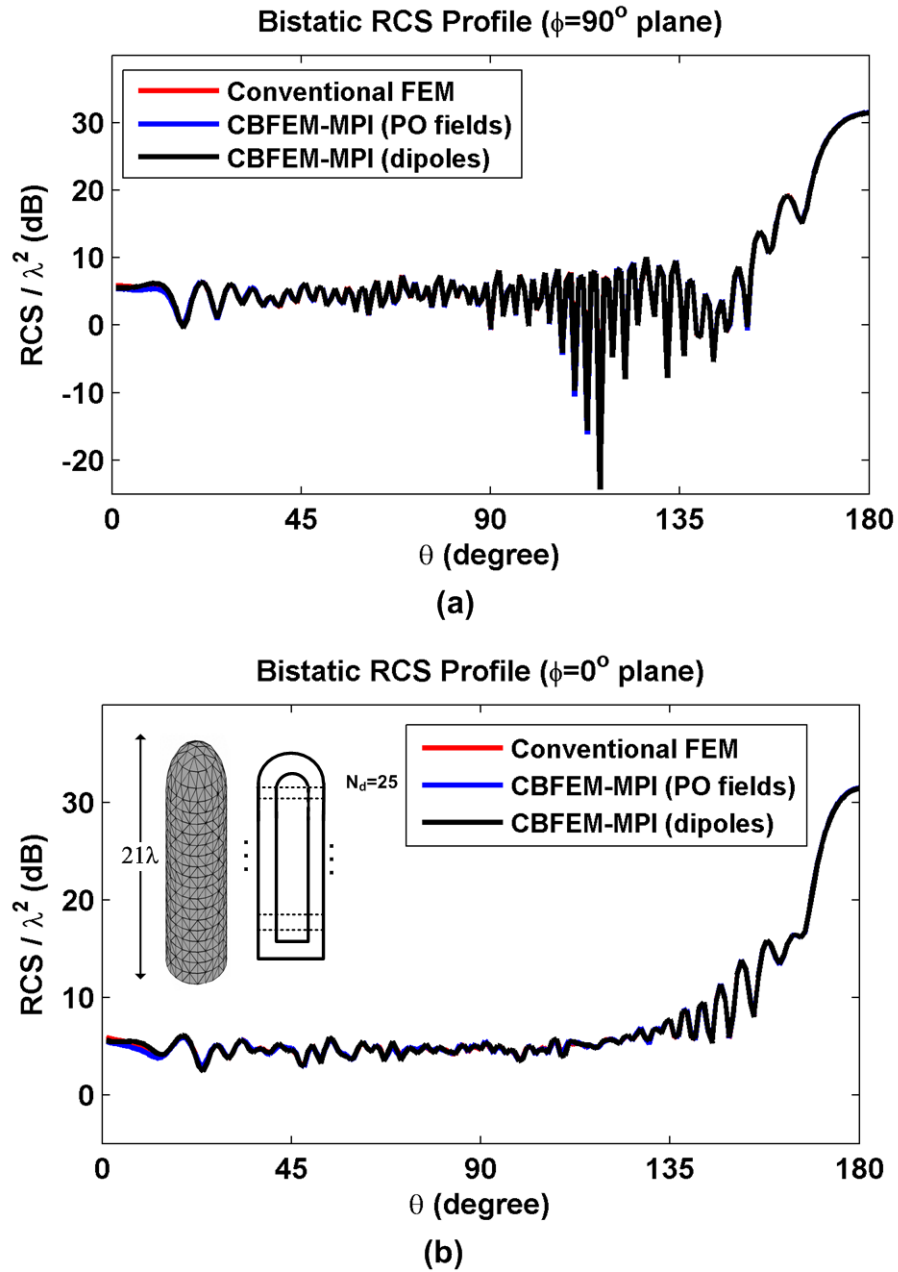


Figure 6. Bistatic RCS profile of 21λ -missile: (a) $\phi=90^\circ$ plane, (b) $\phi=0^\circ$ plane.

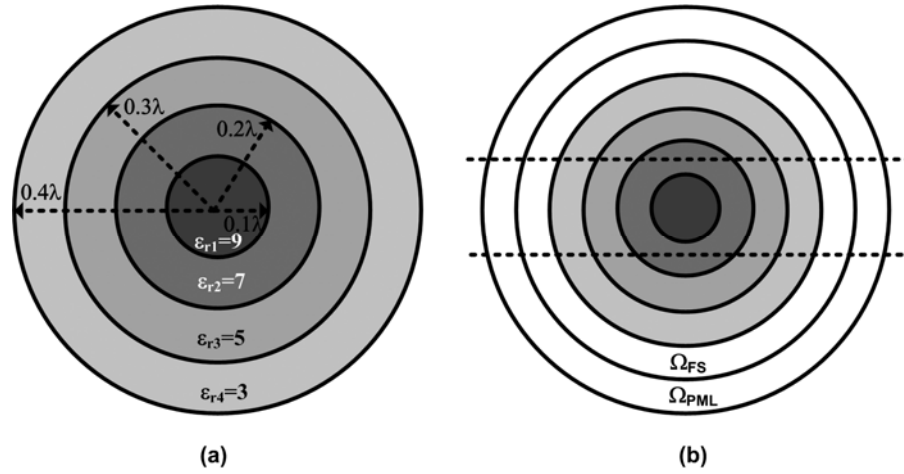


Figure 7. Multi-layered dielectric concentric spheres: (a) Original problem, (b) Partitioned problem.

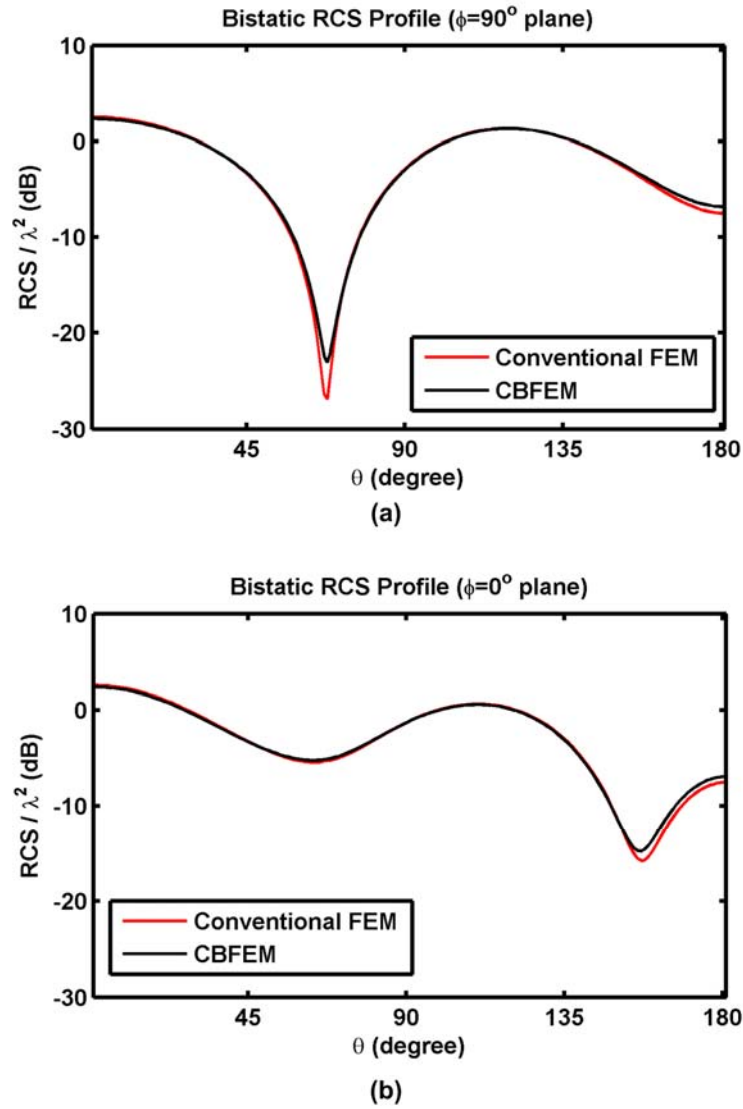


Figure 8. Bistatic RCS profile of multi-layered dielectrics: (a) $\phi=90^\circ$ plane, (b) $\phi=0^\circ$ plane.

Modelling Interference Phenomena between Cosite Radiocommunication Equipments to Evaluate Systems Performance Degradation

E. Yalçin , C. Girard , M. Cabellic , M. Hélier , G. Alquié , J.-L. Montmagnon

¹Thales Communications – TCF/C4ISR/DIS, 160 bld de Valmy, 92704 Colombe, France.

evlin.yalcin@fr.thalesgroup.com

²UPMC Univ Paris 06, EA 2385, L2E, F-75005, Paris - Laboratoire d'Electronique et Electromagnétisme,
BC 252 - 3, rue Galilée, 94200 Ivry-sur-Seine, France.

marc.helier@upmc.fr

Abstract – Electromagnetic Interference (EMI) is part of Electromagnetic Compatibility (EMC) handling all issues of non-intentional interference between transmitters and receivers. In this document, various models and methods are described in order to carry out EMI simulations and evaluate the performance degradation of co-site equipments of a system. A next step will consist in validating the developed EMI simulation tool. The chosen study case is the 2.4 GHz ISM band Bluetooth/WiFi interaction. We have carried out BER measurements which results, summarized at the end of the paper, will be used for the planned validation work.

1. INTRODUCTION

Electromagnetic Interference (EMI) is part of Electromagnetic Compatibility (EMC) handling all issues of non-intentional interference between transmitters and receivers. As a result of the high concentration of radio-communication equipments in limited areas, typically on an aircraft or a frigate, the management of these disturbance problems has become more and more difficult. New well-adapted means of simulation are then necessary. The work described in this paper is about various models and methods developed in order to carry out EMI simulations.

First, we start by introducing and defining the elements of the study. The expected results of these simulations are specified; namely interferences evaluation in terms of performance degradation. The next work is to validate our EMI analysis tool functionalities by comparing simulation results to measured ones. To manage it, we have chosen to test a typical EMI issue: the Bluetooth/WiFi (IEEE 802.11b/g) interaction at 2.4 GHz. It is an interesting study case because these civilian technologies operate on the same ISM band and often coexist. We have carried out BER measurements on a Bluetooth connection near a WiFi transmitter. The tests results are discussed at the end of the paper. We will use these measurements results to carry out the future validation work we have planned.

2. FRAMEWORK AND DEFINITION OF THE ELEMENTS OF THE STUDY

Two types of approach are possible in EMI studies according to the fact that the system already exists or not. The first one is used in the case where the studied system is already built. It corresponds to the “exploitation approach”. In this situation, the goal is to evaluate the performance degradation of a useful link between a transmitter and its receiver, while all the other equipments of the system, to which they belong, are operating too. Couplings created between useful link antennas but also those of the other links, are potentially disturbing, and are the core of the problem here. They are at the origin of incompatibilities that may appear. The objective is then to minimize these couplings as well as possible. The second approach is applied when the studied system does not exist yet. It corresponds to the “design approach”. In this situation, the goal is to evaluate the system performances according to the radio characteristics of electronic components of the equipments. The aim is then to parameterize the characteristics of transmission/arrival stages in order to make these equipments as compatible as possible with the new system, even if it requires changing their primary specifications.

Interferences between radiocommunication equipments can be due not only to their frequency plans but also to their radio characteristics, for instance, the selectivity of the receiver filters. In order to model such a kind of disturbance phenomena, we have to define transmitters and receivers more precisely than using simple “black box” models with just input/output ports. Indeed, we have to go further and take into account the internal and analogical structure of these electronic radio equipments. It appears that superheterodyne architecture is the most widespread, not only for transmitters but also for receivers. That is why we have decided to select the superheterodyne architecture for modelling the internal structure of all these devices. The main characteristics of each stage of the chain, that is to say of each electronic component, are user controlled.

The models are limited to the physical layer of the equipments. The protocols of the MAC layer or, in other words, the management of the message traffic within the network, are not modelled directly here. Then, for modelling the protocols, we have performed statistical computations based on the Monte Carlo method [1]. We consider that, at time t , the frequency as well as the relative time positioning (slotting) of the signals within the system are pseudo-random variables. The interference calculation methods elaborated here aim at temporally slicing the messages traffic of the system into “instantaneous configurations” during which we consider that signals are stationary. With such a method, we are able to analyze systems from the simplest ones, in which each transmitter or receiver operates with its own fixed frequency, to the most complex, called “heterogeneous” or “multi waveforms”, involving signals with different waveforms and even with a frequency hopping mode, as the system in Fig. 1.

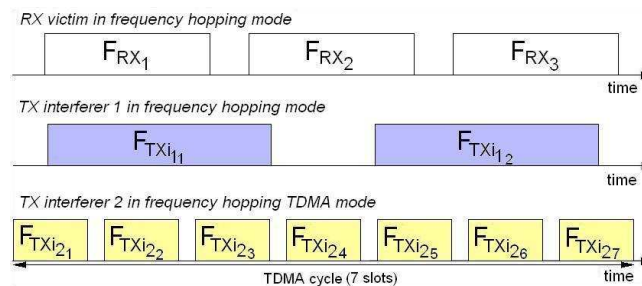


Figure 1: “Multi waveforms” system

We have built a central management tool that gets the models output data and uses calculation methods to provide, at the end of the simulation, the studied system performance estimation. We will explore these models and methods in part 3 and part 4.

3. SIMULATION MODELS

3.1. Transmitter and receiver models

The transmitter and receiver models are based on superheterodyne architecture as it was already mentioned. These models are “parametric” and provide respectively the transmitted signal and susceptibility shape curves [2], according to the studied interference phenomena. The transmitter model is based on two kinds of sub-models. On one hand, its useful spectrum based on numerical and analogical modulation schemes, and on the other hand, the modelling of interference phenomena, which are inherent to the transmitters like phase noise, harmonics, cross-modulation, saturation... As for the receivers, the disturbance phenomena modelled to calculate the various types of their susceptibility curves are, for example, selectivity, saturation, cross-modulation... In addition, we have also modelled the phenomenon of intermodulation.

3.2. Antennas, carriers and propagation models

With regard to the propagation between transmitters and receivers, generic antennas and carriers have been modelled. Thus, we can simulate the radiation of these antennas in “operational configuration”, that is to say on the studied carrier. Fig.2 shows an example of a carrier model meshing at 327 MHz. This way, the precise influence of the carrier on the transmitted fields is taken into account. From radiation patterns, a link budget is computed in order to evaluate the decoupling between the various antennas of the system. Propagation models are also provided in the simulation.

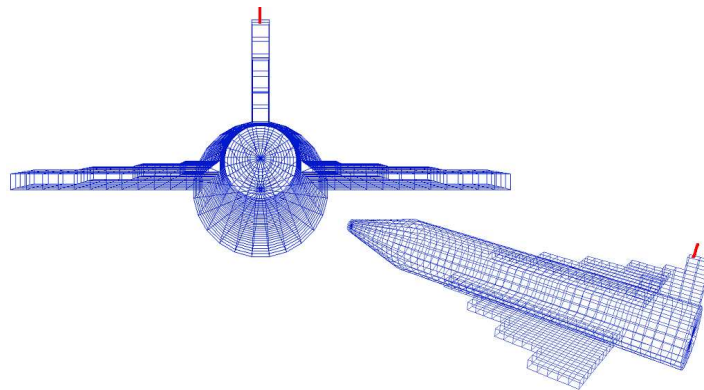


Figure 2: Meshing at 327 MHz of military aircraft model carrying VUHF antenna model on top of vertical stabilizer (back, side view)

4. CALCULATION MODELS

4.1. Slicing into instantaneous frequency configurations method for BER estimation

While the victim receiver “listens to” its environment to detect the useful signal, the transmitters, of the other co-site connections, keep communicating. Those are the potential interferers. In order to calculate their impact on the quality of the useful link, the state of interfering signals transmitted by those

potential interferers, has to be known at each time step, that is to say, their power at the input port of the victim receiver antenna, their frequency and, if the signal is a burst, the slotting of those bursts compared to the watch period of the victim receiver. Indeed, if an interfering signal does only exist partly over the receiving duration, due to the data traffic state, interference intensity will be lower compared to a configuration where the spurious signal is continuous.

To take into account the impact of signals with a “non continuous” shape, the calculation principle is to split the system global state into as many “sub-states” as the number of times that one of the system equipments changes its behaviour: for example, carrier change for devices operating in frequency hopping mode, or transition from transmitting state to silence state for burst signals. In fact, we decompose the system global behaviour into a succession of intermediate states that are each defined by system equipments stationary behaviour. Those equipments operate according to a combination of fixed frequencies; this is why we call such a “sub-state”, “instantaneous frequency configuration”. We show hereafter the various steps of the calculation leading to BER estimation.

4.1.1. Slicing a receiving duration into a stationary state sequence

The first step of interference calculation consists in slicing the victim receiver duration into as many “sub-durations” that there are instantaneous frequency configurations. This slicing operation is directly dependent on the signal waveforms and also on their Medium Access Control (MAC). Their waveforms are the input data of the algorithm and thus are known. However, as the protocols of their MAC layer are not modelled here, we do not know what is the signal state at any time. The solution we have adopted then is to make, for each interferer, their operating mode (transmission or silence) pseudo-random as well as the time start of their bursts, when the victim receiver starts to listen and detect. In addition, if the interferer operates in frequency hopping mode, we also make pseudo-random the frequency of each transmitted burst. The problem is thus probabilistic; then the slicing operation do not lead to only one result but to an infinity of possible configurations. For example, in Fig. 3, we show two possible configurations for one receiving duration, when the victim is tuned on F_{RX2} , while there is two co-site interferers operating in frequency hopping mode.

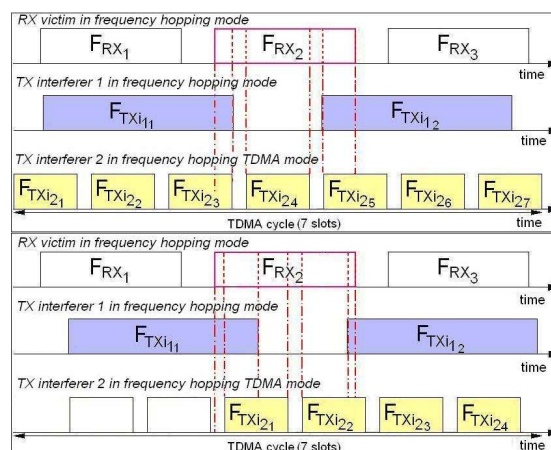


Figure 3: Two possible configurations of signals of the system, among an infinity, according to their slotting and frequencies

Each slicing operation leads to a BER calculation for the receiving duration studied. The objective is to determine a distribution of the BER, for each receiving duration (each receiving frequency). To obtain this distribution, we apply the slicing method a sufficiently large number of times to get a number of samples that ensures the convergence of the Monte Carlo algorithm. The BER calculated for a receiving duration corresponds to the expectation of all BER calculated for “sub-durations” (instantaneous configurations) resulting from one slicing. More precisely, the final BER is the weighted average of “sub-durations” BER which weights are the respective “time-slices” durations, as expressed in (1).

$$E(BER) = \sum_{i=1}^{N_{IC}} BER_{IC_i} \times d_{IC_i} \quad (1)$$

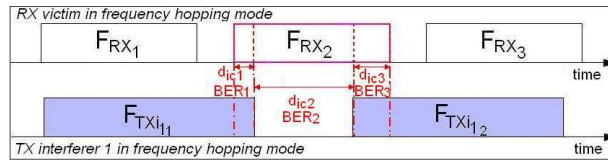


Figure 4: Slicing FRX2 receiving duration into N_{IC} instantaneous frequency configurations

Indeed, (1) gives the BER expectation formula of a receiving duration sliced into N_{IC} instantaneous frequency configurations, each defined with a sub-duration d_{IC} and a BER_{IC} , as depicted in Fig. 4.

4.1.2. Calculation of the BER of an instantaneous frequency configuration

To reach the BER value, we have first to calculate the useful Signal S to Interferer “T” Ratio (SIR). “T” corresponds to the spurious signal transmitted by only one of the interferers; it is not the sum of all interfering signals, because there is not any reason to add linearly the contributions of all interferers of a system in order to estimate the global impact on a connection. Actually, among all the interferers, often only one or two of them have a predominant disturbing effect on the studied victim receiver. Based on this observation, we adopt the following principle. For one “instantaneous configuration”, we retain only the SIR of the predominant interferer.

SIR is obtained with the confrontation of transmitted interfering signal spectrum curve to victim receiver susceptibility curve, which level depends on the sensitivity of the receiver and the chosen interference margin. The first step, called amplitude analysis, consists in the calculation of the maximum value of the difference between transmitted interfering signal spectrum and victim receiver susceptibility curves. It is a first order calculation that allows us to eliminate quickly low impact interferers and highlight the predominant interferer for the studied “instantaneous configuration”.

Once the predominant interferer identified, we carry out the second SIR calculation, which is more precise because it takes into account interfering transmitters and victim receiver bandwidths. Thus, we obtain an adjusted and more precise SIR value. Then, we pick up the BER value corresponding to this value of SIR from the BER(SIR) curves provided for the studied receiver by literature or obtained by measurements, like those carried out for the Bluetooth/WiFi interaction case, explained in part 6.

4.1.3. Estimation of the victim receiver BER for a receiving duration

To estimate the BER for a given receiving duration (receiving frequency), we encode a sampler that generates N number of slices of this receiving duration into “instantaneous configurations”. For each slicing obtained, the calculation of the BER weighted average is carried out according to the method described in the previous paragraphs. We thus get NR values of the BER expectation, as formulated in equation (1). We suppose, a priori, that the BER distribution is, for example, Gaussian. We use Python Monte Carlo PyMC [3] module, containing the Metropolis Hastings algorithm. This algorithm carries out calculations on these NR samples of $E(\text{BER})$ to test the goodness of fit of the observed distribution with the theoretical one specified a priori as well as the convergence of its parameters. Finally, we obtain the most likely values of the average μ and the standard deviation σ ; that is to say the most likely $E(\text{BER})$ distribution for a given receiving duration (receiving frequency).

4.1.4. Estimation of the victim receiver BER

We repeat this process for other receiving durations (receiving frequencies) and also for a sufficiently large number of iterations to ensure stability, using Python Monte Carlo (PyMC[®]) tool [3]. We create a new sampler that generates N_{RX} samples of the receiver frequency. Each of these frequencies corresponds to a receiving duration. The simulation result for each of those receiving durations is the $E(\text{BER})$ distribution already described in this part. Consequently, the sampler provides N_{RX} possible distributions of $E(\text{BER})$; that is to say N_{RX} values of μ and σ . We use again PyMC methods to determine, this time, the distributions of μ and σ . We have thus evaluated the victim link performance.

4.2. Topological cutting method with Huygens surfaces for decoupling calculations

Concerning the calculation of decoupling between antennas, the choice is offered to the user between the direct method, introduced at the end of part III, and the method of topological cutting thanks to a set of Huygens surfaces. Fig. 5 shows an example of the application of this method to calculate spurious signal at a victim receiver antenna input. Whereas the first method consists in carrying out only one simulation with the whole system, the second one consists in breaking up the total simulation into several intermediate simulations of different parts of the system. For applying this method to our EMI analysis, we use the specific tools implemented on the software platform called QUERCY[®] [4]. It contains CAD, field calculation, meshing software and also all the necessary tools, like equivalent sources calculation tool on Huygens surfaces, to apply the topological cutting method.

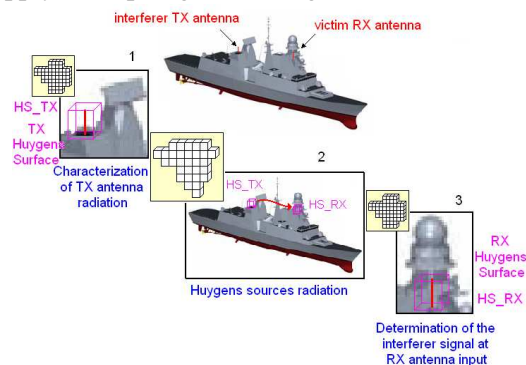


Figure 5: Topological cutting method with Huygens surfaces

5. SIMULATION RESULTS

For a studied scenario, the first expected simulation results are the transmitted signals as well as receiver susceptibility curves. From these curves, the final expected result is the equipment performance degradation, either according to the interference phenomena inherent to transmitters and receivers, or according to the decoupling between antennas. These results are given in terms of the Signal-to-Interference Ratio (SIR) or Bit Error Rate (BER) or even Packets Error Rate (PER).

6. APPLICATION: Bluetooth/WiFi case

The interference issues between Bluetooth and WiFi, operating both on ISM 2.4 GHz band, are quite real and, consequently, lead to a lot of studies like those of the NIST [5] and many others. The experimental work carried out on this study case usually consists in measuring throughputs using COTS (traditional commercial cellular phone or computer provided with Bluetooth/WiFi technologies). For instance, tests carried out by KELLER and MODELSKI [6].

Our goal is to measure the BER of a connection, and not a throughput, when there are, in the same system, interferer signals which waveform characteristics are necessarily known. Without this information about signal radio characteristics, the comparison measures/simulation, in other words the validation, would be impossible. The problem is that COTS do not accept to be tested nor configured; we cannot have any information about signal characteristics nor control them, like the length and the periodicity of transmitted data packets. And these data are input data of the interference calculation algorithm to be validated. This is the reason why we have chosen to use specific Bluetooth and WiFi signals generators in order to give the user the possibility of choosing the parameters of the system signals.

6.1. The study case, its equipment and configuration

We use Bluetooth and WiFi signal generators made by Rohde & Schwarz, respectively the CMU200[®] and the SMJ100A[®] [7]. Contrary to the SMJ100A which can be only used as a generator, the CMU200 not only makes it possible to establish a Bluetooth connection with any device provided with this technology, but also to measure the BER of the link. Consequently, the tests consist in measuring the performances degradation of a Bluetooth connection near a WiFi interferer. We set the connection between the “piconet” Master, the CMU200, and its Slave, a Bluetooth Module (BM), especially configured so that it “accepts” to be tested. We have decided to carry out the tests in free space propagation mode by connecting each generator to quarter-wave antennas tuned to 2.4 GHz, located inside an anechoic chamber. Another antenna, identical to the others, is used for the Bluetooth module. Fig. 6 gives a picture of the system composed with these three antennas.

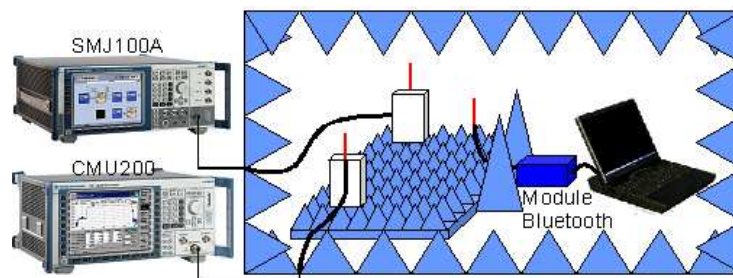


Figure 6: Geometry of the measured configuration

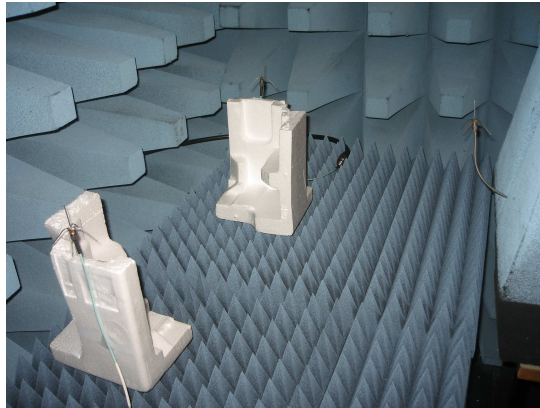


Figure 7: Picture of the antennas in an anechoic chamber (CMU200, MJ100A and BM from left to right)

6.2. Measurements results

The objective is to measure the Bluetooth connection BER as a function of the interfering signal power. Initially, we chose Bluetooth signal operating at only one frequency and transmitting 1 ms length and 2 ms periodicity data packets. We also test interferences on Bluetooth due to other kind of spurious signals like white Gaussian noise, sine or pulses. With all of these tests, we thus can characterize Bluetooth connection performance function of signals waveforms, but also quantify the connection quality improvement due to frequency hopping mode.

The curves of Fig. 8 compare the 2.45 GHz Bluetooth connection BER when the interferer is on the one hand, an additive Gaussian with noise (AWGN), and on the other hand pulses. The results reveal that pulsed signals are more aggressive than AWGN and, in particular, WiFi. Indeed, whereas the BER standard value (0.1%) is reached for a SIR almost equal to zero dB when the interferer is an AWGN, this value is reached for a spurious signal level approximately 8 dB lower when WiFi is the interferer. The curves of Fig. 9 show the performance improvement of a Bluetooth connection when it operates in frequency hopping mode compared to the case where it operates in single channel mode, which has the same frequency as the WiFi signal one. This improvement value is approximately equal to 2 dB. Fig. 10 displays five cases of Bluetooth/WiFi interactions defined by signal duration and periodicity which values are given in table 1. All the curves are almost superimposed. Only one dB of difference is obtained between the most constraining configuration and the least aggressive one.

TABLE 1

Duration (L) and periodicity (T) of packets

case	1	2	3	4	5
<i>LBluetooth (ms)</i>	0.339	0.339	0.339	0.339	2.839
<i>TBluetooth (ms)</i>	1.25	1.25	1.25	1.25	6.25
<i>LWiFi (ms)</i>	1	1	3.1	3.1	1
<i>TWiFi (ms)</i>	2	0.1	2	0.1	5

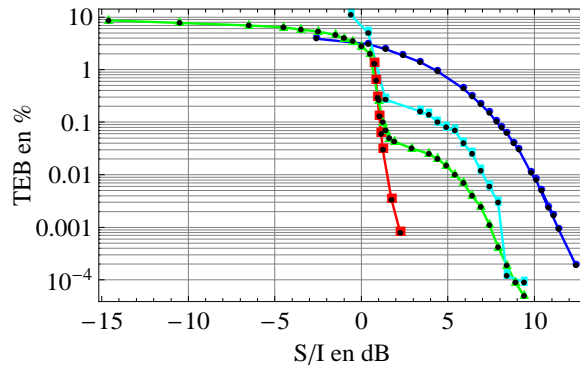


Figure 8: Single channel Bluetooth BER function of SIR when the interferer is AWGN (■), WiFi (●), pulses (Lp=452 μs, Tp=1.252 ms) (▲), pulses (Lp=100 μs, Tp=200 μs) (■) at 2.45 GHz

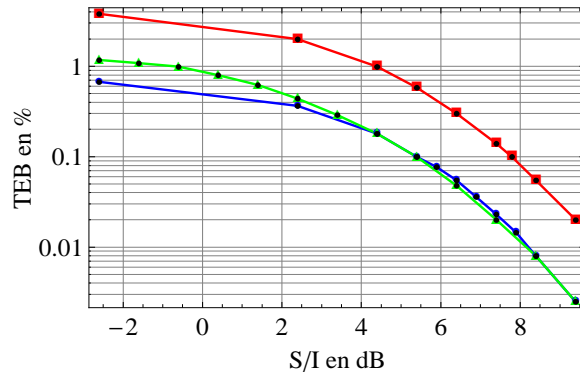


Figure 9: Bluetooth BER function of SIR when the interferer is WiFi at 2.447 GHz and Bluetooth is in single channel mode at 2.447 GHz (■), in frequency hopping mode (●), in reduced mode (▲)

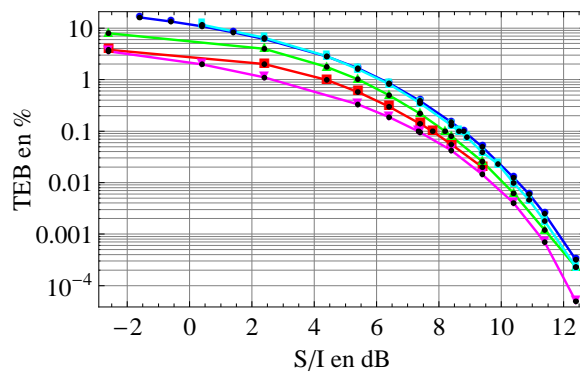


Figure 10: Single channel Bluetooth BER function of SIR when the interferer is WiFi at 2.447 GHz in case 1 (■), case 2 (●), case 3 (▲), case 4 (■) et case 5 (▼)

7. CONCLUSIONS

From these measurements, it may be concluded that quality degradation of a Bluetooth connection due to a WiFi signal increases when the difference between the useful signal and the interfering signal, received by the victim Bluetooth antenna, is lower than approximately 10 dB. Neither the frequency hopping mode, nor the data packets configuration, significantly modify the result. However, WiFi signal power is higher than Bluetooth signal one, up to 20 dB higher. Consequently, it appears that WiFi is very likely to cause interferences to Bluetooth. This observation confirms that Bluetooth/WiFi interaction is a judicious study case for the next step of our work which will consist in validating our Electromagnetic Interference analysis tool, that has been described in this paper.

REFERENCES

- [1] ITU-R, “Monte Carlo simulation methodology for the use in sharing and compatibility studies between different radio services or systems”, report ITU-R SM.2028-1, 2001.
- [2] William G. DUFF, “Electromagnetic Compatibility in Telecommunications”, Volume 7 from a series of Handbooks entitled “Electromagnetic Interference and Compatibility”, Interference Control Technologies, Inc, ISBN 0-944916-07-4, Virginia, 1988.
- [3] C. FONNESBECK, PyMC user’s guide, 2006 http://trichech.us/files/pymc_users_guide.pdf
- [4] C. GIRARD, P.HOFFMANN, V. GOBIN, “QUERCY: Combination of Measurements and Simulation in the Electromagnetic Evaluations and Studies”, European Test and Telemetry Conference, June 2007 .
- [5] N. GOLMIE, R.E. VAN DYCK, A. SOLTANIAN from National Institute of Standards and Technology of Maryland, “Interference of Bluetooth and IEEE 802.11: Simulation Modelling and Performance Evaluation”, Workshop “Modelling, Analysis and Simulation of Wireless and Mobile Systems”, Rome, Italy, July 2001.
- [6] T. KELLER and J. MODELSKI, “Experimental Results of Testing Interferences in 2.4 GHz ISM Band”, 33rd European Microwave Conference, Munich, 2003.
- [7] ROHDE & SCHWARZ, “Measurements on Bluetooth Products using R&S CMU200/CBT and CMUgo/CBTgo”, <http://www.rohde-schwarz.com>.

SECTION 6

- 6.1. Ozgur Ergul and Levent Gurel, “*Contamination of the Accuracy of the Surface Integral Equations with the Discretization Error of the Identity Operator*” 6-1
- 6.2. Tahir Malas and Levent Gurel, “*Iterative Block Near-Field Preconditioners for Surface Integral-Equation Formulations of Dielectric Problems*” 6-13

Contamination of the Accuracy of the Surface Integral Equations with the Discretization Error of the Identity Operator

Özgür Ergül^{1,2} and Levent Gürel^{1,2}

¹Department of Electrical and Electronics Engineering

²Computational Electromagnetics Research Center (BiLCEM)

Bilkent University, TR-06800, Bilkent, Ankara, Turkey

E-mail: ergul@ee.bilkent.edu.tr, lgurel@bilkent.edu.tr

Abstract — We consider the solution of electromagnetics problems formulated with surface integral equations (SIE) and discretized with low-order basis functions, such as the Rao-Wilton-Glisson functions. Normal and mixed SIE formulations involving well-tested identity operators are significantly inaccurate compared to tangential formulations. We show that the well-tested identity operator is a major error source that contaminates the accuracy of SIE formulations. Due to excessive discretization error of the identity operator, matrix equations obtained with tangential, normal, and mixed formulations are incompatible. We also show that, in an iterative solution of a normal or mixed formulation, the minimization of the residual error involves a breakpoint, where a further reduction of the residual error does not improve the solution in terms of compatibility with the corresponding tangential formulation. This breakpoint corresponds to the last useful iteration, where the accuracy of the solution is saturated and a further reduction of the residual error is practically unnecessary.

1. INTRODUCTION

Surface integral equations (SIE) are commonly used for the solution of scattering and radiation problems in electromagnetics [1]. Complicated problems involving three-dimensional metallic and/or homogeneous dielectric structures are formulated rigorously by defining equivalent current on surfaces and applying the boundary conditions. Depending on the testing scheme and the boundary conditions used, there are four basic SIEs, namely, the tangential electric-field integral equation (T-EFIE), the normal electric-field integral equation (N-EFIE), the tangential magnetic-field integral equation (T-MFIE), and the normal magnetic-field integral equation (N-MFIE) [2]. Various SIE formulations can be derived by using diverse combinations of SIEs. For numerical solutions, those formulations are discretized by expanding the equivalent currents and using the method of moments. The resulting dense matrix equations can be solved iteratively by using a Krylov subspace algorithm, which can be accelerated via fast solvers, such as the multilevel fast multipole algorithm [3].

SIE formulations can be categorized into three groups, i.e., tangential, normal, and mixed formulations, depending on their contents. Tangential formulations involve T-EFIE and/or T-MFIE, while normal formulations involve N-EFIE and/or N-MFIE. Mixed formulations are obtained by combining tangential and normal formulations, and they contain at least one tangential equation (T-EFIE and T-MFIE) and one normal equation (N-EFIE and N-MFIE). Using a Galerkin scheme for the discretization, normal and mixed formulations contain well-tested identity operators. It is well-known that matrix equations involving well-tested identity operators are diagonally dominant and they are well-conditioned. Therefore, iterative solutions of normal and mixed formulations are usually more efficient than the solutions of tangential formulations, which do not contain well-tested identity operators. On the other hand, recent studies show that tangential formulations are significantly more accurate than normal

This work was supported by the Scientific and Technical Research Council of Turkey (TUBITAK) under Research Grants 105E172 and 107E136, by the Turkish Academy of Sciences in the framework of the Young Scientist Award Program (LG/TUBA-GEBIP/2002-1-12), and by contracts from ASELSAN and SSM.

and mixed formulations, especially when they are discretized with low-order basis functions [4]–[8], such as the Rao-Wilton-Glisson (RWG) functions [9]. Discrepancy between the results obtained with tangential, normal, and mixed formulations can be reduced by employing more appropriate, especially higher-order, basis functions [10]–[17]. Investigations on the accuracy of SIE formulations also show that the source of the error is the identity operator [5],[18],[19]. Specifically, regularization of the identity operator improves the accuracy of N-MFIE for metallic objects [5],[19].

In this paper, we investigate the contamination of the accuracy of SIEs with the excessive discretization error of the identity operator. By setting up a computational experiment based on nonradiating currents, we prove that the identity operator is truly a major error source in SIE formulations. Since the discretization of the identity operator contaminates the accuracy of normal and mixed formulations, matrix equations obtained with tangential, normal, and mixed formulations for the same problem are incompatible. Then, the iterative solution of a normal or mixed formulation involves a breakpoint, where the compatibility of the solution with the corresponding tangential formulation is saturated. We show that this breakpoint corresponds to the last useful iteration, where the accuracy of the solution cannot be improved anymore.

2. SURFACE INTEGRAL EQUATION FORMULATIONS

Consider a homogeneous domain D_u bounded by a closed surface S_u and that may extend to infinity. T-EFIE is derived by directly testing the boundary condition for the tangential electric field on the surface, i.e.,

$$\hat{\mathbf{t}} \cdot \left\{ \mathcal{T}_u\{\mathbf{J}\}(\mathbf{r}) - \eta_u^{-1} \mathcal{K}_u\{\mathbf{M}\}(\mathbf{r}) - \frac{\Omega_o(\mathbf{r})}{4\pi} \eta_u^{-1} \mathcal{I}^{\times n}\{\mathbf{M}\}(\mathbf{r}) \right\} = -\hat{\mathbf{t}} \cdot \eta_u^{-1} \mathbf{E}^{inc}(\mathbf{r}), \quad (1)$$

where $\Omega_o(\mathbf{r})$ is the external solid angle at the observation point $\mathbf{r} \in S_u$, $\hat{\mathbf{t}}$ is any tangential unit vector, $\mathbf{E}^{inc}(\mathbf{r})$ is the incident electric field produced by the external sources inside D_u , and $\eta_u = \sqrt{\mu_u/\epsilon_u}$ is the wave impedance. In (1), $\mathbf{J}(\mathbf{r}) = \hat{\mathbf{n}} \times \mathbf{H}(\mathbf{r})$ and $\mathbf{M}(\mathbf{r}) = \hat{\mathbf{n}} \times \mathbf{E}(\mathbf{r})$ are equivalent surface currents, where $\hat{\mathbf{n}}$ is the normal vector pointing into D_u . Operators are defined as

$$\mathcal{T}_u\{\mathbf{X}\}(\mathbf{r}) = ik_u \int_{S_u} d\mathbf{r}' \left[\mathbf{X}(\mathbf{r}') + \frac{1}{k_u^2} \nabla' \cdot \mathbf{X}(\mathbf{r}') \nabla \right] g_u(\mathbf{r}, \mathbf{r}') \quad (2)$$

$$\mathcal{K}_u\{\mathbf{X}\}(\mathbf{r}) = \int_{S_u, PV} d\mathbf{r}' \mathbf{X}(\mathbf{r}') \times \nabla' g_u(\mathbf{r}, \mathbf{r}') \quad (3)$$

$$\mathcal{I}^{\times n}\{\mathbf{X}\}(\mathbf{r}) = \hat{\mathbf{n}} \times \mathcal{I}\{\mathbf{X}\}(\mathbf{r}) = \hat{\mathbf{n}} \times \mathbf{X}(\mathbf{r}), \quad (4)$$

where PV indicates the principal value of the integral, $k_u = \omega \sqrt{\mu_u \epsilon_u}$ is the wavenumber, and $g_u(\mathbf{r}, \mathbf{r}')$ denotes the homogeneous-space Green's function defined as

$$g_u(\mathbf{r}, \mathbf{r}') = \frac{\exp(ik_u R)}{4\pi R} \quad \left(R = |\mathbf{r} - \mathbf{r}'| \right). \quad (5)$$

N-EFIE is derived similarly by testing the boundary condition for the electric field projected onto the surface via $\hat{\mathbf{n}}$, i.e.,

$$\hat{\mathbf{n}} \times \left\{ \mathcal{T}_u\{\mathbf{J}\}(\mathbf{r}) - \eta_u^{-1} \mathcal{K}_u\{\mathbf{M}\}(\mathbf{r}) - \frac{\Omega_o(\mathbf{r})}{4\pi} \eta_u^{-1} \mathcal{I}^{\times n}\{\mathbf{M}\}(\mathbf{r}) \right\} = -\hat{\mathbf{n}} \times \eta_u^{-1} \mathbf{E}^{inc}(\mathbf{r}). \quad (6)$$

Finally, T-MFIE and N-MFIE are derived by testing the boundary condition for the tangential magnetic field, i.e.,

$$\left\{ \begin{array}{c} \hat{\mathbf{t}} \cdot \\ \hat{\mathbf{n}} \times \end{array} \right\} \left\{ \mathcal{T}_u\{\mathbf{M}\}(\mathbf{r}) + \eta_u \mathcal{K}_u\{\mathbf{J}\}(\mathbf{r}) + \frac{\Omega_o(\mathbf{r})}{4\pi} \eta_u \mathcal{I}^{\times n}\{\mathbf{J}\}(\mathbf{r}) \right\} = - \left\{ \begin{array}{c} \hat{\mathbf{t}} \cdot \\ \hat{\mathbf{n}} \times \end{array} \right\} \eta_u \mathbf{H}^{inc}(\mathbf{r}), \quad (7)$$

where $\mathbf{H}^{inc}(\mathbf{r})$ is the incident magnetic field.

Table 1. Surface Integral Equation Formulations

Formulation	Integral Equation Content	Object Type
T-EFIE	T-EFIE	Metallic
N-MFIE	N-MFIE	Metallic
T-N-CFIE	T-EFIE+N-MFIE	Metallic
TN-N-CFIE	T-EFIE ₀ +N-EFIE ₀ +N-MFIE ₀ T-EFIE _I +N-EFIE _I +N-MFIE _I	Dielectric
T-PMCHWT and CTF	T-EFIE ₀ +T-EFIE _I T-MFIE ₀ +T-MFIE _I	Dielectric
NMF and MNMF	N-MFIE ₀ +N-MFIE _I N-EFIE ₀ +N-EFIE _I	Dielectric
JMCFIE	T-EFIE ₀ +T-EFIE _I +N-MFIE ₀ +N-MFIE _I T-MFIE ₀ +T-MFIE _I + N-EFIE ₀ +N-EFIE _I	Dielectric

When the surface of D_u is a perfect electric conductor (PEC), the tangential component of the total electric field vanishes on the surface ($\mathbf{M} = 0$). Then, the scattering or radiation problem can be formulated and solved with T-EFIE, N-MFIE, T-MFIE, or N-MFIE, without using any combination. However, to avoid the internal resonance problem, it is necessary to combine EFIE and MFIE leading to a combined-field integral equation (CFIE) [20]. Specifically, a mixed formulation T-N-CFIE, which is obtained by the convex combination of T-EFIE and N-MFIE, is commonly used in the literature [3].

For scattering and radiation problems involving dielectric objects, integral equations are derived for both inner and outer media. These equations should be solved simultaneously to obtain $\mathbf{J}(\mathbf{r})$ and $\mathbf{M}(\mathbf{r})$. Similar to formulations of PEC objects, EFIE and MFIE can be combined in various ways to derive CFIE formulations, which are immune to the internal resonance problem. For example, TN-N-CFIE, which is obtained by combining T-EFIE, N-EFIE, and N-MFIE, was introduced for stable solutions [2]. On the other hand, many different formulations for dielectric objects are obtained by linearly combining the inner and outer equations while solving EFIE, MFIE, or their combinations simultaneously. For example, the tangential Poggio-Miller-Chang-Harrington-Wu-Tsai (T-PMCHWT) [1],[21],[22] formulation involves simultaneous solutions of T-EFIE and T-MFIE. A similar coupling of N-EFIE and N-MFIE leads to the well-known normal Müller formulation (NMF) [23]. Recently, these two formulations are improved by scaling EFIE and MFIE appropriately, leading to the combined tangential formulation (CTF) [13] and the modified normal Müller formulation (MNMF) [24], respectively. Although these formulations are free of the internal resonance problem, mixed formulations involving both tangential and normal equations are derived to obtain more stable solutions. For example, the electric and magnetic current combined-field integral equation (JMCFIE) [25], which involves all four equations, i.e., T-EFIE, N-EFIE, T-MFIE, and N-MFIE, provides fast iterative solutions, and it is preferable especially when the problem size is large [26]. Finally, electromagnetics problems involving composite dielectric-metallic structures can be formulated via hybrid formulations, which are obtained by applying different formulations for different parts of the objects [27]. Table I lists some of the surface formulations that are commonly used in the literature.

3. DISCRETIZATION

For numerical solutions, SIE formulations are discretized by using basis and testing functions. Equivalent currents are expanded in a series of basis functions $\mathbf{b}_n(\mathbf{r})$, i.e.,

$$\mathbf{J}(\mathbf{r}) = \sum_{n=1}^N \mathbf{x}[n] \mathbf{b}_n(\mathbf{r}) \quad (8)$$

$$\mathbf{M}(\mathbf{r}) = \sum_{n=1}^N \mathbf{y}[n] \mathbf{b}_n(\mathbf{r}), \quad (9)$$

where \mathbf{x} and \mathbf{y} are arrays of unknown coefficients. Testing the integral equations using a set of testing functions $\mathbf{t}_m(\mathbf{r})$, matrix equations are constructed and solved to calculate the unknown coefficients. Four basic matrix equations are derived as

$$\bar{\mathbf{T}}_u^T \cdot \mathbf{x} - \eta_u^{-1} \bar{\mathbf{K}}_u^T \cdot \mathbf{y} - \frac{1}{2} \eta_u^{-1} \bar{\mathbf{I}}^{\times n} \cdot \mathbf{y} = -\eta_u^{-1} \mathbf{v}_E \quad (10)$$

$$\bar{\mathbf{T}}_u^N \cdot \mathbf{x} - \eta_u^{-1} \bar{\mathbf{K}}_u^N \cdot \mathbf{y} + \frac{1}{2} \eta_u^{-1} \bar{\mathbf{I}} \cdot \mathbf{y} = -\eta_u^{-1} \mathbf{v}_E^{\times n} \quad (11)$$

$$\bar{\mathbf{T}}_u^T \cdot \mathbf{y} + \eta_u \bar{\mathbf{K}}_u^T \cdot \mathbf{x} + \frac{1}{2} \eta_u \bar{\mathbf{I}}^{\times n} \cdot \mathbf{x} = -\eta_u \mathbf{v}_H \quad (12)$$

$$\bar{\mathbf{T}}_u^N \cdot \mathbf{y} + \eta_u \bar{\mathbf{K}}_u^N \cdot \mathbf{x} - \frac{1}{2} \eta_u \bar{\mathbf{I}} \cdot \mathbf{x} = -\eta_u \mathbf{v}_H^{\times n}, \quad (13)$$

for T-EFIE, N-EFIE, T-MFIE, and N-MFIE, respectively. The interaction between the m th testing function $\mathbf{t}_m(\mathbf{r})$ and the n th basis function $\mathbf{b}_n(\mathbf{r})$ are calculated for different operators (\mathcal{K} , \mathcal{T} , and \mathcal{I}) and testing types (T and N) as

$$K_u^T[m, n] = \int_{S_m} d\mathbf{r} \mathbf{t}_m(\mathbf{r}) \cdot \int_{S_n, PV} d\mathbf{r}' \mathbf{b}_n(\mathbf{r}') \times \nabla' g_u(\mathbf{r}, \mathbf{r}') \quad (14)$$

$$K_u^N[m, n] = \int_{S_m} d\mathbf{r} \mathbf{t}_m(\mathbf{r}) \cdot \hat{\mathbf{n}} \times \int_{S_n, PV} d\mathbf{r}' \mathbf{b}_n(\mathbf{r}') \times \nabla' g_u(\mathbf{r}, \mathbf{r}') \quad (15)$$

$$\begin{aligned} T_u^T[m, n] &= ik_u \int_{S_m} d\mathbf{r} \mathbf{t}_m(\mathbf{r}) \cdot \int_{S_n} d\mathbf{r}' \mathbf{b}_n(\mathbf{r}') g_u(\mathbf{r}, \mathbf{r}') \\ &\quad - \frac{i}{k_u} \int_{S_m} d\mathbf{r} \mathbf{t}_m(\mathbf{r}) \cdot \int_{S_n} d\mathbf{r}' \nabla' \cdot \mathbf{b}_n(\mathbf{r}') \nabla' g_u(\mathbf{r}, \mathbf{r}') \end{aligned} \quad (16)$$

$$\begin{aligned} T_u^N[m, n] &= ik_u \int_{S_m} d\mathbf{r} \mathbf{t}_m(\mathbf{r}) \cdot \hat{\mathbf{n}} \times \int_{S_n} d\mathbf{r}' \mathbf{b}_n(\mathbf{r}') g_u(\mathbf{r}, \mathbf{r}') \\ &\quad - \frac{i}{k_u} \int_{S_m} d\mathbf{r} \mathbf{t}_m(\mathbf{r}) \cdot \hat{\mathbf{n}} \times \int_{S_n} d\mathbf{r}' \nabla' \cdot \mathbf{b}_n(\mathbf{r}') \nabla' g_u(\mathbf{r}, \mathbf{r}') \end{aligned} \quad (17)$$

$$I[m, n] = \int_{S_m} d\mathbf{r} \mathbf{t}_m(\mathbf{r}) \cdot \frac{\Omega_o(\mathbf{r})}{2\pi} \mathbf{b}_n(\mathbf{r}) \quad (18)$$

$$I^{\times n}[m, n] = \int_{S_m} d\mathbf{r} \mathbf{t}_m(\mathbf{r}) \cdot \hat{\mathbf{n}} \frac{\Omega_o(\mathbf{r})}{2\pi} \times \mathbf{b}_n(\mathbf{r}), \quad (19)$$

where S_m is the spatial support of the m th basis or testing function for $m = 1, 2, \dots, N$. Elements of the right-hand-side (RHS) vectors in (10)–(13) are obtained by testing the incident electromagnetic fields, i.e.,

$$\mathbf{v}_E[m] = \int_{S_m} d\mathbf{r} \mathbf{t}_m(\mathbf{r}) \cdot \mathbf{E}^{inc}(\mathbf{r}) \quad (20)$$

$$\mathbf{v}_E^{\times n}[m] = \int_{S_m} d\mathbf{r} \mathbf{t}_m(\mathbf{r}) \cdot \hat{\mathbf{n}} \times \mathbf{E}^{inc}(\mathbf{r}) \quad (21)$$

$$\mathbf{v}_H[m] = \int_{S_m} d\mathbf{r} \mathbf{t}_m(\mathbf{r}) \cdot \mathbf{H}^{inc}(\mathbf{r}) \quad (22)$$

$$\mathbf{v}_H^{\times n}[m] = \int_{S_m} d\mathbf{r} \mathbf{t}_m(\mathbf{r}) \cdot \hat{\mathbf{n}} \times \mathbf{H}^{inc}(\mathbf{r}). \quad (23)$$

Using a Galerkin scheme and choosing the same set of functions as basis and testing functions, the

tangential equations, i.e., T-EFIE and T-MFIE, contain well-tested \mathcal{T} operators, while the normal equations, i.e., N-EFIE and N-MFIE, contain well-tested \mathcal{K} and \mathcal{I} operators [2]. Then, tangential formulations involving T-EFIE and/or T-MFIE contain well-tested \mathcal{T} operators, while normal formulations involving N-EFIE and/or N-MFIE contain well-tested \mathcal{K} and \mathcal{I} operators [13]. In mixed formulations, such as CFIE and JMCFIE, all kinds of operators are well-tested. In general, well-tested identity operators lead to well-conditioned matrix equations, which are easy to solve iteratively [28]. Therefore, for the efficiency of the solutions, normal and mixed formulations are preferable, especially when problems involve large objects discretized with large numbers of unknowns [26],[29],[30]. On the other hand, recent studies show that normal and mixed formulations are significantly inaccurate compared to tangential formulations [4]–[8], especially when they are discretized with low-order basis functions, such as RWG functions. Accuracy of normal and mixed formulations could be improved to the levels of tangential formulations by employing higher-order basis functions [13],[16],[17]. Investigations also show that the excessive error is caused by the well-tested identity operators [5],[18],[19]. In addition to the conditioning of the matrix equations, the identity operator seems to play a key role in the accuracy of the solutions via SIE formulations.

Using RWG functions on planar triangles, discretization of the well-tested identity operator is simple. The integral

$$I[m, n] = \int_{S_m} d\mathbf{r} \mathbf{t}_m(\mathbf{r}) \cdot \frac{\Omega_o(\mathbf{r})}{2\pi} \mathbf{b}_n(\mathbf{r}) = \int_{S_m} d\mathbf{r} \mathbf{t}_m(\mathbf{r}) \cdot \mathbf{b}_n(\mathbf{r}) \quad (24)$$

can be evaluated accurately by using a low-order Gaussian quadrature rule. On the other hand, the identity operator behaves like an operator with a highly-singular kernel [5],[18]. This alternative interpretation can be understood when (24) is rewritten as a double integral over the testing and basis functions as

$$I_{mn} = \int_{S_m} d\mathbf{r} \mathbf{t}_m(\mathbf{r}) \cdot \int_{S_n} d\mathbf{r}' \delta(\mathbf{r}, \mathbf{r}') \mathbf{b}_n(\mathbf{r}'), \quad (25)$$

where $\delta(\mathbf{r}, \mathbf{r}')$ is a Dirac delta function representing a strong singularity. Consequently, the discretization of the identity operator may cause an unexpectedly large error, although its discretization involves very small or no error.

To demonstrate the inaccuracy of normal and mixed formulations compared to tangential formulations, we present the solution of electromagnetics problems involving canonical objects. Fig. 1 presents the results of a radiation problem involving a 1 cm \times 1 cm \times 1 cm PEC box located at the origin. As depicted in Fig. 1, the box is excited with a Hertzian dipole oriented in the z direction and located inside the box at $z = 0.35$ cm. Ideally, the radiated field outside the box should be zero due to the shielding provided by the closed PEC surface. We calculate the radiated field in the far zone on the x - y plane at $\mathbf{r} = (3 \text{ meters}, \pi/2, \phi_p)$, where $\phi_p = (p - 1)\pi/180$ for $p = 1, 2, \dots, 360$. The relative error is defined as the 2-norm of the total electric field divided by the 2-norm of the incident electric field, i.e.,

$$\Delta = \sqrt{\frac{\sum_{p=1}^{360} |E(3, \pi/2, \phi_p)|^2}{\sum_{p=1}^{360} |E^{inc}(3, \pi/2, \phi_p)|^2}} \quad (\phi_p = (p - 1)\pi/180). \quad (26)$$

The total electric field is obtained by adding the incident field due to the Hertzian dipole and the secondary field due to the induced electric current on the cube. Fig. 1 presents the relative error as a function of frequency from 20 GHz to 60 GHz. In this range of frequency, the size of the box varies from 0.67λ to 2λ . The radiation problem is discretized with 7200, 28,800, 115,200, and 460,800 unknowns, and solved by MLFMA without diagonalization [31]. We observe that T-N-CFIE = $0.2 \times$ T-EFIE + $0.8 \times$ N-MFIE is significantly less accurate than T-EFIE. In order to obtain the same accuracy, the number of unknowns of T-N-CFIE should be 16 times larger than that of T-EFIE.

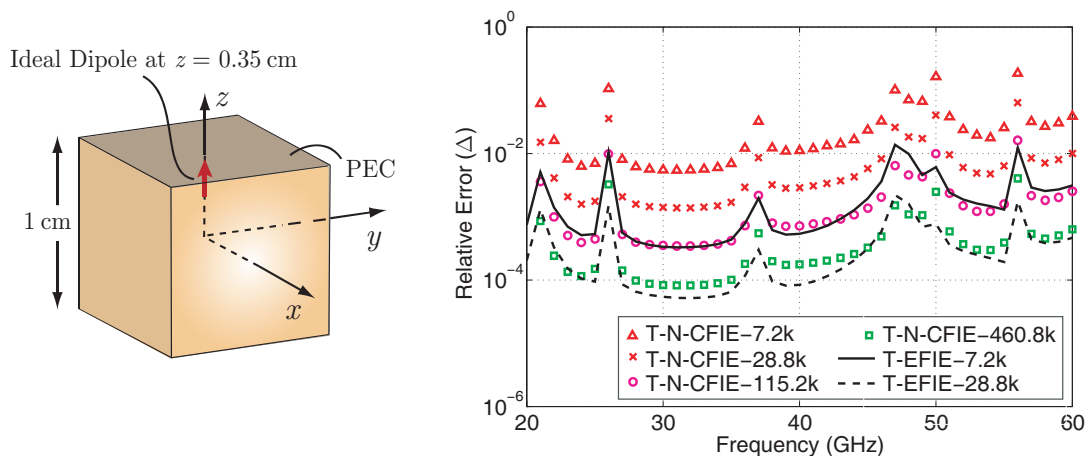


Fig. 1. Solutions of a radiation problem involving a $1\text{ cm} \times 1\text{ cm} \times 1\text{ cm}$ PEC box located at the origin and excited by a Hertzian dipole located inside the box at $z = 0.35\text{ cm}$. Relative error defined in (26) is plotted as a function of frequency from 20 GHz to 60 GHz.

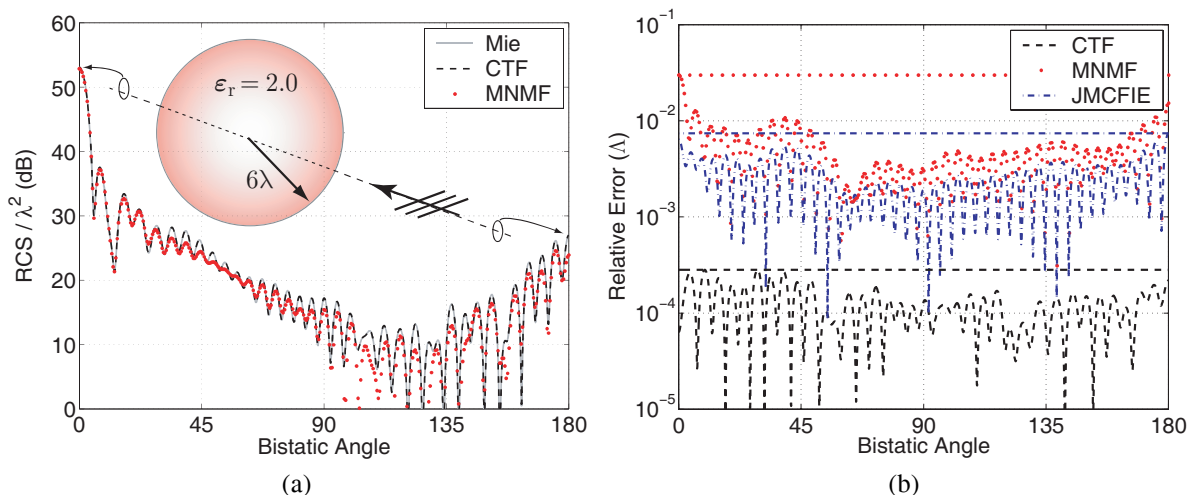


Fig. 2. Solutions of a scattering problem involving a dielectric sphere of radius 6λ illuminated by a plane wave. Relative permittivity of the sphere is 2.0 and it is located in free space. (a) Normalized bistatic RCS (RCS/λ^2) and (b) relative error defined in (27) for different formulations as a function of the bistatic angle.

Fig. 2 presents the solution of a scattering problem involving a dielectric sphere of radius 6λ , where λ is the wavelength outside the sphere (free space). The relative permittivity of the sphere is 2.0 and it is illuminated by a plane wave. The scattering problem is discretized with 264,006 unknowns and solved by MLFMA with three digits of accuracy. Fig. 2(a) presents the normalized radar cross section (RCS/λ^2 in dB) values on the E-plane as a function of the observation angle from 0° to 180° , where 0° corresponds to the forward-scattering direction. Computational values obtained with CTF and MNMF are compared with analytical values obtained by a Mie-series solution. We observe that the tangential formulation CTF provides more accurate results than the normal formulation MNMF. For more quantitative information, Fig. 2(b) presents the relative error in the computational results with respect to the reference analytical solution. In addition to CTF and MNMF, we also consider the error for the mixed formulation JMCFIE. The relative error as a function of bistatic angle φ is

defined as

$$\Lambda(\varphi) = \lim_{r \rightarrow \infty} \frac{|E_C^\infty(\varphi) - E_A^\infty(\varphi)|}{\max_\varphi |E_A^\infty(\varphi)|}, \quad (27)$$

where $E_C^\infty(\varphi)$ and $E_A^\infty(\varphi)$ are computational and analytical values of the far-zone electric field, i.e.,

$$E^\infty(\varphi) = \lim_{r \rightarrow \infty} rE(r, \varphi). \quad (28)$$

The maximum value of the relative error is also indicated by a horizontal line in the figure for each formulation. Fig. 2(b) shows that CTF provides the most accurate results, while MNMF is significantly inaccurate compared to CTF. Being a mixed formulation, accuracy of JMCIE is between CTF and MNMF.

4. EXCESSIVE DISCRETIZATION ERROR OF THE IDENTITY OPERATOR

In this section, we prove that the identity operator is truly a major error source, which contaminates the accuracy of SIE formulations. This is achieved by using the nonradiating property of the tangential incident fields on arbitrary surfaces [32],[33], i.e.,

$$\eta_u \mathcal{T}_u \{ \mathbf{J}^{inc} \}(\mathbf{r}) - \mathcal{K}_u \{ \mathbf{M}^{inc} \}(\mathbf{r}) + \frac{\Omega_i(\mathbf{r})}{4\pi} \mathcal{I}^{\times n} \{ \mathbf{M}^{inc} \}(\mathbf{r}) = 0 \quad (29)$$

$$\frac{1}{\eta_u} \mathcal{T}_u \{ \mathbf{M}^{inc} \}(\mathbf{r}) + \mathcal{K}_u \{ \mathbf{J}^{inc} \}(\mathbf{r}) - \frac{\Omega_i(\mathbf{r})}{4\pi} \mathcal{I}^{\times n} \{ \mathbf{J}^{inc} \}(\mathbf{r}) = 0, \quad (30)$$

where $\Omega_i(\mathbf{r})$ is the internal solid angle and $\{ \mathbf{J}^{inc}(\mathbf{r}), \mathbf{M}^{inc}(\mathbf{r}) \} = \{ \hat{\mathbf{n}} \times \mathbf{H}^{inc}(\mathbf{r}), -\hat{\mathbf{n}} \times \mathbf{E}^{inc}(\mathbf{r}) \}$. Nonradiating currents are expanded in a series of RWG functions, i.e.,

$$\mathbf{J}^{inc}(\mathbf{r}) = \sum_{n=1}^N \mathbf{x}^{inc}[n] \mathbf{b}_n(\mathbf{r}) \quad (31)$$

$$\mathbf{M}^{inc}(\mathbf{r}) = \sum_{n=1}^N \mathbf{y}^{inc}[n] \mathbf{b}_n(\mathbf{r}), \quad (32)$$

by using two methods. First, we consider an identity equation in the form of

$$\begin{bmatrix} \mathcal{I} & 0 \\ 0 & \mathcal{I} \end{bmatrix} \cdot \begin{bmatrix} \hat{\mathbf{n}} \times \mathbf{H}^{inc} \\ -\hat{\mathbf{n}} \times \mathbf{E}^{inc} \end{bmatrix} = \begin{bmatrix} \hat{\mathbf{n}} \times \mathbf{H}^{inc} \\ -\hat{\mathbf{n}} \times \mathbf{E}^{inc} \end{bmatrix}, \quad (33)$$

which can be discretized as

$$\begin{bmatrix} \bar{\mathcal{I}} & 0 \\ 0 & \bar{\mathcal{I}} \end{bmatrix} \cdot \begin{bmatrix} \mathbf{x}^{inc} \\ \mathbf{y}^{inc} \end{bmatrix} = \begin{bmatrix} \mathbf{v}_H^{\times n} \\ -\mathbf{v}_E^{\times n} \end{bmatrix}. \quad (34)$$

This method involves well-tested identity operators. The second method is based on the discretization of (29) and (30), i.e.,

$$\begin{bmatrix} \bar{\mathcal{T}}_u^T & -\eta_u^{-1} \bar{\mathcal{K}}_u^T \\ \eta_u \bar{\mathcal{K}}_u^T & \bar{\mathcal{T}}_u^T \end{bmatrix} \cdot \begin{bmatrix} \mathbf{x}^{inc} \\ \mathbf{y}^{inc} \end{bmatrix} = -\frac{1}{2} \begin{bmatrix} \eta_u^{-1} \mathbf{v}_E \\ \eta_u \mathbf{v}_H \end{bmatrix}, \quad (35)$$

which involves tangentially-tested \mathcal{T} and \mathcal{K} operators and does not contain any identity operator.

Fig. 3 presents the results of experiments involving a sphere of radius 0.5λ and a cube with edges of 0.5λ . Both objects are illuminated by a plane wave with unit amplitude. Nonradiating currents are expanded in a series of RWG functions on the objects using the two methods described above, i.e., using well-tested identity operators and using integro-differential \mathcal{T} and \mathcal{K} operators. Expansion coefficients are calculated and used to compute the radiated fields in the far zone on the E-plane. Fig. 3 presents the far-zone electric field, i.e., $E^\infty(\varphi)$ as a function of bistatic angle φ . Ideally, $\{ \mathbf{J}^{inc}(\mathbf{r}), \mathbf{M}^{inc}(\mathbf{r}) \}$ should not radiate and $E^\infty(\varphi)$ should be zero. Fig. 3(a) shows that the value

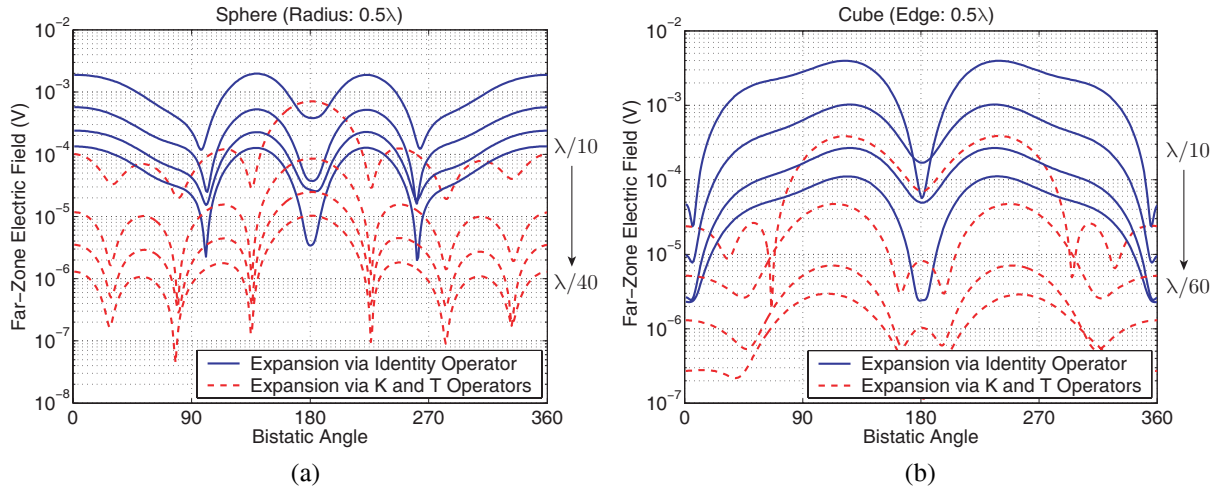


Fig. 3. Far-zone electric field due to nonradiating currents on (a) a sphere of radius 0.5λ and (b) a cube with edges of 0.5λ . Nonradiating currents discretized and expanded in a series of RWG functions by using two different methods involving well-tested identity operators and tangentially-tested integro-differential operators.

of $E^\infty(\varphi)$ drops as the mesh size decreases from $\lambda/10$ to $\lambda/40$ for the sphere. On the other hand, the two methods offer different levels of accuracy. Given a mesh size, error is smaller with the second method using the integro-differential operators, compared to the first method using well-tested identity operators. Fig. 3(b) presents similar results for the cube. The value of $E^\infty(\varphi)$ decreases as the triangulation becomes finer; but the first method generates larger error than the second method. We note that the first and second expansion methods are related to the solutions of electromagnetics problems with normal/mixed and tangential formulations, respectively, where the total currents (instead of nonradiating currents) are expanded in a series of basis functions.

5. CONTAMINATION OF THE ACCURACY OF SURFACE FORMULATIONS

Excessive discretization error of the identity operator contaminates the accuracy of normal and mixed formulations. Therefore, matrix equations obtained with tangential, normal, and mixed formulations for the same problem are incompatible. For example, consider the solution of an electromagnetics problems involving a closed PEC object. The problem can be formulated with T-EFIE and N-MFIE. Due to excessive discretization error of the identity operator in N-MFIE, solutions obtained with T-EFIE and N-MFIE are not equal, i.e.,

$$-\eta_u^{-1} \left\{ \bar{\mathbf{T}}_u^T \right\}^{-1} \cdot \mathbf{v}_E = \mathbf{x}_E \neq \mathbf{x}_M = - \left\{ \bar{\mathbf{K}}_u^N - 0.5\bar{\mathbf{I}} \right\}^{-1} \cdot \mathbf{v}_H^{\times n}, \quad (36)$$

even when the solutions are free of internal resonances. We write

$$\mathbf{x}_M = \mathbf{x}_E + \Delta \mathbf{x}_{ME} \quad (37)$$

and the discrepancy between the solutions is interpreted as the error in N-MFIE. Consider the solution of the same problem with T-N-CFIE = $\alpha \times$ T-EFIE + $(1 - \alpha) \times$ N-MFIE, i.e.,

$$\mathbf{x}_C = - \left\{ \alpha \eta_u \bar{\mathbf{T}}_u^T + (1 - \alpha) (\bar{\mathbf{K}}_u^N - 0.5\bar{\mathbf{I}}) \right\}^{-1} \cdot \left\{ \alpha \mathbf{v}_E + (1 - \alpha) \mathbf{v}_H^{\times n} \right\}, \quad (38)$$

where $0 \leq \alpha \leq 1$. We note that

$$\begin{aligned}
\mathbf{x}_C &= \left\{ \alpha \eta_u \bar{\mathbf{T}}_u^T + (1 - \alpha) (\bar{\mathbf{K}}_u^N - 0.5 \bar{\mathbf{I}}) \right\}^{-1} \cdot \left\{ \alpha \eta_u \bar{\mathbf{T}}_u^T \cdot \mathbf{x}_E + (1 - \alpha) (\bar{\mathbf{K}}_u^N - 0.5 \bar{\mathbf{I}}) \cdot \mathbf{x}_M \right\} \\
&= \left\{ \alpha \eta_u \bar{\mathbf{T}}_u^T + (1 - \alpha) (\bar{\mathbf{K}}_u^N - 0.5 \bar{\mathbf{I}}) \right\}^{-1} \cdot \left\{ \alpha \eta_u \bar{\mathbf{T}}_u^T \cdot \mathbf{x}_E + (1 - \alpha) (\bar{\mathbf{K}}_u^N - 0.5 \bar{\mathbf{I}}) \cdot \mathbf{x}_E \right\} \\
&\quad + \left\{ \alpha \eta_u \bar{\mathbf{T}}_u^T + (1 - \alpha) (\bar{\mathbf{K}}_u^N - 0.5 \bar{\mathbf{I}}) \right\}^{-1} \cdot (1 - \alpha) (\bar{\mathbf{K}}_u^N - 0.5 \bar{\mathbf{I}}) \cdot (\mathbf{x}_M - \mathbf{x}_E) \\
&= \mathbf{x}_E + \Delta \mathbf{x}_{CE},
\end{aligned} \tag{39}$$

where

$$\Delta \mathbf{x}_{CE} = \left\{ \alpha \eta_u \bar{\mathbf{T}}_u^T + (1 - \alpha) (\bar{\mathbf{K}}_u^N - 0.5 \bar{\mathbf{I}}) \right\}^{-1} \cdot (1 - \alpha) (\bar{\mathbf{K}}_u^N - 0.5 \bar{\mathbf{I}}) \cdot \Delta \mathbf{x}_{ME}. \tag{40}$$

Equations (39) and (40) describe how the T-N-CFIE solution is contaminated with the inaccuracy of N-MFIE due to the discretization error of the identity operator.

Consider an iterative solution of T-N-CFIE, where the residual error is minimized, i.e.,

$$\mathbf{r}_C = \alpha \mathbf{v}_E + (1 - \alpha) \mathbf{v}_H^{\times n} + \left\{ \alpha \eta_u \bar{\mathbf{T}}_u^T + (1 - \alpha) (\bar{\mathbf{K}}_u^N - 0.5 \bar{\mathbf{I}}) \right\} \cdot \tilde{\mathbf{x}}_C \rightarrow 0. \tag{41}$$

Rearranging the terms in (41), we obtain

$$\mathbf{r}_C = \alpha \mathbf{r}_{C \rightarrow E} + (1 - \alpha) \mathbf{r}_{C \rightarrow M}, \tag{42}$$

where

$$\mathbf{r}_{C \rightarrow E} = \mathbf{v}_E + \eta_u \bar{\mathbf{T}}_u^T \cdot \tilde{\mathbf{x}}_C \tag{43}$$

$$\mathbf{r}_{C \rightarrow M} = \mathbf{v}_H^{\times n} + (\bar{\mathbf{K}}_u^N - 0.5 \bar{\mathbf{I}}) \cdot \tilde{\mathbf{x}}_C \tag{44}$$

are residual vectors obtained by testing the T-N-CFIE solution in T-EFIE and N-MFIE systems, respectively. When the norm of \mathbf{r}_C in (41) is minimized, norms of $\mathbf{r}_{C \rightarrow E}$ and $\mathbf{r}_{C \rightarrow M}$ are not necessarily minimized. Instead, $\mathbf{r}_{C \rightarrow E}$ and $\mathbf{r}_{C \rightarrow M}$ are scaled with respect to each other, i.e.,

$$\mathbf{r}_{C \rightarrow E} \approx -\frac{(1 - \alpha)}{\alpha} \mathbf{r}_{C \rightarrow M}. \tag{45}$$

Then, an iterative solution of T-N-CFIE involves a breakpoint, where a further reduction of the residual error does not improve the compatibility of the solution with T-EFIE and N-MFIE. In general, iterative solutions of normal and mixed formulations discretized with low-order basis functions involve breakpoints, where the compatibility of the solution with the corresponding tangential formulation is saturated. More importantly, a breakpoint for the compatibility with the tangential formulation corresponds to the last useful iteration to obtain the highest possible accuracy with a normal or mixed formulation.

As an example, we consider the solution of a scattering problem involving a $\lambda \times \lambda \times \lambda$ PEC cube located at the origin. The cube is discretized with 2052 RWG functions and illuminated by a plane wave propagating in the $-x$ direction with the electric field polarized in the y direction. The scattering problem is solved with T-EFIE and T-N-CFIE ($\alpha = 0.2$) formulations. Matrix elements are calculated with a maximum of 1% error and solutions are performed iteratively by using the biconjugate-gradient-stabilized (BiCGStab) algorithm [34]. Fig. 4(a) presents the iterative solution of T-N-CFIE, where the 2-norm of the residual vector \mathbf{r}_C is plotted with respect to BiCGStab iterations. We also plot the norms of $\mathbf{r}_{C \rightarrow E}$ and $\mathbf{r}_{C \rightarrow M}$ denoted by ‘‘T-N-CFIE to T-EFIE’’ and ‘‘T-N-CFIE to N-MFIE’’, respectively. The residual error is reduced to below 10^{-6} in 20 iterations. However, compatibility of the T-N-CFIE solution with the T-EFIE and N-MFIE systems is saturated at about 7th iterations. Fig. 4(b) presents both two solutions with T-EFIE and T-N-CFIE. Using T-EFIE, the residual error is reduced to below 10^{-6} in more than 300 iterations. In addition to residual errors, we calculate the error in the near-zone

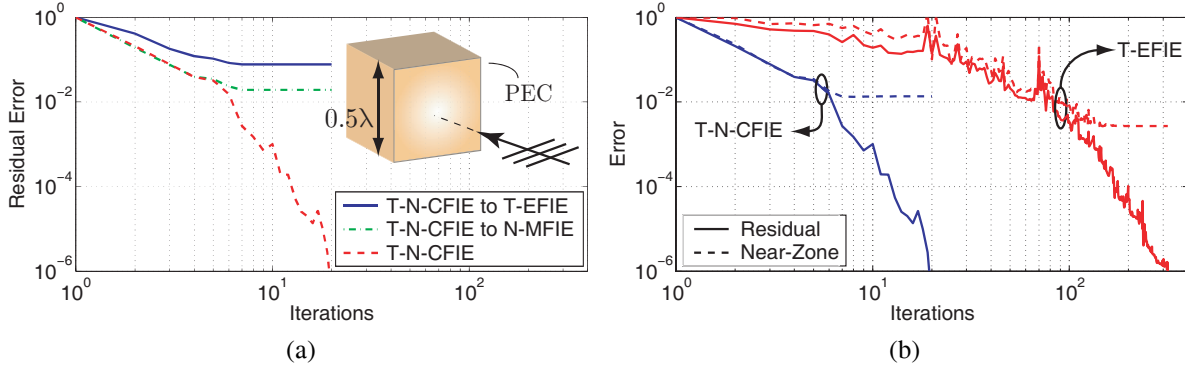


Fig. 4. Iterative solutions of a scattering problem involving a $\lambda \times \lambda \times \lambda$ PEC cube illuminated by a plane wave propagating in the $-x$ direction with the electric field polarized in the y direction. (a) Residual errors with respect to iterations for T-N-CFIE. (b) Residual error and near-zone error defined in (46) with respect to iterations for T-N-CFIE and T-EFIE.

electric field at each iteration. The total electric field, which is obtained by combining the incident plane wave and the secondary field due to the induced electric current, is sampled inside the cube at $19 \times 19 = 361$ regularly-spaced points on the $z = 0$ plane. The total electric field should be zero inside the cube due to the shielding effect of the perfectly-conducting closed surface. Then, we define the near-zone error as

$$\Upsilon = \sqrt{\frac{\sum_{p=1}^{361} |E(x_p, y_p, 0)|^2}{\sum_{p=1}^{361} |E^{inc}(x_p, y_p, 0)|^2}} \quad \left(-\lambda/2 \leq x_p, y_p \leq \lambda/2 \right). \quad (46)$$

As depicted in Fig. 4(b), the near-zone error in the T-EFIE solution is saturated at about 150th iteration, and the minimum achievable error is approximately 2.8×10^{-3} . Accuracy of the solution is saturated since there are various error sources, such as the numerical calculation of the matrix elements, and the overall error cannot be minimized by only reducing the residual error. In the T-N-CFIE solution, however, the minimum achievable error is directly related to the compatibility of the solution with the T-EFIE formulation. In this case, the near-zone error is saturated at 7th iteration, which corresponds to the breakpoint in Fig. 4(a), and the accuracy cannot be improved anymore. Consequently, a further reduction of the residual error is practically unnecessary.

6. CONCLUSION

In this study, we present our investigations on the contamination of SIE formulations with the excessive discretization error of the identity operator. Normal and mixed formulations involving well-tested identity operators are significantly inaccurate compared to tangential formulations, especially when they are discretized with low-order basis functions. By performing a computational experiment based on the nonradiating property of the tangential incident fields on arbitrary surfaces, we show that the identity operator is a major error source. Since normal and mixed formulations are contaminated with the excessive discretization error of the identity operator, matrix equations obtained with SIE formulations are incompatible. Then, minimization of the residual error during an iterative solution of a normal or mixed formulation involves a breakpoint, where the compatibility of the solution with the corresponding tangential formulation cannot be enhanced anymore. We show that the compatibility of a solution with a tangential formulation is an important indicator to determine the last useful iteration for the highest possible accuracy offered by SIE formulations.

REFERENCES

- [1] A. J. Poggio and E. K. Miller, "Integral equation solutions of three-dimensional scattering problems," in *Computer Techniques for Electromagnetics*, R. Mittra, Ed. Oxford: Pergamon Press, 1973, Chap. 4.

- [2] X.-Q. Sheng, J.-M. Jin, J. Song, W. C. Chew, and C.-C. Lu, "Solution of combined-field integral equation using multilevel fast multipole algorithm for scattering by homogeneous bodies," *IEEE Trans. Antennas Propagat.*, vol. 46, no. 11, pp. 1718–1726, Nov. 1998.
- [3] J. Song, C.-C. Lu, and W. C. Chew, "Multilevel fast multipole algorithm for electromagnetic scattering by large complex objects," *IEEE Trans. Antennas Propagat.*, vol. 45, no. 10, pp. 1488–1493, Oct. 1997.
- [4] Ö. Ergül and L. Gürel, "Investigation of the inaccuracy of the MFIE discretized with the RWG basis functions," in *Proc. IEEE Antennas and Propagation Soc. Int. Symp.*, vol. 3, 2004, pp. 3393–3396.
- [5] C. P. Davis and K. F. Warnick, "High-order convergence with a low-order discretization of the 2-D MFIE," *IEEE Antennas Wireless Propagat. Lett.*, vol. 3, pp. 355–358, 2004.
- [6] Ö. Ergül and L. Gürel, "Improved testing of the magnetic-field integral equation," *IEEE Microwave Wireless Comp. Lett.*, vol. 15, no. 10, pp. 615–617, Oct. 2005.
- [7] Ö. Ergül and L. Gürel, "Solid-angle factor in the magnetic-field integral equation," *Microwave Opt. Technol. Lett.*, vol. 45, no. 5, pp. 452–456, June 2005.
- [8] Ö. Ergül and L. Gürel, "On the accuracy of MFIE and CFIE in the solution of large electromagnetic scattering problems," in *Proc. European Conference on Antennas and Propagation (EuCAP)*, no. 350265, 2006.
- [9] S. M. Rao, D. R. Wilton, and A. W. Glisson, "Electromagnetic scattering by surfaces of arbitrary shape," *IEEE Trans. Antennas Propagat.*, vol. AP-30, no. 3, pp. 409–418, May 1982.
- [10] Ö. Ergül and L. Gürel, "Improving the accuracy of the MFIE with the choice of basis functions," in *Proc. IEEE Antennas and Propagation Soc. Int. Symp.*, vol. 3, 2004, pp. 3389–3392.
- [11] E. Ubeda and J. M. Rius, "MFIE MOM-formulation with curl-conforming basis functions and accurate kernel integration in the analysis of perfectly conducting sharp-edged objects," *Microwave Opt. Technol. Lett.*, vol. 44, no. 4, pp. 354–358, Feb. 2005.
- [12] E. Ubeda and J. M. Rius, "Monopolar divergence-conforming and curl-conforming low-order basis functions for the electromagnetic scattering analysis," *Microwave Opt. Technol. Lett.*, vol. 46, no. 3, pp. 237–241, Aug. 2005.
- [13] P. Ylä-Oijala, M. Taskinen, and S. Järvenpää, "Surface integral equation formulations for solving electromagnetic scattering problems with iterative methods," *Radio Science*, vol. 40, RS6002, doi:10.1029/2004RS003169, Nov. 2005.
- [14] E. Ubeda and J. M. Rius, "Novel monopolar MFIE MoM-discretization for the scattering analysis of small objects," *IEEE Trans. Antennas Propagat.*, vol. 54, no. 1, pp. 50–57, Jan. 2006.
- [15] Ö. Ergül and L. Gürel, "The use of curl-conforming basis functions for the magnetic-field integral equation," *IEEE Trans. Antennas Propagat.*, vol. 54, no. 7, pp. 1917–1926, July 2006.
- [16] Ö. Ergül and L. Gürel, "Improving the accuracy of the magnetic field integral equation with the linear-linear basis functions," *Radio Sci.*, vol. 41, RS4004, doi:10.1029/2005RS003307, July 2006.
- [17] Ö. Ergül and L. Gürel, "Linear-linear basis functions for MLFMA solutions of magnetic-field and combined-field integral equations," *IEEE Trans. Antennas Propagat.*, vol. 55, no. 4, pp. 1103–1110, Apr. 2007.
- [18] P. Ylä-Oijala, M. Taskinen, and S. Järvenpää, "Analysis of surface integral equations in electromagnetic scattering and radiation problems," *Engineering Analysis with Boundary Elements*, vol. 32, no. 3, pp. 196–209, Mar. 2008.
- [19] K. F. Warnick and A. F. Peterson, "3D MFIE accuracy improvement using regularization," in *Proc. IEEE Antennas and Propagation Soc. Int. Symp.*, 2007, pp. 4857–4860.
- [20] J. R. Mautz and R. F. Harrington, "H-field, E-field, and combined field solutions for conducting bodies of revolution," *AEÜ*, vol. 32, no. 4, pp. 157–164, Apr. 1978.
- [21] T. K. Wu and L. L. Tsai, "Scattering from arbitrarily-shaped lossy dielectric bodies of revolution," *Radio Sci.*, vol. 12, pp. 709–718, Sep.-Oct. 1977.
- [22] Y. Chang and R. F. Harrington, "A surface formulation for characteristic modes of material bodies," *IEEE Trans. Antennas Propagat.*, vol. AP-25, pp. 789–795, Nov. 1977.
- [23] C. Müller, *Foundations of the Mathematical Theory of Electromagnetic Waves*. New York: Springer, 1969.
- [24] P. Ylä-Oijala and M. Taskinen, "Well-conditioned Müller formulation for electromagnetic scattering by dielectric objects," *IEEE Trans. Antennas Propagat.*, vol. 53, no. 10, pp. 3316–3323, Oct. 2005.

- [25] P. Ylä-Oijala and M. Taskinen, "Application of combined field integral equation for electromagnetic scattering by dielectric and composite objects," *IEEE Trans. Antennas Propagat.*, vol. 53, no. 3, pp. 1168–1173, Mar. 2005.
- [26] Ö. Ergül and L. Gürel, "Comparison of integral-equation formulations for the fast and accurate solution of scattering problems involving dielectric objects with the multilevel fast multipole algorithm," *IEEE Trans. Antennas Propagat.*, accepted for publication.
- [27] P. Ylä-Oijala, M. Taskinen, and J. Sarvas, "Surface integral equation method for general integral equation method for general composite metallic and dielectric structures with junctions," *Progress In Electromagnetics Research (PIER)*, vol. 52, pp. 81-108, doi:10.2528/PIER04071301, 2005.
- [28] D. R. Wilton and J. E. Wheeler III, "Comparison of convergence rates of the conjugate gradient method applied to various integral equation formulations," *Progress in Electromagnetics Research PIER 05*, pp. 131–158, 1991.
- [29] L. Gürel and Ö. Ergül, "Comparisons of FMM implementations employing different formulations and iterative solvers," in *Proc. IEEE Antennas and Propagation Soc. Int. Symp.*, vol. 1, 2003, pp. 19–22.
- [30] L. Gürel and Ö. Ergül, "Fast and accurate solutions of integral-equation formulations discretised with tens of millions of unknowns," *Electronics Lett.*, vol. 43, no. 9, pp. 499–500, Apr. 2007.
- [31] L. J. Jiang and W. C. Chew, "A mixed-form fast multipole algorithm," *IEEE Trans. Antennas Propagat.*, vol. 53, no. 12, pp. 4145–4156, Dec. 2005.
- [32] G. C. Hsiao and R. E. Kleinman, "Mathematical foundations for error estimation in numerical solutions of integral equations in electromagnetics," *IEEE Trans. Antennas Propagat.*, vol. 45, no. 3, pp. 316–328, Mar. 1997.
- [33] Ö. Ergül and L. Gürel, "Stabilization of integral-equation formulations for the accurate solution of scattering problems involving low-contrast dielectric objects," *IEEE Trans. Antennas Propagat.*, vol. 56, no. 3, pp. 799–805, Mar. 2008.
- [34] H. A. van der Vorst, "Bi-CGSTAB: A fast and smoothly converging variant of Bi-CG for the solution of nonsymmetric linear systems," *SIAM J. Sci. Statist. Comput.*, vol. 13, no. 2, pp. 631–644, Mar. 1992.

Iterative Block Near-Field Preconditioners for Surface Integral-Equation Formulations of Dielectric Problems

Tahir Malas^{1,2} and Levent Gürel^{1,2}

¹Department of Electrical and Electronics Engineering

²Computational Electromagnetics Research Center (BiLCEM)

Bilkent University, TR-06800, Bilkent, Ankara, Turkey

E-mail: tmalas@ee.bilkent.edu.tr, lgurel@bilkent.edu.tr

Abstract — We improve the convergence behaviour of the two commonly used integral-equation formulations of dielectric problems, namely, the combined tangential formulation and the electric and magnetic current combined-field integral equation, using iterative block preconditioners, which are obtained from approximate block solutions of the near-field matrix system. The effectiveness of the proposed preconditioners is demonstrated on large dielectric problems.

1. INTRODUCTION

Many real-life problems in computational electromagnetics necessitate the use of integral-equation formulations of dielectric problems, such as simulations of photonic crystals [1], development of effective lenses [2], and optical analysis of blood for blood-related diseases [3]. Some recently proposed formulations for dielectrics that are suitable for iterative solutions include the combined tangential formulation (CTF) and the electric and magnetic current combined-field integral equation (JMCFIE). These two formulations are of utmost interest since CTF yields more accurate scattering results and JMCFIE yields better-conditioned systems than other formulations [9].

Integral-equation formulations of dielectric problems are obtained by simultaneous discretization of the electric and magnetic surface currents and result in block-partitioned linear systems in the form

$$\begin{bmatrix} \bar{\mathbf{Z}}_{11} & \bar{\mathbf{Z}}_{12} \\ \bar{\mathbf{Z}}_{21} & \bar{\mathbf{Z}}_{22} \end{bmatrix} \cdot \begin{bmatrix} \mathbf{a}_J \\ \mathbf{a}_M \end{bmatrix} = \begin{bmatrix} \mathbf{v}_1 \\ \mathbf{v}_2 \end{bmatrix} \quad (1)$$

or

$$\bar{\mathbf{Z}} \cdot \mathbf{a} = \mathbf{v}, \quad (2)$$

where \mathbf{a}_J and \mathbf{a}_M are the coefficient vectors of the basis functions expanding the electric and magnetic currents, respectively, and $\mathbf{v}_{1,2}$ represent excitation vectors obtained by testing the incident fields. Iterative solutions of the resulting dense systems become feasible with the multilevel fast multipole algorithm (MLFMA) [4], which performs a matrix-vector multiplication of each block in (1) in $\mathcal{O}(n \log n)$ complexity for a block of size n . However, iterative solutions of such block-partitioned matrices often suffer from slow convergence, due to highly indefinite nature of resulting matrices. In Fig. 1, we depict the spectra of the $\bar{\mathbf{Z}}$ matrix and its dense matrix blocks in the complex plane, for a sphere problem with 0.5λ radius and a dielectric constant of 4.0. The matrices of both formulations are highly indefinite (the eigenvalues are distributed in the left half-plane), hence it is difficult to achieve convergence without preconditioning [10]. For CTF, there are many eigenvalues close to the origin, which makes the convergence of CTF more difficult than JMCFIE [5]. Hence, effective preconditioners should be applied to these systems in order to increase robustness and efficiency.

This work was supported by the Scientific and Technical Research Council of Turkey (TUBITAK) under Research Grant 105E172, by the Turkish Academy of Sciences in the framework of the Young Scientist Award Program (LG/TUBA-GEBIP/2002-1-12), and by contracts from ASELSAN and SSM.

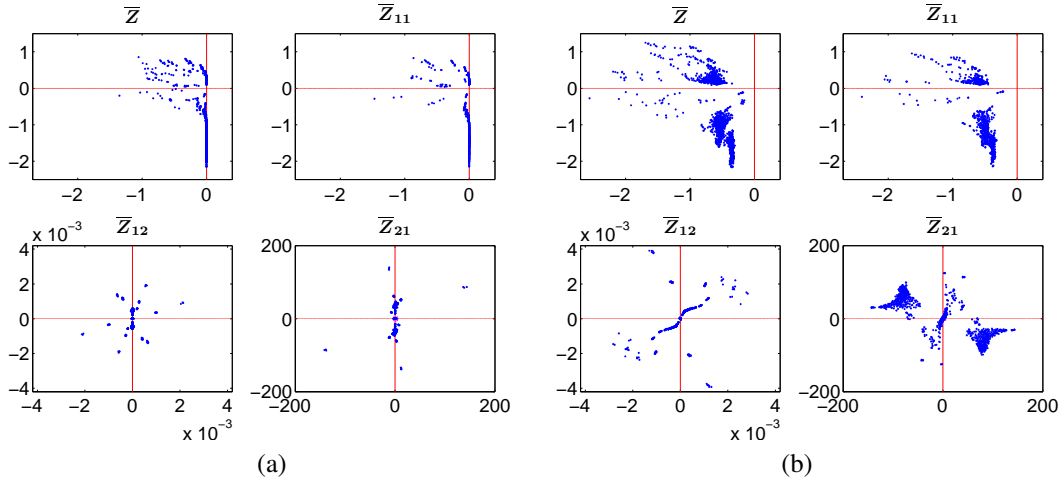


Fig. 1. The spectra of the system matrix and its blocks for (a) CTF and (b) JMCFIE on a sphere problem with 1,860 unknowns. The inside of the sphere has a dielectric constant of 4.0. Note that $\bar{Z}_{11} = \bar{Z}_{22}$ for these two formulations.

2. BLOCK PRECONDITIONERS FOR DIELECTRIC FORMULATIONS

Preconditioning refers to finding a suitable matrix \bar{M} that approximates the system matrix \bar{Z} , for which the solution of the system

$$\bar{M} \cdot \mathbf{u} = \mathbf{b} \quad (3)$$

is cheaper compared to the solution of the original system (2). Given the input vector \mathbf{b} , the solution vector \mathbf{u} is required in each step of the iterative solver. In this way, instead of the original system, one of the two preconditioned systems

$$\bar{M}^{-1} \cdot \bar{Z} \cdot \mathbf{a} = \bar{M}^{-1} \cdot \mathbf{v} \quad (4)$$

or

$$(\bar{Z} \cdot \bar{M}^{-1}) \cdot (\bar{M} \cdot \mathbf{a}) = \mathbf{v} \quad (5)$$

can be solved, for left or right preconditioning, respectively. The better the preconditioner \bar{M} approximates the matrix \bar{Z} , the faster the convergence is. However, better approximation comes with higher construction and application costs. Hence, a balance should be struck between the approximation level and the efficiency, so that the matrix system can be solved rapidly and reliably.

MLFMA decomposes the system matrix into its far-field and near-field components as

$$\begin{bmatrix} \bar{Z}_{11} & \bar{Z}_{12} \\ \bar{Z}_{21} & \bar{Z}_{22} \end{bmatrix} = \begin{bmatrix} \bar{Z}_{11}^{NF} & \bar{Z}_{12}^{NF} \\ \bar{Z}_{21}^{NF} & \bar{Z}_{22}^{NF} \end{bmatrix} + \begin{bmatrix} \bar{Z}_{11}^{FF} & \bar{Z}_{12}^{FF} \\ \bar{Z}_{21}^{FF} & \bar{Z}_{22}^{FF} \end{bmatrix} \quad (6)$$

or

$$\bar{Z} = \bar{Z}^{NF} + \bar{Z}^{FF}, \quad (7)$$

where the far-field matrix \bar{Z}^{FF} is not stored in the memory and the application of \bar{Z}^{FF} to a vector is computed on the fly. Hence, we use the near-field matrix for preconditioning, *i.e.*, $\bar{M} = \bar{Z}^{NF}$. For the solution of the system (3), the Schur complement reduction method is used [10]. This method reduces the solution of the block-partitioned system

$$\begin{bmatrix} \bar{Z}_{11}^{NF} & \bar{Z}_{12}^{NF} \\ \bar{Z}_{21}^{NF} & \bar{Z}_{22}^{NF} \end{bmatrix} \cdot \begin{bmatrix} \mathbf{x} \\ \mathbf{y} \end{bmatrix} = \begin{bmatrix} \mathbf{f} \\ \mathbf{g} \end{bmatrix} \quad (8)$$

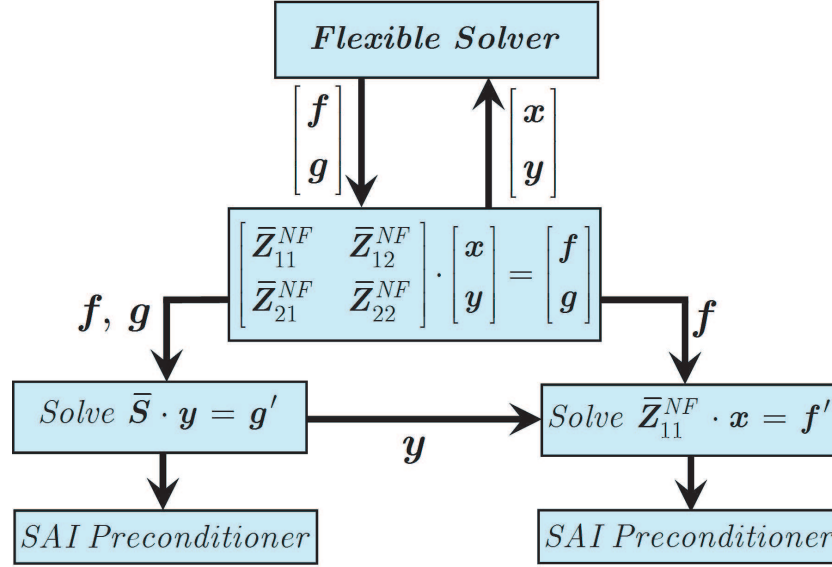


Fig. 2. Illustration of the application of IBP in a step of an iterative solver.

into the solutions of

$$\bar{\mathbf{Z}}_{11}^{NF} \cdot \mathbf{x} = \mathbf{f}' \quad (9)$$

and

$$\bar{\mathbf{S}} \cdot \mathbf{y} = \mathbf{g}', \quad (10)$$

where

$$\mathbf{f}' = \mathbf{f} - \bar{\mathbf{Z}}_{12}^{NF} \cdot \mathbf{y}, \quad (11)$$

$$\bar{\mathbf{S}} = \bar{\mathbf{Z}}_{22}^{NF} - \bar{\mathbf{Z}}_{21}^{NF} \cdot (\bar{\mathbf{Z}}_{11}^{NF})^{-1} \cdot \bar{\mathbf{Z}}_{12}^{NF} \quad (12)$$

is the Schur complement matrix, and

$$\mathbf{g}' = \mathbf{g} - \bar{\mathbf{Z}}_{21}^{NF} \cdot (\bar{\mathbf{Z}}_{11}^{NF})^{-1} \cdot \mathbf{f}. \quad (13)$$

Since the inversion of the sparse matrix $\bar{\mathbf{Z}}_{11}^{NF}$ is unfeasible, we approximate the inverse of $\bar{\mathbf{Z}}_{11}^{NF}$ with a sparse approximate inverse (SAI) of $\bar{\mathbf{Z}}_{11}^{NF}$ [8] in Eqs. (12) and (13). Then, solutions of (9) and (10) are approximated by a few iterations of the generalized minimal residual method (GMRES) solver. We call these preconditioning solutions inner solutions and the preconditioning scheme the iterative block preconditioner (IBP). Note that we do not need to compute and store the Schur complement matrix $\bar{\mathbf{S}}$; we only have to provide the application of $\bar{\mathbf{S}}$ to a vector in each step of the inner iterative solver of (10).

However, there is no guarantee that the solutions of these systems will be acquired fast enough. An efficient way to accelerate the convergence of these solutions is to use the available SAI of $\bar{\mathbf{Z}}_{11}^{NF}$ as a preconditioner for (9) and (10). We note that for CTF and JMCFIE, $\bar{\mathbf{Z}}_{11}^{NF} = \bar{\mathbf{Z}}_{22}^{NF}$, hence SAI of $\bar{\mathbf{Z}}_{11}^{NF}$ serves as a useful preconditioner for (10), assuming that $\bar{\mathbf{Z}}_{22}^{NF}$ is the dominant term in the Schur complement matrix. The application of IBP in a step of an iterative solver is illustrated in Fig. 2. Since IBP requires the solution of two systems for each iterative step, we need to use a flexible solver for the solution of (1) [6].

In Table 1, we evaluate the performance of the SAI preconditioner for the solutions of (9) and (10), where we compare the number of iterations obtained with the SAI-preconditioner and the

Table 1. Number of iterations of the systems in (9) and (10) for the sphere problem.

Number of Unknowns	CTF				JMCFIE			
	$\overline{\mathbf{Z}}_{11}^{NF} \cdot \mathbf{x} = \mathbf{f}'$		$\overline{\mathbf{S}} \cdot \mathbf{y} = \mathbf{g}'$		$\overline{\mathbf{Z}}_{11}^{NF} \cdot \mathbf{x} = \mathbf{f}'$		$\overline{\mathbf{S}} \cdot \mathbf{y} = \mathbf{g}'$	
	No PC	SAI	No PC	SAI	No PC	SAI	No PC	SAI
1,860	167	9	166	10	38	7	40	10
7,446	195	10	193	10	37	6	40	10
29,742	217	10	213	10	38	6	43	9
65,724	243	10	238	9	39	6	44	9
264,006	294	10	282	9	41	6	45	9

no-preconditioner (No PC) cases for 10^{-6} residual error. For both formulations, we observe that SAI is very successful and decreases the iteration counts drastically. Furthermore, contrary to the the no-preconditioner case, number of iterations does not increase for the SAI preconditioner as the number of unknowns increase. Hence, the use of SAI in this context significantly increases the performance of IBP.

3. RESULTS

The numerical experiments are carried out in a server with two Intel Xeon 5355 CPU and 16 GB of RAM. We use flexible GMRES with no restart as the solver. We note that the solutions of dielectric problems require many more matrix-vector multiplications with other nonsymmetric solvers, such as the biconjugate gradient stabilized (BiCGStab) method [9]. Iterations are performed until the norm of the initial residual is reduced by 10^{-3} . This error level is practical and in accordance with the error performed in MLFMA. Zero initial guess and right preconditioning are used in all solutions. RHSs are determined by plane wave excitations.

We demonstrate the performance of IBP on a sphere and a lens [2] with inner dielectric constants of, 4.0 and 12.0, respectively, as shown in Fig. 3.

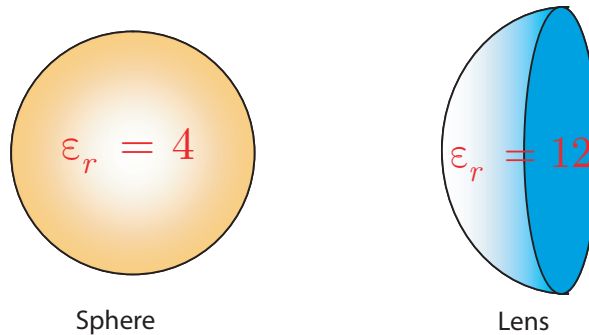


Fig. 3. Sphere and lens problems that are used in the experiments.

3.1 Selection of the Inner Stopping Criteria

A critical issue for the performance of IBP is the selection of the stopping tolerances for (9) and (10). The accuracy of these inner solves should be optimized to minimize the overall solution time. For this purpose, in Fig. 4, we analyze the convergence behaviour of SAI-preconditioned solutions for the sphere problem with 264,006 unknowns and for the lens problem with 158,286 unknowns. Note that for both formulations, only two iterations suffice to obtain a 0.1 residual error. However, for the lens problem, which has a higher dielectric constant than that of sphere,

the solution of the Schur system (10) requires more iterations to reduce the norm of the residual to 10^{-3} . Hence, we set our inner stopping criteria as one order residual drop with a maximum of three iterations. The results of the experiments show that with such a relaxed stopping criteria we achieve very strong preconditioners.

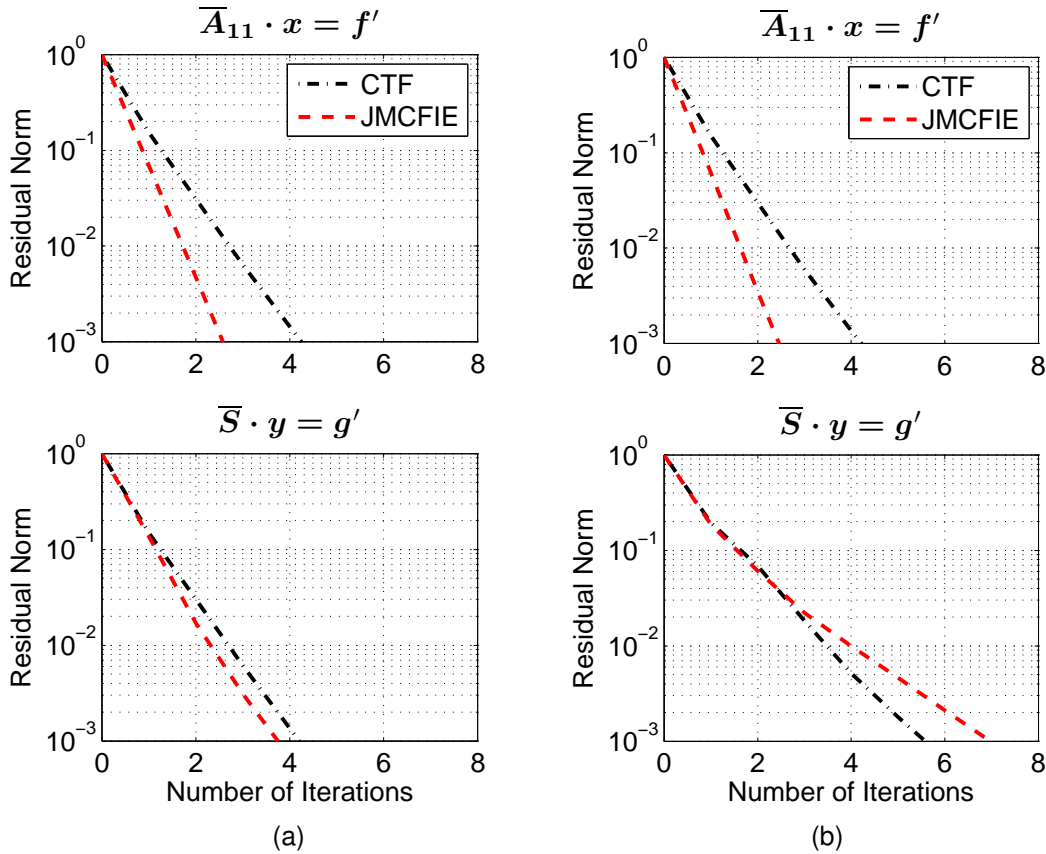


Fig. 4. SAI-preconditioned residual plots of inner solutions for (a) sphere and (b) lens problems.

3.2 Sphere Results

In Table 2, we show the solution frequencies and corresponding number of unknowns for the sphere problem. We use sphere problem since the accuracy of the solutions can be evaluated by comparing them with analytical solutions. In Fig.5, we show the iteration counts and in Fig. 6 we show the solution times for these problems. In [9], a four-partition block-diagonal preconditioner (4PBDP) has been proposed for the solution of dielectric problems, which use the self interactions of the lowest-level clusters MLFMA. However, for CTF, this preconditioner decelerates the convergence and increases the number of iterations, hence we do not include it in CTF solutions. We summarize our observations about the sphere solutions as follows:

- When a strong preconditioner is not used for CTF, even though we use the robust FGMRES solver, the iteration counts grow rapidly as the problem sizes get larger. Even though iteration counts are less for JMCFIE compared to CTF, for problems having larger than 100,000 unknowns iteration counts get larger also for JMCFIE. Hence, JMCFIE solutions can still benefit from a strong preconditioner. We also note that, without a preconditioner, it becomes even more difficult to attain convergence of these formulations with other non-optimal but less memory-hungry solvers, such as BiCGStab.

- For CTF, convergence is attained at least four times faster with IBP compared to the no-preconditioning case. For JMCFIE, IBP provides convergence three times faster compared to the no-preconditioning case, and two times faster compared to 4PBDP.
- For the sphere problem, the solution times of CTF problems become close to those of JMCFIE. Since CTF requires less memory and produces better accuracy [9], it may be preferable to JMCFIE for sphere solutions when accelerated by IBP.

Table 2. Information about sphere problems.

Problem	Frequency (GHz)	Size (λ)	MLFMA Levels	Number of Unknowns
S1	0.5	1	3	1,860
S2	1.0	2	4	7,446
S3	2.0	4	6	29,742
S4	3.0	6	6	65,724
S5	6.0	12	7	264,006
S6	7.5	15	7	412,998
S7	8.5	17	8	540,450

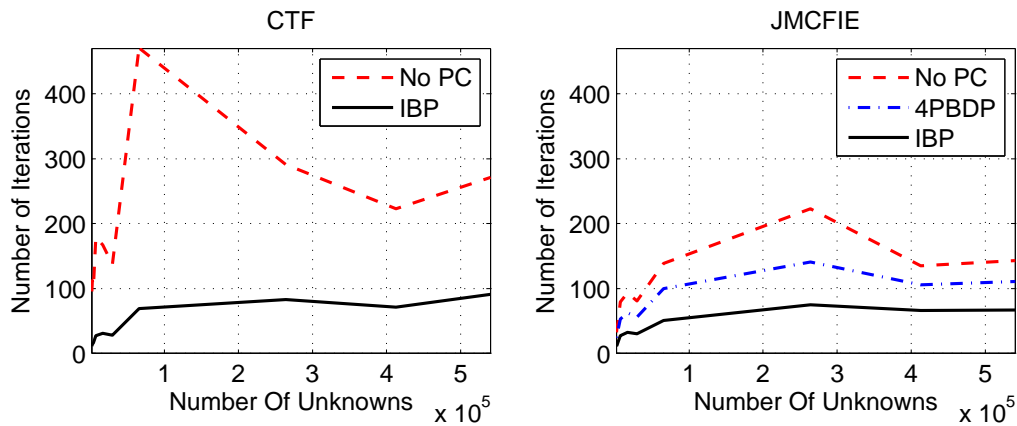


Fig. 5. Number of iterations of the sphere problem for CTF and JMCFIE.

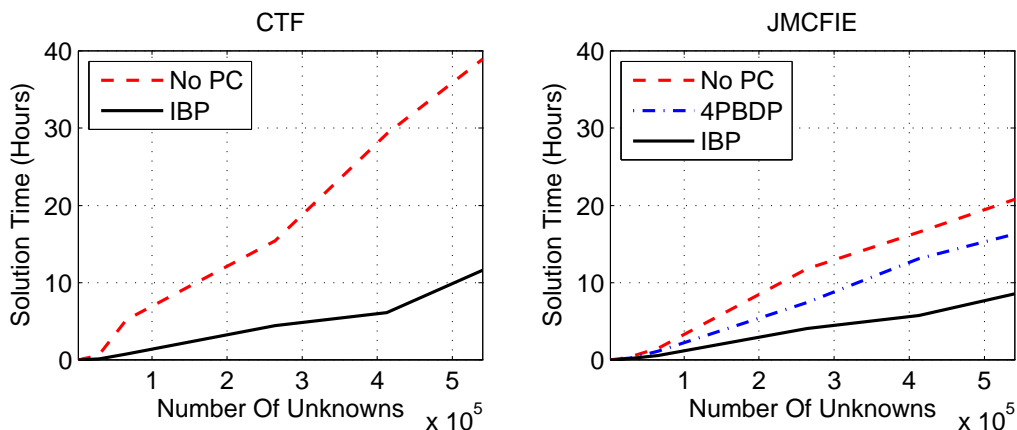


Fig. 6. Solution times of the sphere problem for CTF and JMCFIE.

3.3 Lens Results

For radiometric remote sensing applications, delicate simulations of dielectric lenses are required for a wide spectrum beginning from 30 GHz [2]. In this section, we analyze preconditioned iterative solutions of this important problem. We solve problems from 30 GHz to 120 GHz as shown in Table 3. The inner dielectric constant of the hemisphere is 12.0. Note that the solution of the Schur system becomes more difficult as the inner dielectric constant is increased, as shown in Fig. 4-(b).

Table 3. Information about lens problems.

Problem	Frequency (GHz)	Size (λ)	MLFMA Levels	Number of Unknowns
L1	30	2.5	6	38,466
L2	60	5.0	7	158,286
L3	90	7.5	7	353,646
L4	120	10.0	8	632,172

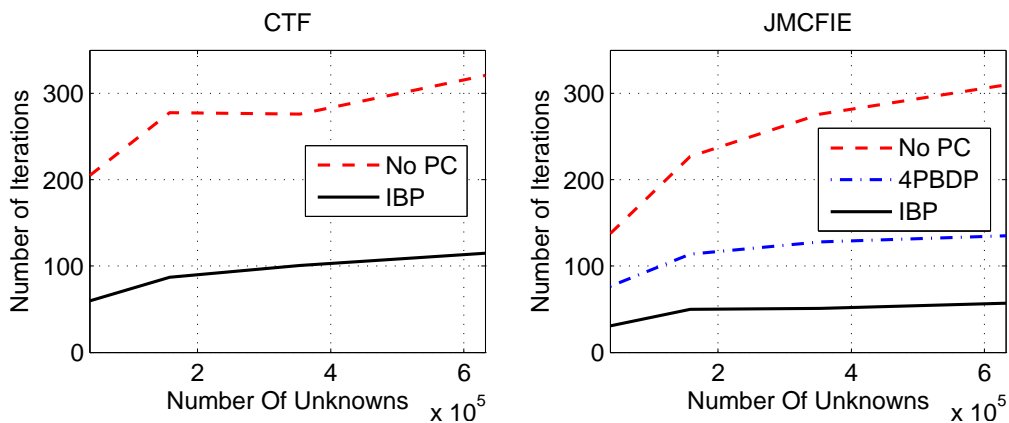


Fig. 7. Number of iterations of the lens problem for CTF and JMCFIE.

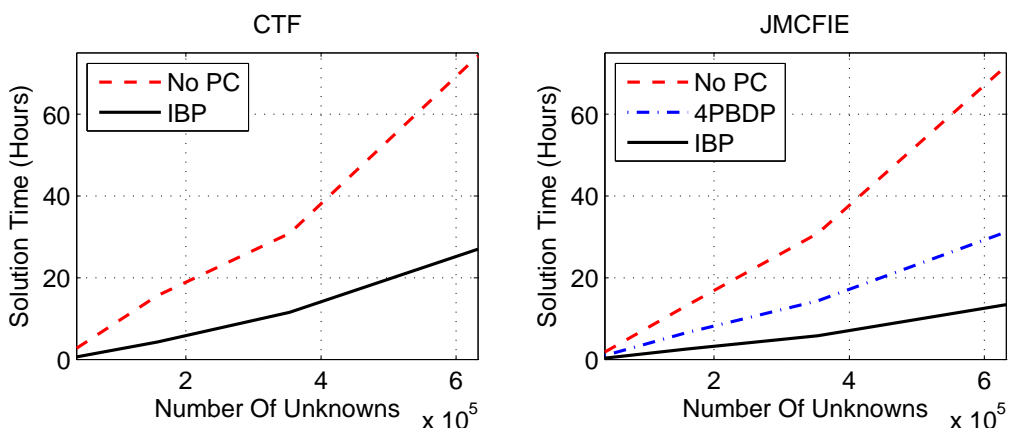


Fig. 8. Solution times of the lens problem for CTF and JMCFIE.

In Figs. 7 and 8, we depict the iteration counts and solution times, respectively. We summarize

our comments on the solutions of the lens problem as follows:

- We see that particularly for JMCIE, the iteration counts are larger than the sphere problem if preconditioner is not used. Hence, preconditioning of CTF and JMCIE becomes more critical for real-life problems having high inner dielectric constants.
- CTF solves the problems three times faster with respect to the no-preconditioning case. The solutions of CTF with IBP are as fast as those of JMCIE with 4PBDP.
- JMCIE solution times has been significantly reduced by IBP for the lens problem. We see that solutions are obtained 5-6 times faster with respect to no preconditioner and 2.5-3 times faster with respect to 4PBDP. JMCIE with IBP provides fastest solutions for the lens problem.

4. CONCLUSION

In this work, we propose an efficient block preconditioner generated from the near-field matrix of MLFMA to accelerate the convergence of the two common dielectric formulations. We show how to optimize the inner solutions so that maximum efficiency is obtained. Both of the formulations CTF and JMCIE highly benefit from IBP. For the sphere problem with an inner dielectric constant of 4.0, CTF solutions can be obtained as fast as those of JMCIE when IBP is utilized. For the lens problem, however, when accelerated by IBP, JMCIE provides solutions faster than CTF. For both problems, solution times are significantly reduced by IBP compared to both no-preconditioner case and previously proposed 4PBDP.

REFERENCES

- [1] Loschialpo P., D. W. Forester, and J. Schelleng, "Anomalous transmission through near unit index contrast dielectric photonic crystals," *J. Appl. Phys.*, Vol. 86, No. 10, 5342–5347, 1999.
- [2] Pavacic A. P., D. Llorens del Rio, J. R. Mosig, and G. V. Eleftheriades, "Three-dimensional ray-tracing to model internal reflections in off-axis lens antennas," *IEEE Trans. Antennas Propagat.*, Vol. 54, 604–612, 2006.
- [3] Lloyd T. W., J. M. Song, and M. Yang, "Numerical Study of Surface Integral Formulations for Low-Contrast Objects," *IEEE Antenna Wireless Propag. Lett.*, Vol. 4, 482–485, 2005.
- [4] Chew, W. C., J.M. Jin, E. Michielssen, and J. Song, *Fast and Efficient Algorithms in Computational Electromagnetics*. Boston, MA: Artech House, 2001.
- [5] Trefethen, L. N., and D.,III, Bau, *Numerical Linear Algebra*. SIAM, Philadelphia, USA, 1997.
- [6] Saad Y., *Iterative Methods for Sparse Linear Systems*, SIAM, Philadelphia, USA, second ed., 2003.
- [7] Malas, T. and L. Gürel, "Sequential and Parallel Preconditioners for Large-Scale Integral-Equation Problems," in *CEM'07 Computational Electromagnetics Workshop*, Izmir, Turkey, Aug. 2007, 35–43
- [8] Malas, T. and L. Gürel, "Accelerating the Multilevel Fast Multipole Algorithm with the Sparse-Approximate-Inverse (SAI) Preconditioning," *SIAM J. Sci. Comput.*, submitted for publication, Feb. 2008.
- [9] Ergül, Ö. and L. Gürel, "Comparison of integral-equation formulations for the fast and accurate solution of scattering problems involving dielectric objects with the multilevel fast multipole algorithm," *IEEE Trans. Antennas Propagat.*, accepted for publication, Sept. 2008.
- [10] Benzi, M., G. H. Golub, and J. Liesen, "Numerical solution of saddle point problems", *Acta Numer.*, vol. 14, 2005, 1–137.
- [11] Balay S., W. D. Gropp, L. C. McInnes, and B. F. Smith, "PETSc Users Manual," Tech. Report ANL-95/11 - Revision 2.1.5, Argonne National Laboratory, 2004.

SECTION 7

- 7.1. Jianping Zheng and Kazuya Kobayashi, “*Diffraction by a Semi-Infinite Parallel-Plate Waveguide with Sinusoidal Corrugation: Combined Wiener-Hopf and Perturbation Analysis*” 7-1
- 7.2. Feray Hacıvelioğlu, Alinur Büyükaksoy and Gökhan Uzgören, “*Radiation characteristics of a coaxial waveguide with opposing dielectric filled grooves*” 7-3
- 7.3. Burak Polat, “*Approximate Boundary Conditions on an Arbitrary Penetrable Sheet*” 7-5

Diffraction by a Semi-Infinite Parallel-Plate Waveguide with Sinusoidal Corrugation: Combined Wiener-Hopf and Perturbation Analysis

Jianping Zheng¹ and Kazuya Kobayashi²

^{1,2}Department of Electrical, Electronic, and Communication Engineering, Chuo University
1-13-27 Kasuga, Bunkyo-ku, Tokyo 112-8551, Japan
Tel: +81-3-3817-1869, 1846 Fax: +81-3-3817-1847
¹zheng@kazuya.elect.chuo-u.ac.jp, ²kazuya@tamacc.chuo-u.ac.jp

The analysis of wave scattering by gratings and waveguides with periodic structures is important in electromagnetic theory and optics. Various analytical and numerical methods have been developed so far and the diffraction phenomena have been investigated for many kinds of periodic structures. However, there are only a few treatments of the diffraction by periodic structures using rigorous function-theoretic methods. Das Gupta [1] analyzed the plane wave diffraction by a half-plane with sinusoidal corrugation by means of the Wiener-Hopf technique together with a perturbation scheme. The analysis by Das Gupta has been generalized thereafter by Chakrabarti and Dowerah [2] for the analysis of the H -polarized plane wave diffraction by two parallel sinusoidal half-planes using the Wiener-Hopf technique. We have considered a finite sinusoidal grating as another important generalization and analyzed the plane wave diffraction by means of the Wiener-Hopf technique [3].

In this paper, we shall reconsider, from a mathematical point of view, the problem solved by Chakrabarti and Dowerah [2] for the H -polarized plane wave incidence, and analyze the E -polarized plane wave diffraction by a semi-infinite parallel-plate waveguide with sinusoidal corrugation using the Wiener-Hopf technique. The geometry of the problem is shown in Fig. 1, where ϕ^i is the incident field of E polarization. The surface of the waveguide plates is assumed to be infinitely thin, perfectly conducting, and uniform in the y -direction, being defined by $x = \pm b + h \sin mz (z < 0)$, where m and h are positive constants. Assuming that the corrugation amplitude $2h$ is small compared with the wavelength, the original problem can be approximately replaced by the problem of diffraction by a semi-infinite parallel-plate waveguide with impedance-type boundary conditions. Taking the Fourier transform of the Helmholtz equation and applying approximate boundary conditions in the transform domain, the problem is formulated in terms of the simultaneous Wiener-Hopf equations. The Wiener-Hopf equations are then solved via the factorization and decomposition procedure together with the perturbation scheme leading to the efficient zero- and first-order solutions. Numerical examples of the scattered far field are presented, and the scattering characteristics of the waveguide are discussed in detail. Main results of this paper were already presented elsewhere [4-6].

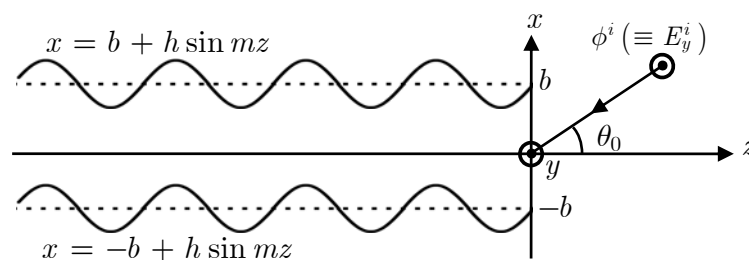


Fig. 1. Geometry of the problem.

REFERENCES

1. S. P. Das Gupta, "Diffraction by a corrugated half-plane," *Proc. Vib. Prob.*, vol. 3, pp. 413-424, 1970.
2. A. Chakrabarti and S. Dowerah, "Traveling waves in a parallel plate waveguide with periodic wall perturbations," *Can. J. Phys.*, vol. 62, pp. 271-284, 1984.
3. K. Kobayashi and T. Eizawa, "Plane wave diffraction by a finite sinusoidal grating," *IEICE Trans.*, vol. E74, pp. 2815-2826, 1991.
4. J. P. Zheng and K. Kobayashi, "Plane wave diffraction by two parallel, corrugated half-planes," *IEEJ Technical Report*, no. EMT-07-39, May 2007.
5. J. P. Zheng and K. Kobayashi, "Wiener-Hopf analysis of the plane wave diffraction by two parallel, corrugated half-planes," *Proc. 2007 URSI International Symposium on Electromagnetic theory (EMTS 2007)*, O11-32-6, July 2007.
6. J. P. Zheng and K. Kobayashi, "Plane wave diffraction by two parallel, corrugated half-planes: evaluation of the scattered field," *Proc. 2008 Progress In Electromagnetics Research Symposium (PIERS 2008 Hangzhou)*, p. 698, March 2008.

Radiation Characteristics of a Coaxial Waveguide with Opposing Dielectric Filled Grooves

Feray Haciveliolu, Alinur Büyükaksoy and Gökhan Uzgören

Not available at the time of publication

Approximate Boundary Conditions on an Arbitrary Penetrable Sheet

Burak Polat

Not available at the time of publication

SECTION 8

- 8.1. Ozlem Ozgun and Mustafa Kuzuoglu, “*Realization of Anisotropic Metamaterials via Coordinate Transformations*” 8-1
- 8.2. Yu. V. Shestopalov, Yu. G. Smirnov and V. V. Yakovlev, “*Development of Mathematical Methods for Reconstructing Complex Permittivity of a Scatterer in a Waveguide*” 8-11
- 8.3. Ali Eren Culhaoglu, Andrey Osipov and Peter Russer, “*Numerical analysis of focusing by a metamaterial lens*” 8-13

Realization of Anisotropic Metamaterials via Coordinate Transformations

Ozlem Ozgun^{1,2} and Mustafa Kuzuoglu²

¹Dept. of Electrical Engineering, Middle East Technical University, Northern Cyprus Campus,
Guzelyurt, Mersin 10, TURKEY

²Dept. of Electrical Engineering, Middle East Technical University,
06531, Ankara, TURKEY

Abstract – We present novel coordinate transformation techniques, which are utilized by anisotropic metamaterials (AMMs), to control the propagation of electromagnetic fields in several surprising and useful applications. Material specifications of the AMMs are designed by using the form-invariance property of Maxwell's equations under coordinate transformations. We demonstrate the applications of the proposed techniques via several finite element simulations.

1. INTRODUCTION

Metamaterials have recently exhibited tremendous promise in the design of electromagnetic devices with new functionalities in various optical and microwave applications, due to their exotic constitutive parameters that do not exist in nature. The coordinate transformation technique provides an intuitive way of designing anisotropic metamaterials (AMM) to tune the electromagnetic fields in a desired manner. The most familiar application that utilizes this technique is the design of a cloaking device for obtaining electromagnetic invisibility [1]. Another application is the design of perfectly matched layers (PMLs), which are employed as artificial absorbers in mesh truncation of the finite methods [2]. The coordinate transformation approach is based on the fact that Maxwell's equations are form-invariant under coordinate transformations. Specifically, coordinate transformations yield spatially-varying anisotropic media, and the original forms of Maxwell's equations are still preserved in the transformed space.

In this study, we present novel coordinate transformation techniques in a wide range of electromagnetic applications. First, we will discuss a transformation technique for the purpose of “reshaping” objects in electromagnetic scattering. That is, if an object of certain shape is coated by a suitably-designed AMM layer, an observer located at an arbitrary point perceives this object as if it has a different shape. Second, we will introduce a coordinate transformation technique for “reshaping” waveguides. We will show that a waveguide, which is filled with AMM, acts as a different waveguide, whose cross-section is ‘reshaped’. Consequently, this technique can enable a waveguide to support electromagnetic wave propagation below the cutoff frequency, and thus, can be employed in waveguide miniaturization and transitions. Third, we will propose an interesting simulation tool for efficient solution of low-frequency scattering problems via AMMs, and show that various low-frequency scattering problems involving arbitrarily-shaped ‘small’ objects can efficiently be solved by using only a single

mesh and by modifying only the constitutive parameters inside the AMM layer. Finally, we will present a technique to compress the excessive white space (i.e. free-space) inside the computational domain of the finite methods for solving radiation/scattering problems. This technique can be used as a numerical simulation tool to reduce the number of unknowns, especially in high-frequency applications, wherein a finite method requires an electrically-large computational domain. We demonstrate the proposed techniques via representative examples that are simulated by the Finite Element Method.

2. Form-Invariance of Maxwell's Equations under Coordinate Transformations

A general coordinate transformation ($\vec{r} \rightarrow \tilde{\vec{r}} = T(\vec{r})$ and $T: \Omega \rightarrow \tilde{\Omega}$) yields a spatially-varying anisotropic material, in which the original forms of Maxwell's equations are still preserved in the transformed space. Specifically, Maxwell's equations are form-invariant under space transformations, and a general coordinate transformation leads to the following expressions for the permittivity and permeability tensors:

$$\bar{\bar{\epsilon}} = \epsilon \bar{\bar{\Lambda}} \quad \bar{\bar{\mu}} = \mu \bar{\bar{\Lambda}} \quad \bar{\bar{\Lambda}} = (\det \bar{\bar{J}}) (\bar{\bar{J}}^T \cdot \bar{\bar{J}})^{-1} \quad (1)$$

where $\bar{\bar{J}}$ is the Jacobian tensor defined in Cartesian coordinates as $\bar{\bar{J}} = \partial(\tilde{x}, \tilde{y}, \tilde{z}) / \partial(x, y, z)$. If the original medium is an arbitrary anisotropic medium with parameters $(\bar{\bar{\epsilon}}', \bar{\bar{\mu}}')$, then the parameters of the metamaterial in the transformed space are obtained as follows:

$$\bar{\bar{\epsilon}} = (\bar{\bar{J}}^{-1})^T \cdot \bar{\bar{\epsilon}}' \cdot (\bar{\bar{J}}^{-1}) / \det(\bar{\bar{J}}^{-1}) \quad \bar{\bar{\mu}} = (\bar{\bar{J}}^{-1})^T \cdot \bar{\bar{\mu}}' \cdot (\bar{\bar{J}}^{-1}) / \det(\bar{\bar{J}}^{-1}) \quad (2)$$

3. Reshaping Objects in Electromagnetic Scattering

We introduce a coordinate transformation technique to “reshape” perfectly conducting objects in electromagnetic scattering [3]. If an object of an arbitrary shape is coated by an AMM layer, which is designed by a suitable coordinate transformation, an observer at an arbitrary location views this object as if it has a different shape. Thus, this phenomenon can be called ‘reshaping’ or ‘metamorphosis’, only in terms of the perceptual abilities of the observer. This technique is basically a generalization of the cloaking approach. That is, the cloak transforms an object to a point, and thus, makes this object invisible. On the other hand, in the reshaping method, the AMM layer transforms an object to another object with reference to an observer. We illustrate the technique in Fig. 1. In order to design the AMM layer, each point P inside the AMM layer (Ω_M) is mapped to \tilde{P} inside the transformed region $\tilde{\Omega} = \Omega \cup \Omega_M$. This mapping is defined as a coordinate transformation as follows:

$$\tilde{\vec{r}} = \frac{\|\vec{r}_M - \vec{r}_n\|}{\|\vec{r}_M - \vec{r}_o\|} (\vec{r} - \vec{r}_o) + \vec{r}_n \quad (3)$$

where \vec{r}_M , \vec{r}_o and \vec{r}_n are the position vectors of P_M , P_o and P_n . The unit vector \hat{a} is computed

emanating from a point inside the innermost domain, such as the center-of-mass point that can be determined as the origin, in the direction of the point P inside the AMM layer.

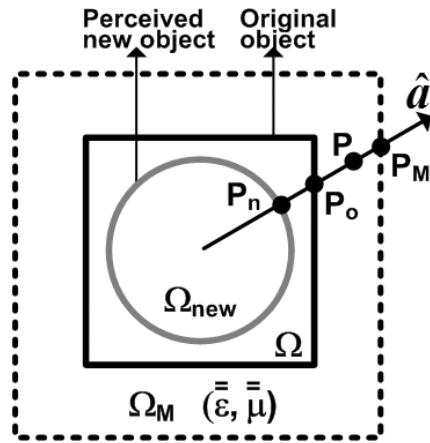


Figure 1. Reshaping scatterers via coordinate transformation.

4. Reshaping Waveguides

We introduce a coordinate transformation technique, which transforms the shape of a waveguide to another shape [4-5]. In other words, it enables a waveguide, which is filled by a suitably-designed AMM, to act as a different waveguide whose cross-section is ‘reshaped’. These two waveguides are equivalent and they support the same type of wave propagation, because they have identical cutoff frequencies (i.e., eigenvalues) and the fields (i.e., eigenvectors) inside these waveguides are inherently related to each other. A special consequence of this approach is that it can be employed in designing miniaturized waveguides, because it can render a waveguide to support electromagnetic wave propagation below the cutoff frequency. We illustrate the technique in Fig. 2. The AMM layer is designed by transforming each point P

inside Ω_M to \tilde{P} inside the transformed region $\tilde{\Omega} = \Omega \cup \Omega_M$

$$\tilde{r} = \frac{\|\tilde{r}_o\|}{\|r_e\|} \tilde{r} \tag{4}$$

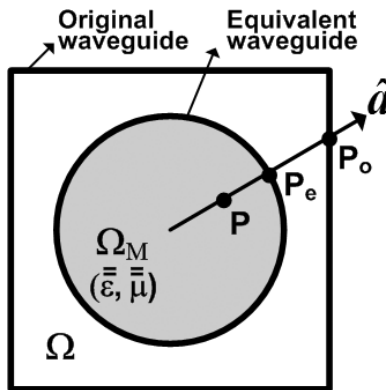


Figure 2. Reshaping waveguides via coordinate transformation.

5. Solution of Low-Frequency Scattering Problems

We present a simulation technique to solve efficiently low-frequency electromagnetic scattering problems by using coordinate transformations [6]. Accurate numerical solution of the low-frequency scattering problems in finite methods is still a challenging task because the mesh usually requires a large number of unknowns to define the fine sections of the electrically-small objects with high numerical precision (see Fig. 3(a)). In addition, in order to employ the mesh truncation techniques, such as PML or absorbing boundary condition (ABC), in scattering problems, the truncation boundary must be located sufficiently far away from the object to reduce spurious reflections. Therefore, this results in large number of unknowns inside the white-space that is not occupied by the object. However, in the new approach, we solve the equivalent problem by designing an AMM layer, which is located at an arbitrary distance from the object (see Fig. 3(b)). The equivalent problem contains both near- and far-field of the object. The equivalent problem transforms the original problem into a relatively high-frequency problem. An interesting feature of the equivalent problem is that the same mesh can be used for any arbitrarily-shaped ‘small’ object by simply changing the constitutive parameters of the AMM layer with respect to the geometry of that object. In this approach, the AMM layer is constructed at an arbitrary but sufficiently large distance from the ‘small’ object. Each point P inside the AMM layer (Ω_M) is mapped to \tilde{P} inside the transformed region $\tilde{\Omega} = \Omega \cup \Omega_M$ by using the following coordinate transformation:

$$\tilde{\vec{r}} = \frac{\|\vec{r}_a - \vec{r}_c\|}{\|\vec{r}_a - \vec{r}_b\|} (\vec{r} - \vec{r}_b) + \vec{r}_c \quad (5)$$

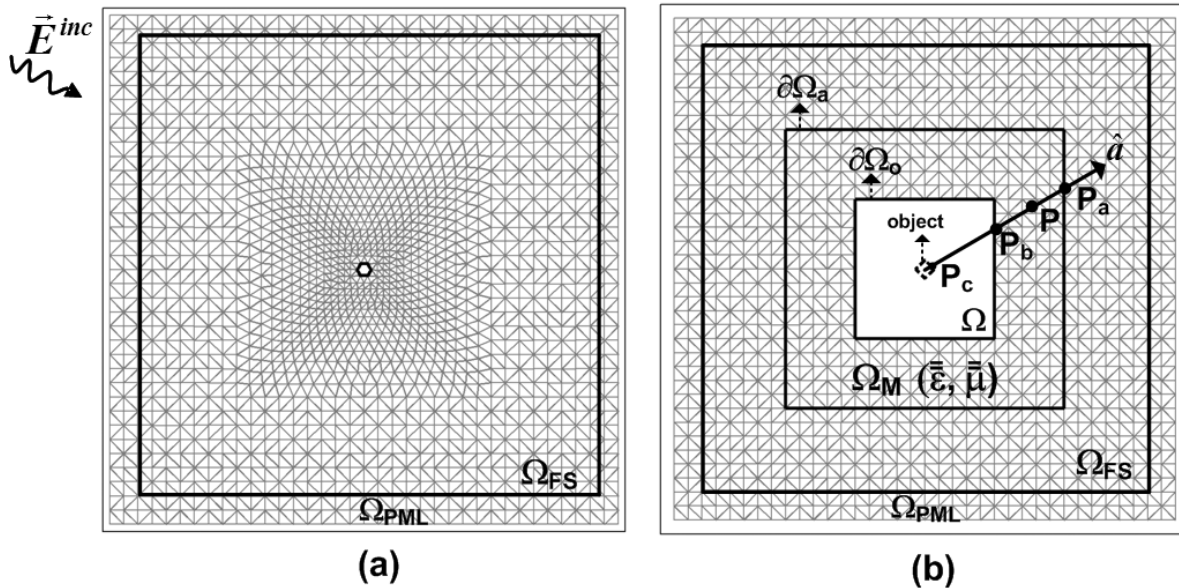


Figure 3. Low-frequency scattering problem: (a) Original problem, (b) Equivalent problem.

6. Spatial Domain Compression in Finite Methods

We present a new strategy, which compresses excessive white space in the computational domain of the finite methods by using AMM layers, and thus, eliminates the unknowns in this white space. In some problems involving an electrically-large non-convex object or multiple objects, the computational domain requires the employment of *excessive* white-space because it must be designed as convex over the object(s) to take into account the mutual couplings between different parts of the object(s). However, in this new technique, we design an AMM layer to reduce the number of unknowns by compressing the excessive white space. We define a special coordinate transformation to compress the excessive white space in such a way that electromagnetic waves are bended and guided inside the AMM layer, without altering the wave behavior in the remaining part of the computational domain. The technique is illustrated in Fig. 4, where an L-shaped object is illuminated by a plane-wave. The AMM layer is designed by mapping each point P inside the AMM layer to \tilde{P} inside the transformed region $\tilde{\Omega} = \Omega'_{FS} \cup \Omega'_{PML} \cup \Omega_M$ by using the following coordinate transformation:

$$\tilde{\vec{r}} = \frac{\|\vec{r}' - \vec{r}_b\|}{\|\vec{r}_a - \vec{r}_b\|} (\vec{r} - \vec{r}_b) + \vec{r}_b \quad (6)$$

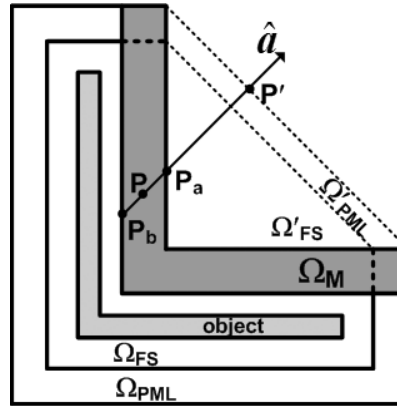


Figure 4. Domain compression: (a) Original problem, (b) Equivalent problem.

7. Finite Element Simulations

In order to illustrate the applicability of the proposed techniques, we now present the results of finite element simulations. In the first example, a square infinitely-long cylindrical scatterer is reshaped as a circular scatterer by means of an AMM layer. We plot the contours of the electric field inside the computational domain in Fig. 5. In the second example, a square scatterer is made invisible, as shown in Fig. 6.

Next, we reshape a square waveguide as a circular waveguide. We plot the patterns of the z -component of the electric (TM_z) fields in both original and equivalent waveguides for TM_{22} mode in Fig. 7(a). We also tabulate the cutoff wavenumbers for some selected modes in Table I. In addition, we consider the parallel-plate waveguide to demonstrate the coordinate transformation technique to simultaneously handle waveguide miniaturization and transitions, in Fig. 7(b).

Furthermore, we consider the low-frequency scattering problem where a plane wave, whose angle of incidence is 180° with respect to the x -axis, is incident to a circular cylinder whose radius is $\lambda/20$. We plot the field contours and RCS profiles in Fig. 8.

Finally, we deal with the domain compression technique. We consider a scattering problem, where a plane wave is incident to a ‘thin’ L-shaped cylinder, whose edge-length is 8λ . We plot the field contours and RCS profiles in Fig. 9.

8. CONCLUSIONS

We have presented new metamaterial design techniques by means of coordinate transformations, which are specially-tailored to various electromagnetic applications. We have shown that the coordinate transformation techniques yield spatially-varying anisotropic materials inside the transformed space, wherein the Maxwell’s equations are still satisfied in their original forms. We have numerically explored the functionality of all techniques in various configurations with the aid of finite element simulations.

(While this research was conducted, the first author was with the Dept. of Electrical Engineering, Middle East Technical University, 06531, Ankara, TURKEY)

REFERENCES

- [1] Pendry JB, Schurig D., and Smith DR, “Controlling electromagnetic fields,” *Science*, vol. 312, pp. 1780-1782, 2006.
- [2] Ozgun O., and Kuzuoglu M., “Non-Maxwellian locally-conformal PML absorbers for finite element mesh truncation,” *IEEE Trans. Antennas Propagat.*, vol. 55, no. 3, pp. 931-937, 2007.
- [3] Ozgun O., and Kuzuoglu M., “Electromagnetic metamorphosis: Reshaping scatterers via conformal anisotropic metamaterial coatings,” *Microwave Opt. Technol. Lett.*, vol. 49, no. 10, pp. 2386-2392, 2007.
- [4] Ozgun O., and Kuzuoglu M., “Utilization of anisotropic metamaterial layers in waveguide miniaturization and transitions,” *IEEE Microw. Wireless Comp. Lett.*, vol. 17, no. 11, pp. 754-756, 2007.
- [5] Ozgun O., and Kuzuoglu M., “Form-invariance of Maxwell’s equations in waveguide cross-section transformations,” *Electromagnetics*, 2008 (to appear).
- [6] Ozgun O., and Kuzuoglu M., “Efficient finite element solution of low-frequency scattering problems via anisotropic metamaterial layers,” *Microwave Opt. Technol. Lett.*, vol. 50, no. 3, pp. 639-646, 2008.

Table I. Cut-off wavenumbers for square-to-circular waveguide transformation.

Mode	Analytical	Original	Equivalent
TM ₁₁	2.2214	2.2216	2.2225
TM ₂₁ , TM ₁₂	3.5124	3.5130	3.5162
TM ₂₂	4.4429	4.4443	4.4523
TE ₁₀ , TE ₀₁	1.5708	1.5708	1.5720
TE ₁₁	2.2214	2.2216	2.2250
TE ₂₂	4.4429	4.4443	4.4571

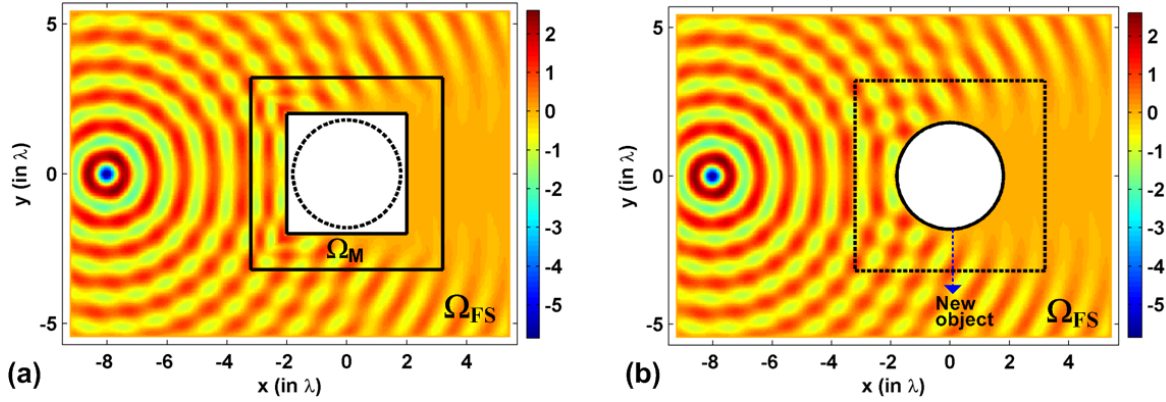


Figure 5. Electric field contours in reshaping a square scatterer as a circular scatterer: (a) Equivalent problem, (b) Original problem [Field values in Ω_{FS} are identical].

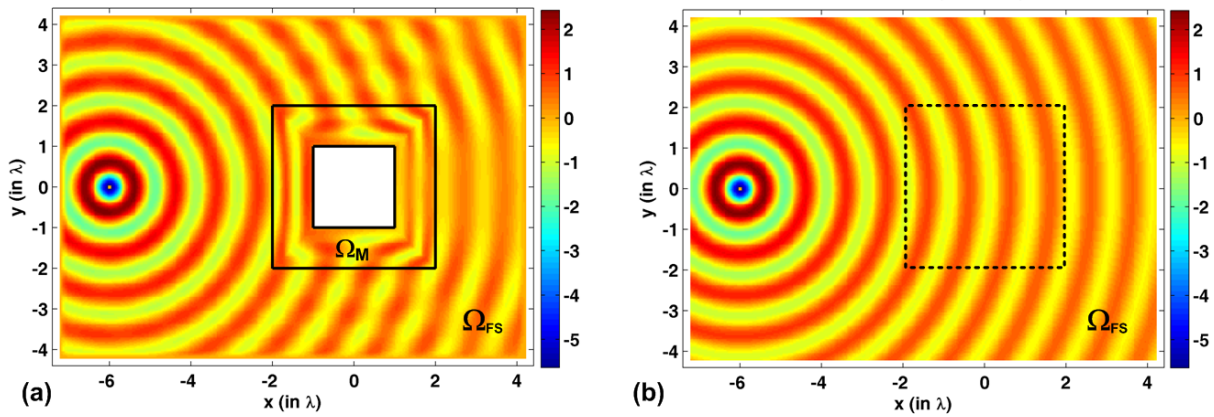


Figure 6. Electric field contours in making a square scatterer invisible: (a) Equivalent problem, (b) Original problem [Field values in Ω_{FS} are identical].

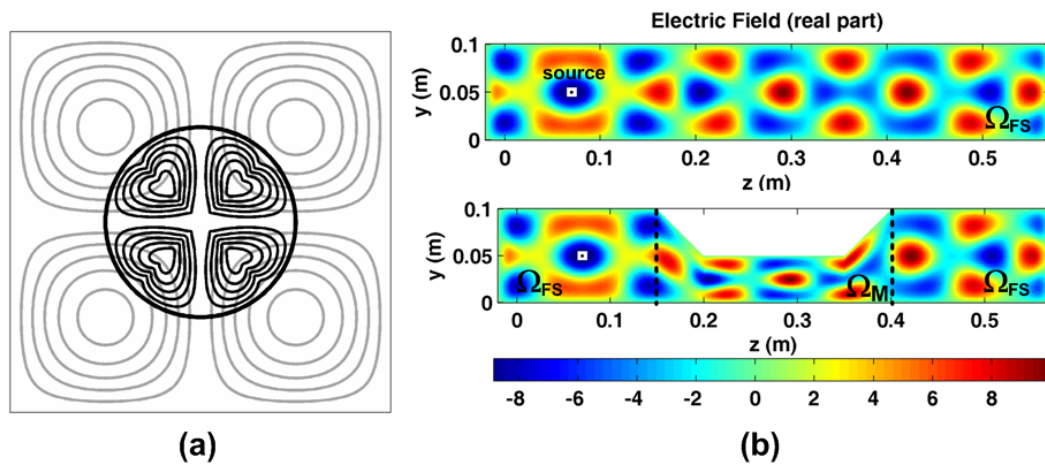


Figure 7. (a) Field patterns in reshaping a square waveguide as a circular waveguide [The *black* and *gray* patterns represent the fields in the equivalent and original waveguides, respectively], (b) Miniaturization in parallel-plate waveguides [Field values in Ω_{FS} are identical].

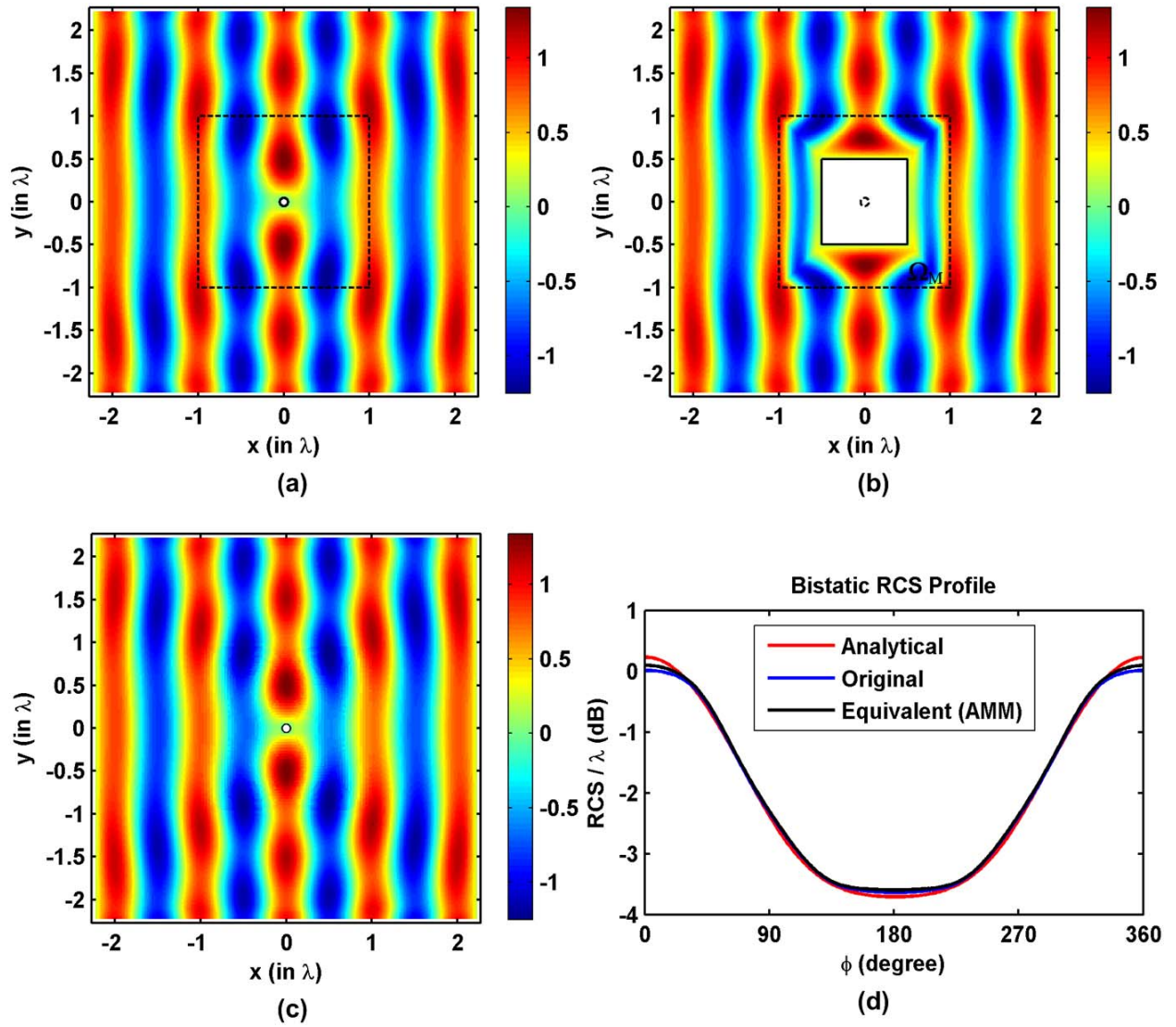


Figure 8. Finite element simulations for low-frequency scattering: (a) Field contour in original problem, (b) Field contour in equivalent problem, (c) Field contour in equivalent problem after transforming the field values, (d) Bistatic RCS profiles

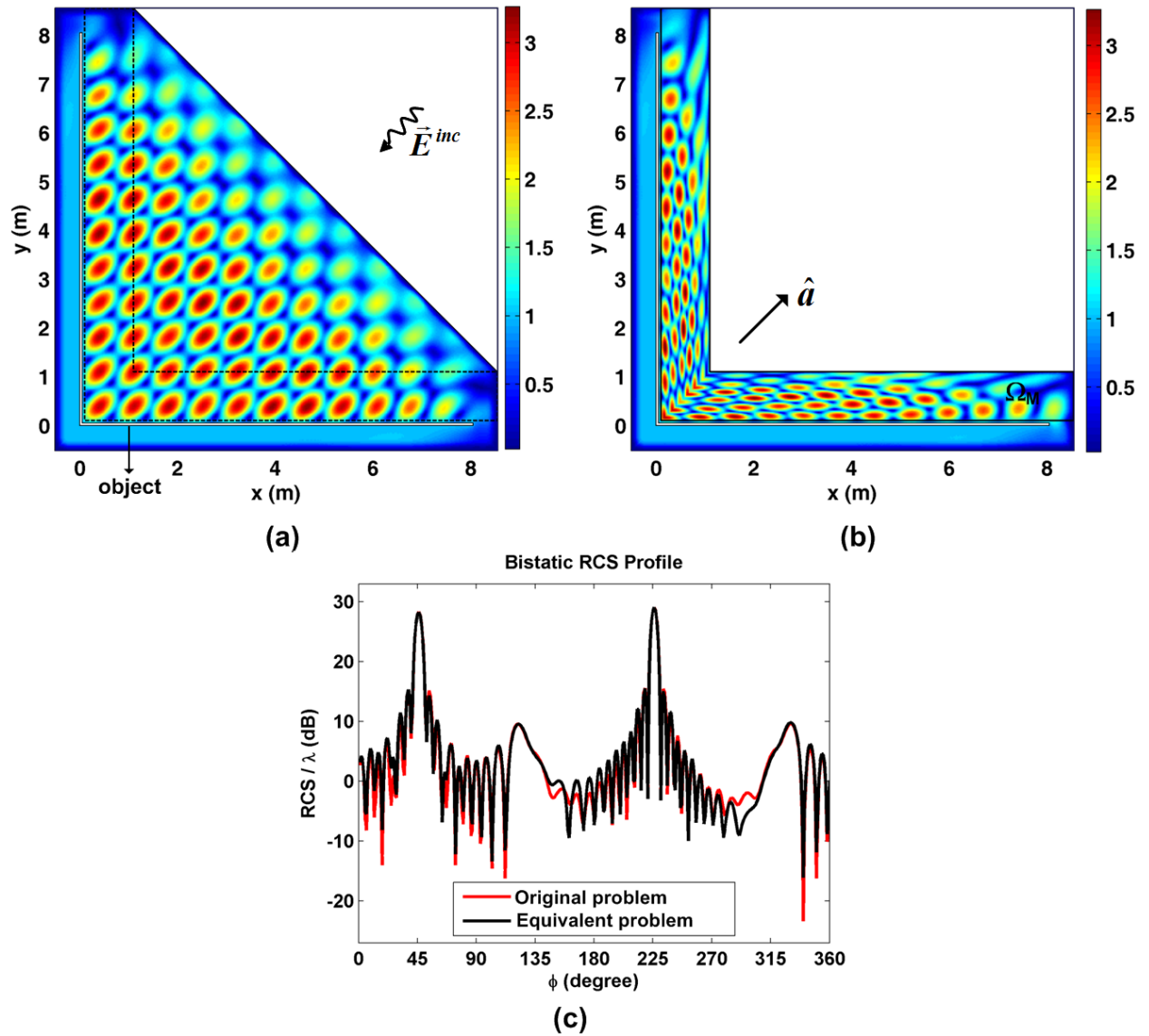


Figure 9. Finite element simulations for domain compression: (a) Field contour in original problem, (b) Field contour in equivalent problem, (c) Bistatic RCS profile.

Development of Mathematical Methods for Reconstructing Complex Permittivity of a Scatterer in a Waveguide

Yu. V. Shestopalov (Karlstad University, Karlstad, Sweden)

Yu. G. Smirnov (Penza State University, Penza, Russia)

V. V. Yakovlev (Worcester Polytechnic Institute, Worcester, MA USA)

Solution techniques for reconstructing permittivity of a scatterer in a waveguide have been recently given a substantial attention. The methods of reconstructing the scatterer's shape or its permittivity were developed in [1] for the cases when the obstacles are perfectly conducting or dielectric bodies in two- or three-dimensional space. The paper [2] suggests the technique for cylindrical scatterers whose cross sections are formed by the domains with infinite noncompact boundaries. However, when a dielectric body is situated in a waveguide, similar results concerning the unique solvability and efficient techniques for reconstructing permittivity or shape of the scatterer are not available. Foundations of the appropriate methods that can be used for solving direct and inverse boundary value problems for Maxwell's and Helmholtz equations associated with the wave propagation in waveguides with dielectric inclusions are elaborated in [3, 4]. In [5] it is shown that determination of complex permittivity of a body in a parallel-plane waveguide is unique when the permittivity values are reconstructed from the related reflection and transmission coefficients. The purpose of this work is to develop the methods set forth in [3-5] for parallel-plane waveguides and in [6-9] for three-dimensional waveguides in order to study the inverse problem for a dielectric inclusion in a three-dimensional waveguide. The analysis of the direct scattering problem is based on the volume singular integral equation (VSIE) method [5-7]. The first problem that may lead to creating an efficient algorithm for reconstructing the permittivity of an inclusion is the electromagnetic wave diffraction in a three-dimensional waveguide of rectangular cross section containing a dielectric body in the form of a parallelepiped. For a body of coordinate shape it is possible to obtain explicit results, including explicit asymptotic representations for the field and formulas for transmission and reflection coefficients, using the Green's functions of rectangular waveguides [3-5] and the approach employing VSIE method [7-9]. Numerical solution of the problem under study is performed on the basis of the VSIE method [7].

1. Colton, D. and R. Kress, *Inverse Acoustic and Electromagnetic Scattering Theory*, Springer, Berlin (1998).
2. Shestopalov, Yu. and V. Lozhechko, Direct and inverse problems of the wave diffraction by screens with arbitrary finite inhomogeneities, *J. Inverse Ill-Posed Problems*, **11**, 643-653 (2003).
3. Shestopalov, V. and Yu. Sirenko, *Dynamical Theory of Gratings*, Naukova Dumka, Kiev (1989).
4. Shestopalov, V. and Yu. Shestopalov, *Spectral Theory and Excitation of Open Structures*, P. Peregrinus, London (1996).
5. Shestopalov, Yu., and V. Yakovlev, Uniqueness of complex permittivity reconstruction in a parallel-plane waveguide, *Radio Science*, **42**, 6, RS6S20 (2007).
6. Samokhin, A., *Integral Equations and Iteration Methods in Electromagnetic Scattering*, Y. Shestopalov, Ed., VSP Int. Science Publishers, Utrecht, Boston, Köln, Tokyo (2001).
7. Smirnov Yu., and A. Tsupak, Analysis of Electromagnetic Diffraction Problem on a Dielectric Body by the Method of Volume Singular Integral Equation, *Zh. Vych. Matem. Matem. Fis.*, **44**, 2264-2279 (2004).
8. Smirnov, Yu. and Yu. Shestopalov, The diffraction in a class of unbounded domains connected through a hole, *Math. Meth. App. Sci.*, **26**, 1363-1389 (2003).
9. Kobayashi, K, Yu. Smirnov, and Yu. Shestopalov, Investigation of electromagnetic diffraction by a dielectric body in a waveguide using the method of volume singular integral equations, *Proc. Progress in Electromagnetics Research Symposium, Hangzhou, China, March 24--28, 2008*, 4 p.

Numerical analysis of focusing by a metamaterial lens

Ali Eren Culhaoglu¹, Andrey Osipov¹ and Peter Russer²

¹ Microwaves and Radar Institute, German Aerospace Center
82234 Wessling Germany
email: Ali.Culhaoglu@dlr.de

² Institute for High Frequency Engineering, Technische Universität München
Arcisstrasse 21, 80333 Munich Germany
email: russer@tum.de

Abstract Over the last several years there has been a surge of interest in artificial materials because of their potential to expand the range of electromagnetic properties in materials. The so called metamaterials, also known as left-handed (LHM) or double-negative (DNG) materials with negative permittivity and permeability have attracted growing interest. An important application area is the realization of flat superlenses with imaging properties beyond that of conventional lenses. This work investigates the focusing properties of a lossless planar DNG slab with a relative permittivity and permeability both approaching the value -1. The relation between the imaging quality and the material parameters is examined both analytically and numerically. Results obtained from numerical simulations via the transmission line matrix method are compared to the analytical solution.

1. Introduction

Incident and emerging waves from a DNG slab will undergo negative refraction [1]. As a consequence a slab with finite thickness d and material parameters $\varepsilon_r = \mu_r = -1$ (refractive index $n = \sqrt{\varepsilon_r \mu_r} = -1$) focuses waves emitted from a point source located at a distance l in front of the slab to a point at a distance of $d - l$ behind the slab [2, 3]. As seen in Fig. 1(a) the waves emitted from a point source are focused inside and outside the slab due to negative refraction at the slab interfaces. Furthermore modes with large wavenumbers excite surface waves along the slab interfaces restoring the evanescent field which decays exponentially away from the source [4]. Therefore a transversely unbounded slab is capable of focusing every mode of the emitted spectrum from a point source reproducing a perfect image. On the contrary the focusing quality in a conventional lens is largely determined by its curvature and aperture size which results in a diffraction limited pattern [5]. The impact of the lateral extension of a finite sized DNG slab (i.e. having finite aperture) onto its imaging quality has already been investigated numerically in [6]. As it will be shown in the following sections, the electromagnetic field behavior at the image plane is largely determined by resonant peaks occurring in the transmission coefficient of the slab. The effect of the deviation from the ideal material parameters of $\varepsilon_r = \mu_r = -1$ onto the imaging quality will be investigated by the method described in [7]. Thereby a slight perturbation σ is applied to ε_r and μ_r whilst retaining the refractive index of $n = -1$ and considering the problem in the limiting case as $\sigma \rightarrow 0$. Finally numerical simulations, based on the modified transmission line matrix (TLM) scheme are carried out and the results are compared to the analytical solution.

2. Analytical Solution

We consider the setup given in Fig. 1(a). Since the configuration is unbounded in the transversal direction circular-cylindrical coordinates (ρ, z) will be used. A hertzian dipole

$$J(\rho, z) = I_0 \delta(\rho) \delta(z - z') \hat{\mathbf{z}} \quad (1)$$

is placed on the z -axis at $z' = z_0 < 0$ in front of a DNG slab with refractive index $n = -\sqrt{\epsilon_r \mu_r}$ and thickness d . The impedances and spectral wavenumbers along the optical axis (z -axis) are

$$k_z^{air} = \sqrt{k_0^2 - k_t^2} \quad \text{and} \quad Z_0 = \frac{k_z^{air}}{\omega \epsilon_0}, \quad (2)$$

in free space and

$$k_z^{slab} = \sqrt{n^2 k_0^2 - k_t^2} \quad \text{and} \quad Z = \frac{k_z^{slab}}{\omega \epsilon_r} \quad (3)$$

inside the slab, where $k_t = \sqrt{k_\phi^2 + k_\rho^2}$ is the transversal wave number parallel to the plane of the slab interface. The resulting electromagnetic fields behind the slab $z > d$, for a time dependence of $e^{-i\omega t}$, are given as [8, 9]

$$\mathbf{E}(\rho, z) = \frac{-I_0}{8\pi\omega\epsilon_0} \nabla \times \nabla \times \int_{\infty_{e^{i\pi}}}^{\infty} \frac{k_t}{k_z^{air}} H_0^{(1)}(k_t \rho) e^{ik_z^{air}(z-d+|z_0|)} T(k_t) dk_t \quad (4)$$

$$\mathbf{H}(\rho, z) = \frac{iI_0}{8\pi} \nabla \times \int_{\infty_{e^{i\pi}}}^{\infty} \frac{k_t}{k_z^{air}} H_0^{(1)}(k_t \rho) e^{ik_z^{air}(z-d+|z_0|)} T(k_t) dk_t. \quad (5)$$

$T(k_t)$ being the transmission coefficient of the slab and is defined as

$$T(k_t) = \frac{1}{\cos(k_z^{slab} d) - \frac{i}{2} \sin(k_z^{slab} d) \left(\frac{Z}{Z_0} + \frac{Z_0}{Z} \right)}. \quad (6)$$

The integration is over the entire spectrum containing both propagating ($k_t < k_0$) and evanescent ($k_t > k_0$) modes. For the perfect imaging condition $\epsilon_r = \mu_r = -1$ the integrals in (4) and (5) simplify to

$$\int_{\infty_{e^{i\pi}}}^{\infty} \frac{k_t}{\tilde{k}} H_0^{(1)}(k_t \rho) e^{i\tilde{k}(z-2d+|z_0|)} dk_t \quad (7)$$

where $\tilde{k} = k_z^{air} = k_z^{slab}$. The integration is performed in closed form (equation 6.616 - 3 in [10]) and the result is

$$\mathbf{E}(\rho, z) = \frac{iI_0}{4\pi\omega\epsilon(z)} \nabla \times \nabla \times \frac{e^{ik_0 \sqrt{\rho^2 + (z-2d+|z_0|)^2}}}{\sqrt{\rho^2 + (z-2d+|z_0|)^2}} \quad (8)$$

and

$$\mathbf{H}(\rho, z) = \frac{I_0}{4\pi} \nabla \times \frac{e^{ik_0 \sqrt{\rho^2 + (z-2d+|z_0|)^2}}}{\sqrt{\rho^2 + (z-2d+|z_0|)^2}}, \quad (9)$$

which are identical to that of a dipole situated at $z = 2d - |z_0|$. Therefore it is evident that a perfect reproduction of the source is obtained. In order to investigate the sensitivity of the imaging quality to the material parameters they are perturbed from their ideal values of $\varepsilon_r = \mu_r = -1$ by σ according to

$$\varepsilon_r = -(1 + \sigma) \quad \text{and} \quad \mu_r = -\frac{1}{1 + \sigma}. \quad (10)$$

The refractive index remains thereby unchanged and retains its value of $n = -1$. The impedance is no more unity and becomes $\sqrt{\frac{\mu_r}{\varepsilon_r}} = \frac{1}{1 + \sigma}$. Note that as $\sigma \rightarrow 0$ the impedance of the slab will be unity and therefore perfectly matched to free space. Substituting these parameters into the integrals (4) and (5) results in the following expression

$$-\int_{-\infty - i\pi}^{\infty} \frac{k_t H_0^{(1)}(k_t \rho) 2(1 + \sigma) e^{ik(z-d+|z_0|)}}{\tilde{k}(-2 \cos(\tilde{k}d) - 2 \cos(\tilde{k}d)\sigma + 2i \sin(\tilde{k}d) + 2i \sin(\tilde{k}d)\sigma + i \sin(\tilde{k}d)\sigma^2)} dk_t \quad (11)$$

with an additional pole at the critical wavenumber

$$k_c = \pm k_0 \sqrt{1 + \left[\frac{1}{k_0 d} \tanh^{-1} \left(\frac{2 + 2\sigma}{2 + 2\sigma + \sigma^2} \right) \right]^2}. \quad (12)$$

The integral can now be evaluated numerically along the contour shown in Fig. 1(b). The wavenumber k_c is associated with the excitation of surface waves and has a strong effect onto the minimum resolvable feature by the slab. The resolution enhancement is dependent on the value of k_c and can be given as the ratio of k_c/k_0 [11]. Note that the main contribution to the integral (11) comes from that part of the spectrum determined by resonant peaks occurring in the transmission coefficient of the slab. As $\sigma \rightarrow 0$ $k_c \rightarrow \infty$ and the ideal case of $\varepsilon_r = \mu_r = -1$ with a perfect resolution will be achieved.

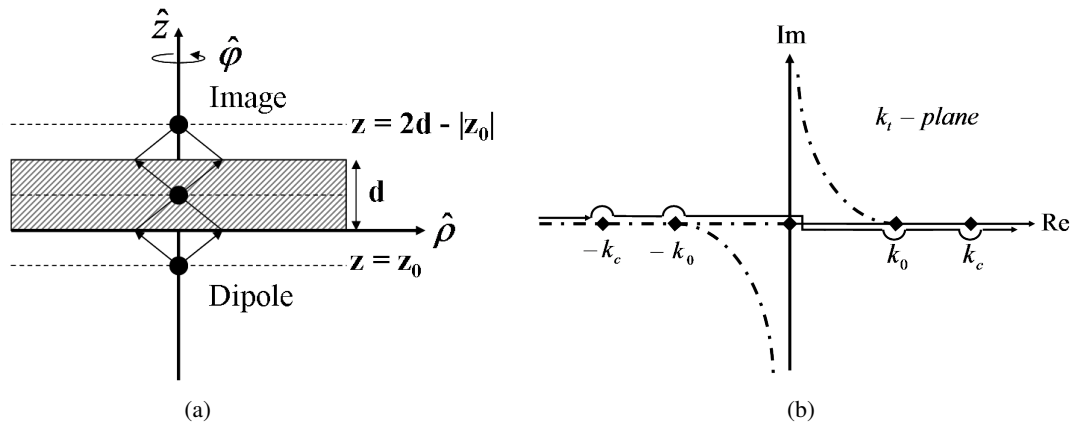


Fig. 1: (a) Focusing property of a metamaterial slab of thickness d , with a point source placed at $z = z_0$ (b) Contour of integration. The path is deformed into small semicircles at the poles.

3. Numerical Simulations

The modified transmission line matrix (TLM) scheme yields a general framework for the modeling of a composite right left handed (CRLH) metamaterial. The simulations have been carried out with MEFISTo-3D Pro, a full wave time domain electromagnetic simulation tool based on the TLM method. Negative refractive index materials are modeled by matching an inter cell network to a standard 3D SCN node. As explained in [12] the discretization of the structure plays thereby an important role and the cell

size Δl should be much smaller than the operating wavelength ($\Delta l/\lambda \ll 1$). In this work we consider a lossless and impedance matched (to free space) CRLH slab with $\epsilon_r = \mu_r = -1$ at a design frequency of $f = 5$ GHz. A dipole oscillating at 5 GHz is placed at distance of $\lambda/4$ in front of the slab whose thickness is varied between $\lambda/3 < d < 2\lambda$. The simulation region has dimensions of $10\lambda \times 10\lambda$ and is terminated by a perfectly matched absorbing boundary layer condition (Fig. 2). The spatial step size is $\lambda/60$. All simulations have been truncated at $t = 4000\Delta t$, where a steady state has been reached. Field monitors are placed along the expected image plane at a distance of $d - \lambda/4$ behind the slab and the intensity distribution is calculated by computing the time averaged electric field intensities. The spot size R which gives a measure for the focusing quality is defined as the full width at half maximum (FWHM) value of the main lobe of the intensity pattern

$$R = \frac{\Delta\rho}{\lambda} \quad (13)$$

with $\Delta\rho = \rho_{I_{max}} - \rho_{I_{max}/2}$ being the distance over which the intensity falls to half its maximum value along the image plane. The enhancement in resolution is then given by R^{-1} .

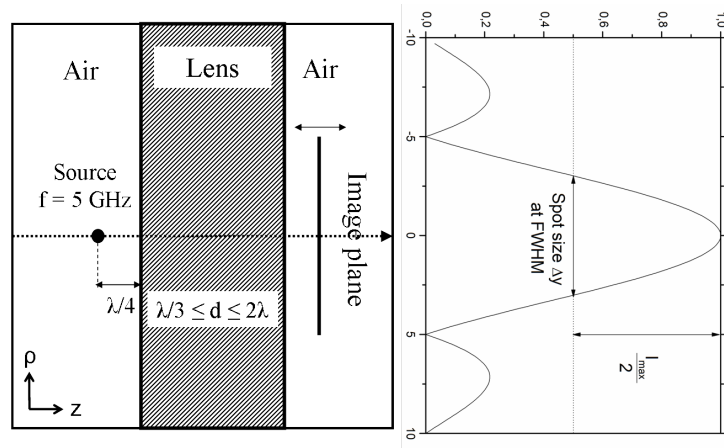


Fig. 2: Simulation space and expected intensity distribution along image plane.

4. Results

For a perfect image the spot size defined in (13) should become infinitesimally small as $\sigma \rightarrow 0$ resulting in an arbitrarily fine resolution $R^{-1} = \infty$. Therefore it is expected that $\Delta\rho$ gets smaller as $\sigma \rightarrow 0$. Fig. 3(a) shows the intensity patterns along the image plane for a slab of thickness $d = \lambda/2$ and various values of σ obtained from the analytical model by integrating (11) numerically. The intensity pattern is normalized with respect to the the maximum intensity at $\rho = 0$. As expected the width of the main lobe narrows as $\sigma \rightarrow 0$ which indicates an enhancement in the resolution. A direct comparison between the numerical and analytical results reveals that the simulation results correspond to the analytical model with a perturbation factor of $\sigma = 0.1$ and a resolution enhancement of $R^{-1} = 4$. The DNG medium model is implemented in MEFISTo-3D Pro by a matching network. As explained in [12] the discretization of the structure plays thereby an important role and the cell size Δl should be much smaller than the operating wavelength ($\Delta l/\lambda \ll 1$). Throughout the simulations a discretization of 1 mm was used which corresponds to $\lambda/60$. Therefore it is expected that the simulated resolution will enhance by discretizing the structure with a finer mesh. The resolution enhancement R^{-1} obtained from the analytical model as a function of σ is plotted in Fig. 3(c). As $\sigma \rightarrow 0$ the resolution increases in accordance with the wavenumber given in (12), which varies for small values of σ as $\ln \sigma$. On the other hand for larger

perturbation values it can be seen that the resolution degrades significantly. Furthermore the impact of the slab thickness on the focusing quality has been investigated. The thickness of the slab is varied between $\lambda/3$ and 2λ , while the point source is held fixed at a distance of $\lambda/4$ from the slab. The results are plotted in Fig. 3(b). It is observed that the focusing quality degrades with increasing slab thickness. From Fig. 3(d) it can be seen that the improvement in the resolution is very significant for thin slabs. A further increase of the slab thickness, beyond a thickness to wavelength ratio of approximately $d/\lambda = 1$ results only in a small enhancement of the resolution.

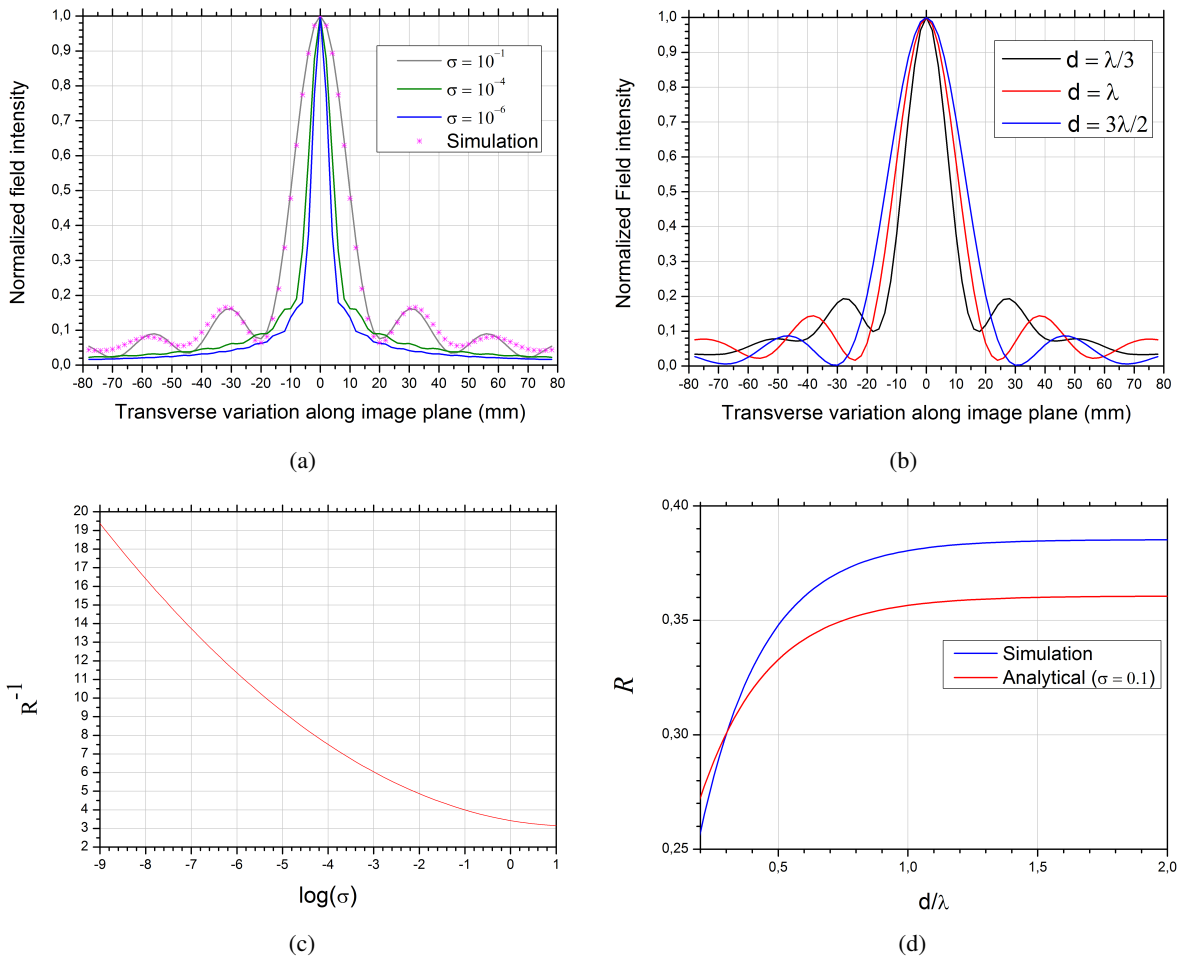


Fig. 3: (a) Comparison of intensity distribution along image plane obtained from the analytical model (by integrating (11)) for various perturbation values and MEFISTo simulation results ($d = \lambda/2$, $z_0 = -\lambda/4$, $f = 5$ GHz) (b) MEFISTo simulation results. Intensity distribution along image plane for varying slab thicknesses ($\lambda/3 < d < \lambda$). The source is held fixed at $z_0 = -\lambda/4$ and the position of the image plane adjusted according to the slab thickness (c) Resolution enhancement as a function of $\log \sigma$ obtained by integrating (11) (d) Effect of slab thickness on resolution.

5. Conclusion

The focusing property of a 2D metamaterial slab was studied both analytically and numerically. The analysis was carried out through a perturbation of the material parameters from their ideal values of $\epsilon_r = \mu_r = -1$, for which $k_c \rightarrow \pm\infty$. Thereby it was shown that the resolution enhancement depends primarily on the extent by which the surface waves are excited. The main contribution to the integral

in (11) comes from the part of the evanescent spectrum close to the wavenumber by which surface waves are excited at the interfaces of the slab. Small deviations from the ideal material parameters result in a significant loss of the focusing quality. The accuracy of the numerical calculations are strongly dependent on the discretization and are valid for electrically short transmission lines with $\Delta l/\lambda \ll 1$. Therefore it is difficult to simulate a perfect image in which case a very fine meshing is required. However subwavelength imaging with a resolution enhancement of $R^{-1} = 4$ was achieved. To sum up the perfect imaging phenomena is very sensitive to the material parameters and even a small deviation from them will result in a significant degradation of the imaging quality.

References

- [1] V. G. Veselago, The Electrodynamics of Substances with Simultaneously Negative Values of ϵ and μ , *Sov. Phys. Uspekhi*, Vol. 10, pp. 509, 1968.
- [2] J. B. Pendry, Negative Refraction Makes a Perfect Lens, *Phys. Rev. Lett.*, vol. 85, no. 18, pp. 2933, 2000.
- [3] A. Grbic and G. V. Eleftheriades, Overcoming the Diffraction Limit with a Planar Left-Handed Transmission-Line Lens, *Phys. Rev. Lett.*, vol. 92, no. 11, 2004.
- [4] Nicholas Fang and Xiang Zhang, Imaging properties of a metamaterial superlens, *Appl. Phys. Lett.*, vol. 82, no. 2, pp. 161, 2003.
- [5] E. Born and Emil Wolf, Principles of Optics: Electromagnetic Theory of Propagation, Interference and Diffraction of Light, *Cambridge Univ. Pr.*, 1999.
- [6] Ali Eren Culhaoglu, Michael Zedler, Wolfgang J. R. Hofer, Andrey Osipov and Peter Russer, Full Wave Numerical Simulation of a Finite 3D Metamaterial Lens, *Conference Proceedings ACES 2008*, Niagra Falls Canada.
- [7] O. E. French, K. I. Hopcraft and E Jakeman, Perturbation on the perfect lens: the near perfect lens, *New Journal of Physics*, vol. 8, no. 8, pp. 271, 2006.
- [8] L. B. Felsen and N. Marcuvitz, Radiation and scattering of waves, *IEEE Press*, 1994.
- [9] R. W. Ziolkowski and Ehud Heyman, Wave Propagation in Media Having Negative Permittivity and Permeability, *Phys. Rev. E*, vol. 64, no. 056635, 2001.
- [10] I.S. Gradshteyn and I.M. Ryzhik, Table of Integrals Series and Products, 7th Edition, Elsevier Academic Press, 2007.
- [11] D. R. Smith, D. Schurig, M. Rosenbluth, S. Schultz, S. A. Ramakrishna and J. Pendry, Limitations on Subdiffraction Imaging With a Negative Refractive Index Slab, *Appl. Phys. Lett.*, vol. 82, no. 10, pp. 1506, 2003.
- [12] Poman P. M. So, Huilian Du and W. J. R. Hofer, Modeling of Metamaterials with Negative Refractive Index Using 2-D Shunt and 3D- SCN TLM Networks, *IEEE Trans. on Microwave Theory and Techniques*, vol. 53, no. 4, pp. 9480, 2005.

SECTION 9

- 9.1. Yusuf Z. Umul, “*Nonuniform currents of the physical theory of diffraction in terms of the modified theory of physical optics*” 9-1
- 9.2. Ugur Saynak, Alper Colak, Yasin Avcibasi, Deniz Bolukbas, I. Hakki Tayyar and Caner Ozdemir, “*2-D ISAR Imaging of Complex Objects Using Shooting-Bouncing Ray (SBR) and Physical Theory of Diffraction (PTD) Techniques*” 9-7
- 9.3. H. Avni Serim, H. Arda Ülkü, Soner Karaca, Hilmi Öztürk, and A. Arif Ergin, “*Geometric Evaluation of Physical Optics Integrals Using A Time-Domain Approach*” 9-15

Non-uniform Currents of the Physical Theory of Diffraction in Terms of the Modified Theory of Physical Optics

Y. Z. Umul

Cankaya University, Türkiye

Abstract – The fringe currents of the physical theory of diffraction are evaluated in the context of the modified theory of physical optics. Since the modified theory of physical optics leads to the exact field expressions for the perfectly conducting half-plane and wedge, the currents are expressed in terms of a line integral which contains all of the terms with respect to the powers of the wave-number. The fields are evaluated for the Dirichlet boundary conditions. The radiated fringe waves are plotted numerically.

1. INTRODUCTION

The physical theory of diffraction (PTD), which was invented by Ufimtsev, is a high frequency asymptotic technique that proposes to correct the surface currents of the physical optics (PO) [1]. PO is a high frequency integrative method, which is generally used to evaluate the scattered fields by defining a tangential surface current on the illuminated side of the scatterer [2]. Although PO leads to the correct geometrical optics (GO) waves asymptotically, the edge diffracted fields that are found from the edge point contributions of the scattering integrals are wrong. Since PO proposes an infinite tangential plane at the point of scattering, a sudden discontinuity on the surface leads to incorrect field expressions [3]. Ufimtsev named the surface currents of PO as uniform currents and suggested to add a second current component which is called as the fringe or non-uniform currents. Since the exact solution of the PEC wedge problem is known in literature, Ufimtsev obtained the fringe currents by subtracting the high frequency asymptotic expression of PO diffracted waves from the rigorous solution [4]. PTD is a widely used method in the literature for the evaluation of high frequency scattered fields [5-8].

In this paper, we aim to obtain the fringe currents by using the modified theory of physical optics (MTPO) for a PEC half-plane. Since MTPO gives the exact scattered waves for the PEC half-plane and wedge geometries [9, 10], there is no need to consider the asymptotic expressions of the diffracted fields. If the surface integral of PO is directly subtracted from the MTPO integrals, the resultant expression will lead to the fringe waves, which are radiated by the non-uniform currents of PTD. The Dirichlet boundary conditions (soft surface) will be taken into account on the surface. The resultant fringe waves will be plotted numerically and compared asymptotic approach of Ufimtsev.

A time factor of $\exp(j\omega t)$ is considered and suppressed throughout the paper. ω is the angular frequency.

2. FRINGE WAVES

A PEC half-plane, which is illuminated by the plane wave of $u_0 \exp[jk(x \cos \alpha + y \sin \alpha)]$, is taken into

account. k is the wave-number. The half-plane is at $S = \{(x, y, z); x \in (0, \infty), y = 0, z \in (-\infty, \infty)\}$. u_0 is the constant amplitude of the electric field.

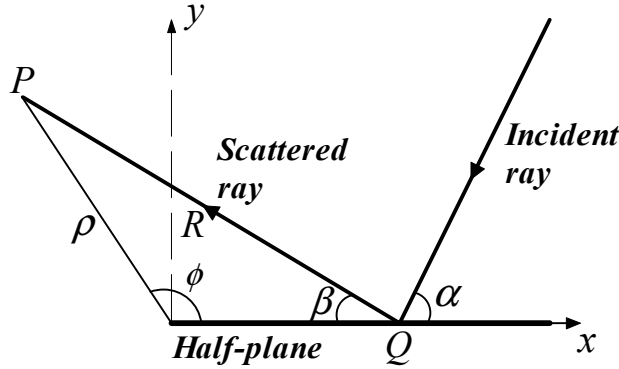


Fig. 1. Geometry of the half-plane

The geometry of the problem is given in Fig. 1. P and Q are the observation and scattering points, respectively. A soft surface is defined by the Dirichlet boundary conditions and requires that the total field is equal to zero on the surface of the scatterer. The MTPO integral for the total scattered field can be written as

$$u_s(P) = u_i(P) + \frac{ke^{j\frac{\pi}{4}}}{\sqrt{2\pi}} \int_0^\infty u_i(Q) \left(\sin \frac{\beta - \alpha}{2} - \sin \frac{\beta + \alpha}{2} \right) \frac{e^{-jkR}}{\sqrt{kR}} dx' \quad (1)$$

for R is equal to $\sqrt{\rho^2 + (x')^2 - 2\rho x' \cos \phi}$ [11]. u_i is the incident plane wave. The PO integral reads

$$u_{PO}(P) = u_i(P) - \frac{ke^{j\frac{\pi}{4}}}{\sqrt{2\pi}} \int_0^\infty u_i(Q) \sin \alpha \frac{e^{-jkR}}{\sqrt{kR}} dx' \quad (2)$$

for this case. u_{PO} can be found by taking $\beta = \alpha$ in Eq. (1). The fringe waves can be evaluated directly by the equation of

$$u_f(P) = u_s(P) - u_{PO}(P) \quad (3)$$

which yields

$$u_f(P) = \frac{ke^{j\frac{\pi}{4}}}{\sqrt{2\pi}} \int_0^\infty u_i(Q) q(\beta, \alpha) \frac{e^{-jkR}}{\sqrt{kR}} dx' \quad (4)$$

where $q(\beta, \alpha)$ is equal to

$$q(\beta, \alpha) = \sin \frac{\beta - \alpha}{2} - \sin \frac{\beta + \alpha}{2} + \sin \alpha \quad (5)$$

Equation (4) represents the fringe field, which is radiated by the non-uniform current component, for a soft surface. As a second step, we will represent the integral, in Eq. (4), in terms of the Fresnel function,

which can be defined as

$$F[x] = \frac{e^{j\frac{\pi}{4}}}{\sqrt{\pi}} \int_x^{\infty} e^{-jt^2} dt. \quad (6)$$

The phase function of the integral is equal to $x' \cos \alpha - R$. The first derivative of the phase function gives two stationary points at $\beta = \alpha$ and $\beta = -\alpha$. The first stationary point represents the reflected GO rays whereas the second one leads to the incident GO field [12, 13]. The formula, derived in Ref. [14], will be used for the evaluation of Eq. (4). The term of $q(\beta, \alpha)$ can be rewritten as

$$q(\beta, \alpha) = \left[1 - \frac{\cos(\alpha/2)}{\cos(\beta/2)} \right] \sin \frac{\beta - \alpha}{2} + \left[\frac{\cos(\alpha/2)}{\cos(\beta/2)} - 1 \right] \sin \frac{\beta + \alpha}{2}. \quad (7)$$

The GO fields, at

For equations, $\beta = \alpha$ and $\beta = -\alpha$, become zero in Eq. (7). The uniform fringe field is found to be

$$u_f(P) = I_i + I_r \quad (8)$$

for I_i and I_r are equal to

$$I_i = \left[1 - \frac{\cos(\alpha/2)}{\sin(\phi/2)} \right] e^{jk\rho \cos(\phi - \alpha)} \text{sign}(\xi_i) F[\xi_i] \quad (9)$$

and

$$I_r = - \left[1 - \frac{\cos(\alpha/2)}{\sin(\phi/2)} \right] e^{jk\rho \cos(\phi + \alpha)} \text{sign}(\xi_r) F[\xi_r] \quad (10)$$

respectively. $\text{sign}(x)$ is the signum function, which is equal to 1 for $x > 0$ and -1 otherwise. ξ_i and ξ_r can be defined as

$$\xi_i = -\sqrt{2k\rho} \cos \frac{\phi - \alpha}{2} \quad (11)$$

and

$$\xi_r = -\sqrt{2k\rho} \cos \frac{\phi + \alpha}{2}. \quad (12)$$

Equation (8) is the exact representation of the fringe fields for a soft half-plane. The approximate expression of the fringe fields that were introduced by Ufimtsev [4] can be obtained by using the relation of

$$\text{sign}(x)F[x] = \frac{e^{-j\left(x^2 + \frac{\pi}{4}\right)}}{2\pi x} \sum_{i=0}^{\infty} \frac{\Gamma\left(i + \frac{1}{2}\right)}{(-jx^2)^i} \quad (13)$$

for $|x| \rightarrow \infty$. I_i and I_r can be written approximately as

$$I_i = \left[1 - \frac{\cos(\alpha/2)}{\sin(\phi/2)} \right] \frac{e^{-j(k\rho + \frac{\pi}{4})}}{2\sqrt{\pi\xi_i}} \quad (14)$$

and

$$I_r = - \left[1 - \frac{\cos(\alpha/2)}{\sin(\phi/2)} \right] \frac{e^{-j(k\rho + \frac{\pi}{4})}}{2\sqrt{\pi\xi_r}} \quad (15)$$

respectively.

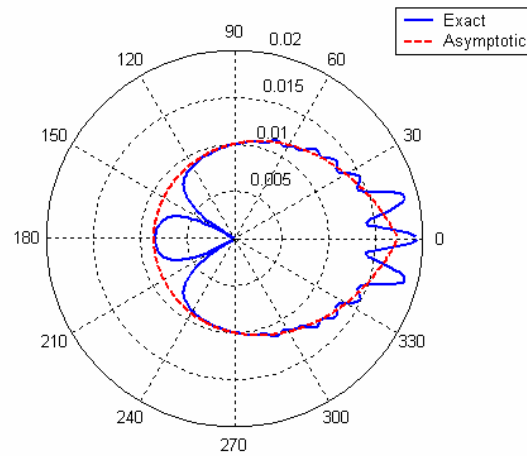


Fig. 2. Comparison of the exact and asymptotic fringe waves for $\phi_0=30^\circ$

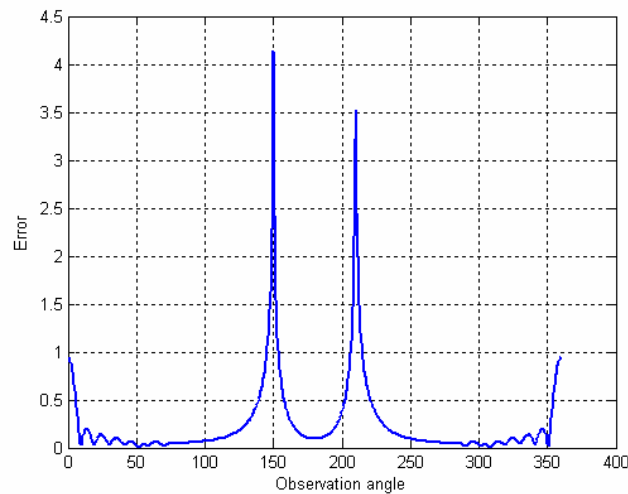


Fig. 3. Logarithmic error for $\phi_0=30^\circ$

The exact and asymptotic expressions of the fringe waves will be compared numerically. The distance of observation is taken as 6λ . Figure 2 shows the variation of the fringe field versus the observation angle in polar coordinates. The angle of incidence is equal to 30° . The asymptotic field is not

harmonious with the exact waves. Especially the error intensifies at the reflection and shadow boundaries. The error function is defined by the equation of

$$f_e = \left| \log \frac{u_{exact}}{u_{asympt}} \right|. \quad (16)$$

The variation of the error function is given in Fig. 3.

3. CONCLUSIONS

In this paper, we analyzed the error of the asymptotic fringe waves, used in the definition and application of PTD. The method of MTPO enabled us to express the exact solution of the half-plane problem in terms of a PO integral. The integral representations of the exact and classical PO fields are transformed into Fresnel functions. A more correct expression is obtained for the fringe waves. The results are compared with the asymptotic expressions, used in the literature. The error of the actual asymptotic representation is put forward.

REFERENCES

- [1] Ufimtsev, P. Ya., "Fast convergent integrals for non-uniform currents on wedge faces," *Electromagnetics*, Vol. 18, No. 3, 289-313, 1998.
- [2] Silver, S., *Microwave Antenna Theory and Design*, McGraw-Hill, New York, 1949.
- [3] Stutzman, W. L. and G. A. Thiele, *Antenna Theory and Design*, Wiley, New York, 1981.
- [4] Ufimtsev, P. Ya., *Fundamentals of the Physical Theory of Diffraction*, Wiley, New Jersey, 2007.
- [5] Jakobus, U. and F. M. Landstorfer, "Improvement of the PO-MoM hybrid method by accounting for effects of perfectly conducting wedges," *IEEE Trans. Antennas Propag.*, Vol. 43, No. 10, 1123-1129, 1995.
- [6] Ufimtsev, P. Ya., "Comments on "Improvement of the PO-MoM hybrid method by accounting for effects of perfectly conducting wedges"," *IEEE Trans. Antennas Propag.*, Vol. 45, No. 9, 1440-1441, 1997.
- [7] Knott, E. F., "A progression of high frequency RCS prediction techniques," *Proc. IEEE*, Vol. 73, No. 2, 252-264, 1985.
- [8] Knott, E. F., Shaeffer, J. F. and M. T. Tuley, *Radar Cross Section*, SciTech, Raleigh, 2004.
- [9] Umul, Y. Z., "Modified theory of physical optics," *Opt. Express*, Vol. 12, No. 20, 4959-4972, 2004.
- [10] Umul, Y. Z., "Modified theory of physical optics approach to wedge diffraction problems," *Opt. Express*, Vol. 13, No. 1, 216-224, 2005.
- [11] Umul, Y. Z., "Edge-dislocation waves in the diffraction process by an impedance half-plane," *J. Opt. Soc. Am. A*, Vol. 24, No. 2, 507-511, 2007.
- [12] Umul, Y. Z., "Diffraction by a black half plane: Modified theory of physical optics approach," *Opt. Express*, Vol. 13, No. 19, 7276-7287, 2005.
- [13] Umul, Y. Z., "Scattering of a Gaussian beam by an impedance half-plane," *J. Opt. Soc. Am. A*, Vol. 24, No. 10, 3159-3167, 2007.
- [14] Umul, Y. Z., "Diffraction of evanescent plane waves by a resistive half-plane," *J. Opt. Soc. Am. A*, Vol. 24, No. 10, 3226-3232, 2007.

2-D ISAR Imaging of Complex Objects Using Shooting-Bouncing Ray (SBR) and Physical Theory of Diffraction (PTD) Techniques

U. Saynak¹, A. Çolak¹, Y. Avcıbaşı¹, D. Bölükbaş¹, İ.H. Tayyar^{1,2}, C. Özdemir^{1,3}

¹TÜBİTAK MAM, Information Technologies Institute, 41470 Gebze, Kocaeli, Turkey
ugur.saynak@bte.mam.gov.tr, alper.colak@bte.mam.gov.tr, yasir.avcibasi@bte.mam.gov.tr,
deniz.bolukbas@bte.mam.gov.tr

²Gebze Institute of Technology, Department of Electronics, 41400 Gebze, Kocaeli, Turkey,
tayyar@gyte.edu.tr

³Mersin University, Faculty of Engineering, Department of Electrical-Electronics
33343 Mersin, Turkey, cozdemir@mersin.edu.tr

Abstract - In this work we investigate the two-dimensional (2-D) inverse synthetic aperture radar (ISAR) imaging of large and complex targets with the help of a hybrid and approximate technique for far field electromagnetic wave scattering at high-frequencies. The body of the target is modeled using facets and wedges. The well-known shooting-bouncing ray (SBR) SBR method [1,2] combined with Physical Theory of Diffraction (PTD) technique [3] is employed to estimate the far field scattered field of the facets and wedges on the object, respectively. First, the accuracy of the method in this work is tested and validated with analytical results that are known for some canonical structures such as sphere, plate and dihedral reflectors. Then, 2-D ISAR [4] images of different large and complex platforms are generated by using the computed electric field data over frequencies and far field look angles. Despite conventional approaches that usually take into account only the SBR method to generate the ISAR image; in this paper, wedge diffraction concept in addition to SBR methodology is taken into account to demonstrate the effect of the diffraction energy to the final ISAR image. Therefore; visual demonstrations that show the contribution of diffracted fields to the final ISAR image are provided for various test targets.

1. INTRODUCTION

In radar signature applications, ISAR images of a target are useful and well-known method for target identification and classification purposes. The complex ISAR image represents the reflectivity function of the target and it can be used for various goals such as the determination of scattering centers on the target. Such information can be very useful in understanding the major scattering points (or hot spots) that are responsible for the most of the scattered energy. The complex ISAR image of a target is typically formed either by Fourier transforming the scattered field data over a finite range of look angles and frequencies or by using the range-Doppler methodology [5].

In this work we strive to develop an analysis model for visualizing the 2-D ISAR images of complex targets. This model is based on the SBR method and the PTD technique. The SBR is known to be a powerful high frequency electromagnetic (EM) simulation method for the estimation of EM scattering from large, complex bodies. In SBR, the multiple-scattered field terms can also be calculated as well as the single-bounce term. At high frequencies, the diffracted field computation is generally done with the PTD technique which has been well developed in the past few decades and has been implemented in CAD-based radar cross section (RCS) computation environment in the military and civilian industries [6-7].

2. ANALYSIS

In SBR technique [1], rays are shot from the transmitter towards the target and are traced according to the laws of geometrical optics. To find the contribution of each ray to the total scattered field, we calculate the far field contribution of the first and the last hit points for each ray before leaving the target. Only the physical optics (PO) contribution is calculated from the first hit point of each ray. On the other hand, a ray-tube integration is performed for the last hit point.

In this work all targets are assumed to be perfect conductors. Under this construct, Physical Optics contribution to the scattered field can be written as:

$$\mathbf{E}_{po}^S(r, \theta, \phi) = \frac{jk_0 Z}{4\pi r} e^{-jk_0 r} \iint_S (\hat{\mathbf{k}}_s \times \hat{\mathbf{k}}_s \times \mathbf{J}(\mathbf{r}')) e^{jk_0 \hat{\mathbf{k}}_s \cdot \mathbf{r}'} ds' \quad (1a)$$

where $\mathbf{J}(\mathbf{r}')$ is the current density calculated as follows:

$$\mathbf{J} \approx \begin{cases} 2\hat{\mathbf{n}} \times \mathbf{H}_i & \text{illuminated} \\ 0 & \text{shadowed} \end{cases} \quad (1b)$$

In the above equation, $\hat{\mathbf{n}}$ is the surface normal of the illuminated part of the target. In the equation (1a), k_0 is the wave number of the free space, $\hat{\mathbf{k}}_s$ is the unit vector directed from origin to observation point and Z is the characteristic impedance of the surrounding medium. Now the integral in equation (1a) can be calculated analytically as given in [8].

The contribution of the ray-tube integration at last hit point of i^{th} ray to the scattered field is calculated as follows:

$$\mathbf{E}_i^S = \frac{e^{-jk_0 r}}{r} [\hat{\theta}^S A_{\theta i} + \hat{\phi}^S A_{\phi i}] \quad (2a)$$

with

$$\begin{bmatrix} A_{\theta i} \\ A_{\phi i} \end{bmatrix} = \begin{bmatrix} B_{\theta i} \\ B_{\phi i} \end{bmatrix} \left(\frac{jk_0}{2\pi} \right) (\Delta A_i)_{\text{exit}} S_i(\theta, \phi) e^{jk_0 \hat{\mathbf{k}}_s \cdot \vec{r}_{A_i}} \quad (2b)$$

Finally the total scattered field due to ray-tube integration can be obtained by the summation of contributions of the each rays to the scattered field.

$$\mathbf{E}_{sbr}^S(\mathbf{r}) = \sum_{i^{\text{th}} \text{ ray}} \mathbf{E}_i^S(\mathbf{r}) \quad (2c)$$

In equation (2b) \vec{r}_{A_i} is the vector from the origin to the last hit point of the i^{th} ray, $(\Delta A_i)_{\text{exit}}$ is the cross section of the i^{th} exit ray-tube and the expressions $B_{\theta i}$, $B_{\phi i}$ and $S_i(\theta, \phi)$ are defined in [2]. As a result, PO and ray-tube integration contributions to the scattered field are summed:

$$\mathbf{E}^S = \mathbf{E}_{po}^S + \mathbf{E}_{sbr}^S \quad (3)$$

It has to be noted that RCS results using SBR method and determined from the measurement are not identical and give some differences. The reason for a possibly considerable difference is the neglect of the edge diffraction in SBR solution. For a more reliable result, edge effects should be included as well. The PTD method used in this paper to calculate a diffraction contribution for each ray hits the platform's surface vicinity of an edge. Because of the studied platforms are CAD models, whose surfaces are made up of triangular facets, wedges formed by these triangles are specified an angle between the normal vectors of adjacent triangles. All wedges can be obtained by simply relating each triangle to its neighbors. The diffracted field strength can be calculated from the electric edge currents \mathbf{I} and the magnetic edge currents \mathbf{M} as following [3],

$$\vec{E}_d(\vec{r}) = jk \int_C \left[Z\vec{I}(\vec{r}')\hat{s} \times (\hat{s} \times \hat{t}) + \vec{M}(\vec{r}')\hat{s} \times \hat{t} \right] \frac{e^{-jks}}{4\pi s} dl \quad (2)$$

where s is the distance between the integration point and the observation point, \vec{r}' is the position of the current on the edge, \hat{t} is a unit vector along the edge, \hat{s} is the unit vector from \vec{r}' to the point of observation \vec{r} . Then, the final equation for the diffracted field is obtained as

$$\vec{E}_d = \frac{e^{-jks}}{2\pi s} dl \left[(D_m - D'_\perp) (\vec{E}_i \hat{e}_{\perp,i}) \hat{e}_{\perp,s} - (D_e - D'_\parallel) \frac{\sin \beta}{\sin \beta'} (\vec{E}_i \hat{e}_{\parallel,i}) \hat{e}_{\parallel,s} - (D_{em} \sin \beta' - D'_x) \frac{\sin \beta}{\sin \beta'} (\vec{E}_i \hat{e}_{\perp,i}) \hat{e}_{\parallel,s} \right] \quad (3)$$

where \vec{E}_i is the incident electric field strength and the parameters \hat{e} , β , β' and D are defined in [9]. Finally, we can get the 2-D ISAR image by using the following formulation defined in [4]:

$$ISAR(x, y) = \int_{-\infty}^{\infty} \int_{-\infty}^{\infty} E^S(k, \phi) \cdot e^{j2k \cdot x} \cdot e^{j2k_c \phi \cdot y} \cdot d(k) \cdot d(k_c \phi) \quad (4)$$

Some various examples are presented in the following section to show the visual demonstration for ISAR image with SBR formulation and the diffracted field contribution to the final ISAR image.

3. RESULTS

For verification of the PO algorithm combined with PTD technique, scattering from a cone is studied and compared with the exact solution obtained by method of moments (MoM) solution. Fig.1 shows the monostatic RCS for the vertical polarization case. As obvious form the figure, PO with PTD result gives good agreement with the MoM solution for the considered polarization

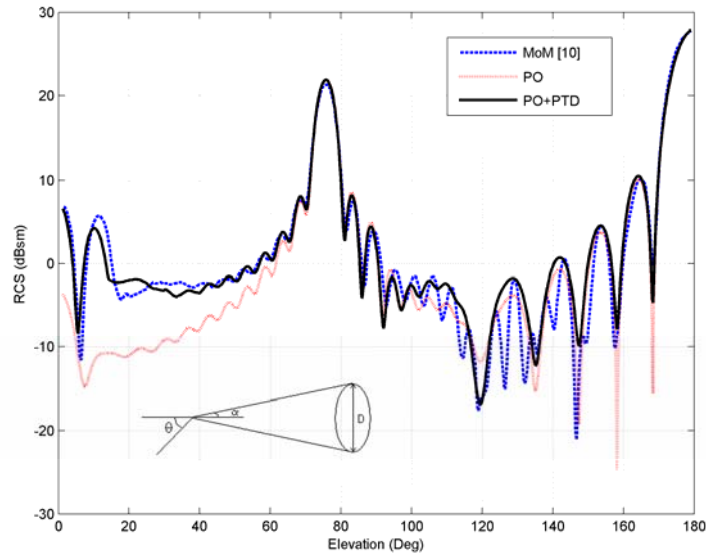


Figure 1: Monostatic RCS of a perfectly conducting cone with $\alpha = 15^\circ$, $D = 3\lambda$ (VV polarization case).

The second simulation shows verification of the both PO and SBR algorithms. Scattering from a trihedral (Fig.2a) is studied and compared with the solution obtained by FDTD [11]. Fig.2b shows the monostatic RCS for an incident angle $\theta = 66^\circ$ as the angle ϕ varies from 0° to 90° . The size of trihedral plate was taken to be 5λ . Comparison of the PO with SBR result to the FDTD result provides a fairly good agreement as well.

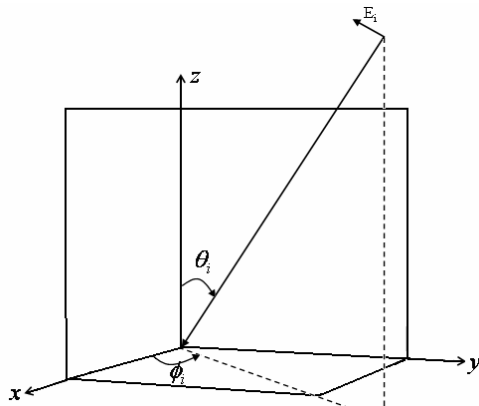


Figure 2a: Geometry of the square trihedral corner reflector.

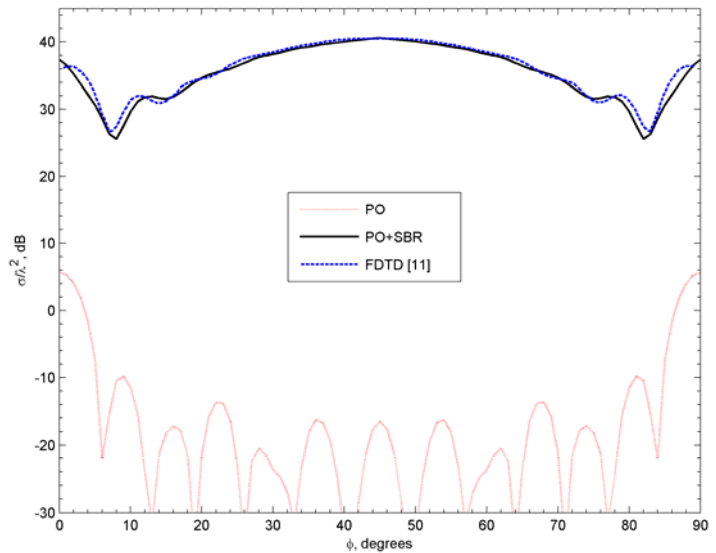


Figure 2b: Monostatic RCS of the trihedral corner reflector with $5\lambda \times 5\lambda$ square plates: $\theta_i = 66^\circ$ for the VV polarized incident wave.

For the validation of our PO, SBR and PTD based codes; only small canonical objects were studied as presented in Fig.1 and Fig.2. Next, we will investigate a much more complex and large target that is look like an airplane as its CAD model is shown in Fig.3. The size of this airplane model is $10\lambda \times 8\lambda \times 3\lambda$. It contains some open and close structures to cause multiple scattering. After the EM simulation of this target, SAR image of the target is obtained as demonstrated in Fig. 4 by only considering the PO contribution. During the EM simulation of this target, the center frequency of operation is selected as 18 GHz and the azimuth ($\phi=0^\circ$) and the elevation ($\theta=90^\circ$) angles correspond to nose-on incidence. Next two figures (Fig. 5 and Fig. 6) show ISAR images of the test target for both VV and HH polarizations by using PO with PTD results. As obvious from the ISAR image for VV polarization, wing of the plane becomes clearer after including the PTD contribution.



Figure 3: Geometry of the generic plane model.

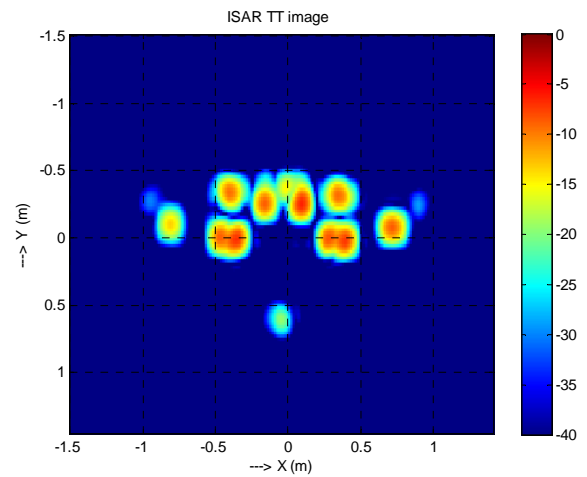


Figure 4: ISAR image of the plane model. Only PO contribution is considered.

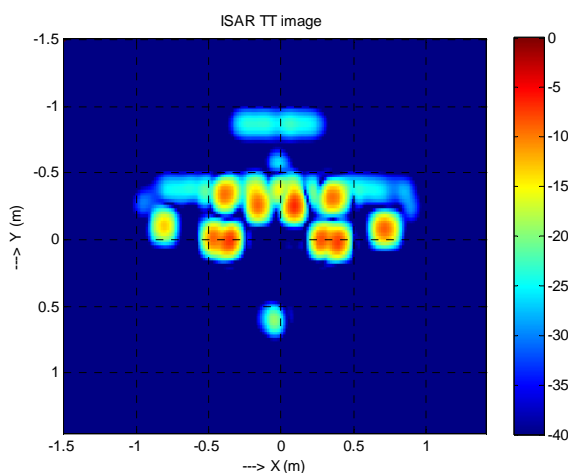


Figure 5: ISAR image of the plane model. PO+PTD contributions are considered. VV polarization.

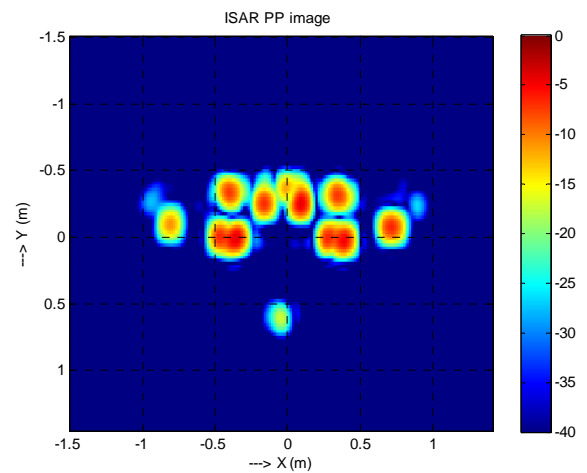


Figure 6: ISAR image of the plane model. PO+PTD contributions are considered. HH polarization.

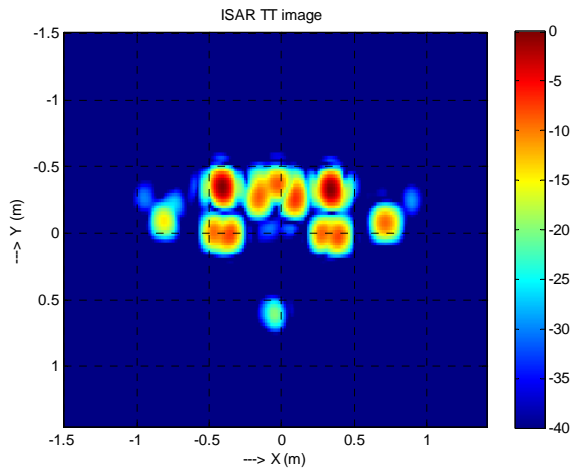


Figure 7: ISAR image of the plane model. PO+SBR contributions are considered. VV polarization.

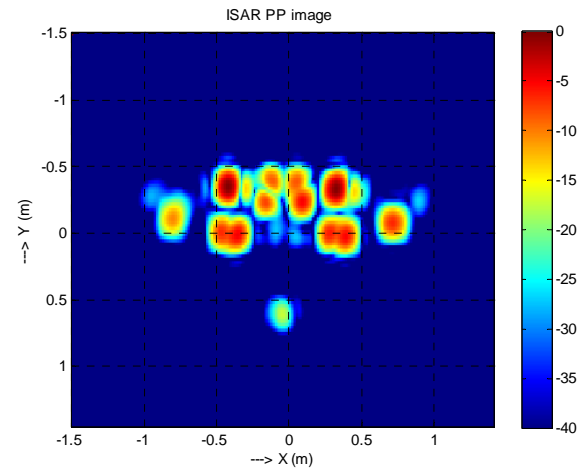


Figure 8: ISAR image of the plane model. PO+SBR contributions are considered. HH polarization.

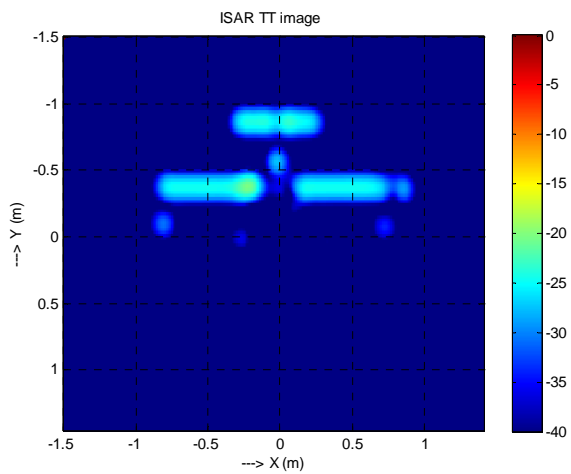


Figure 9: ISAR image of the plane model. Only PTD contribution is considered. VV polarization.

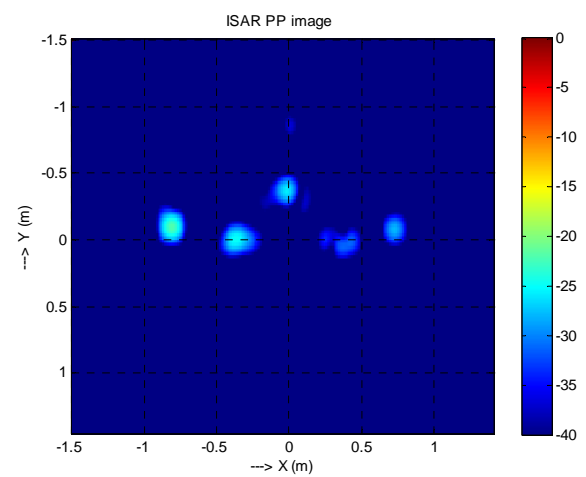


Figure 10: ISAR image of the plane model. Only PTD contribution is considered. HH polarization.

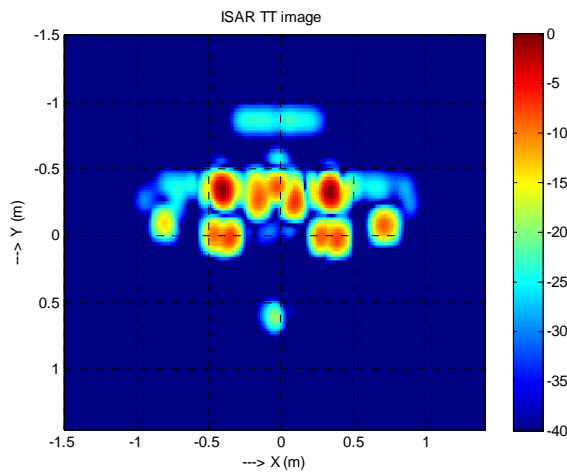


Figure 11: ISAR image of the plane model. PO+SBR+PTD contributions are considered. VV polarization.

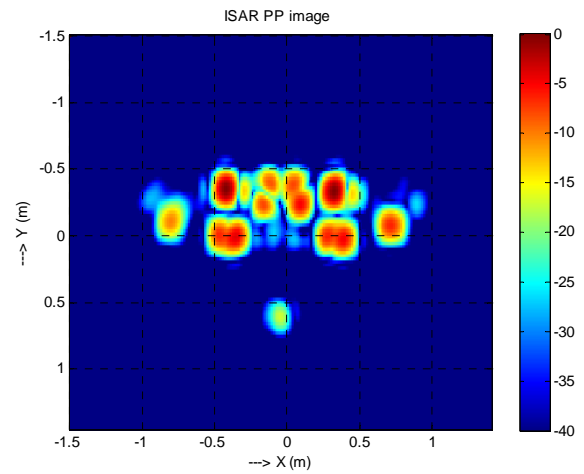


Figure 12: ISAR image of the plane model. PO+SBR+PTD contributions are considered. HH polarization.

4. CONCLUSIONS

In this work, the PO, SBR and PTD solutions of a large, complex target is studied and corresponding ISAR images are presented. First, the validity of the computer codes for each method is checked with different canonical targets of known shape. After getting a very good match with the theoretical/analytical scattered field with the calculated ones, a much more complex and large platform is selected for the complete ISAR analysis of the methods. Since we can compute the distribution from all three methods, we can also image the scattering and/or diffraction field calculated via these methods. The use of ISAR images for this work helps us to understand the locations of the hot spots caused by scattering or diffraction.

REFERENCES

- [1] Ling, H., R. C. Chou and S. W. Lee, "Shooting and Bouncing Rays: Calculating the RCS of an Arbitrary Shaped Cavity," *IEEE Tran. on Antennas and Prop.*, Vol. 37, No. 2, 1989.
- [2] Bhalla, R. and H. Ling, "Image Domain Ray Tube Integration Formula for the Shooting and Bouncing Ray Technique," *Radio Science*, Vol. 30, No. 5, 1435-1446, 1995.
- [3] Michaeli, A., "Equivalent Edge Currents for Arbitrary Aspects of Observation," *IEEE Tran. on Antennas and Prop*, Vol. 32, No. 3, 1984.
- [4] Özdemir, C., *Synthetic Aperture Radar*, Editor: K. Chang, *Encyclopedia of RF and Microwave Engineering*, Wiley Interscience, p. 5067-5080, 2005.
- [5] Mensa, D. L., *High Resolution Radar Cross-Section Imaging*, Artec House, Boston, MA, 1991.
- [6] Song, J. M., C. C. Lu, W. C. Chen and S. W. Lee, "Fast Illinois Solver Code (FISC)," *IEEE Tran. on Antennas and Prop*, Vol. 40, No. 3, 27-34, 1998.
- [7] Rius, J. M., M. Ferrando, L. Jofre, "GRECO: Graphical Electromagnetic Computing for RCS Prediction in Real Time," *IEEE Antennas and Prop. Magazine*, Vol. 35, No. 2, 7-17, 1993.
- [8] Bolukbas, D. and A. A. Ergin, "A Radon Transform Interpretation of the Physical Optics Integral", *Microwave and Opt. Tech. Letters*, Vol.44, No.3, 284-288, 2005.
- [9] Knott E. F., "The relationship between Mitzner's ILDC and Michaeli's equivalent currents," *IEEE Tran. on Antennas and Prop*, Vol. 33, No.1, 112-114, 1985.
- [10] Senior, T. B. A. and J. L. Volakis, *Approximate Boundary Conditions in Electromagnetics*, IEE Electromagnetic wave series, London, 1995.
- [11] Polycarpou, A. C., C. A. Balanis and P.A. Tirkas, "Radar Cross Section Evaluation of the Square Trihedral Corner Reflector Using PO and MEC", *Antennas and Prop. Soc. Int. Symp., AP-S. Digest*, Vol. 3, 1428-1431, 1993.

Geometric Evaluation of Physical Optics Integrals Using A Time-Domain Approach

H. Avni Serim, H. Arda Ülkü, Soner Karaca,
Hilmi Öztürk, and A. Arif Ergin*

Gebze Institute of Technology, Istanbul Cad. 101, Gebze, Kocaeli, TURKEY

It has been recently shown that the classical physical optics (PO) integral can be interpreted as a Radon transform and can be easily evaluated using geometric means. Specifically, it was shown that if the scatterer consists of triangular patches, analytical expression for the PO integral for each patch exists (D. Bölükbaş and A.A. Ergin, *Microwave and Optical Technology Letters*, 44(3), 284-288, 2005). It was further shown that if the scatterer is modeled with NURBS surfaces, the PO surface integral reduces to a line integral that can be easily evaluated using geometric-numeric techniques (H.A. Serim and A.A. Ergin, *IEEE Antennas and Wireless Propagation Letters*, accepted for publication).

In these published work, the incident field is assumed to be a plane-wave and the observer is assumed to be at the far-field region of the scatterer. Under these circumstances, it was shown that the time dependent PO integral reduces to a line integral over the curve defined by the intersection of a plane (an implicit surface) with the scatterer. The position of the plane is time-dependent. In this work, we show that the time-domain approach to evaluation of the PO integral can be extended to scenarios in which either the source or the observer or both are in the near-field of the scatterer. More specifically, it will be shown that when either the source or the observer is in the near-field, the implicit surface turns out to be a paraboloid and when both the source and observer are in the near-field it turns out to be an ellipsoid. The size of the implicit surface still changes with time in a trivial manner. The PO integral is still a line integral over the intersection of the implicit surface with the scatterer.

The full derivation for all the cases will be shown and the assumptions and limitations of the results will be discussed during the presentation. Applications pertaining to scatterers modeled with triangular patches and NURBS surfaces will be shown.

SECTION 10

- 10.1. Beyza Ardic, Adnan Kaya, Ozlem Coskun and Ahmet Irkin, “*Slot-Loaded Microstrip Antenna Design of Broadband Transceiver for Wireless Data Communication in ISM Band*” 10-1
- 10.2. Ozgur Ergul and Levent Gurel, “*Hierarchical Parallelization of MLFMA for the Efficient Solution of Large-Scale Electromagnetics Problems*” 10-3

SLOT- LOADED MICROSTRIP ANTENNA DESIGN OF BROADBAND TRANSCEIVER FOR WIRELESS DATA COMUNICATION IN ISM BAND

Beyza Ardic, Adnan KAYA, Özlem Coşkun, Ahmet Irkin

Abstract

This paper presents presentation of the designed procedure of the microstrip antenna operating at 2.4 GHz transceiver for RF front-end for ISM-band digital wireless communication. The aim of this project is to present several types of compact microstrip patch antennas for ISM 2.4 GHz band, and then to compare and interpret the results. Besides, some information was provided as to the ISM band and transceiver systems.

The different geometries of microstrip antennas are simulated such as recessed microstrip line feed, microstrip patch arrays, slot-loaded microstrip patch arrays, dual-band and slot-loaded rectangular microstrip patch with AWR Microwave Office software, using Moment Method. A slot-loaded rectangular microstrip antenna with meandering slots in the ground plane was designed; then this antenna was simulated and studied in detail. Furthermore, the effect of the results is studied by changing the parameters of the meandered antenna. The results also show that the return loss levels of the meandered antennas vary from -12.8dB to -18.9 dB . The designed antenna operates at 2.4 GHz with 105 MHz bandwidth, having $|S_{11}|$ of -12.8 dB at resonant frequency.

Key words: Microstrip antenna, ISM Band, transceiver, Sloat-Loaded

Department of Electronics and Communication Engineering

Süleyman Demirel University, **Isparta, Turkey, 32260**

Hierarchical Parallelization of MLFMA for the Efficient Solution of Large-Scale Electromagnetics Problems

Özgür Ergül^{1,2} and Levent Gürel^{1,2}

¹Department of Electrical and Electronics Engineering

²Computational Electromagnetics Research Center (BiLCEM)

Bilkent University, TR-06800, Bilkent, Ankara, Turkey

E-mail: ergul@ee.bilkent.edu.tr, lgurel@bilkent.edu.tr

Abstract — We present the details of a hierarchical partitioning strategy for the efficient parallelization of the multilevel fast multipole algorithm (MLFMA) on distributed-memory architectures. Unlike previous parallelization approaches, this strategy is based on the simultaneous distribution of clusters and their fields by considering the optimal partitioning of each level separately. Using the hierarchical strategy, load-balancing is improved, computations on the tree structure are distributed evenly among processors, and the number of communication events between processors is reduced. We demonstrate the effectiveness of the resulting parallel implementation by solving very large scattering problems involving both canonical and complicated targets discretized with more than 100 million unknowns.

1. INTRODUCTION

The multilevel fast multipole algorithm (MLFMA) [1],[2] is a powerful method for the fast and efficient solution of scattering and radiation problems in electromagnetics. Formulations of problems involving three-dimensional metallic objects can be achieved rigorously via surface integral equations [3]. Accurate solutions of integral-equation formulations require discretizations of surfaces with small elements, e.g., triangles, with respect to wavelength. Application of the method of moments (MOM) [4] leads to $N \times N$ dense matrix equations, which can be solved iteratively by using a Krylov-subspace algorithm. MLFMA can perform the required matrix-vector multiplications in $\mathcal{O}(N \log N)$ time by using $\mathcal{O}(N \log N)$ memory, hence it enables the solution of large matrix equations arising from the discretization of large-scale objects. However, many real-life problems require discretizations with tens of millions of unknowns, which may not be handled easily with the sequential implementations of MLFMA running on a single processor. In order to achieve the solution of such large problems, MLFMA can be parallelized and employed on a cluster of computers.

MLFMA is usually parallelized on relatively inexpensive computing platforms with distributed-memory architectures [5]–[13]. Unfortunately, parallelization of this algorithm is not trivial, and it can be difficult to obtain a sufficient parallelization efficiency, especially when the number of processors is large and problems involve complex objects. This is mainly due to the complicated structure of MLFMA, which involves a multilevel tree including clusters of discretization elements and samples of radiating/incoming fields. Simple parallelization strategies, which are based on distributing clusters among processors, usually fail to provide efficient solutions. Problems arise mainly for the higher levels of MLFMA, which involve small numbers of clusters with densely-sampled fields. Hybrid strategies are developed to improve the parallelization of MLFMA by applying different partitioning techniques for the lower and the higher levels of tree structures [6]–[11]. By distributing samples of fields instead of clusters in the higher levels, load-balancing is enhanced significantly, which leads to higher parallelization efficiency. On the other hand, the improved efficiency offered by the hybrid

This work was supported by the Scientific and Technical Research Council of Turkey (TUBITAK) under Research Grants 105E172 and 107E136, by the Turkish Academy of Sciences in the framework of the Young Scientist Award Program (LG/TUBA-GEBIP/2002-1-12), and by contracts from ASELSAN and SSM.

parallelization strategies may not be sufficient, especially when the number of processors is large.

In this paper, we present the details of a hierarchical parallelization strategy [12],[13], which provides significantly higher efficiency than the previous parallelization approaches, especially as the number of processors increases. This strategy is based on the simultaneous distribution of clusters and their fields by considering the optimal partitioning of each level separately, and it is well suited for the multilevel structure of MLFMA. Using the hierarchical strategy, computations on the tree structure are distributed among processors with improved load-balancing, and the number of communication events between processors is reduced. We demonstrate the effectiveness of our algorithm by solving very large scattering problems involving both canonical and complicated targets discretized with 120–135 million unknowns.

2. MLFMA SOLUTIONS OF SURFACE INTEGRAL EQUATIONS

We use surface integral equations to formulate time-harmonic electromagnetics problems involving three-dimensional perfectly-conducting objects with arbitrary shapes. Consider a metallic object with an electrical dimension of kD , where $k = \omega\sqrt{\epsilon\mu} = 2\pi/\lambda$ is the wavenumber. For numerical solutions, the surface of the object is discretized by using $\lambda/10$ planar triangles, and the electric current induced on the surface is expanded in a series of basis functions, i.e.,

$$\mathbf{J}(\mathbf{r}) = \sum_{n=1}^N a_n \mathbf{b}_n(\mathbf{r}), \quad (1)$$

where $N = \mathcal{O}(k^2 D^2)$. In (1), $\mathbf{b}_n(\mathbf{r})$ for $n = 1, 2, \dots, N$ represents the n th basis function with an unknown coefficient a_n . Applying the method of moments and testing the boundary conditions on the surface of the object lead to $N \times N$ dense matrix equations in the form of

$$\bar{\mathbf{Z}} \cdot \mathbf{a} = \mathbf{v}, \quad (2)$$

where matrix elements $\bar{\mathbf{Z}}[m, n]$ for $m, n = 1, 2, \dots, N$ represent electromagnetic interactions of discretization elements, i.e., basis and testing functions, while \mathbf{v} represents the excitation vector obtained by testing incident fields created by external sources. Applying a Galerkin scheme, we use the same set of Rao-Wilton-Glisson (RWG) [14] functions as basis and testing functions.

Matrix equations in the form of (2) can be solved iteratively via a Krylov subspace algorithm, where the required matrix-vector multiplications are performed efficiently by MLFMA [1],[2]. A tree structure with $L = \mathcal{O}(\log N)$ levels is constructed by placing the object in a cubic box and recursively dividing the computational domain into subdomains, until the box size is about 0.15λ – 0.3λ . The number of nonempty boxes, i.e., clusters, can be approximated as

$$N_l \approx 4^{(1-l)} N_1 \quad (3)$$

for levels $l = 1, 2, \dots, L$, where $N_1 = \mathcal{O}(N)$ is the number of clusters in the lowest level ($l = 1$). Applying a one-box-buffer scheme, interactions between the basis and testing functions that are located in the same cluster or in two touching clusters in the lowest level are calculated directly and stored in the memory. During iterative solutions, these near-field interactions are used to perform the partial matrix-vector multiplications

$$\mathbf{y}_{NF} = \bar{\mathbf{Z}}_{NF} \cdot \mathbf{x}, \quad (4)$$

where \mathbf{x} is a vector of coefficients provided the iterative algorithm. There are $\mathcal{O}(N)$ near-field interactions and the sparsity of $\bar{\mathbf{Z}}_{NF}$ is $\mathcal{O}(1/N)$. Using MLFMA, matrix-vector multiplications involving the far-field interactions, i.e.,

$$\mathbf{y}_{FF} = \bar{\mathbf{Z}}_{FF} \cdot \mathbf{x} = (\bar{\mathbf{Z}} - \bar{\mathbf{Z}}_{NF}) \cdot \mathbf{x}, \quad (5)$$

are performed approximately and efficiently by using the diagonalization and factorization of the homogenous-space Green's function [15]. In each matrix-vector multiplication, three main stages,

called aggregation, translation, and disaggregation, are performed on the multilevel tree structure.

The aggregation stage involves the calculation of radiated fields of clusters from the lowest level ($l = 1$) to the top of tree structure ($l = L$). Radiated fields are sampled on the unit sphere at

$$S_l = S_l^\theta \times S_l^\phi = (T_l + 1) \times 2(T_l + 1) \quad (6)$$

points, where

$$T_l \approx 1.73ka_l + 2.16(d_0)^{2/3}(ka_l)^{1/3} \quad (7)$$

is the truncation number determined by the excess bandwidth formula [16]. In (7), a_l is the box size at level l , and d_0 is the desired digits of accuracy. We choose samples regularly spaced in the ϕ direction and use the Gauss-Legendre quadrature in the θ direction [15]. The truncation number depends on the electrical size of the clusters, i.e., $T_l = \mathcal{O}(ka_l)$, and the number of samples can be approximated as

$$S_l = S_l^\theta \times S_l^\phi \approx 2^{(l-1)}S_1^\theta \times 2^{(l-1)}S_1^\phi = 4^{(l-1)}S_1, \quad (8)$$

where $S_1 = \mathcal{O}(1)$.

In the lowest level, the radiated field of a cluster C at a reference point (center of the cluster) r_C can be obtained by combining the radiation patterns of the basis functions inside the cluster, i.e.,

$$\left[\mathbf{F}_C^\theta \right]_{S_1 \times 1} = \sum_{n \in C} x_n \left[\mathbf{f}_n^\theta \right]_{S_1 \times 1} \quad (9)$$

$$\left[\mathbf{F}_C^\phi \right]_{S_1 \times 1} = \sum_{n \in C} x_n \left[\mathbf{f}_n^\phi \right]_{S_1 \times 1}, \quad (10)$$

where \mathbf{f}_n^θ and \mathbf{f}_n^ϕ represent arrays of S_1 elements containing the θ and ϕ components of the radiation pattern of the n th basis function. Similarly, \mathbf{F}_C^θ and \mathbf{F}_C^ϕ are arrays of S_1 elements containing θ and ϕ components of the radiated field of the cluster C . Radiation patterns of basis functions are calculated during the setup of the program and stored in memory to be used multiple times during the iterative solution.

The radiated field of a cluster C in a level $l > 1$ can be obtained by shifting and combining the radiated fields of its sub-clusters $sub\{C\}$, i.e.,

$$\left[\mathbf{F}_C^{\theta, \phi} \right]_{S_l \times 1} = \sum_{C' \in sub\{C\}} \left[\tilde{\mathbf{Y}}_{C \leftarrow C'} \right]_{S_l \times S_l} \cdot \left[\bar{\mathbf{\Gamma}}_{l \leftarrow (l-1)} \right]_{S_l \times S_{l-1}} \cdot \left[\mathbf{F}_{C'}^{\theta, \phi} \right]_{S_{l-1} \times 1}, \quad (11)$$

where $\bar{\mathbf{\Gamma}}_{l \leftarrow (l-1)}$ is a $S_l \times S_{l-1}$ sparse interpolation matrix. We use local Lagrange interpolation to match different sampling rates of consecutive levels [17]. Memory required for interpolations can be reduced significantly by using independent samplings in the θ and ϕ directions, and decomposing interpolation matrices as outer products of vectors. In (11), $\tilde{\mathbf{Y}}_{C \leftarrow C'}$ is a diagonal matrix involving exponential functions to shift the radiated field of cluster C' to the center of C .

In the translation stage, radiated fields computed during the aggregation stage are translated into incoming fields. For each cluster at any level, there are $\mathcal{O}(1)$ clusters to translate the radiated field to. The incoming field to the center of a cluster C due to translations is calculated as

$$\left[\tilde{\mathbf{G}}_C^{\theta, \phi} \right]_{S_l \times 1} = \sum_{C' \in far\{C\}} \left[\tilde{\mathbf{W}} \right]_{S_l \times S_l} \cdot \left[\bar{\mathbf{\Pi}}_{C \leftarrow C'} \right]_{S_l \times S_l} \cdot \left[\mathbf{F}_{C'}^{\theta, \phi} \right]_{S_l \times 1}, \quad (12)$$

where $far\{C\}$ represents clusters that are far from C , $\tilde{\mathbf{W}}$ is a diagonal matrix containing weights of the angular integrations performed at the end of the disaggregation stage, and $\bar{\mathbf{\Pi}}_{C \leftarrow C'}$ is a diagonal

translation operator. Using cubic (identical) clusters, the number of different translation operators is $\mathcal{O}(1)$, independent of the level, due to the symmetry [2]. We also use optimized interpolation methods to calculate translation operators in $\mathcal{O}(N)$ time during the setup stage, i.e., before iterations [18].

Finally, in the disaggregation stage, total incoming fields at cluster centers are calculated from the top of the tree structure to the lowest level. The total incoming field to the center of a cluster C in level $l < L$ is obtained by combining incoming fields due to translations and the total incoming field to the center of its parent cluster $P\{C\}$, i.e.,

$$\left[\mathbf{H}_C^{\theta, \phi} \right]_{S_l \times 1} = \left[\bar{\mathbf{G}}_C^{\theta, \phi} \right]_{S_l \times 1} + \left[\bar{\mathbf{\Gamma}}_{l \leftarrow (l+1)}^T \right]_{S_l \times S_{l+1}} \cdot \left[\bar{\mathbf{Y}}_{C \leftarrow P\{C\}} \right]_{S_{l+1} \times S_{l+1}} \cdot \left[\mathbf{H}_{P\{C\}}^{\theta, \phi} \right]_{S_{l+1} \times 1}, \quad (13)$$

where $\bar{\mathbf{\Gamma}}_{l \leftarrow (l+1)}^T$ is a $S_l \times S_{l+1}$ sparse antepolation (transpose interpolation) matrix [19]. In the lowest level, total incoming fields are received by testing functions, i.e.,

$$\left\{ \bar{\mathbf{z}}^{FF} \cdot \mathbf{x} \right\} [m] = \left[\mathbf{g}_m^\theta \right]_{1 \times S_1} \cdot \left[\mathbf{H}_C^\theta \right]_{S_1 \times 1} + \left[\mathbf{g}_m^\phi \right]_{1 \times S_1} \cdot \left[\mathbf{H}_C^\phi \right]_{S_1 \times 1}, \quad (14)$$

where \mathbf{g}_m^θ and \mathbf{g}_m^ϕ represent arrays of S_1 elements containing the θ and ϕ components of the receiving pattern of the m th basis function inside a cluster C . Similar to radiation patterns of basis functions, receiving patterns are also calculated during the setup of MLFMA.

3. HIERARCHICAL PARALLELIZATION OF MLFMA

In MLFMA, processing time and memory required for all operations at level l are proportional to the product of the number of clusters and the number of samples, i.e.,

$$N_l S_l \approx 4^{(1-l)} N_1 4^{(l-1)} S_1 = N_1 S_1 = \mathcal{O}(N). \quad (15)$$

Then, all levels of MLFMA have equal importance with $\mathcal{O}(N)$ complexity in terms of processing time and memory. Consequently, an efficient parallelization of MLFMA should attempt to obtain the best partitioning for each level. Simple partitioning strategies based on distributing clusters among processors usually fail to provide efficient solutions, since higher levels of MLFMA involve few clusters with large numbers of field samples. Hybrid partitioning strategies, which apply different partitioning strategies for the lower and higher levels, are developed to improve the efficiency of the parallelization of MLFMA [6]–[11]. In those implementations, each cluster at the higher levels is shared by all processors, while each processor is assigned to the same portion of fields for all clusters. Even though hybrid partitioning strategies increase the parallelization efficiency significantly, compared to simple parallelization approaches, the improvement can be insufficient, especially when the number of processors is large.

Recently, we developed a hierarchical partitioning strategy that is well suited for the multilevel structure of MLFMA [13]. In this strategy, clusters and their fields are simultaneously partitioned, and we adjust the number of partitions by considering the number clusters and the number of samples at each level. As an example, Fig. 1 presents a hierarchical partitioning of a four-level tree structure among eight processors labeled 1 to 8. Each level is represented by a three-dimensional rectangular prism. Dimensions of prisms represent the number of clusters and the number of field samples in θ and ϕ directions. From a level to the next higher level, the number of clusters decreases by a factor of four, while the number of samples in each direction increases by a factor of two. At the lowest level, clusters are distributed among eight processors, and each cluster is assigned to a single processor, without any partitioning of field samples. At the next level ($l = 2$), field samples along the θ direction are partitioned among two groups of processors, while the number of cluster partitions is reduced to four. We note that samples of each cluster at this level are shared by two processors. In addition, there is no partitioning in the ϕ direction to avoid excessive communications during the interpolation and antepolation operations. At the third level in Fig. 1, the number of cluster partitions is reduced to two, while samples along θ are distributed among four groups of processors. Finally, at the highest

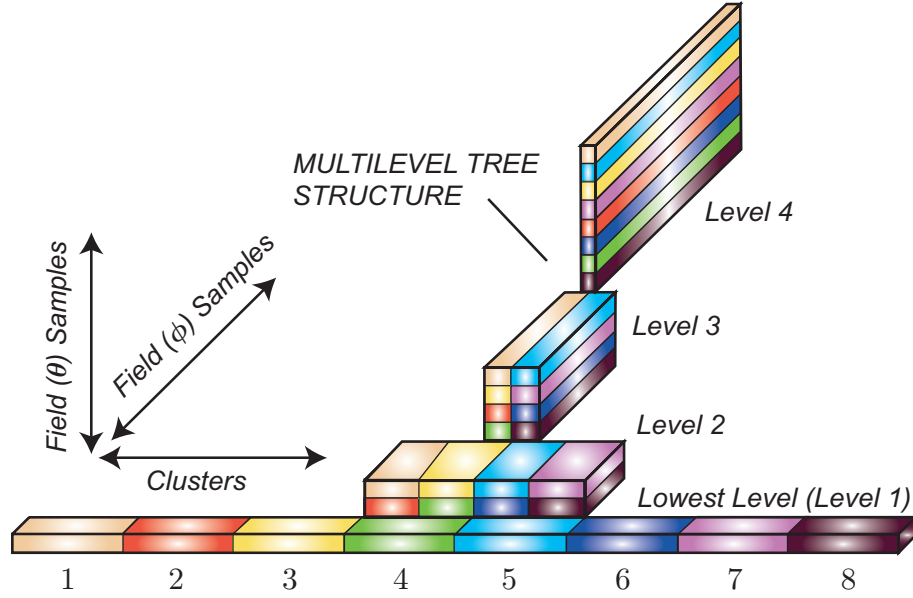


Fig. 1. Hierarchical partitioning of a four-level tree structure among eight processors labeled 1 to 8.

level, clusters are not distributed, while field samples are partitioned along the θ direction among eight processors.

3.1. Hierarchical Partitioning

In general, consider a hierarchical parallelization of MLFMA among $p = 2^i$ processors for some integer i . We choose the number of cluster partitions at level l as

$$p_{l,c} = \max \left\{ \frac{p}{2^{(l-1)}}, 1 \right\} = \max \{ p 2^{(1-l)}, 1 \}. \quad (16)$$

Then, the number of clusters assigned to each processor can be approximated as

$$N_l^p \approx \frac{N_l}{p_{l,c}} \approx \begin{cases} 2^{(1-l)} N_1 / p, & l \leq \log_2(p) \\ 4^{(1-l)} N_1, & l > \log_2(p) \end{cases}. \quad (17)$$

In addition, samples of fields are divided into

$$p_{l,s} = \frac{p}{p_{l,c}} = \min \{ 2^{(l-1)}, p \} \quad (18)$$

partitions along the θ direction, and the number of θ samples assigned to each processor is

$$S_l^{\theta,p} \approx \frac{S_l^\theta}{p_{l,s}} \approx \begin{cases} S_1^\theta, & l \leq \log_2(p) \\ 2^{(l-1)} S_1^\theta / p, & l > \log_2(p) \end{cases}. \quad (19)$$

Also considering the sampling in the ϕ direction, the total number of samples per processor can be approximated as

$$S_l^p = S_l^{\theta,p} S_l^\phi \approx \begin{cases} 2^{(l-1)} S_1, & l \leq \log_2(p) \\ 4^{(l-1)} S_1 / p, & l > \log_2(p) \end{cases}. \quad (20)$$

3.2. Aggregation Stage

Aggregation from a level l to the next higher level $(l + 1)$ starts with one-to-one communications among processors for $1 < l < L$. Data exchanges are required between processors to inflate the local

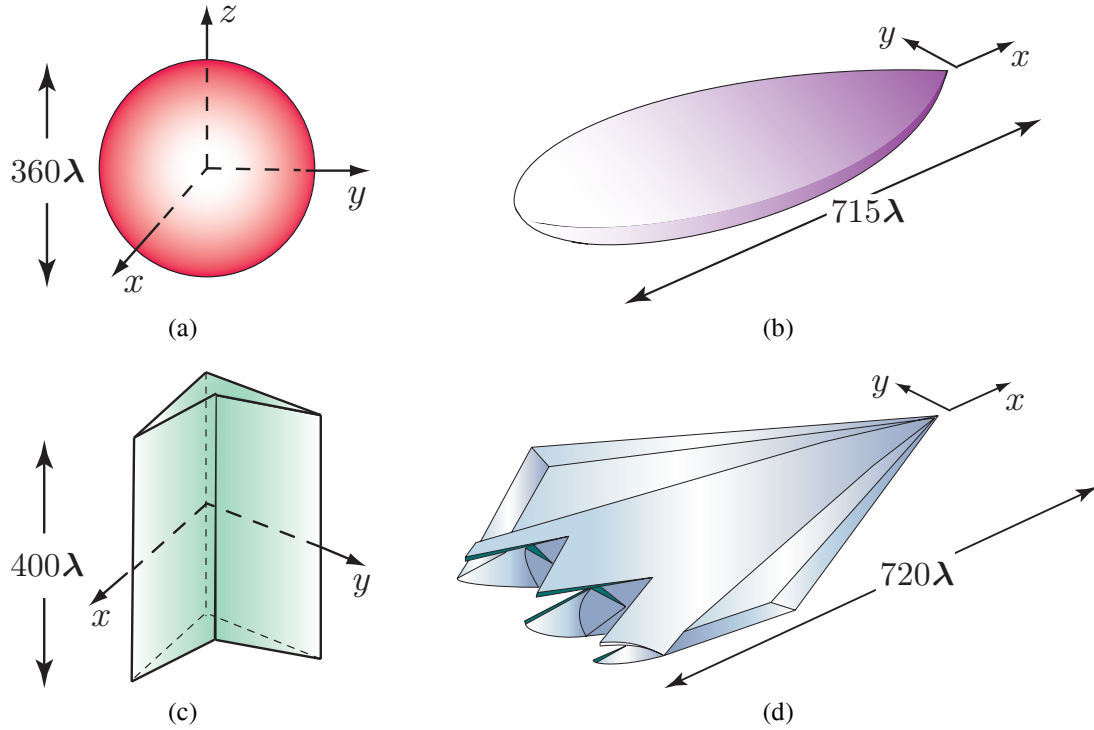


Fig. 2. Large metallic objects involved in scattering problems solved by the parallel MLFMA implementation. (a) Sphere, (b) NASA Almond, (c) wing-shaped object, and (d) Flamme.

data in accordance with interpolation requirements. In general, each processor exchanges data with two other processors, and the communication time is bounded as

$$t_{int,l} \leq N_1 S_1^\phi / p, \quad (21)$$

which is independent of l . We note that aggregations at the lowest level do not involve one-to-one communications to inflate data, since samples are not partitioned in this level. After interpolations and shift operations, radiated fields of clusters at level $(l + 1)$ are obtained. If $l \leq \log_2(p)$, half of the produced data is exchanged between pairs of processors to modify the partitioning in accordance with the hierarchical strategy. The communication time required for those exchanges is bounded as

$$t_{exc,l} \leq N_1 S_1 / p, \quad (22)$$

which is again independent of l .

3.3. Translation Stage

Using the hierarchical partitioning strategy, one-to-one communications are also required during the translation stage for levels $l \leq \log_2(p)$. Because clusters are partitioned and some translations are needed among clusters located in different processors. These communications are performed by pairing processors and transferring radiated fields of clusters between the pairs. Each processor is paired one by one with other $(p_{l,c} - 1) = p 2^{(l-1)} - 1$ processors. Once a pairing is established, radiated fields are transferred. The communication time for these transfers is bounded as

$$t_{trans,l} \leq N_1 S_1 / 2^{(l-1)}, \quad (23)$$

which depends on the level. Communications during translations may become significant for the lower levels, i.e., when l is small. In fact, due to these communications, the translation stage is the major bottleneck in the hierarchical parallelization of MLFMA [20]. In addition to inter-processor translations, there are also intra-processor translations, which are related to clusters located in the

Table 1. Scattering Problems Discretized with More Than 100 Million Unknowns

Problem	Size	Unknowns	Levels	Smallest Box Size	Number of Clusters	Truncation Numbers	Near-Field Sparsity	BiCGStab Iterations
Sphere	360λ	135,164,928	10	0.176λ	23,631,268	5–1009	8.19×10^{-7}	23
Almond	715λ	125,167,104	11	0.175λ	17,213,028	5–1982	9.29×10^{-7}	20
Wing	400λ	121,896,960	10	0.195λ	10,590,407	6–1118	1.17×10^{-6}	17
Flamme	720λ	134,741,760	11	0.176λ	16,209,969	5–1996	1.07×10^{-6}	44

Table 2. Processing Time and Efficiency for the Solution of Problems in Table 1

Problem	16 Processors	32 Processors		64 Processors	
	Processing Time	Processing Time	Efficiency	Processing Time	Efficiency
Sphere	975 minutes	511 minutes	96%	292 minutes	84%
Wing	546 minutes	289 minutes	94%	162 minutes	84%
Almond	769 minutes	394 minutes	98%	215 minutes	90%
Flamme	1186 minutes	646 minutes	92%	345 minutes	86%

Table 3. Memory and Efficiency for the Solution of Problems in Table 1

Problem	16 Processors	32 Processors		64 Processors	
	Total Memory	Total Memory	Efficiency	Total Memory	Efficiency
Sphere	424 GB	438 GB	97%	467 GB	91%
Wing	431 GB	443 GB	97%	500 GB	86%
Almond	385 GB	414 GB	93%	471 GB	82%
Flamme	427 GB	455 GB	94%	513 GB	83%

same processor and that can be performed without any communication.

3.4. Disaggregation Stage

In the disaggregation stage, operations in the aggregation stage are performed in a reverse manner. When incoming fields are calculated at cluster centers at a level $l \leq \log_2(p)+1$, partitioning is modified via data exchanges among processors. Then, incoming fields at cluster centers are interpolated and shifted to the centers of subclusters. Finally, data produced by interpolation operations is deflated via communications between processors.

4. RESULTS

Using the hierarchical partitioning strategy, we are able to solve very large electromagnetics problems discretized with more than 100 million unknowns. As an example, we present the solution of scattering problems involving various metallic objects depicted in Fig. 2. These are (a) a sphere of radius 180λ , (b) a 400λ long wing-shaped object with sharp edges and corners, (c) the NASA Almond of length 715λ , and (d) the stealth airborne target Flamme with a maximum dimension of 720λ . The sphere is illuminated by a plane wave propagating in the $-x$ direction with the electric field polarized in the y direction (H polarization). Other three objects are illuminated by a plane wave propagating in the x - y plane at a 30° angle from the x axis with the electric field polarized in the z direction (V polarization). Problems are formulated with the combined-field integral equation and solved iteratively by using the biconjugate-gradient-stabilized (BiCGStab) algorithm.

In this study, our major purpose is solving very large electromagnetics problems both *fast* and *accurately*. Our comments regarding these solutions are as follows:

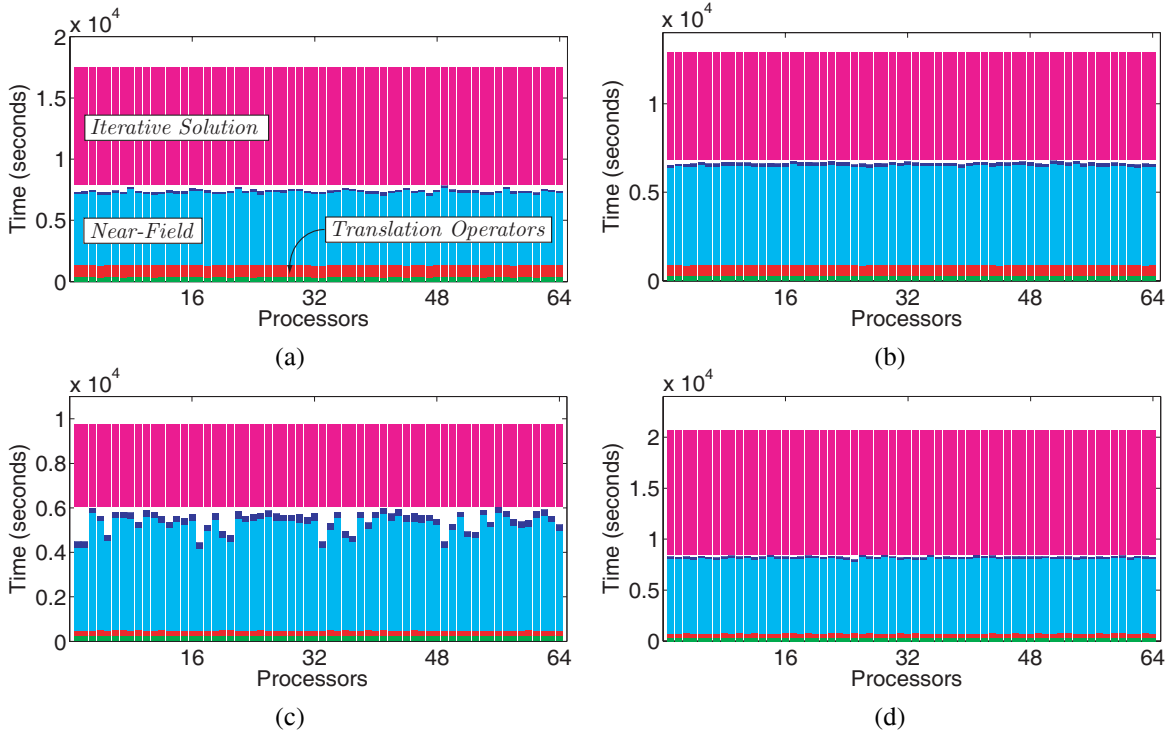


Fig. 3. Details of the processing time for the solution of scattering problems listed in Table 1. (a) Sphere, (b) NASA Almond, (c) wing-shaped object, and (d) Flamme.

- Accuracy: Problems are solved accurately by discretizing objects with $\lambda/10$ triangles. Both near-field and far-field interactions (matrix elements) are calculated with maximum 1% error. We note that the accuracy affects the efficiency of solutions significantly. For example, most of the communications during aggregation and disaggregation stages could be avoided by reducing the number of interpolation points. This would increase the parallelization efficiency and reduce the processing time, but the accuracy would deteriorate. In addition, solutions could be relaxed by using coarser discretizations or by reducing the truncation numbers, which would enable the solution of larger problems by sacrificing the accuracy.
- Efficiency: Problems are solved efficiently with the minimum processing time. Larger problems could be solved at the cost of increasing processing time by performing some of the computations on the fly and reducing the memory requirements. Such tricks would also increase the parallelization efficiency since the computations would dominate the communications. In addition, problems are solved on a 16-node cluster of relatively fast 3.0 GHz Intel Xeon processors. Using slower processors would increase parallelization efficiency due to slower computations, but the processing time would also increase.

Table 1 lists important parameters related to solutions. Tree structures, which involve 10–11 levels and 10–24 million clusters, are constructed by using a top-down clustering scheme. Truncation numbers vary from 5 to 1996, and the sparsity of near-field interactions is about 10^{-6} for all problems. Iterative solutions involve 17 to 44 iterations for 10^{-3} residual error. Table 2 presents the processing time when solutions are parallelized among 16, 32, and 64 processors. In addition to total times including setup and iterative solution parts, we provide the parallelization efficiency obtained for 32 and 64 processors with respect to 16 processors. Using 64 processors, the parallelization efficiency in terms of processing time is more than 80% for all problems. Due to this relatively high efficiency provided by the hierarchical partitioning strategy, we are able to perform each solution in 3 to 6 hours. Table 3 lists the total memory required for solutions. Increasing the number of processors raise the memory requirement since the efficiency of the parallelization is not perfectly 100%. Nevertheless, using 64

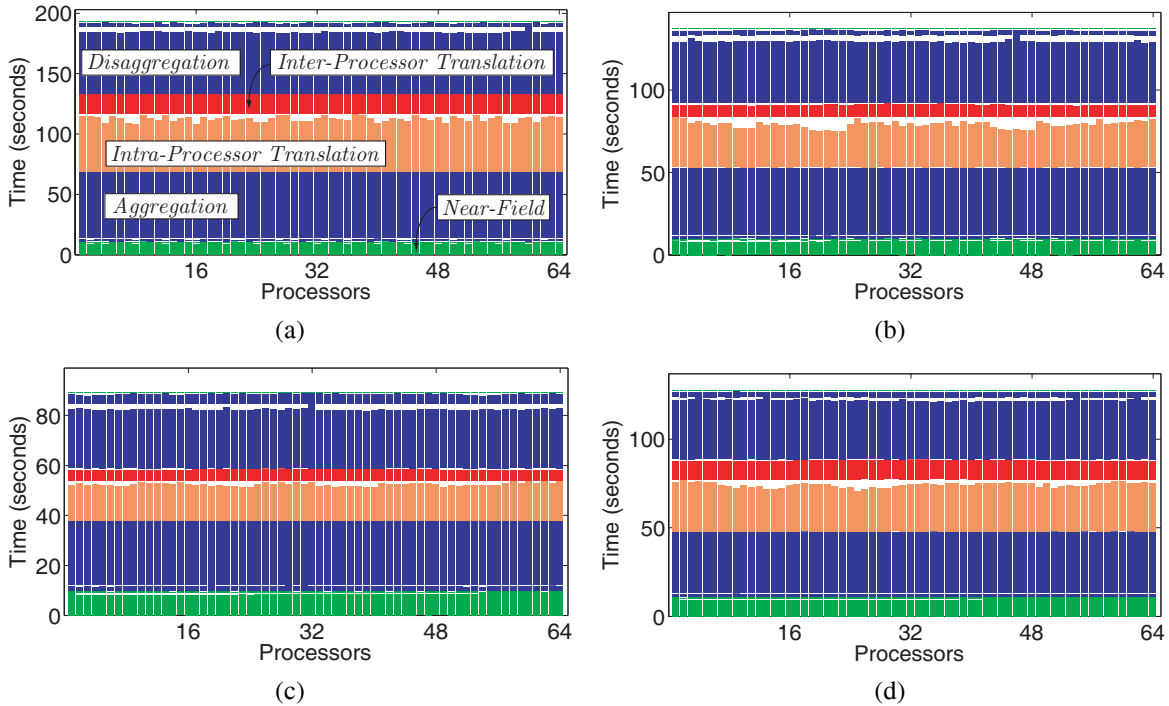


Fig. 4. Details of the matrix-vector multiplications for the solution of scattering problems listed in Table 1. (a) Sphere, (b) NASA Almond, (c) wing-shaped object, and (d) Flamme.

processors, the parallelization efficiency in terms of memory usage is also more than 80% for all problems. Solutions using 64 processors are detailed in the next subsections.

4.1. Details of Processing Time

Fig. 3 presents the details of the processing time for 64-processor solutions. We observe that the calculation of near-field interactions and the iterative solution are dominant parts. The processing time for near-field interactions is perfectly balanced among processors for all cases, except for the wing-shaped object. We use load-balancing algorithms in order to distribute near-field interactions evenly among processors. For the wing-shaped object, however, this strategy does not lead a perfect parallelization in terms of processing time. Because, we calculate all interactions accurately with 1% error by using adaptive integration methods, and the number of integration points, thus the processing time, for an interaction depends on the relative positions of the basis and testing functions. On the discretized wing-shaped object, there are very difficult interactions that require longer processing times, compared to other interactions. Using a load-balancing algorithm without considering the computation time, those difficult interactions are accumulated in some processors, leading to unequal processing times for the near-field stage. Nevertheless, we still prefer distributing near-field interactions equally among processors, since this is optimal in terms of memory and it is difficult to guess the computation time for each interaction a priori. Finally, for 64-processor solutions, Fig. 4 presents the details of matrix-vector multiplications, which involve near-field, aggregation, intra-processor translation, inter-processor translation, and disaggregation stages.

4.2. Details of Memory Usage

Fig. 4 presents the details of the memory usage for 64-processor solutions. Instead of processors, we consider memory used in each computing node from 1 to 16. A majority of memory is required to store near-field interactions and radiation/receiving patterns of basis and testing functions. Another significant contribution is due to aggregation/disaggregation arrays, which contain radiated and in-

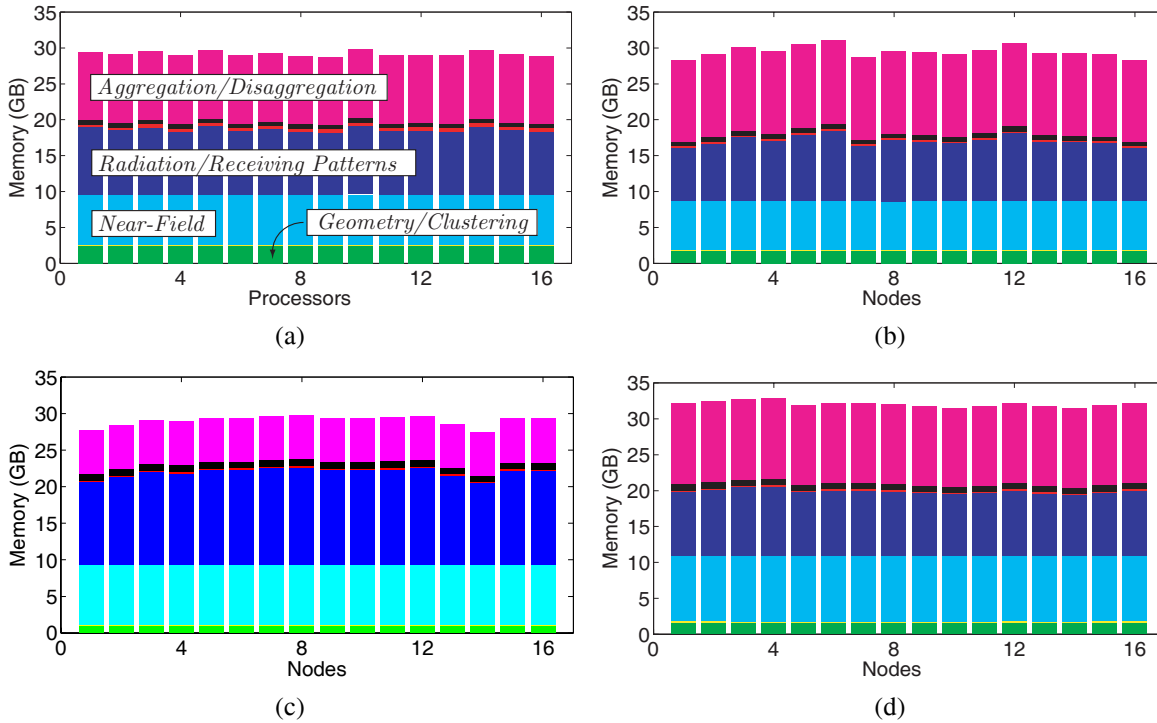


Fig. 5. Details of memory used for the solution of scattering problems listed in Table 1. (a) Sphere, (b) NASA Almond, (c) wing-shaped object, and (d) Flamme.

coming fields of clusters calculated during matrix-vector multiplications. Memory used in computing nodes are not equal, mostly due to different amounts of radiation and receiving patterns of basis and testing functions assigned to processors. Those patterns are distributed according to the partitioning of the tree structure. In general, lowest-level clusters are distributed equally among processors. However, populations of clusters, i.e., numbers of basis and testing functions in clusters, may vary significantly. A load-balancing algorithm, which accounts for populations of clusters, could be used to improve the distribution of radiation and receiving patterns. However, this method would deteriorate the load-balancing of matrix-vector multiplications in terms of both memory and processing time.

4.3. Radar Cross Section

To demonstrate the accuracy of solutions, we present the bistatic radar cross section (RCS) values for the sphere of radius 180λ . In Fig. 6(a), the normalized RCS ($RCS/\pi a^2$, where a is the radius of the sphere in meters) is plotted in decibels (dB). In the figure, 0° and 180° correspond to the back-scattering and forward-scattering directions, respectively. Computational values are compared with analytical values obtained by a Mie-series solution. For an easy comparison, Fig. 6(b) presents the same results from 175° and 180° . We observe that computational and analytical results perfectly agree with each other. In Fig. 7, we present RCS values for large geometries depicted in Figs. 1(b)–(d), namely, the NASA Almond, a wing-shaped object, and the Flamme. The normalized RCS (RCS/λ^2) is plotted in dB on the x - y plane as a function of the bistatic angle. In the plots, 30° and 210° correspond to back-scattering and forward-scattering directions, respectively. Fig. 7(a) present VV and VH polarizations, respectively, of the RCS of the NASA Almond. We observe relatively high co-polar RCS values from 90° to 210° , while the RCS in the back-scattering direction is considerably small. Fig. 7(b) present RCS values for the wing-shaped object. In this case, the back-scattered RCS is quite large, and we observe peaks at diverse angles due to strong reflections. Finally, Fig. 7(c) present RCS values for the stealth airborne target Flamme. The back-scattered RCS of this target is extremely low; it is 100 dB less than the forward-scattered RCS.

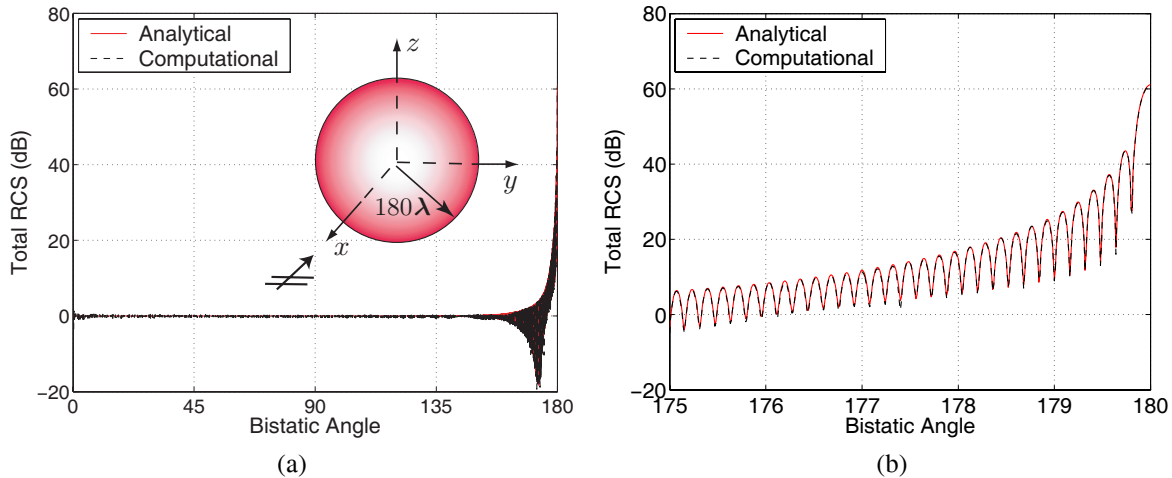


Fig. 6. Bistatic RCS (in dB) of a sphere of radius 180λ (a) from 0° to 180° and (b) from 175° to 180° , where 180° corresponds to the forward-scattering direction.

REFERENCES

- [1] J. Song, C.-C. Lu, and W. C. Chew, "Multilevel fast multipole algorithm for electromagnetic scattering by large complex objects," *IEEE Trans. Antennas Propagat.*, vol. 45, no. 10, pp. 1488–1493, Oct. 1997.
- [2] W. C. Chew, J.-M. Jin, E. Michielssen, and J. Song, *Fast and Efficient Algorithms in Computational Electromagnetics*. Boston, MA: Artech House, 2001.
- [3] A. J. Poggio and E. K. Miller, "Integral equation solutions of three-dimensional scattering problems," in *Computer Techniques for Electromagnetics*, R. Mittra, Ed. Oxford: Pergamon Press, 1973, Chap. 4.
- [4] R. F. Harrington, *Field Computation by Moment Methods*. New York: Macmillan, 1968.
- [5] S. Velamparambil, W. C. Chew, and J. Song, "10 million unknowns: Is it that big?," *IEEE Ant. Propag. Mag.*, vol. 45, no. 2, pp. 43–58, Apr. 2003.
- [6] S. Velamparambil and W. C. Chew, "Analysis and performance of a distributed memory multilevel fast multipole algorithm," *IEEE Trans. Antennas Propag.*, vol. 53, no. 8, pp. 2719–2727, Aug. 2005.
- [7] Ö. Ergül and L. Gürel, "Efficient parallelization of multilevel fast multipole algorithm," in *Proc. European Conference on Antennas and Propagation (EuCAP)*, 2006.
- [8] L. Gürel and Ö. Ergül, "Fast and accurate solutions of integral-equation formulations discretised with tens of millions of unknowns," *Electronics Lett.*, vol. 43, no. 9, pp. 499–500, Apr. 2007.
- [9] Ö. Ergül and L. Gürel, "Fast and accurate solutions of large-scale scattering problems with parallel multilevel fast multipole algorithm," in *Proc. IEEE Antennas and Propagation Soc. Int. Symp.*, 2007, pp. 3436–3439.
- [10] Ö. Ergül and L. Gürel, "Parallel-MLFMA solution of CFIE discretized with tens of millions of unknowns," in *Proc. 2nd European Conference on Antennas and Propagation (EuCAP)*, 2007.
- [11] Ö. Ergül and L. Gürel, "Efficient parallelization of the multilevel fast multipole algorithm for the solution of large-scale scattering problems," *IEEE Trans. Antennas Propagat.*, vol. 56, no. 8, pp. 2335–2345, Aug. 2008.
- [12] Ö. Ergül and L. Gürel, "Hierarchical parallelization of the multilevel fast multipole algorithm for the efficient solution of large-scale scattering problems," in *Proc. IEEE Antennas and Propagation Soc. Int. Symp.*, 2008.
- [13] Ö. Ergül and L. Gürel, "Hierarchical parallelisation strategy for multilevel fast multipole algorithm in computational electromagnetics," *Electronics Lett.*, vol. 44, no. 1, pp. 3–5, Jan. 2008.
- [14] S. M. Rao, D. R. Wilton, and A. W. Glisson, "Electromagnetic scattering by surfaces of arbitrary shape," *IEEE Trans. Antennas Propagat.*, vol. AP-30, no. 3, pp. 409–418, May 1982.
- [15] R. Coifman, V. Rokhlin, and S. Wandzura, "The fast multipole method for the wave equation: a pedestrian prescription," *IEEE Ant. Propag. Mag.*, vol. 35, no. 3, pp. 7–12, Jun. 1993.

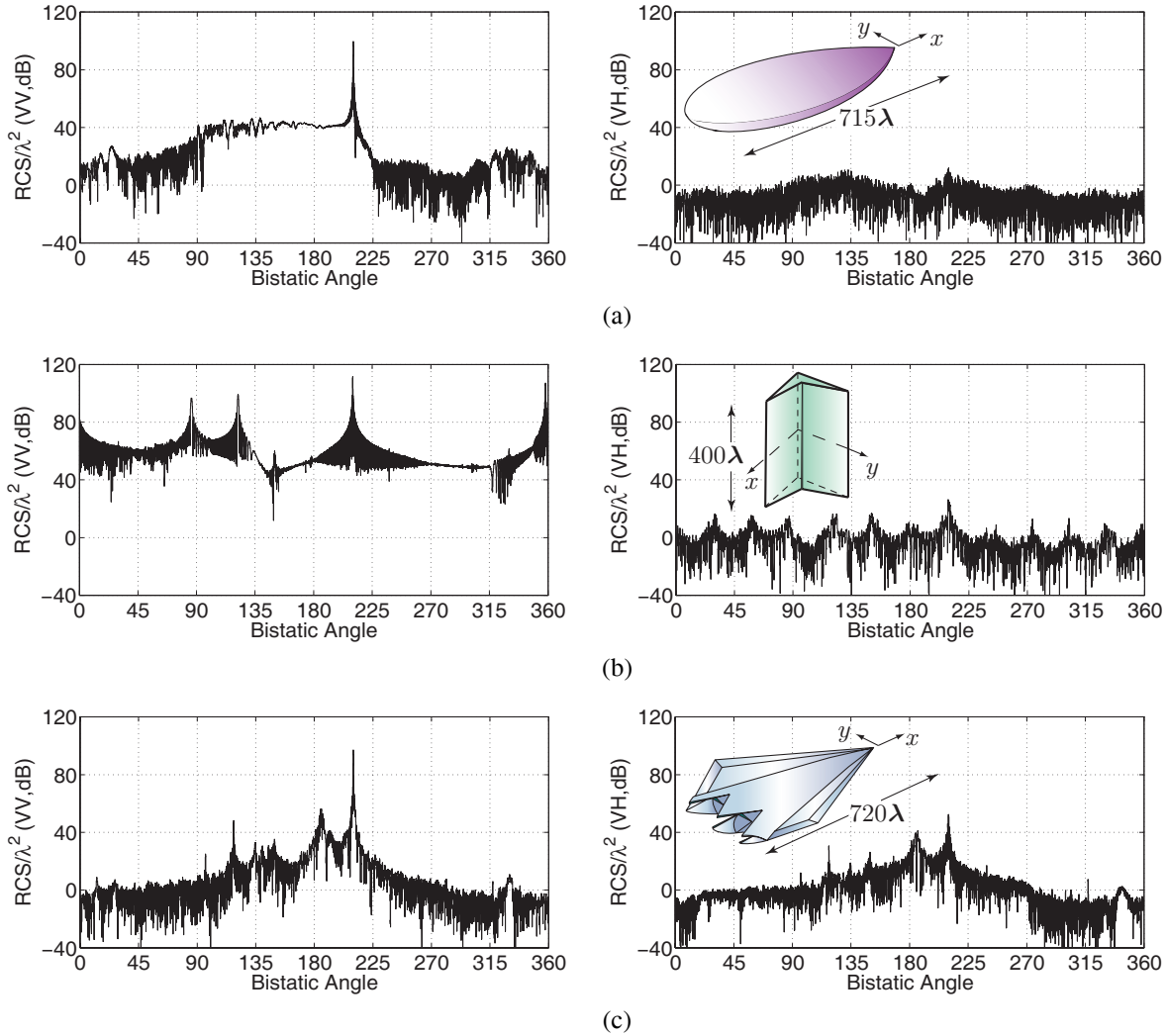


Fig. 7. Normalized bistatic RCS (RCS/λ^2 in dB) of the targets in Figs. 1(b)–(d) on the x - y plane, where 30° and 210° correspond to the back-scattering and forward-scattering directions, respectively. (a) NASA Almond, (b) wing-shaped object, and (c) Flamme.

- [16] S. Koc, J. M. Song, and W. C. Chew, "Error analysis for the numerical evaluation of the diagonal forms of the scalar spherical addition theorem," *SIAM J. Numer. Anal.*, vol. 36, no. 3, pp. 906–921, 1999.
- [17] Ö. Ergül and L. Gürel, "Enhancing the accuracy of the interpolations and antepolations in MLFMA," *IEEE Antennas Wireless Propag. Lett.*, vol. 5, pp. 467–470, 2006.
- [18] Ö. Ergül and L. Gürel, "Optimal interpolation of translation operator in multilevel fast multipole algorithm," *IEEE Trans. Antennas Propag.*, vol. 54, no. 12, pp. 3822–3826, Dec. 2006.
- [19] A. Brandt, "Multilevel computations of integral transforms and particle interactions with oscillatory kernels," *Comp. Phys. Comm.*, vol. 65, pp. 24–38, Apr. 1991.
- [20] Ö. Ergül and L. Gürel, "Efficient parallelization of the multilevel fast multipole algorithm using a hierarchical partitioning strategy," *IEEE Trans. Antennas Propag.*, submitted for publication.

SECTION 11

- 11.1. M. B. Tabakcioglu and A. Kara, “*Discussions of Various UTD and PO Solutions for Multiple-Edge Diffractions in Urban Radio Propagation Modeling*” 11-1
- 11.2. V. B. Yurchenko and A. Altintas , “*Advanced Physical Optics Modeling of THz Dielectric Lenses*” 11-7
- 11.3. Mustafa Turkmen, Sabri Kaya, Celal Yildiz and Kerim Guney, “*Adaptive Neuro-Fuzzy Inference System for Calculating the Characteristic Impedances of Multilayer Homogeneous Coupling Structures*” 11-15
- 11.4. A. Kara, E. Uray Aydin, M.E. Ozbek, N. Cagiltay, R. Oktem, C.C. Aydin, E. Ozyurt, M. Atas and A.C. Yapici, “*Remote Experimentation in RF and Microwaves*” 11-21

Discussions of Various UTD and PO Solutions for Multiple-Edge Diffractions in Urban Radio Propagation Modeling

M. B. Tabakcioglu¹, A. Kara¹

¹Atilim University, Turkey

Abstract – This paper presents a class of algorithms based on Uniform Theory of Diffraction (UTD) for multiple edge transition zone diffraction. It aims to discuss simulation results for comparison of UTD and its improved version including slope UTD model (S-UTD) and slope UTD with convex hull model (S-UTD-CH). Comparison of the models are presented for both accuracy and computation time. Moreover, S-UTD is compared with a particular numerical solution of Kirchhoff-Huygens integrals, i.e., Physical Optics (PO). Results of extensive simulations are summarized, and accuracy of S-UTD and PO based model are discussed.

1. INTRODUCTION

Multiple edge diffraction has been considered in many radio propagation models for radio network planning in radio communications and broadcasting systems. When one edge is placed in the transition zone of the neighbouring edge (i.e., multiple edge transition zone diffraction), direct application of ray optical techniques such as Uniform Theory of Diffraction (UTD) fail [1-5]. Improvements to UTD in order to handle multiple edge transition zone diffraction problems have been discussed in [4] and its references. On the other hand, field predictions in environment models involving multiple edge transition zones could easily be solved numerically via physical optics (PO) based approaches [6, 7]. In general, there is, however, a trade off between accuracy and computation time when radio propagation for multiple edge diffraction problems is considered [1-5].

In this paper, firstly, UTD based models are reviewed shortly and improved models of UTD proposed in [2-5] are described briefly. Then, simulation results for comparison of improved UTD solutions, namely, Slope UTD (S-UTD) [1-3] and Slope UTD with convex hull (S-UTD-CH) [4] are presented. Finally, comparison of S-UTD/S-UTD-CH with physical optics (PO) solutions based on Kirchhoff-Huygens approximation [6, 7] is presented, and their accuracy and computation time is discussed.

2. SLOPE UTD (S-UTD)

UTD has been used to estimate field strength in complex building structures urban and suburban environments. In case of multiple edge transition zone diffraction, UTD is unable to predict accurate field strengths [1], and requires a first order derivative, known as slope UTD (S-UTD), to improve its accuracy [1-5]. For a single edge, the field strength predicted by S-UTD is [1-5]

$$E = \left[E_i D(\alpha) + \frac{\partial E_i}{\partial \alpha} d_s(\alpha) \right] A(s) e^{-jks} \quad (1)$$

where E_i is the incident field, α is the angle between the incident and the diffracted ray as

illustrated in Fig. 1, $A(s)$ is the spreading factor and k is the wave number. $D(\alpha)$ and $d_s(\alpha)$ are amplitude and slope diffraction coefficients, respectively [1]. The distance parameters L and L_s , appearing in amplitude and slope diffraction coefficients have to be calculated via amplitude, slope and phase continuities as discussed in [2-5]. In case of multiple transition zone diffraction, it has been shown that shadow boundary points, (P_1, P_2 and P_4) as illustrated in Fig.1, should be taken into account in calculating the distance parameters, L and L_s [2-5].

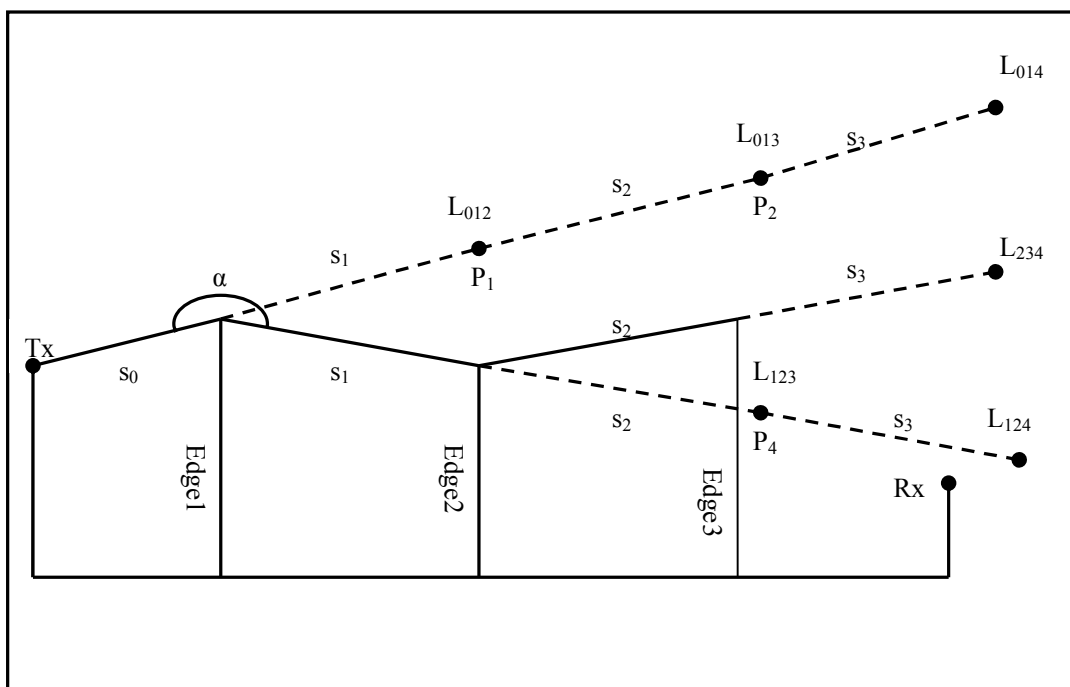


Fig. 1 Ray geometry of multiple knife edge diffraction for S-UTD

3. SLOPE UTD WITH CONVEX HULL (S-UTD-CH)

S-UTD-CH is based on the use of Fresnel Zone concept along with S-UTD, and provides an improvement to S-UTD implementation in terms of computation time and accuracy. As discussed in detail in [4, 5], Fresnel zone concept is not new, and has widely been used in UTD based radio propagation modeling in urban/suburban and rural areas. For multiple edge geometry such as the one shown in Fig. 1, convex hull is described as a polygon formed by some selected edges between the transmitter and receiver positions. Selection of the edges (or ignored edges) forming the convex hull is based on Fresnel zone concept and implementation of the algorithm is described in [4]. The motivation for this approach was to reduce both computation time and error arising in S-UTD model itself when the number of diffraction exceeds 10 [1-4].

4. COMPARISON OF RAY THEORETIC MODELS

To compare accuracy of ray theoretic models (UTD, S-UTD and S-UTD-CH), a particular multiple edge geometry having 9 equally-spaced edges (or screens) is considered. All simulations are conducted in the following parameter ranges that might represent a canonical multiple edge transition zone diffraction geometry as reported in [2, 4]:

The transmitting and receiving antenna heights (h_T , h_R): 18m and 1.5m

Heights of edges (h): uniformly distributed with $[18-\Delta h, 18-\Delta h]$, $\Delta h=1, 3$ and 6

Distance between the edges (d): 25 and 50m

Operating frequency (f): 0.9GHz, 1.8GHz and 2.1GHz

Instead of analyzing contributions of each parameter range to the field strength prediction or accuracy of the approach, a combined parameter called transition region width [2] is used in simulations. For $d \gg \Delta h$, transition region width (TRW) is calculated [2, 4] via

$$TRW \cong \frac{\Delta h^2}{\lambda d} \quad (2)$$

Algorithms for UTD, S-UTD and S-UTD-CH have been developed in MATLAB environment, and simulations were performed to cover all parameter ranges listed above. Table 1 shows the mean (μ) and standard deviation (σ) of error for excess loss predicted by UTD and S-UTD-CH assuming that S-UTD is the most accurate one. All parameter ranges listed above can be represented by some TRW values calculated from (2). In Table 1, the rightmost column represents “average number of ignored edges” by S-UTD-CH model (for each run, actually this is an integer number out of 9 edges). Average computation time of each model including S-UTD is also presented in Table 1. In simulations, there were 10 runs for each model at each TRW value, and mean error (μ) and standard deviation (σ) values of error are calculated accordingly. In all model implementation, phase summing of ray fields is used.

Table 1 Comparison of UTD based models (accuracy and computation time)

TRW	μ (dB) (S-UTD-CH)	σ (dB) (S-UTD-CH)	μ (dB) (UTD)	σ (dB) (UTD)	Time (s) (S-UTD-CH)	Time (s) (S-UTD)	Time(s) (UTD)	Edge (#)
0,2	0,01	0,01	4,97	2,22	937,2	1113,1	5,0	0,2
0,3	0,01	0,02	4,31	3,00	962,8	1166,1	5,6	0,3
0,5	0,04	0,05	3,21	3,14	618,8	1121,0	5,3	0,8
1,1	0,09	0,12	3,92	2,50	179,4	1133,7	5,5	2,0
1,3	0,08	0,09	3,42	3,73	208,8	1192,0	6,0	1,7
2,2	0,09	0,09	1,35	1,03	108,8	1085,4	5,2	3,1
2,5	0,11	0,18	1,47	1,35	46,1	1092,6	5,1	2,9
4,3	0,09	0,08	1,00	0,79	3,4	1111,3	5,4	3,9
4,9	0,13	0,18	1,29	1,31	94,8	1043,2	5,0	2,2
5,0	0,09	0,09	1,29	0,86	2,4	1091,7	5,5	4,3
8,6	0,14	0,30	1,48	1,24	32,0	1006,5	4,5	3,9
9,7	0,09	0,09	1,16	1,47	23,2	1076,1	5,0	3,5

10,1	0,14	0,12	0,91	1,35	3,9	1040,0	4,9	4,6
------	------	------	------	------	-----	--------	-----	-----

First, UTD and S-UTD can be compared for accuracy as reported in [2, 4]. Then, S-UTD and S-UTD-CH can be compared for computation time. For multiple transition zone diffraction for $TRW=0.2$ or lower, while UTD is faster (~ 5 s) and simpler to implement than S-UTD (~ 1100 s), it is not as accurate as S-UTD (>4 dB mean error). Therefore, S-UTD-CH can be used in some TRW ranges ($TRW>1$). For example, S-UTD-CH predicts field strength as accurate as S-UTD for $TRW>0.5$ with relatively smaller computation time (179 s vs. 1133 s). In such cases, eliminating one edge might reduce computation time pretty much due to the complexity of slope diffraction algorithm itself. However, S-UTD-CH has no advantage for very small TRW values (<0.5) where there is no edge ignored in this case. For $TRW>3$ values, UTD might be satisfactory for accurate prediction if small error can be tolerated as reported in [4].

5. COMPARISON OF RAY THEORETIC MODELS WITH PO

Another class of models to solve multiple edge diffraction problems is based on numerical evaluation of physical optics (PO) integrals or so-called PO solutions [5]. Since these models involve numerical computation of PO integrals at each point in field domain, they are considered to have ultimate accuracy [2, 6 and 7]. However, these models have extremely large computation times compared with improved UTD models introduced in section 2. In this section, accuracies and computation time of improved UTD models are compared with a PO model that has been reported in [6]. In this sense, this would be the first time that the accuracy of ray theoretic models, i.e. S-UTD and S-UTD-CH, is statistically compared with a well-known PO model for multiple edge diffraction problems. In simulations, structural parameters of screens for the PO model proposed in [6] were chosen appropriately to simulate absorbing knife edges (screens).

There will be two different simulations for accuracy and computation time in this section. The first canonical multiple edge geometry in section 2 is used with the following parameters:

The transmitting antenna height (h_T): 5 and 10m, Heights of edges (h): uniformly distributed over $[10-\Delta h, 10-\Delta h]$ with $\Delta h=4$ m, Distance between the edges (d): 50m, operating frequency (f): 1.8GHz

Firstly, randomly distributed edge heights for 10 equally-spaced edges are generated. Then, the field strength is calculated at the tip of the last edge using the three models for the height distribution. There was a total of 25 height distributions generated in simulations. The PO model [4] is taken as the reference model since it is a fully numerical algorithm and highest accuracy compared with the ray models (S-UTD-CH and S-UTD). Then, the mean error (μ) and standard deviation (σ) for excess loss predicted by ray theoretic models, i.e. S-UTD-CH [4] and S-UTD [2-4], are calculated accordingly. Table 2 presents the results of the simulations for two transmitting antenna heights. Here, since the motivation was to investigate the accuracy of S-UTD compared with PO for multiple edge transition zone diffraction, only lower transmitting antenna heights ($h_T=5, 10$ m) are considered (transition zone diffraction situation). For elevated transmitting antenna heights, UTD is satisfactory for most cases [2, 4 and 7] and the field predicted is less dependent on transition zone diffraction effects. Because direct rays or single diffracted rays are considered to dominant in this case, and their contributions to the received field strength are relatively higher than higher order rays.

As shown in Table 2, S-UTD exhibits a mean error of less than 0.6 dB after 9 diffractions. Simulations were carried out up to 9 diffractions since S-UTD has an increasing error after 9 diffractions for equally-spaced edge geometry as reported in [2, 3]. This error inherent in S-UTD was one of the motivations in developing S-UTD-CH algorithm in [4]. As it is well-known, PO model requires very large computation times since it is based on computation of field at each point over the screens. Therefore, S-UTD and PO were not compared for computation time.

A rather fast and a similar algorithm based on selection of dominant edges (isolated diffracting edges-IDE) contributing much to the field strength has been proposed and compared with the PO model in [7]. However, the accuracy of the model was reported to be unsatisfactory, especially, for lower transmitting antenna heights where transition zone diffraction is the dominant mechanism [2-7]. It was the transition zone diffraction effects that cause this error.

Table 2 Comparison of ray theoretic models with the PO model for accuracy

h_T (m)	μ (dB) (S-UTD-CH)	σ (dB) (S-UTD-CH)	μ (dB) (S-UTD)	σ (dB) (S-UTD)
5	0.42	7.51	0.58	7.43
10	0.55	7.29	0.60	7.28

The second canonical multiple edge geometry in section 2 is used with the same parameters for elevated transmitting antennas. (h_T): 15 and 20m

Firstly, again randomly distributed edge heights for 15 equally-spaced edges are generated. Then, the field strength is calculated at the top of the last edge using the three models (UTD, S-UTD-CH and PO) for the height distribution. There was a total of 20 height distributions generated in simulations. Then, the mean error (μ) and standard deviation (σ) for excess loss predicted by ray theoretic models, i.e. S-UTD-CH, are calculated accordingly. Also ray theoretic models are compared with each other. Table 3 presents the results of the simulations for elevated two transmitting antenna heights. Here, since the motivation was to investigate the accuracy of S-UTD-CH compared with PO and the accuracy of S-UTD-CH compared with UTD for multiple edge transition zone diffraction, higher transmitting antenna heights ($h_T=15, 20$ m) are considered.

In Table 3, leftmost column shows the transmitter height. Next three column shows the average computation time. Simulations are made in C/C++ environment. Next two columns shows mean error and standard deviation for excess loss predicted by S-UTD-CH. The rightmost columns show the mean error and standard deviation for excess loss between S-UTD-CH and UTD. S-UTD-CH exhibits a mean error of less than 1.33 dB after 14 diffractions. Moreover, as can be seen from the Table 3, UTD is not as accurate solution as S-UTD-CH. Furthermore, S-UTD-CH is faster than the PO method.

Table 3 Comparison of S-UTD-CH with the PO and UTD for accuracy and computation time

h_T (m)	μ (s) (UTD)	μ (s) (S-UTD-CH)	μ (s) (PO)	μ (dB) (PO)	σ (dB) (PO)	μ (dB) (UTD)	σ (dB) (UTD)
15	128	789	802	1.33	7.36	3.14	7.85
20	101	4	802	-1.27	7.53	2.81	2.13

6. CONCLUSION

In this paper, comparison of UTD and its improved version for multiple transition zone diffraction problems are presented. Transition region width (TRW) has been used as a geometrical parameter for measuring transition zone diffraction effects. For smaller TRW values, contribution of S-UTD cannot be ignored while UTD without slope diffraction can be used for relatively larger TRW values. For multiple transition diffraction, S-UTD has larger computation time with higher accuracy while UTD has small computation time with lower accuracy. It has been shown that S-UTD-CH that uses a selection algorithm of diffracting edges based on Fresnel zone concept would be used for a range of TRW values. S-UTD-CH provides not only very low computation time but also very accurate results for multiple edge transition zone diffractions in this TRW range ($\sim 1 < \text{TRW} < 3$).

On the other hand, S-UTD and S-UTD-CH have been compared with the PO [6] for the first time for accuracy in this paper. It has been shown that S-UTD exhibits very small error for 9 diffractions (all are in transition zones). Furthermore, S-UTD-CH has been compared with PO and UTD for accuracy and computation time. It has been shown that S-UTD-CH shows very small error for 14 diffractions with less computation time.

As a conclusion, UTD based models can still be used for radio planning tools due to the fact that they have relatively small computation time. However, they still require further improvements for more accurate field predictions in case of multiple edge transition zone diffractions.

ACKNOWLEDGEMENT

This work is partially supported by TUBITAK (The Scientific and Technological Research Council of Turkey) under the Grant No.105E083.

REFERENCES

1. Andersen, J. B., "UTD multiple-edge transition zone diffraction", *IEEE Trans. Antennas and Prop.*, Vol. 45, 1093-1097, 1997
2. Rizk, K., Valenzuela, R., Chiznik, D. and Gardiol, F., "Application of the slope diffraction method for urban microwave propagation prediction", *IEEE Vehicular Tech. Conf.*, Ottawa, Canada, May 1998 Vol. 2, 1150 – 1155.
3. Tzaras, C. and Saunders, S. R., "An improved heuristic UTD solution for multiple-edge transition zone diffraction", *IEEE Trans. Antenna Propagation*, Vol. 49, No. 12, 1678 -1682, 2001
4. Tabakcioglu, M. B. and Kara, A., "On the improvements in the multiple edge transition zone diffraction", *EuCAP'2007*, Edinburgh, UK, November 2007.
5. Koutitas, G. and Tzaras, C., "A slope UTD solution for cascade of multi-shaped canonical objects", *IEEE Trans. Antenna Propagation*, Vol. 54, No. 10, 2969 -2976, 2006
6. Chung, H. K. and Bertoni, H. L. "Range-Dependent Path-Loss Model in Residential Areas for the VHF and UHF Bands", *IEEE Trans. Antenna Propagation*, Vol. 50, No. 1, 1 -11, 2002
7. Chung, H. K. and Bertoni, H. L., "Application of isolated diffraction edge (IDE) method for urban microwave path loss prediction", *IEEE Vehicular Tech. Conf.*, Florida, USA, 2003, Vol. 1, 205 – 209

Advanced Physical Optics Modeling of THz Dielectric Lenses

V. B. Yurchenko¹ and A. Altintas²

¹Institute of Radiophysics and Electronics, National Academy of Sciences of Ukraine
12 Proskura St., Kharkov, Ukraine

²Electrical and Electronics Engineering Dept., Bilkent University, Ankara, Turkey

Abstract – We propose an advanced physical optics formulation for the accurate modeling of dielectric lenses used in quasi-optical systems of millimeter, submillimeter, and infrared wave applications. For the comparison, we obtain a full-wave solution of a two-dimensional lens problem and use it as a benchmark for testing and validation of asymptotic models being considered.

1. INTRODUCTION

Accurate design of large-scale THz quasi-optical systems with dielectric lenses requires advanced asymptotic modeling of lenses similar to physical optics simulations of reflector antennas. An example of a system of this kind is QUaD, a millimeter-wave Cassegrain telescope with re-focusing dielectric lenses designed to measure the cosmic microwave background polarization properties [1]. For the high precision instrument to be made, an extremely accurate modeling of aberrations introduced by the telescope is needed. In the meantime, because of large electrical size of lenses, no full-wave solution can be obtained in these cases. This requires advanced asymptotic methods for the wave-like modeling of dielectric lenses used by the telescope optics. Other applications of advanced asymptotic methods may include optics for infrared and THz imaging (e.g., in security checks), automotive radars for collision-avoidance systems [2], special microlenses for optical recording devices [3-6], etc.

In this work, we propose and analyze a few wave-like (physical optics) asymptotic approximations for the enhanced modeling of dielectric lenses in quasi-optical imaging systems of millimeter, submillimeter and infrared wave applications. For the comparison, we develop a full-wave solution of two-dimensional (2D) lens problem and use it as a benchmark for testing and validation of asymptotic models being proposed.

Exact methods for scattering problems are, typically, limited to systems of small size, often less than ten wavelengths in diameter. Besides, there is only a limited number of exact solutions for dielectric lenses described in the literature. One example is the modeling of a micro-cylindrical axilens [4] by using the integral equations with no regularization. Another example involves regularization in the problem of a body of special geometry considered as a resonator [7, 8]. A promising hybrid technique is developed for diffractive microlenses [3] where the finite difference method solves the problem in the near field and the partial plane wave propagation is used to transform the solution to the far field.

It seems, however, there are no exact solutions published for conventional lens geometries, e.g., for a common biconvex lens of standard shape. Similarly, there are no asymptotic methods developed for lenses that outperform simulations based on the ray tracing approach [9]. Conventional wave theory of lenses [9] is, in fact, the paraxial Fourier-optics, where non-paraxial cases are classified as a standing problem yet to

be solved. The same limitations and relevant approximations (scalar waves etc) lay in the basis of quasi-optical simulation models [1] which, therefore, do not account for polarization effects and non-paraxial issues in the interaction of electromagnetic waves with dielectric lenses.

In the meantime, lenses of intermediate quasi-optical size (a few dozens to a few hundreds of radiation wavelength) do, usually, require the account for both the large-angle incidence and the vector character of the electromagnetic field, while being too large for exact simulations. It is this kind of lenses that needs an enhanced physical optics asymptotic methods as those considered in this publication.

2. FULL-WAVE SIMULATIONS OF 2D DIELECTRIC LENSES

Full-wave analytic solutions for 2D dielectric lenses can be obtained by using cylindrical wave expansions of incident and scattered fields with respect to O_1 and O_2 frames associated with the circular arcs S_{1L} and S_{2L} that form the lens cross-section profile (Fig. 1).

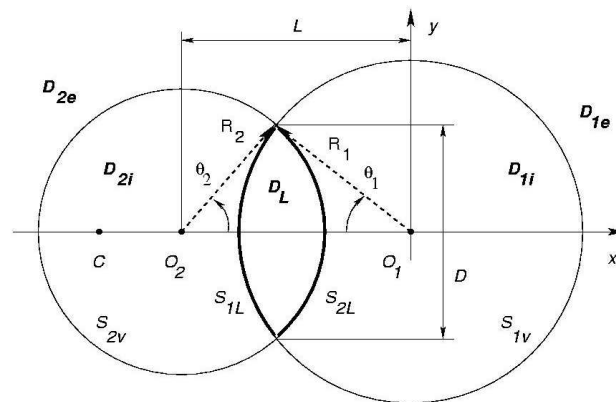


Figure 1. Geometry of a 2D dielectric lens (cross-section profile). The excitation wave of either TM ($E \parallel Oz$) or TE ($H \parallel Oz$) polarization is incident from the left.

The lens geometry is defined by the lens diameter D and the arc surface curvature radii R_1 and R_2 , respectively. The Neumann addition theorem for cylindrical functions is used for transforming the expansions from one frame to another when satisfying the boundary conditions for tangential field components at the lens surfaces. Because of rapid growth or decay of cylindrical functions with the angular harmonic index, direct solutions of this kind are limited to lenses of relatively small size (in practice, when R_1 and R_2 up to 10λ).

In this work, we consider waves of TE ($H \parallel Oz$) and TM ($E \parallel Oz$) polarization excited with two kinds of sources, namely, the uniform plane wave (PW) and cylindrical wave (CW) incident from the left. The incident wave in PW case propagates along the positive direction of x -axis. In CW case, the incident wave is radiated from a line source C in front of lens (a point source in xy -plane at the distance LC from O_1).

The results showing the wave focusing effects in both the PW and CW cases are plotted in Figs. 2-3. Power density P_z associated with E_z and H_z field components of TM and TE waves, respectively, is shown in the focal domain of lens in transverse (y) and longitudinal (x) cuts passing through the focal point F_1 . We choose the lens refractive index $n=1.5$ so that, in the case of PW incidence, the geometrical focal point F_1 of a thin symmetric lens coincides with the frame origin O_1 [10].

A common feature of these and other simulations is that the TE polarized waves produce a greater

power density at the focal point as compared to the TM waves of the same incident power. This is due to the difference in TE and TM wave transmission at oblique incidence at the lens surfaces as expressed by the Fresnel coefficients. The effect is more complicated for small lenses and cylindrical waves (Fig. 3, a), though, typically, it remains of a similar kind.

The second common feature is that the width of the focal spot defined as the distance between the first minima of the field is twice the wavelength in all the cases of PW focusing (Fig. 2, b). In the meantime, the width of diffraction fringes is one wavelength for lenses of different size, with nearly identical patterns in both polarizations. In the case of CW focusing, the focal spot is, typically, wider and the focusing effect is more complicated, see below.

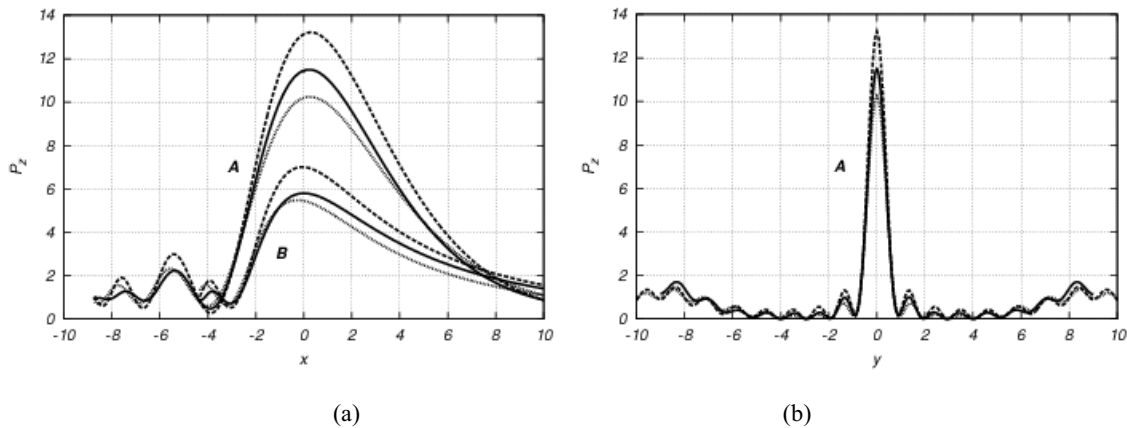


Figure 2. Exact (solid curves) and asymptotic solutions (dashed curves for RS2 and dotted curves for KU models, see below) in the case of TM PW incidence on a symmetric 2D dielectric lens: (a) x-cut and (b) y-cut of P_z power distribution behind the lens when $R_1=R_2=D$ (A and B groups of curves correspond to $D=12\lambda$ and $D=6\lambda$, respectively).

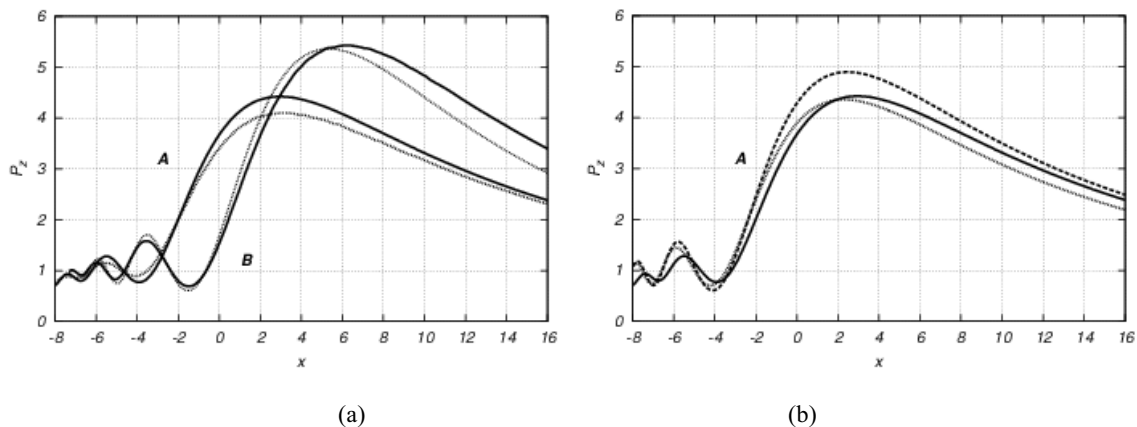


Figure 3. (a) Exact solutions in TE (solid curves) and TM (dotted curves) cases of CW incidence on a lens with $R_1=10\lambda$ when (A) $D=R_2=8\lambda$ and (B) $D=R_2=10\lambda$ at $LC=30\lambda$ and (b) the comparison of exact (solid curve) and asymptotic solutions (dashed curves for RS2 and dotted curves for KU models, see below) in case A of TE CW incidence.

3. PHYSICAL OPTICS MODELING OF DIELECTRIC LENSES

Asymptotic approximations proposed in this work are based on various forms of diffraction integrals [9] that represent wave propagation from the lens exit surface to the observation points behind the lens. The integral transforms of such a kind are needed in any near-field to far-field propagation in free space.

Inside the lens, propagation of the incident wave from the entrance surface S1L to the exit surface S2L can be evaluated by using the ray tracing through the lens body. In this work, the ray tracing is implemented with account of (a) the transmission Fresnel coefficients at S1L and S2L surfaces, (b) phase increments along the rays inside the lens and (c) wave amplitude increments (decrements) due to the ray convergence (divergence) because of refraction. This evaluation is quite accurate for typical lenses because of relatively short ray propagation path inside the lens as compared to the lens transverse dimensions.

The first method we consider is based on the two-term Kirchhoff diffraction integral. The integral is evaluated over the extended exit surface S2 that consists of the lens exit surface S2L and the free-space surface S2F extended from the lens rim to infinity in transverse direction. The first term depends on the wave amplitude U that is directly evaluated at the exit surface S2 as explained above. The second term depends on the normal derivative of U at S2, which is approximated by using the U values at S2 and the set of ray directions that define the inclination of the wave front (we denote this approach as KU model).

Another asymptotic model is obtained by using the one-term Rayleigh-Sommerfeld diffraction integral modified in a certain manner for non-planar (curved) exit surfaces. Since the idea of the original Rayleigh-Sommerfeld formulation is the choice of the Green's function that vanishes at the plane integration surface (thus, removing the second, poorly defined term in the Kirchhoff formulation), we further modify the Green's function to make it identically zero at the curved lens exit surface S2L while using the original form at the planar free-space surface S2F outside the lens. We denote this formulation as an RS2 model.

Notice, the Green's function defined above is an exact one for the domain of given geometry. It means that, assuming the field on the exit surface S2 is known precisely, the formulation is exact. Therefore, the RS2 model is superior to other forms of Rayleigh-Sommerfeld approach proposed for curved surfaces as, e.g., those where no modification of the Green's function is made [5] or an alternative four-term Green's function proposed [6] (which, however, generates entirely wrong results when tested in our simulations).

The comparison of KU and RS2 simulations with full-wave solutions is presented in Figs. 2 and 3 (b). The lenses considered are characterized by the focal length $f \sim D > \lambda$. In these and other simulations [10], KU and RS2 models show, generally, quite a good accuracy for various kinds of lenses and excitation waves. An interesting feature observed in asymptotic solutions is that the values of power density computed with KU and RS2 models usually provide the lower and upper bounds for the exact solution, respectively. Therefore, by combining both the KU and RS2 results, we can, to a certain extent, evaluate and improve the accuracy of asymptotic modeling.

Capabilities of asymptotic models in computing 2D field distributions are shown in Fig. 4. Fig. 4 (a) shows an exact TE power pattern in the focal domain of lens presented in case B of Fig. 3 (CW excitation by the line source at $LC=30\lambda$ when $D=R1=R2=10\lambda$). One can see a pair of specific fringes originating at the lens rim due to the edge diffraction (the waves aside of lens are partially suppressed by this effect near the lens rim). The lens is suspended freely in space as shown in Fig. 1.

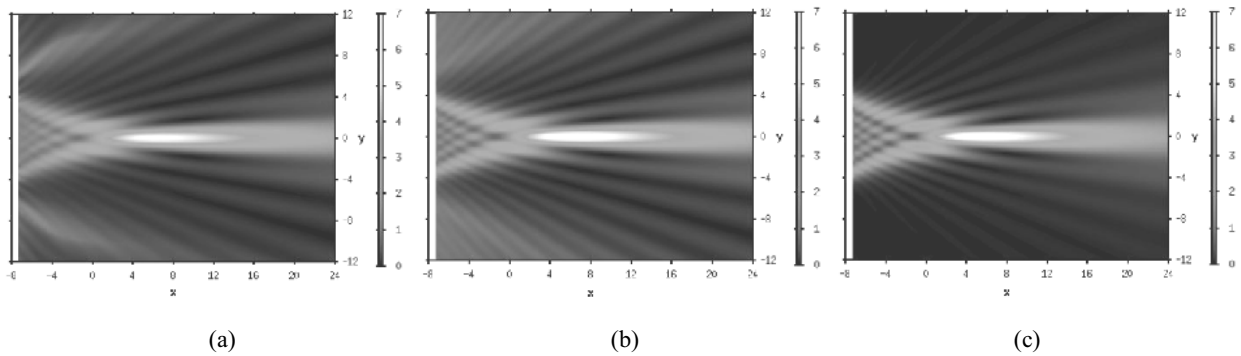


Figure 4. Power patterns behind the lens in case B of Fig. 3 in TE CW incidence: (a) exact solution for a lens suspended in free space, (b) RS2 simulation for the same case, and (c) RS2 simulation for the same lens mounted in a stop.

Fig. 4 (b) shows the pattern computed for the same lens with RS2 asymptotic model. There is a clear similarity between the patterns (a) and (b) in all the main features such as the focal spot, basic diffraction fringes in the focal domain, two rather bright caustics and even specific interference structure along the caustics consistent with fringes behind the lens. A noticeable difference is only the absence of significant edge diffraction and no suppression of waves aside the lens, respectively (there is no special account for edge diffraction in this model).

In practice, the lens is usually mounted in a stop that is not transparent for the incident waves. The stop is not accounted for by an exact solution described above. The asymptotic models can, however, easily account for the stop. Fig. 4 (c) shows the pattern computed with RS2 model for the same lens as described above, which is mounted in the stop. The stop is simulated as an absorbing screen orthogonal to the x -axis with an aperture of size D where the lens is fixed by its rim. The pattern shows significant suppression of the side waves behind the screen except those diffracted by lens, though all the wave features in the focal domain are the same as in Figs. 4 (a) and (b).

4. OPTIMAL ASYMPTOTIC APPROXIMATION FOR ASYMMETRIC LENSES

Generally, asymptotic models are more accurate for large lenses as compared to small ones. The shape of lens is, however, also significant. Essentially, there are two kinds of parameters that control the accuracy of simulations, (a) the lens curvature radii and (b) their ratios to the lens diameter (equivalently, the lens aperture angles). The discrepancy between KU and RS2 models decreases with increasing the size of lens, though the error is more significant for bulky lenses ($R_1, R_2 \sim D$), being the consequence of general difficulty in solving non-paraxial lens problems [9]. Thin lenses ($R_1, R_2 \gg D$) are much better simulated by asymptotic methods, including both the cases of symmetric and asymmetric lenses.

There is, however, a special case of bulky asymmetric lenses of essentially curved exit surface ($R_1 \gg R_2 \sim D$) when two asymptotic methods produce qualitatively different results (Fig. 5, a, dashed and dotted curves in case A). The difference is less pronounced for greater lenses, though the tendency remains the same. The effect signifies a failure of some sort of asymptotic modeling under certain conditions.

A detailed analysis revealed that, in these cases, we observe the effect of total internal reflection of rays passing near the lens rim. Due to this effect, no wave can propagate through the lens in the rim area

(Fig. 5, b). Moreover, the area near the rim where the wave would experience total internal reflection may be quite significant. Notice, even though both the KU and RS2 models take account of this effect by assigning zero wave amplitude in the relevant area on the exit surface, inconsistency of approximate field distributions (and also of the field normal derivative in the KU model) may be much too significant for certain models to be reliable.

In order to compare the applicability of different models for asymmetric lenses and find an optimal asymptotic method, we computed exact solutions in those cases where it was possible (Fig. 5, a, solid curves). The comparison of asymptotic and exact modeling has shown that the Rayleigh-Sommerfeld model RS2 based on the modified Green's function has an advantage over the Kirchhoff formulation KU. The reason for the advantage of RS2 model over the KU one (and, indeed, over other modifications of Rayleigh-Sommerfeld type of models [4-6]) is that, in this form, it uses an integral representation with an exact Green's function, which is chosen to precisely match the lens geometry. In all the cases considered, the RS2 method proved to be capable of rather accurate representation of waves of asymmetric lenses when compared to the exact solutions whereas the KU method failed substantially in these circumstances.

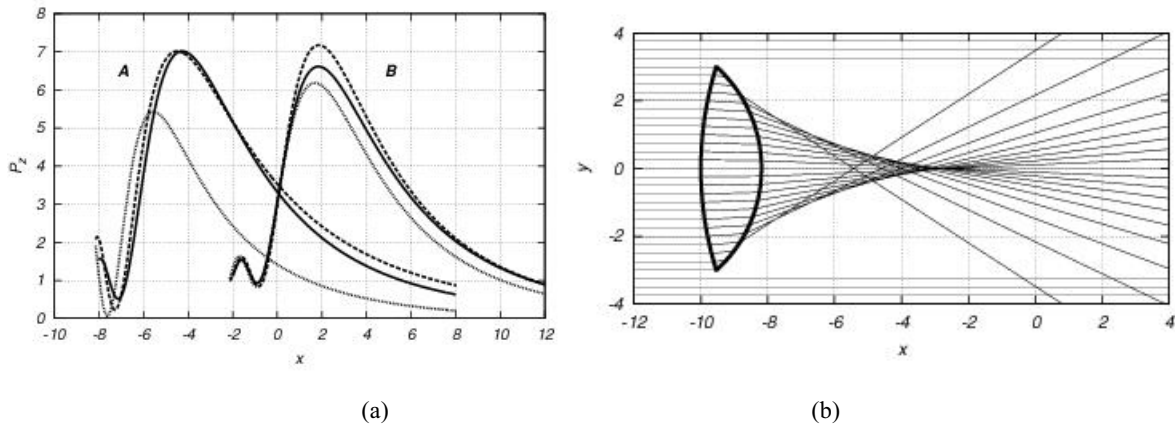


Figure 5. (a) Power density in the focal domain of a bulky asymmetric lens in A and B orientations ($D=6\lambda$, $R1=10\lambda$, $R2=4\lambda$ in case A) computed with KU (dotted curves) and RS2 (dashed curves) asymptotic methods as compared to exact solutions (solid curves), and (b) total internal reflection near the lens rim in case A as illustrated by ray tracing (a few rays near the rim in this plot do not propagate through the lens).

5. CONCLUSIONS

We proposed and analyzed a few asymptotic wave-like approximations for the accurate and efficient modeling of dielectric lenses used in quasi-optical systems of millimeter, submillimeter and infrared wave applications. For the comparison, we developed an exact full-wave analytic solution of two-dimensional focusing lens problem and used it as a benchmark for testing and validation of asymptotic models being proposed.

The main asymptotic methods considered are the two-term Kirchhoff model with an appropriate approximation of the normal derivative of complex wave amplitude at the lens surface (KU) and the one-term Rayleigh-Sommerfeld diffraction integral formulation modified for non-planar (curved) exit lens surfaces (RS2). The Rayleigh-Sommerfeld approximation modified for curved surfaces (RS2 model) is

found to be more general and better suited for various kinds of dielectric lenses, including symmetric and asymmetric, thin and thick, rather large and relatively small lenses.

Both the Kirchhoff model (KU) and the Rayleigh-Sommerfeld representation modified for non-planar surfaces (RS2) are remarkably accurate for large lenses ($f, D \gg \lambda$) where no total internal reflection effects occur (i.e., typically, for symmetric lenses or sufficiently thin asymmetric ones with relatively flat exit surface). Both the KU and RS2 approximations are also surprisingly accurate for small lenses, including microlenses, when both the lens diameter D and the focal length f are comparable with the radiation wavelength λ ($f \sim D \sim \lambda$), though small lenses have to be symmetric for minimizing the possibility of total internal reflection effects. The KU model fails, however, for bulky asymmetric lenses with rather convex exit surface ($R1 \gg R2 \sim D$) where the effect of total internal reflection occurs for the waves near the lens rim.

ACKNOWLEDGEMENT

The authors are grateful to J. A. Murphy for useful discussions.

REFERENCES

- [1] O'Sullivan, C. et al., "The quasi-optical design of the QUaD telescope," *Infrared Physics and Technology*, Vol. 51, 277–286, 2008.
- [2] Wenig, P., M. Schneider and R. Weigel, "Performance analysis of a cylindrical dielectric lens antenna for 77 GHz Automotive Radar," in *Proceedings of International Radar Symposium IRS'2008*, Wroclaw, Poland, May 2008, paper B1-1.
- [3] Feng, D. et al., "Axial focusing characteristics of diffractive microlenses based on a rigorous electromagnetic theory," *J. Opt. A Pure Appl. Opt.*, Vol. 6, No. 12, 1067–1071, 2004.
- [4] Ye, J.-S. et al., "Analysis of a closed-boundary axilens with long focal depth and high transverse resolution based on rigorous electromagnetic theory," *J. Opt. Soc. Am. A*, Vol. 19, No. 10, 2030–2035, 2002.
- [5] Ye, J.-S. et al., "Application of improved first Rayleigh-Sommerfeld method to analyze the performance of cylindrical microlenses with different f-numbers," *J. Opt. Soc. Am. A*, Vol. 22, No. 5, 862–869, 2005.
- [6] Duan, K. and B. Lu, "Improved diffraction integral for studying the diffracted field of a spherical microlens," *J. Opt. Soc. Am. A*, Vol. 22, No. 12, 2677–2681, 2005.
- [7] Boriskina, S. V. et al., "Accurate simulation of two-dimensional optical microcavities with uniquely solvable boundary integral equations and trigonometric Galerkin discretization," *J. Opt. Soc. Am. A*, Vol. 21, No. 3, 393–402, 2004.
- [8] Boriskina, A. V. et al., "Lens or resonator? Electromagnetic behavior of an extended hemielliptic lens for a submillimeter-wave receiver," *Microwave and Opt. Technol. Letters*, Vol. 43, No. 12, 515–518, 2004.
- [9] Walther, A., *The Ray and Wave Theory of Lenses*, Cambridge Univ. Press, Cambridge, 2006.
- [10] Yurchenko, V. B. and A. Altintas, "Asymptotic wave-like modeling of dielectric lenses," in *Proceedings of the 6th International Conference on Antenna Theory and Techniques (ICATT'2007)*, Sevastopol, Ukraine, September 2007, 93–98.

Adaptive Neuro-Fuzzy Inference System for Calculating the Characteristic Impedances of Multilayer Homogeneous Coupling Structures

M. Turkmen, S. Kaya, C. Yildiz, and K. Guney

Erciyes University, Faculty of Engineering,
Department of Electrical and Electronics Eng., 38039, Kayseri

Abstract – In this work, an alternative method based on adaptive neuro-fuzzy inference system (ANFIS) was introduced to compute the even- and odd-mode characteristic impedances of multilayer homogeneous coupling structures (MHCSs). The ANFIS is a fuzzy inference system (FIS) implemented in the framework of an adaptive fuzzy neural network. It has the advantages of expert knowledge of FISs and learning capability of artificial neural networks. A hybrid learning algorithm, which combines the least square method and the backpropagation algorithm, is used to identify the parameters of ANFIS. The ANFIS results are compared with the results available in the literature. There is very good agreement between the results of ANFIS models and conformal mapping method.

1. INTRODUCTION

Multilayer monolithic microwave integrated circuits (MMICs) which utilize narrow width microstrip lines on thin dielectric materials have received a widespread attention [1-3]. Furthermore, as a means of fabricating unique and multifunctional circuits, which are difficult in single layer configurations, these technologies have shown considerable capability. Various coupling structures incorporating multilayered dielectrics have been studied in the literature [4-8].

The multilayer homogeneous coupling structure (MHCS) was proposed and analyzed by Gillick et al. [5] in 1993. It offers reduced current crowding at the conductor edges, and is particularly suitable for integration with coplanar waveguide, slot line, and microstrip transmission lines in multilayer MMICs. The closed-form analytical formulas for the characteristic impedances and coupling coefficients of MHCS were derived by using conformal mapping method (CMM) in [5]. Synthesis formulas for computing the physical dimensions of MHCSs for the required design specifications have been proposed by Guney et al. [7, 8]. This kind of transmission lines can be analyzed by using quasi-static methods or full-wave methods. The methods used to obtain the characteristic parameters of the transmission lines have some disadvantages. While full-wave methods are the most accurate tools for obtaining the transmission line characteristics and analytically extensive, quasi-static methods are quite simple but do not threaten the dispersive nature of generic transmission line. So they are not very attractive for the interactive CAD models.

The adaptive neuro-fuzzy inference system (ANFIS) combines the benefits of artificial neural networks and fuzzy inference systems in a single model [9, 10]. Fast and accurate learning, excellent explanation facilities in the form of semantically meaningful fuzzy rules, the ability to accommodate both data and existing expert knowledge about the problem, and good generalization capability features have made neuro-fuzzy systems popular in the last few years [11-16]. A distinct advantage of the ANFIS computation is that, after proper training, ANFIS completely bypasses the repeated use of complex iterative processes for new cases presented to it. In this study, the even- and odd-mode characteristic impedances of MHCSs have been determined with the use of the ANFIS. In order to further validate the ANFIS method, the coupling coefficient is also calculated by using ANFIS results. Hybrid learning algorithm, which combines the least square method and the backpropagation algorithm, is used to identify the parameters of the ANFIS. The ANFIS results are in very good agreement with the results of CMM [5]. Consequently, these good agreements show the validation of the proposed ANFIS model.

2. DETERMINATION OF CHARACTERISTIC IMPEDANCES OF MHCSs BY USING CMM

The cross-section of a MHCS is depicted in Figure 1. In this figure, the total thickness of the dielectric material with relative permittivity ϵ_r is represented by $2H$, the conductor spacing between the coupled lines is illustrated by $2S$, and consequently the gap width in the center ground planes is given by $2W$. The placing of coupled lines, perpendicular to their ground planes, provides an improved alternative to coplanar edged coupled lines, where conductor edge current crowding needs to be minimized [5]. It is assumed that the ground planes are infinitely wide and all the conductors are infinitely thin and perfectly conducting.

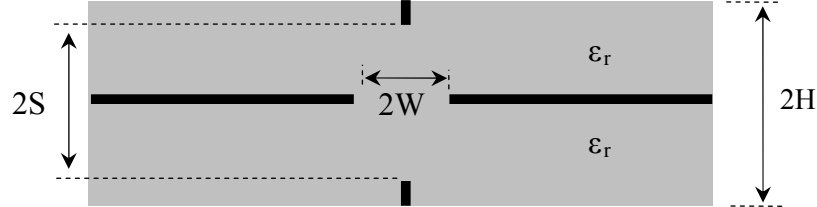


Figure 1. Cross-section of a MHCS.

The MHCS supports two fundamental modes, namely even and odd. The even- and odd-mode characteristic impedances (Z_0) of the MHCS can be evaluated by using the following formulas [5];

$$Z_{0(e)} = \frac{60\pi}{\sqrt{\epsilon_r}} \cdot \frac{K(k_1')}{K(k_1)} \quad (1)$$

and

$$Z_{0(o)} = \frac{60\pi}{\sqrt{\epsilon_r}} \cdot \frac{K(k_2')}{K(k_2)} \quad (2)$$

with

$$k_1 = \frac{\cos\left(\frac{\pi \cdot S}{2 \cdot H}\right)}{\cosh\left(\frac{\pi \cdot W}{2 \cdot H}\right)} \quad \text{and} \quad k_2 = \cos\left(\frac{\pi \cdot S}{2 \cdot H}\right) \quad (3)$$

where $K(k_i)$ and $K(k_i')$ are the complete elliptic integrals of the first kind with the modulus of k_i and k_i' . k_i' is a complementary modulus of k_i and equals to $(1 - k_i^2)^{1/2}$.

The coupling coefficient C_c is computed by using the following formula [5]

$$C_c = \frac{Z_{0(e)} - Z_{0(o)}}{Z_{0(e)} + Z_{0(o)}} \quad (4)$$

3. ADAPTIVE NEURO-FUZZY INFERENCE SYSTEM (ANFIS)

The FIS forms a useful computing framework based on the concepts of fuzzy set theory, fuzzy if-then rules, and fuzzy reasoning [9]. The ANFIS is a class of adaptive networks which are functionally equivalent to FISs. The ANFIS used in this article implements a first-order Sugeno fuzzy model. For this model, a typical rule set with two fuzzy if-then rules can be expressed as follows:

$$\text{Rule 1: If } x \in A_1 \text{ and } y \in B_1 \text{ then } z_1 = p_1x + q_1y + r_1 \quad (5)$$

$$\text{Rule 2: If } x \in A_2 \text{ and } y \in B_2 \text{ then } z_2 = p_2x + q_2y + r_2 \quad (6)$$

where A_i and B_i are the fuzzy sets in the antecedent, and p_i , q_i , and r_i are the design parameters that are determined during the training process. The ANFIS consists of five layers. Every node i in the first layer is an adaptive node with a node function:

$$O_i^1 = \mu_{A_i}(x), \quad i=1,2 \quad (7)$$

and

$$O_i^1 = \mu_{B_{i-2}}(y), \quad i=3,4 \quad (8)$$

where x (or y) is the input of node i . $\mu_{A_i}(x)$ and $\mu_{B_{i-2}}(y)$ can adopt any fuzzy membership function (MF). In this paper, the generalized bell MFs are used. Parameters in the first layer are referred to as *the premise parameters*. Every node in the second layer represents the firing strength of a rule by multiplying the incoming signals and forwarding the product as:

$$O_i^2 = \omega_i = \mu_{A_i}(x)\mu_{B_i}(y), \quad i=1,2 \quad (9)$$

The i th node in the third layer calculates the ratio of the i th rule's firing strength to the sum of all rules' firing strengths:

$$O_i^3 = \bar{\omega}_i = \frac{\omega_i}{\omega_1 + \omega_2}, \quad i=1,2 \quad (10)$$

where $\bar{\omega}_i$ is referred to as *the normalized firing strengths*. The node function in the fourth layer is represented by

$$O_i^4 = \bar{\omega}_i z_i = \bar{\omega}_i(p_i x + q_i y + r_i), \quad i=1,2 \quad (11)$$

where $\bar{\omega}_i$ is the output of layer 3, and $\{p_i, q_i, r_i\}$ is the parameter set. Parameters in this layer are referred to as *the consequent parameters*.

The single node in the fifth layer computes the overall output as the summation of all incoming signals, which is expressed as:

$$O_1^5 = \sum_{i=1}^2 \bar{\omega}_i z_i = \frac{\omega_1 z_1 + \omega_2 z_2}{\omega_1 + \omega_2} \quad (12)$$

When the premise parameter values of the MF are fixed, the output of the ANFIS can be written as a linear combination of the consequent parameters:

$$z = (\bar{\omega}_1 x)p_1 + (\bar{\omega}_1 y)q_1 + (\bar{\omega}_1)r_1 + (\bar{\omega}_2 x)p_2 + (\bar{\omega}_2 y)q_2 + (\bar{\omega}_2)r_2 \quad (13)$$

The least square method can be used to find the optimal values of the consequent parameters. When the premise parameters are not fixed, the search space becomes larger and the convergence of training becomes slower. The hybrid learning algorithm [9, 10] combining the least-square method and the backpropagation algorithm can be used to solve this problem.

4. APPLICATION TO THE PROBLEM

In this work, the ANFIS successfully introduced to determine the even- and odd-mode characteristic impedances of MHCS. The inputs of ANFIS are β , ε_r , W/H , and S/H , and the output is the characteristic impedance. β is a constant, and $\beta = 1$ and $\beta = 10$ are used to compute even- and odd-mode characteristic impedance of MHCS, respectively. The ANFIS model used in computing the

characteristic impedances of MHCSs is shown in Figure 2. 1701 data sets have been used to train the ANFIS models. The ranges of training data sets are among $2 \leq \epsilon_r \leq 21$, $0.1 \leq W/H \leq 2.0$, and $0.01 \leq S/H \leq 0.98$. 972 data sets, which are completely different from training data set, were used for testing the models. Training an ANFIS with the use of the hybrid learning algorithm to compute the even- and odd-mode characteristic impedances of MHCSs involves presenting it sequentially with different sets (β , ϵ_r , W/H , and S/H) and corresponding characteristic impedances (Z_0). Differences between the target outputs and the actual outputs of the ANFIS are evaluated by the hybrid-learning algorithm. The adaptation is carried out after the presentation of each set (β , ϵ_r , W/H , and S/H) until the calculation accuracy of the ANFIS is deemed satisfactory according to some criterion (for example, when the errors between target and the actual output for all the training set falls below a given threshold) or when the maximum allowable number of epochs is reached. The number of epoch was 500 for training. Three MFs are used for each input variables. The number of rules is then 81 ($3 \times 3 \times 3 \times 3 = 81$). The generalized bell MFs are specified by three parameters. Therefore, the ANFIS used here contains a total of 441 fitting parameters, of which 36 ($3 \times 3 + 3 \times 3 + 3 \times 3 + 3 \times 3 = 36$) are the nonlinear parameters and 405 ($5 \times 81 = 405$) are the linear parameters.

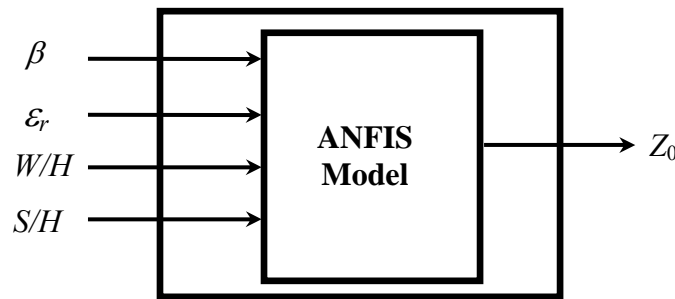


Figure 2. ANFIS model for characteristic impedances of MHCS.

5. RESULTS AND CONCLUSION

The even- and odd-mode characteristic impedance test results obtained by using ANFIS model are compared with the results of the CMM [5] in Figure 3. This figure illustrates how the even- and odd-mode characteristic impedances of MHCS varies with S/H for different values of W/H where $\epsilon_r = 9$ and $H = 400 \mu\text{m}$. It should be noted that the odd-mode characteristic impedances ($Z_{0(o)}$) of MMCSs does not depend on the gap width W [5]. It is clear from Figure 3 that the results of ANFIS are in very good agreement with the results of the CMM. This very good agreement supports the validity of ANFIS method proposed in this study.

It is apparent from eq. (4) that the values of the coupling coefficient can be calculated by using the even- and odd-mode characteristic impedance values obtained from the ANFIS. In order to further validate the ANFIS method, the coupling coefficient is also calculated by using ANFIS results. The test results of ANFIS for the coupling coefficient are compared with the results CMM [5] in Figure 4 for $\epsilon_r = 9$ and $H = 400 \mu\text{m}$. It is clear from Figure 4 that the ANFIS results are in very good agreement with the results of CMM.

As a consequence, a new method based on the ANFIS was successfully introduced to compute the even- and odd-mode characteristic impedances of MHCS. The coupling coefficient is also computed by using ANFIS results. The close agreement is satisfied between the results available in the literature. A hybrid learning algorithm is used to optimize the parameters of ANFIS. In this algorithm, the parameters defining the shape of the MFs are identified by the backpropagation algorithm while the consequent parameters are identified by the least square method. The main advantage of the method proposed here is that only one ANFIS model is used to calculate both the even- and odd-mode characteristic impedances of MHCSs. This method can easily be applied to other microwave problems. The ANFIS offers an accurate and efficient alternative to previous techniques for the calculating the characteristic impedances of MHCSs.

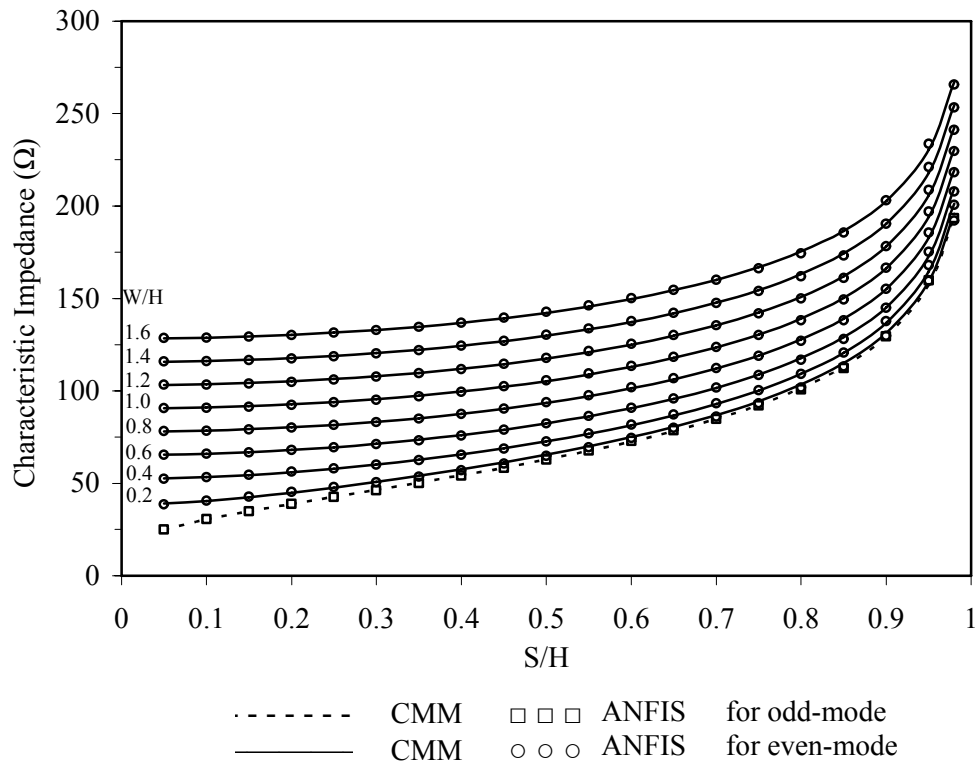


Figure 3. Comparison results of ANFIS and CMM [5] for the even- and odd-mode characteristic impedances of MHCS with $\epsilon_r = 9$ and $H = 400 \mu\text{m}$.

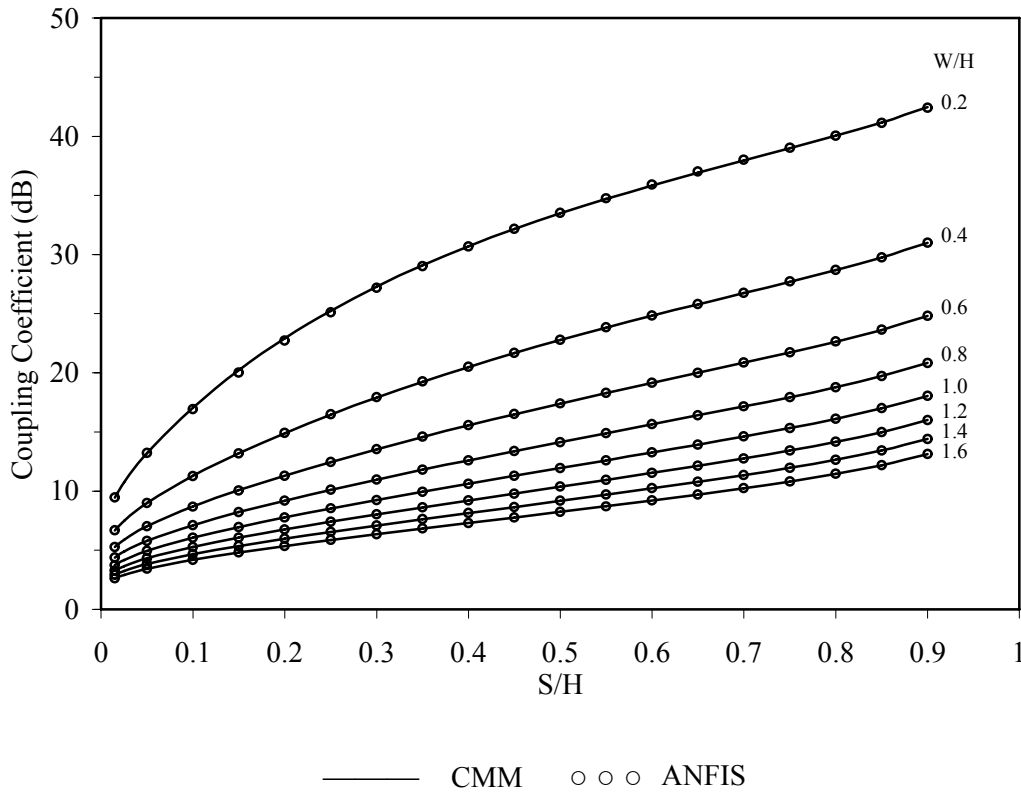


Figure 4. Comparison results of ANFIS and CMM [5] for coupling coefficients of MHCSs with $\epsilon_r = 9$ and $H = 400 \mu\text{m}$.

ACKNOWLEDGMENT

The work described in this paper is supported by The Scientific and Technological Research Council of Turkey, 2008, Project No: TUBITAK - 107E258.

REFERENCES

- [1] Ogawa, H., T. Hasegawa, S. Banba, and H. Nakamoto, "MMIC transmission lines for multilayered MMIC's," in *IEEE MTT-S Dig*, 1991, 1067-1070.
- [2] Hirota, T., A. Minakawa, and M. Muraguchi, "Reduced-size branch-line and rat-race hybrids for uniplanar MMIC's," *IEEE Trans Microwave Theory Tech.*, Vol. 38, 270-275, 1990.
- [3] Hasegawa, T., S. Banba, H. Ogawa, and H. Nakamoto, "Characteristics of valley microstrip lines for use in multilayer MMIC's," *IEEE Microwave Guided Wave Lett.*, Vol. 1, 275-277, 1991.
- [4] Toyoda, I., T. Hirota, T. Hiraoka, and T. Tokumitsu, "Multilayer MMIC branch-line coupler and broad-side coupler," in *IEEE Microwave and Millimeter-Wave Monolithic Circuits Symp*, 1992, 79-82.
- [5] Gillick, M., I. D. Robertson, and J. S. Joshi, "Design analysis of novel coupling structures for multilayer MMIC's," *IEEE Trans Microwave Theory Tech.*, Vol. 41, 346-349, 1993.
- [6] Banba, S. and H. Ogawa, "Multilayer MMIC directional couplers using thin dielectric layers," *IEEE Trans Microwave Theory Tech.*, Vol. 43, 1270-1275, 1995.
- [7] Guney, K., C. Yildiz, S. Kaya, and M. Turkmen, "New and accurate synthesis formulas for multilayer homogeneous coupling structure," *Microwave and Optical Technology Letters*, Vol. 49, No. 10, 2486-2489, 2007.
- [8] Guney, K., C. Yildiz, S. Kaya, and M. Turkmen, "Synthesis formulas for multilayer homogeneous coupling structure with ground shielding," *Journal of Electromagnetic Waves and Applications*, Vol. 21, No. 14, 2073-2084, 2007.
- [9] Jang, J.-S. R., "ANFIS: Adaptive-network-based fuzzy inference system," *IEEE Trans Systems Man and Cybernetics*, Vol. 23, 665-685, 1993.
- [10] Jang, J.-S. R., C. T. Sun, and E. Mizutani, *Neuro-Fuzzy and Soft Computing: A Computational Approach to Learning and Machine Intelligence*, Prentice-Hall, Upper Saddle River, NJ, 1997.
- [11] Brown, M. and C. Haris, *Neuro-Fuzzy Adaptive Modeling and Control*, Prentice-Hall, Englewood Cliffs, NJ, 1994.
- [12] Kim, J. and N. Kasabov, "Hy FIS: Adaptive neuro-fuzzy inference systems and their application to nonlinear dynamical systems," *Neural Networks*, Vol. 12, 1301-1319, 1999.
- [13] Rahouyi, E. B., J. Hinojosa, and J. Garrigos, "Neuro-fuzzy inference modeling techniques for microwave components," *IEEE Microwave and Wireless Components Letters*, Vol. 16, 72-74, 2006.
- [14] Ubeyli, E. D. and I. Guler, "Adaptive neuro-fuzzy inference system to compute quasi-TEM characteristic parameters of microshield lines with practical cavity sidewall profiles," *Neurocomputing*, Vol. 70, 196-304, 2006.
- [15] Turkmen, M., S. Kaya, C. Yildiz, and K. Guney, "Adaptive neuro-fuzzy models for conventional coplanar waveguides," *Progress In Electromagnetics Research B*, Vol. 6, 93-107, 2008.
- [16] Yildiz, C., K. Guney, M. Turkmen, and S. Kaya, "Adaptive neuro-fuzzy models for the quasi-static analysis of microstrip line," *Microwave and Optical Technology Letters*, Vol. 50, No. 5, 1191-1196, 2008.

Remote Experimentation in RF and Microwaves

Ali Kara¹, Elif Uray Aydın¹, Mehmet Efe Özbek¹, Nergiz Çağiltay², Ruşen Öktem¹, Cansu Çiğdem Aydın³, Erdem Özyurt¹, Musa Ataş⁴ and Alparslan Çağrı Yapıcı¹

⁽¹⁾ Department of Electrical and Electronics Engineering
Atılım University
Incek, Ankara

⁽²⁾ Department of Software Engineering
Atılım University
Incek, Ankara

⁽³⁾ Department of Management
Atılım University
Incek, Ankara

⁽⁴⁾ Informatic Institute
Middle East Technical University
Ankara

This study presents an initiative (European remote Radio Laboratory-ERRL) that aims to develop a remote laboratory platform to provide theoretical and particularly practical RF and Microwaves training to engineering students, graduates and other technical personnel via distant access to high technology equipment through the Internet. As a transnational laboratory, the ERRL intends to allow its users perform web-based experiments, and follow related course materials in Radio frequency (RF), microwave and communication field.

ERRL experimental content includes wide range of areas in RF and microwaves: from reflection and transmission (return loss, SWR, reflection coefficient) concepts to modulations, antenna measurements and time and frequency analysis of signals using state of the art instrumentation including spectrum analyzer, vector network analyzer (VNA) and a digital oscilloscope at various frequency ranges.

aktif nesar

AWR

Applied Wave Research

CST



GATE
ELEKTRONİK



keytek



ANTALYA ENERJİ ÜRETİM A.Ş.
ELEKTRİK SANTRALI